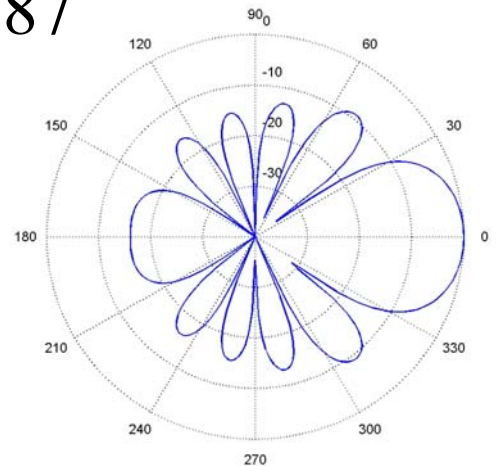
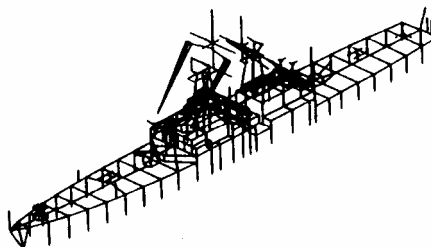
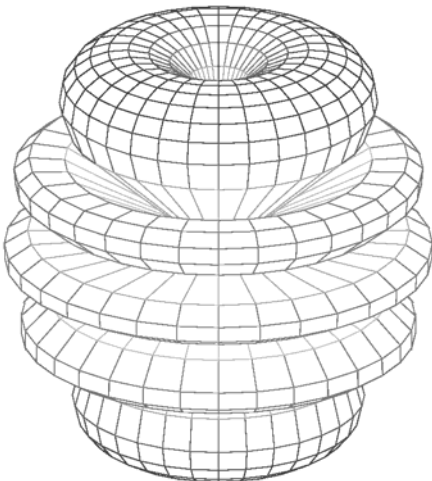
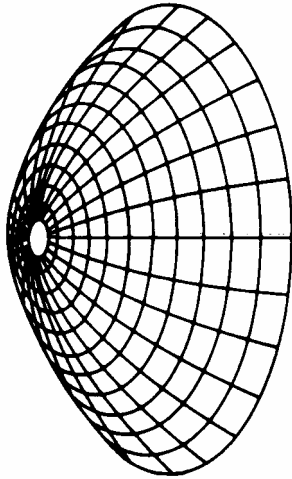
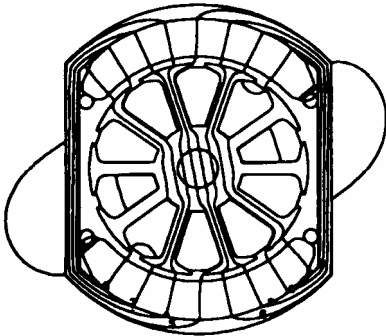
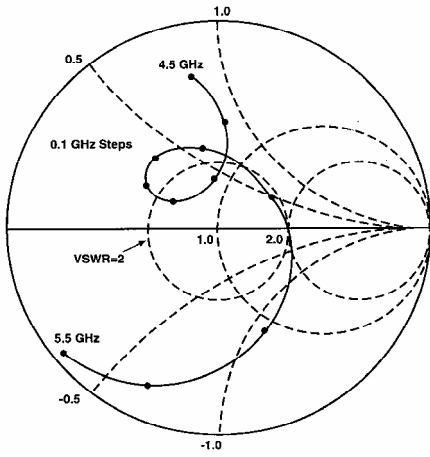


Applied Computational Electromagnetics Society Journal

Editor-in-Chief
Atef Z. Elsherbeni

October 2009
Vol. 24 No. 5
ISSN 1054-4887



GENERAL PURPOSE AND SCOPE: The Applied Computational Electromagnetics Society (*ACES*) Journal hereinafter known as the *ACES Journal* is devoted to the exchange of information in computational electromagnetics, to the advancement of the state-of-the art, and the promotion of related technical activities. A primary objective of the information exchange is the elimination of the need to “re-invent the wheel” to solve a previously-solved computational problem in electrical engineering, physics, or related fields of study. The technical activities promoted by this publication include code validation, performance analysis, and input/output standardization; code or technique optimization and error minimization; innovations in solution technique or in data input/output; identification of new applications for electromagnetics modeling codes and techniques; integration of computational electromagnetics techniques with new computer architectures; and correlation of computational parameters with physical mechanisms.

SUBMISSIONS: The *ACES Journal* welcomes original, previously unpublished papers, relating to applied computational electromagnetics. Typical papers will represent the computational electromagnetics aspects of research in electrical engineering, physics, or related disciplines. However, papers which represent research in applied computational electromagnetics itself are equally acceptable.

Manuscripts are to be submitted through the upload system of *ACES* web site <http://aces.ee.olemiss.edu> See “Information for Authors” on inside of back cover and at *ACES* web site. For additional information contact the Editor-in-Chief:

Dr. Atef Elsherbeni

Department of Electrical Engineering
The University of Mississippi
University, MS 386377 USA
Phone: 662-915-5382 Fax: 662-915-7231
Email: atef@olemiss.edu

SUBSCRIPTIONS: All members of the Applied Computational Electromagnetics Society who have paid their subscription fees are entitled to receive the *ACES Journal* with a minimum of three issues per calendar year and are entitled to download any published journal article available at <http://aces.ee.olemiss.edu>.

Back issues, when available, are \$15 each. Subscriptions to *ACES* is through the web site. Orders for back issues of the *ACES Journal* and changes of addresses should be sent directly to *ACES*:

Dr. Allen W. Glisson

302 Anderson Hall
Dept. of Electrical Engineering
Fax: 662-915-7231
Email: aglisson@olemiss.edu

Allow four week’s advance notice for change of address. Claims for missing issues will not be honored because of insufficient notice or address change or loss in mail unless the Executive Officer is notified within 60 days for USA and Canadian subscribers or 90 days for subscribers in other countries, from the last day of the month of publication. For information regarding reprints of individual papers or other materials, see “Information for Authors”.

LIABILITY. Neither *ACES*, nor the *ACES Journal* editors, are responsible for any consequence of misinformation or claims, express or implied, in any published material in an *ACES Journal* issue. This also applies to advertising, for which only camera-ready copies are accepted. Authors are responsible for information contained in their papers. If any material submitted for publication includes material which has already been published elsewhere, it is the author’s responsibility to obtain written permission to reproduce such material.

APPLIED COMPUTATIONAL ELECTROMAGNETICS SOCIETY JOURNAL

Editor-in-Chief
Atef Z. Elsherbeni

October 2009
Vol. 24 No. 5
ISSN 1054-4887

The ACES Journal is abstracted in INSPEC, in Engineering Index, DTIC, Science Citation Index Expanded, the Research Alert, and to Current Contents/Engineering, Computing & Technology.

The first, fourth, and sixth illustrations on the front cover have been obtained from the Department of Electrical Engineering at the University of Mississippi.

The third and fifth illustrations on the front cover have been obtained from Lawrence Livermore National Laboratory.

The second illustration on the front cover has been obtained from FLUX2D software, CEDRAT S.S. France, MAGSOFT Corporation, New York.

THE APPLIED COMPUTATIONAL ELECTROMAGNETICS SOCIETY

<http://aces.ee.olemiss.edu>

ACES JOURNAL EDITOR-IN-CHIEF

Atef Elsherbeni

University of Mississippi, EE Dept.
University, MS 38677, USA

ACES JOURNAL ASSOCIATE EDITORS-IN-CHIEF

Sami Barmada

University of Pisa, EE Dept.
Pisa, Italy, 56126

Erdem Topsakal

Mississippi State University, EE Dept.
Mississippi State, MS 39762, USA

Fan Yang

University of Mississippi, EE Dept.
University, MS 38677, USA

ACES JOURNAL EDITORIAL ASSISTANTS

Matthew J. Inman

University of Mississippi, EE Dept.
University, MS 38677, USA

Mohamed Al Sharkawy

Arab Academy for Science and Technology
ECE Dept.
Alexandria, Egypt

ACES JOURNAL EMERITUS EDITORS-IN-CHIEF

Duncan C. Baker

EE Dept. U. of Pretoria
0002 Pretoria, South Africa

Allen Glisson

University of Mississippi, EE Dept.
University, MS 38677, USA

David E. Stein

USAF Scientific Advisory Board
Washington, DC 20330, USA

Robert M. Bevensee

Box 812
Alamo, CA 94507-0516, USA

Ahmed Kishk

University of Mississippi, EE Dept.
University, MS 38677, USA

ACES JOURNAL EMERITUS ASSOCIATE EDITORS-IN-CHIEF

Alexander Yakovlev

University of Mississippi, EE Dept.
University, MS 38677, USA

OCTOBER 2009 REVIEWERS

Rene Allard

Sami Barmada

Indira Chatterjee

William Davis

Nihad Dib

Alistar Duffy

Teixeira Fernando

Ali Gharsallah

Todd Hubing

Darko Kajfez

Fernando Las-Heras

Natalia Nikolova

Kubilay Sertel

Christopher Trueman

Shaoqiu Xiao

Fan Yang

THE APPLIED COMPUTATIONAL ELECTROMAGNETICS SOCIETY
JOURNAL

Vol. 24 No. 5

October 2009

TABLE OF CONTENTS

“New Compact and Broadband Patch Antenna Configurations for Wireless Applications” A. F. Almutairi, N. A. Aljuhaishi, and S. F. Mahmoud.....	437
“Design and Optimization of Single, Dual, and Triple Band Transmission Line Matching Transformers for Frequency-Dependent Loads” M. Khodier.....	446
“Scan Angle Extension by Array with Pattern Reconfigurable Elements” S. Xiao, Y.-Y. Bai, B.-Z. Wang, and S. Gao.....	453
“Quantitative Analysis of Breast Skin for Tumor Detection Using Electromagnetic Waves” D. A. Woten and M. El-Shenawee.....	458
“High Reflector by One-dimensional Quasi-Periodic Thue-Morse Multilayered Band Gap Structure at Ultra High Frequency Band” Y. Trabelsi, N. Ben Ali, Y. Bouazzi, and M. Kanzari.....	464
“Simulation of Lightning Return Stroke Currents and Its Effect to Nearby Overhead Conductor” M. O. Goni, E. Kaneko, and A. Ametani.....	469
“Dispersion Analysis of a Negative Group Velocity Medium with MATLAB” G. Monti and L. Tarricone.....	478
“RCS Estimation of 3D Metallic Targets Using the Moment Method and Rao-Wilton-Glisson Basis Functions” G. K. Carvajal, D. J. Duque, and A. J. Zozaya.....	487
“A Fast Spectral Domain Solver for the Characterization of Larger Microwave Structures in Multilayered Environments” T. Vaupel.....	493
“An Adaptive Approximate Inverse-Based Preconditioner Combined with the Fast Multipole Method for Solving Dense Linear Systems in Electromagnetic Scattering” B. Carpentieri.....	504

“Fast and Accurate Cascaded Particle Swarm Gradient Optimization Method for Solving 2-D Inverse Scattering Problems”
M. Farmahini-Farahani, R. Faraji-Dana, and M. Shahabadi.....511

“Layer-Based Integration Arithmetic of Conformal PML”
Y. J. Zhang and Q. Sun.....518

New Compact and Broadband Patch Antenna Configurations for Wireless Applications

A. F. Almutairi, N. A. Aljuhaishi, and S. F. Mahmoud

EE Dept., Kuwait University, P.O. Box 5969, Safat, 13060, Kuwait
alialmut@eng.kuniv.edu.kw

Abstract – We present new compact patch antenna configurations with broadband capabilities for wireless applications. Analytical, simulation, and experimental work is performed on semi-circular and quarter-circular patch antennas with a shorting pin. The resonant frequencies and radiation fields of the dominant cavity modes of the shorted patch are derived. For the shorted semi-circular patch, the broadband operation is based on the efficient excitation of two staggered modes of the patch. It is shown that a relative bandwidth of 58% is achieved with a patch area that is only 13.6% of the central wavelength squared. The shorted quarter circular patch with the same radius as the half circular one provides a relative bandwidth of about 30%.

Keywords: Patch antennas, shorted patch, cavity modes, compact antennas, and wideband wireless communication.

I. INTRODUCTION

With the advancement of wireless communication services and networks, broadband operation and compact size have become essential parts of antenna design. Due to their many advantages, microstrip antennas are leading candidates for use in many fixed and portable wireless devices. Microstrip antennas are known for their low fabrication cost using printed circuit technology, light weight, low profile configuration, conformability to mounting host, and easy integration with microwave circuits on the same substrate [1-3]. Furthermore, they can easily produce linear polarization (LP) and circular polarization (CP) and they can be made in a compact form [4-6]. On the other hand, microstrip antennas suffer from some disadvantages such as low power handling capability. Therefore, they cannot be used in high power stages of radar and high power transmitters. However, they can be used in low power transmitters and wireless receivers in systems such as Bluetooth, Wi-Fi, Wi-Max, and ultrawideband (UWB).

Increasing the bandwidth of microstrip antennas has been an active and attractive research goal in the field of antenna's design. Efforts concentrating on broadening the bandwidth have been described in details in [7,8] and the

references within. Reducing the size of microstrip antenna patch to be hosted in hand held wireless devices has also attracted many researchers lately. Effective ways of reducing the size of an antenna patch include patch loading by shorting posts [9,10] and/or introducing slots in the patch as has been detailed out in [11,12].

Microstrip patch antennas are widely designed to operate in the broad range of frequency from few hundreds of MHz to several GHz [8]. Several designs of microstrip antennas have been proposed in the literature to operate as multiband or broadband antennas. For example, a multiband H-shaped microstrip antenna designed to support modes with resonance frequencies at 2.2 GHz, 2.8 GHz, 3 GHz, and 5 GHz has been presented in [13]. Dual, triple, or quad band operations of the H-antenna were possible by the proper location of the coaxial feed in order to excite the required modes. An E-shaped wideband microstrip antenna design is proposed in [14] and a bandwidth of about 32.3% is achieved. The antenna is designed by incorporating two parallel slots into a square patch antenna to expand the bandwidth. In [15], a rectangular patch with a U-shaped slot is introduced as a broadband antenna with 27.5 % bandwidth referenced to the center frequency 1815 MHz. A compact polygonal patch antenna is achieved by designing a compact reactive ground plane made of a pattern of metallic patches [16]. A compact Y-shaped patch antenna that has two feeder ports and can be utilized in compact wireless devices to provide diversity signal or as a duplexer has been proposed in [17]. The effect of feed shape on the antenna bandwidth is studied in [18] where a rectangular microstrip antenna with an L-shaped probe is introduced. The L-shaped feed is shown to provide impedance matching over a broad band and a 28% bandwidth is reported. A modified bow-tie patch antenna has been introduced by Eldek et al [19] to operate in the wide band 5.5-12.5 GHz covering the C- and X bands. A circular microstrip patch antenna with a shorting post has been proposed and analyzed [20]. The authors show analytically that for a given operating frequency, a considerable reduction of patch size is possible by exciting the dominant mode. The analysis has been also extended to a 2-pin loaded circular patch [21], which can then operate as a dual or triple band antenna. The same

patch antenna can operate as a wideband antenna as shown in [22] where a bandwidth as high as 45% of the central frequency has been demonstrated.

In this paper, we propose a pin-loaded half and quarter circular patch antenna designs. In addition to their reduced patch size, these designs have wideband characteristics and can be used in many wireless devices. First, theory of the cavity modes of the pin loaded half circular patch is presented. The theoretical results lead to universal design curves for multiband or broadband operation of the antenna, so that an initial selection of the patch dimensions can be made. Simulations are then used to refine the design for a broadband operation. Simulation and experimental results are presented here to show the characteristics of the half and quarter circular patch antenna designs. As will be shown in the next section, compact and broadband performance is achieved by the proposed designs.

The rest of the paper is organized as follows: In section II, designs of broadband half and quarter circular patch antennas are outlined. In section III, computational results of selected antenna designs are presented. Experimental results for half and quarter circular antennas are shown, in section IV and concluding remarks are presented in section V.

II. ANALYSIS OF A SEMICIRCULAR PATCH ANTENNA

The purpose of this section is to find an analytical solution to the cavity modes on a half circular patch. As depicted in Fig. 1(a), a half circular patch of radius (a) lies on a grounded dielectric layer of thickness (h) and relative dielectric constant (ϵ_r). The patch is shorted at ($r=r_0$, $\phi=+\alpha$) by a shorting pin of radius (b) which is assumed much less than the patch radius. For an electrically thin substrate ($kh \ll 1$), the modal fields are independent of the z -coordinate so that the dominant modes are TM to z modes where E_z is the only nonzero component of the electric field. Adopting the cavity model for the patch, the planar boundary ($\phi = 0, \pi$) and the circular cylindrical boundary $r = a (0 \leq \phi < \pi)$ are considered to behave as magnetic walls. To account for field fringing, we take (a) as an effective radius which is slightly greater than the physical radius and given by well known formulae [1].

Since the plane ($\phi = 0, \pi$) is considered as a magnetic wall, E_z being tangential to the plane will have a peak value on it. Hence, it is allowable to write $E_z(r, \phi)$ for a given cavity mode as,

$$E_z(r, \phi) = \sum_{n=0}^{\infty} A_n \cos(n\phi) J_n(kr) \exp(j\omega_r t) \quad (1)$$

for $0 \leq r \leq r_0$, and,

$$E_z(r, \phi) = \sum_{n=0}^{\infty} B_n \cos(n\phi) [J_n(kr) Y_n'(ka) - J_n'(ka) Y_n(kr)] \exp(j\omega_r t) \quad (2)$$

for $r_0 \leq r \leq a$, where ω_r is the cavity mode resonant frequency and $k = \omega_r \sqrt{\epsilon_o \epsilon_r \mu_o}$. The functions $J_n(x)$ and $Y_n(x)$ are the Bessel functions of first and second kind and the prime stands for differentiation with respect to the argument.

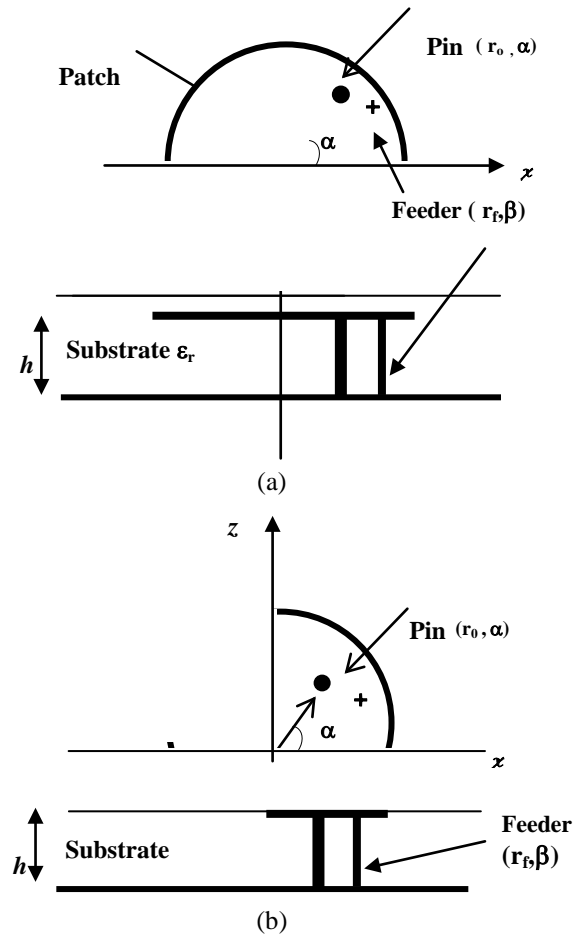


Fig. 1. Geometry of the proposed antennas composed of a half and quarter circular patch of radius " a " that is loaded by a pin and fed by a coaxial line. The pin of radius " b " is located at (r_0, α°) and the feed position at (r_f, β°) .

In equation (2), it is guaranteed that $\partial E_z / \partial r$ is equal to zero at $r = a$ which amounts to $H_\phi = 0$ on the magnetic wall. Next, we enforce the boundary condition at the pin position $r = r_0$. These conditions require the continuity of E_z across $r = r_0$ and the discontinuity of H_ϕ by the pin current. Enforcing these two boundary conditions, we get,

$$A_n J_n(kr_0) =$$

$$B_n [J_n(kr_o)Y_n'(ka) - J_n'(ka)Y_n(kr_o)], \quad (3)$$

$$H_\phi(r_o^+) - H_\phi(r_o^-) = \int_r J_z(r, \phi) r_o d\phi = I \delta(\phi - \alpha) \quad (4)$$

where $J_z(r, \phi)$ is the pin current density and ' I ' is the total pin current, assumed concentrated on its axis. since $H_\phi = \frac{-1}{j\omega\mu} \frac{\partial E_z}{\partial r}$, equation (4) leads to,

$$-\frac{1}{j\omega\mu} \left\{ \sum_{n=0}^{\infty} B_n \cos(n\phi) k [J_n'(kr_o) Y_n'(ka) - J_n'(ka) Y_n'(kr_o)] - \sum_{n=0}^{\infty} A_n \cos n\phi (kJ_n'(kr_o)) \right\} = I \delta(\phi - \alpha) = \frac{2I}{\pi} \sum_{n=0}^{\infty} \chi_n \cos n\phi \cdot \cos n\alpha$$

where $\chi_n = 1$ for $n \geq 1$, and $\chi_0 = 1/2$ for $n = 0$.

Equating coefficient of $\cos n\phi$ on both side of the above equation, we get,

$$I \frac{2}{\pi} \chi_n \cos n\alpha = \frac{-k}{j\omega\mu} [B_n (J_n'(kr_o) Y_n'(ka) - J_n'(ka) Y_n'(kr_o))] + \frac{k}{j\omega\mu} [A_n J_n'(kr_o)] \quad (5)$$

using equations (2) and (5), we get the coefficient A_n and B_n ,

$$A_n = j\omega\mu I \chi_n \cos n\alpha \frac{J_n(kr_o) Y_n'(ka) - J_n'(ka) Y_n(kr_o)}{J_n'(ka)}$$

$$B_n = j\omega\mu I \chi_n \cos n\alpha \frac{J_n(kr_o)}{J_n'(ka)} \quad (6)$$

where we have used the Wronskian relation $J_n(x) Y_n'(x) - J_n'(x) Y_n(x) = 2/\pi x$.

Finally, the modal equation for the resonant frequency ω_r is obtained by imposing the boundary condition of vanishing E_z at the pin surface. Since the pin radius (b) is assumed very small relative to the field spatial variation, we are allowed to satisfy the vanishing of E_z at one line on the pin surface; say line ($r = r_o - b$, $\phi = \alpha$). So, using equation (1) and enforcing $E_z(r_o - b, \phi)$ to be zero, after some manipulations we get:

$$Y_o(kb) \pm Y_o(2kr_o \sin \alpha) - 4 \sum_{n=0}^{\infty} \chi_n \cos^2 \alpha [J_n(k(r_o - b) J_n(kr_o))] \frac{Y_n'(ka)}{J_n'(ka)} = 0 \quad (7)$$

which is the modal equation for the normalized resonant frequencies ka , where $ka = \omega_r a \sqrt{\epsilon_r} / c$, with $\omega_r = \omega_{r_1} = \omega_{r_2} \dots$ being the modal resonant frequencies. The radiation fields of any particular cavity mode can be derived from the aperture E- field on the surface $r=a$ as detailed in the Appendix.

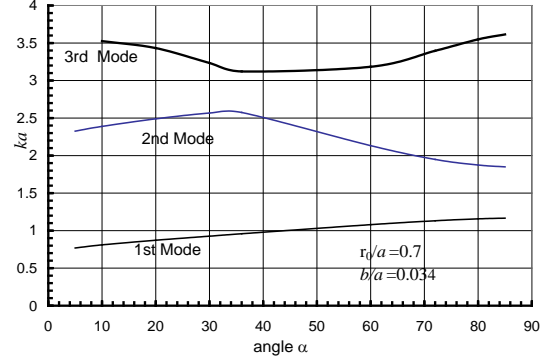


Fig. 2. Normalized resonant frequency ka for first 3 TM_n modes (in ascending order of ka) versus angle α . Here $b/a=0.034$ and $r_o/a=0.7$. a is the effective patch radius accounting for field fringing.

By solving the modal equation (7), we obtain Universal curves for the normalized resonant frequency ka of the first three modes as a function of the pin angular position ' α ' for fixed r_o/a and b/a in Fig. 2. At this point, it is important to note that the field of any of these modes is a weighted sum of azimuthal harmonics ($\cos n\phi$) of ϕ (see equations (1) and (2)). Thus one cannot identify modes as TM_{nm} where n indicates a fixed ϕ - harmonic in the usual way. Instead modes are identified as TM_m , $m=1,2,\dots$, where each mode is characterized by a set of harmonic weights (A_n and B_n) as given by equation (6).

The lowest order mode TM_1 is the one having the lowest resonant frequency and therefore can provide a compact antenna design as demonstrated in [20] for the full circular patch with a shorting pin. For the parameters in Fig. 2, this mode resonates when ka is less than unity or $a \leq \lambda/2\pi$. However, operating in this mode will result in a narrowband operation [20]. Since in this paper we are interested in a broadband design, we will investigate this possibility by exciting the second and third order modes. This will be done in the next section.

III. BROADBAND SEMICIRCULAR PATCH ANTENNA DESIGN

Referring to Fig. 2, it is possible to achieve broadband operation of the semi-circular patch by

efficiently exciting the second and third order modes TM_2 and TM_3 and maintaining good matching between their resonant frequencies f_2 and f_3 . This can be attained by a suitable choice of the feed position using the IE3D simulator as will be seen. Firstly we choose the patch radius 'a' and the pin angular position α such as to place f_2 and f_3 within the frequency band of interest. The parameters r_0/a and b/a are fixed at their values in Fig. 2 although they can have other values.

To start a broadband design, we choose a patch radius of 35.38 mm on a substrate of relative permittivity (ϵ_r) = 2.2 and thickness = 6.28 mm. The effective patch radius, accounting for field fringing, is 39.39 mm. The pin has a radius (b) = 1.35 mm and is positioned at $(r_0, +\alpha) = (27.57, +60^\circ)$. Using Fig. 2, these choices fix the frequencies of the second and third TM_2 and TM_3 modes at 1.95 GHz and 2.91 GHz respectively. Now we need to optimize the feed size and position in order to excite these modes and achieve matching over a broadband encompassing the range of frequencies f_2 to f_3 . To this end, we have performed numerous simulations with varied feed positions on the IE3D software in order to maximize the bandwidth over which the input SWR is less than 2. These simulations are presented and discussed in the next section.

IV. SIMULATION RESULTS FOR THE SEMI-CIRCULAR PATCH

A. Standing Wave Ratio (SWR)

The Zealand IE3D software is used to simulate the semi-circular patch antenna using the patch and substrate parameters stated above. Numerous simulations are attempted with different feed radii and positions. It was concluded that broadband matching is achieved for a feed radius of 1.35 mm and radial position $r_f=r_0$. The angular position ' β ' was found to be detrimental in realizing broadband matching. The simulation results for the standing wave ratio are plotted in Fig. 3 for $\beta = 0^\circ, 5^\circ, 10^\circ, 15^\circ$ and 20° . It is seen that the bandwidth, corresponding to $SWR \leq 2$ depends on β . It is seen that maximum bandwidth occurs for $\beta = 10^\circ$. A summary of the results on percentage bandwidth and center frequency versus β are tabulated in Table 1. Here the center frequency is defined as the arithmetic mean of the upper and lower frequencies corresponding to $SWR=2$. The percentage bandwidth is maximum for $\beta = 10^\circ$ and equals 58 % around the center frequency 2.98 GHz (over the band 2.12-3.85 GHz). At this value of the feed angular position, the simulated complex input impedance is plotted against frequency in Fig. 4(a). The resistive component varies around 50 Ohms; between 30 to 100 Ohms over the band 2.1-3.9 GHz. Meanwhile the reactance oscillates slightly around zero Ohm. The Smith chart presentation of the complex

impedance is given in Fig. 4(b). The circles around the center of the chart indicate a broadband operation.

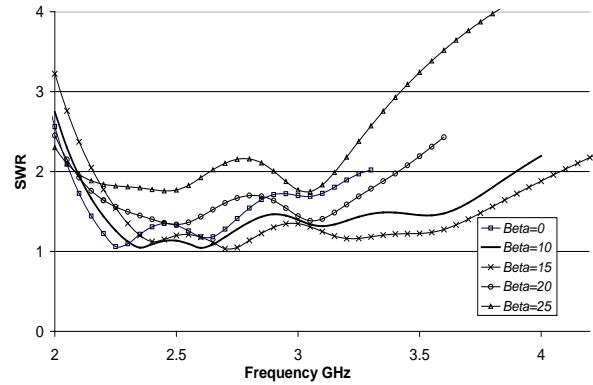


Fig. 3. SWR for a pin loaded semicircular patch with parameters (in mm): $a = 35.38$, $h = 6.28$, $b = b_f = 1.35$, $r_0 = r_f = 27.57$, $\alpha = 60^\circ$. The feed angular position $\beta = 0^\circ, 10^\circ, 15^\circ$, and 20° .

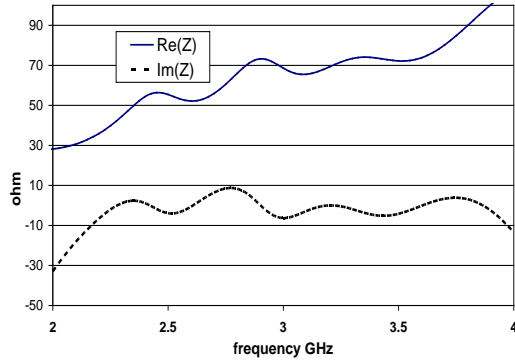
Table 1. Relative Bandwidth vs. Feed angular position.

	Angle β	Relative BW	@Center Frequency
1	0°	43%	2.61GHz
2	5°	56%	2.96GHz
3	10°	58%	2.98GHz
4	15°	56%	3.10GHz
5	20°	45%	2.71GHz

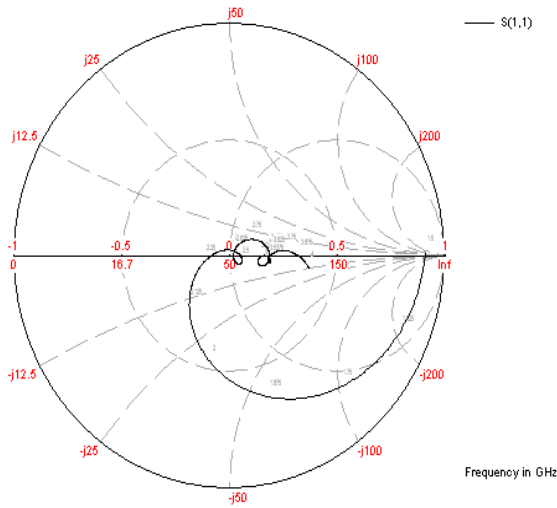
B. Directivity and Radiation Pattern

The simulated directivity and gain versus frequency are shown in Fig. 5 for the two representative cases of $\beta = 0^\circ$ and 10° . It is seen that the directivity is quite flat with maximum deviation of ~ 0.5 dB around 8 dB over the band 1.6 GHz to 3.2 GHz for $\beta = 0^\circ$ and over the band 1.5 GHz to 4.0 GHz for $\beta = 10^\circ$. Thus, the antenna is not only broadband in terms of reflection loss, but also broadband in terms of directivity. On the other hand, the simulated gain varies over the bandwidth between 1 dB to 4.5 dB. This is less than the gain of the full circular patch of the same radius [21] which reaches a maximum of about 6 dB. This is not surprising and comes about as a consequence of size reduction.

The simulated two dimensional radiation patterns (or gain pattern) for $\beta = 10^\circ$ are given in Fig. 6(a) and (b) at the frequencies $f=2.6$ GHz and $f=3.3$ GHz, respectively. In these figures, the electric field components E_θ and E_ϕ are plotted in the E and H-planes. The radiation is mainly roadside and the crosspolar to copolar ratio is in the order of -8 dB.



(a)



(b)

Fig. 4. (a) Real and Imaginary Parts of Z-Parameters for a pin loaded semi circular patch for $\beta=10^0$, (b) the Smith Chart for a pin loaded semicircular patch for $\beta=10^0$.

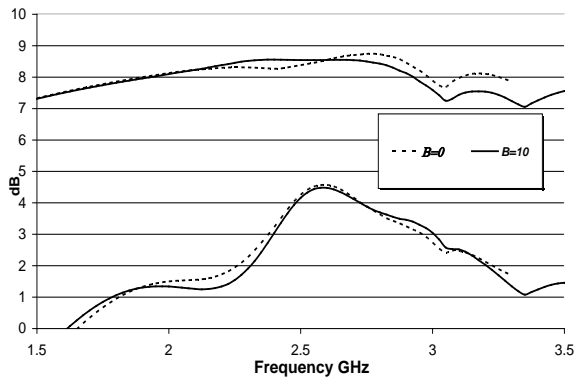
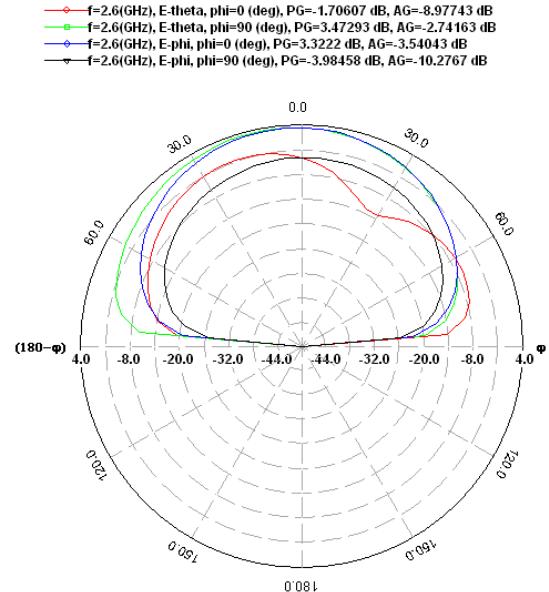
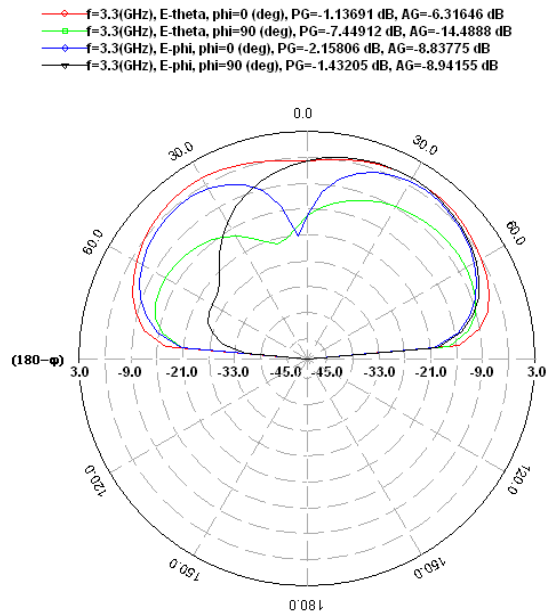


Fig. 5. Maximum directivity, gain versus frequency in simulation results for a pin loaded, semicircular patch for $\beta=0^0$, and 10^0 , the parameters are those given in Fig. 3.



(a) $f=2.6$ GHz



(b) $f=3.3$ GHz

Fig. 6. The radiation pattern (2D) of E_θ and E_ϕ in the two principal planes $\phi=0$ and 90^0 for a pin loaded semi circular patch at (a) $f = 2.6$ GHz and (b) 3.3 GHz ($\beta=10^0$).

V. QUARTER CIRCULAR PATCH ANTENNA

As a further reduction of the patch size, a quarter circular patch is considered. The quarter circular patch is shorted at ($r = r_0, \phi = +\alpha$) by a shorting pin as shown in Figure 1(b). Again the feed is placed at ($r_f = r_0, \beta^0$). We have run several simulations with the same patch radius and same pin location as in the case of a half circular patch for easy comparison between the two configurations. The feed position is optimized for maximum impedance bandwidth.

A. Simulation Results for the Quarter-Circular Patch

The Zealand IE3D simulator is used to plot the standing wave ratio for the pin shorted quarter circular patch in Fig. 7. The feed angular position β takes the values $0, 10, 20$ and 25° . From the simulation results, the percentage bandwidths corresponding to $SWR \leq 2$ are summarized, along with the center frequency, in Table 2. It is seen that the relative bandwidth obtained when $\beta = 10^\circ$ is about $\sim 29\%$ around the center frequency of 3.04 GHz. Note that the lowest frequency for which $SWR=2$ is higher for the quarter circular patch; being ~ 2.7 GHz compared to ~ 2.1 GHz for the semi-circular patch. A reduction for the lowest frequency end would dictate an increase of the quarter patch radius, which would offset the size reduction to a certain extent. The real and imaginary parts of the input impedance are plotted versus frequency in Fig. 8(a) and the Smith chart representation is given in Fig. 8(b). The resistive component varies between 40 and 100 Ohm and the reactive component varies between -30 and 15 Ohm in the frequency range 2.7-3.7 GHz.

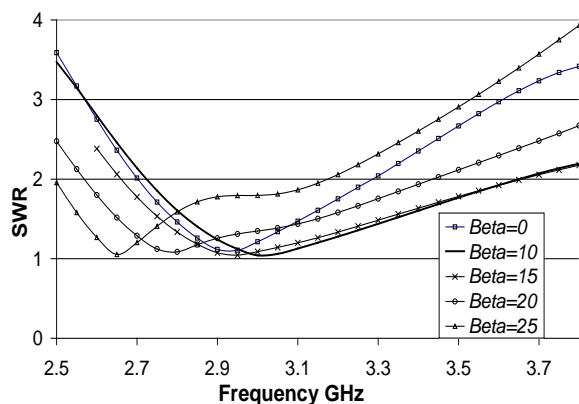
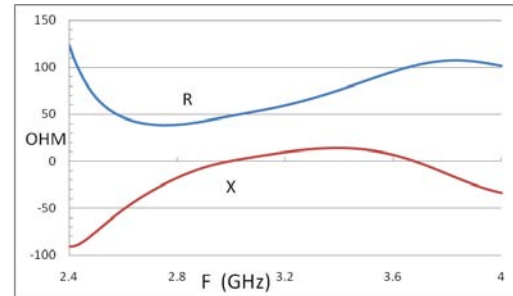
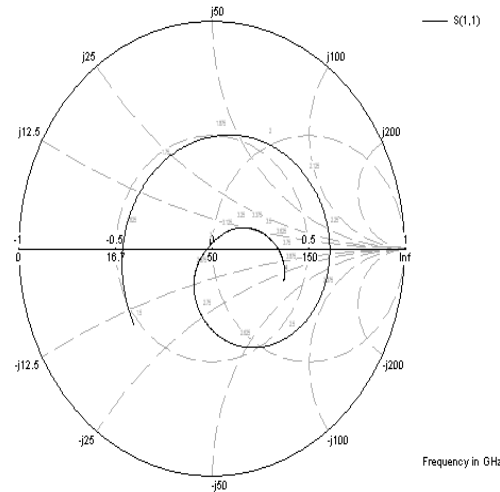


Fig. 7. SWR for a pin loaded quarter circular patch with parameters (in mm): $a=35.38, h = 6.28, b = b_f = 1.35, r_o = r_f = 27.57$ mm, $\alpha=60^\circ$. The feeder angular position $\beta = 0^\circ, 10^\circ, 15^\circ, 20^\circ$ and 25° .



(a)



(b)

Fig. 8. (a) Real and Imaginary Parts of input impedance for a pin loaded quarter circular patch for $\beta=10^\circ$, (b) Smith chart representation of the input impedance for a pin loaded quarter circular patch for $\beta=10^\circ$.

B. Directivity, Gain and Radiation Pattern of the Quarter-Circular Patch Antenna

Simulated directivity and gain versus frequency are shown in Fig. 9 for the representative cases of $\beta=0^\circ$ and $\beta=10^\circ$. It is seen that the directivity varies between ~ 6 dB to 8.3 dB over the band 2.1 to 3.5 GHz. This is a wide range of variation (~ 2.8 dB) compared to the half patch antenna (~ 0.5 dB). The simulated gain varies between 0 and 5.2 dB over the band 2.1 GHz to 3.5 GHz. Metal losses is expected to be higher for the quarter patch compared to the half circular patch and this accounts for the reduced gain at the lower frequency end. The two dimensional gain patterns at the frequencies GHz are plotted in Fig. 10. As is the case with the semi-circular patch, the radiation is mainly broadside with moderate crosspolar to copolar ratio (-9 dB). Low crosspolar radiation is not an important issue in wireless applications.

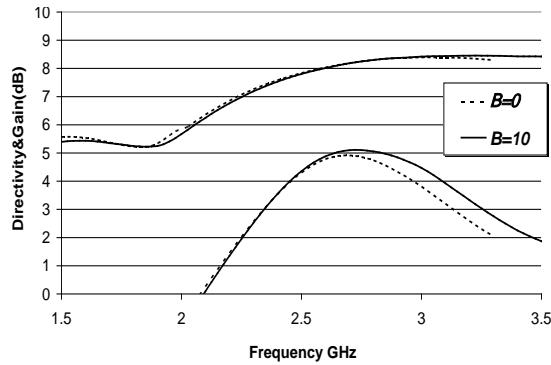


Fig. 9. Maximum directivity, gain versus frequency simulation results for a pin loaded quarter circular patch: $\beta = 0^0$ and 10^0 .

VI. EXPERIMENTAL RESULTS

In order to verify the above analytical and simulated designs, a prototype half and quarter circular patch antennas were built on a grounded dielectric substrate. The latter had a relative dielectric constant of 2.2 and thickness= 6.28 mm (made of four layers of 1.57 mm thickness each). The ground plane was a square of dimensions 15x15 cm. The patch geometry was chosen to match the simulated ones for direct comparison with simulation results. In the following, we present the experimental results on both patch geometries.

A. Half Circular Patch Antenna

To perform the measurements, the antenna is connected to the Vector Network Analyzer, Wiltron Model 360B. The measured SWR is shown in Fig. 11. The experimental results demonstrate the operation of the antenna in the range 2.0-4.1 GHz Compared with the simulation results (Fig. 3), a slight shift in the range of operation is noticed (2.1-3.85 GHz in the simulations). This is attributed to several imperfections of connectors, cables substrate permittivity and thickness.

B. Quarter Circular Patch Antenna

The measured SWR for the quarter patch antenna is shown in Fig. 12. The experimental results demonstrate the operation of the antenna in the range 3.1-4.7 GHz compared to 2.75-3.6 GHz in the simulations (Fig. 6). The lowest operating frequency in the measurements is thus shifted to a higher value. However, if the acceptable SWR level can be relaxed to $SWR \leq 2.5$ instead of 2, the lower frequency end will be shifted down to 1.7 GHz, giving a substantial increase of the useful bandwidth.

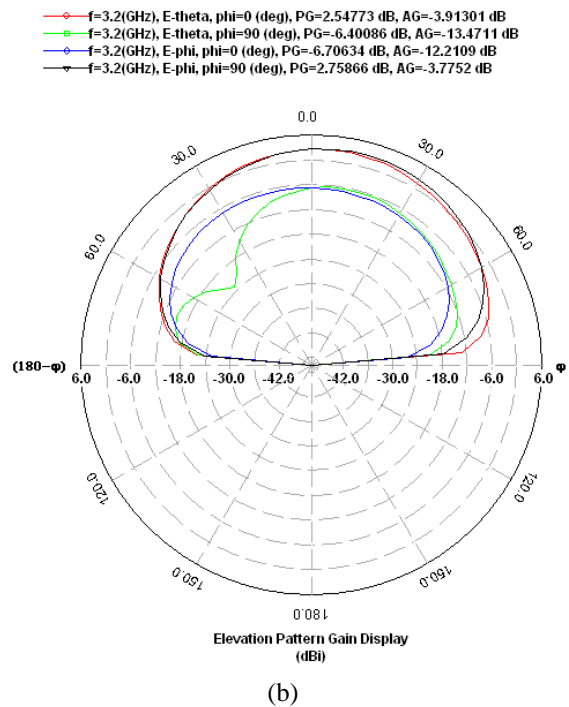
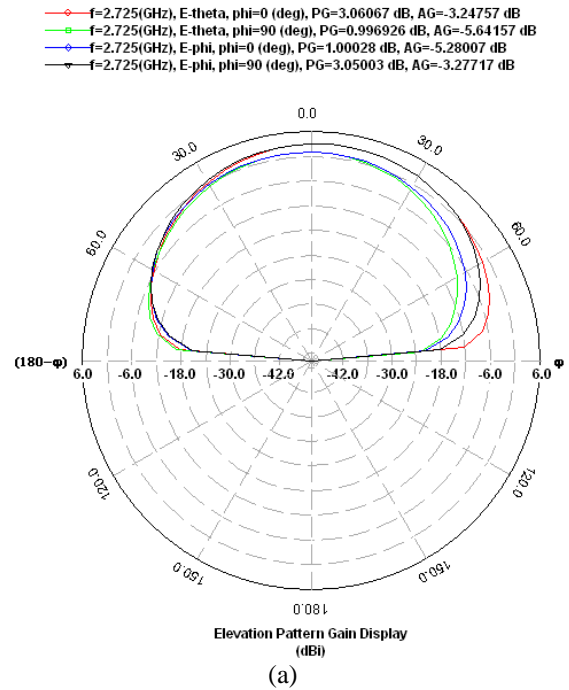


Fig. 10. The radiation pattern (2D) of E_θ and E_ϕ in the two principal planes $\phi=0$ and 90^0 for a pin loaded quarter circular patch for $\beta = 10^0$, (a) at $f = 2.6$ GHz, (b) $f = 3.2$ GHz.

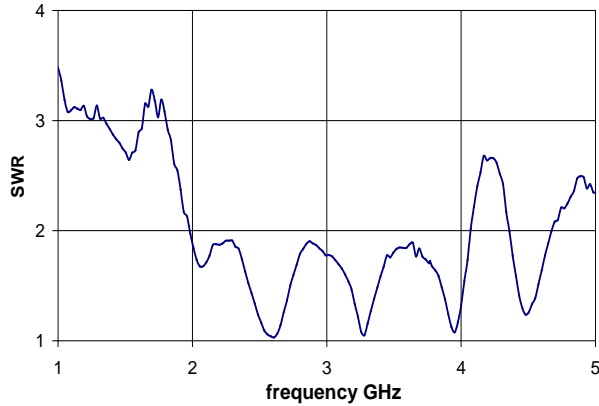


Fig. 11. Experimental result of SWR for semi-circular patch antenna. A broadband operation is achieved over the band $2.0 < f < 4.1$ GHz

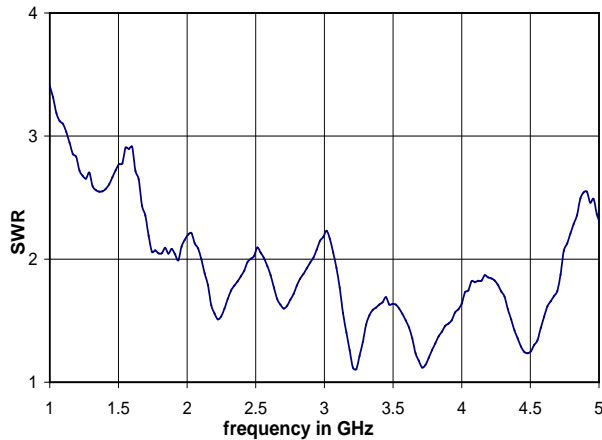


Fig. 12. Experimental result of SWR for quarter circular patch antenna. A broadband operation is achieved over the band $3.1 < f < 4.7$ GHz.

VII. DISCUSSIONS AND CONCLUSIONS

In an attempt to reach a broadband and compact patch antenna for wireless applications, we have performed theoretical, simulation and experimental work on a pin-loaded half circular and quarter circular patch antennas. The cavity modes of the half circular patch are derived in terms of their resonant frequencies and an initial design of patch geometry for broadband operation is deduced. The design is based on operating the antenna in the band encompassing the resonant frequencies of the second and the third cavity modes. The first mode, having the lowest resonant frequency, can provide a compact, but a narrow band operation as demonstrated earlier in [20, 22] for a full circular shorted patch. Simulation on the Commercial IE3D Zealand software is then used to optimize the feed radius and location for wide band operation.

It is demonstrated that a 58% bandwidth around a center frequency of 2.98 GHz is achievable by using a pin

loaded semicircular patch of radius 35.38 mm on an 6.28mm thick substrate of $\epsilon_r=2.2$. Note that the patch area is merely 13.6% of a free space wavelength squared at 2.5 GHz. The simulated pin loaded quarter circular patch of the same radius gave a 29% bandwidth around the center frequency 3.04 GHz. The patch area is now only 10% of the center wavelength squared. These figures confirm that the broadband operation and antenna compactness are two contradictory requirements. Nevertheless, depending on the application, the attainment of broadband as well as compact antenna designs is possible. The measured results show reasonable agreement with simulated results. For comparison, a conventional circular patch loaded by a chip resistor in [8, p.59-60] is reported to have a 10dB reflection loss bandwidth of only 10.9% and a gain around 4 dBi.

APPENDIX

The aperture field E_z at $r=a$ for a given cavity mode is obtained from equation (2) as,

$$E_z(a, \phi) = \sum_{n=0}^{\infty} [2B_n / \pi ka] \cos n\phi \quad (\text{A1})$$

where B_n is given by equation (7) and E_z above is valid over the surface $|z| \leq h$, and $0 \leq \phi \leq \pi$. This aperture field is equivalent to a ϕ -oriented magnetic current radiating in the outside air region. The radiation fields are obtained by following [20] to get,

$$E_\theta(R, \theta, \phi) = \frac{j2he^{-jk_0R}}{\sqrt{\epsilon_r}R} \sum_{n=0}^{\infty} j^n B_n J'_n(k_0 a \sin \theta) \cos n\phi \quad (\text{A2})$$

$$E_\phi(R, \theta, \phi) = \frac{j2he^{-jk_0R}}{\sqrt{\epsilon_r}R} \cos \theta \times \sum_{n=1}^{\infty} j^n B_n n \frac{J_n(k_0 a \sin \theta)}{(k_0 a \sin \theta)} \sin n\phi. \quad (\text{A3})$$

In the above (R, θ, ϕ) are spherical coordinates with origin at the projection of the patch center on the ground plane.

REFERENCES

- [1] K. R. Carver and J. W. Mink, "Microstrip antenna technology," *IEEE Trans. Antennas Propagat.*, vol. AP-29, no. 1, pp. 2-24, Jan. 1981.
- [2] D. M. Pozar and D. H. Schaubert (Eds.), *The Analysis and Design of Microstrip Antennas and Arrays*, IEEE Press, New York, 1996.
- [3] R. A. Sainati, *CAD of Microstrip Antenna for Wireless Applications*, Artech House, norwood, MA, 1996.

- [4] J. R. James and P. S. Hall, eds, "Handbook of Microstrip Antennas," London, UK, Peter Peregrinus, Ltd, ch. 4. 1989.
- [5] P. C. Sharma and K. C. Gupta, "Analysis and optimized design of single feed circularly polarized microstrip antennas," *IEEE Trans. Antennas Propagat.*, vol. 31, no. 6, pp. 949-955, Nov. 1983.
- [6] G. Dubost and G. Beauquet, "Linear transmission line model analysis of a circular patch antenna," *Electronic Letters*, vol. 22, pp. 1174-1176, Oct. 1986.
- [7] G. Kumar and K. P. Ray, *Broadband Microstrip Antennas*, Artech House, Norwood, MA, 2003.
- [8] Kin-Lu Wong, "Compact and Broadband Microstrip Antennas," John Wiley, 2002
- [9] R. B. Waterhouse, "Small microstrip patch antenna," *Electronics Letters*, vol. 31, no. 8, pp. 604-605, April 1995.
- [10] R. B. Waterhouse, S. D. Targonski, and D. M. Kokotoff, "Design and performance of small printed antennas," *IEEE Trans. Antennas Propagat.*, vol. 46, no. 11, pp. 1629-1633, 1998.
- [11] S. Dey and R. Mittra, "Compact microstrip patch antenna," *Microwave Optical Technology Letters*, vol. 13, pp. 12-14, Sept. 1996.
- [12] K. Wong, C. Tang, and H. T. Chen, "A Compact meandered circular microstrip antenna with a shorting post," *Microwave and Optical Tech. Letters*, vol. 15, no. 3, pp. 147-149, June 1997.
- [13] A. F. Sheta, A. Mohra, and S. F. Mahmoud, "A Multi-band operation of compact H-shape microstrip antennas," *Microwave and Optical Technology Letters*, vol. 35, no. 5, pp. 363-367, Dec. 2002.
- [14] F. Yang, X. Zhang, X. Ye, and Y. R. Samii, "Wide-band e-shaped patch antennas for wireless communication," *IEEE Trans. Antennas Propagat.*, vol. 49, no. 7, pp. 1088-1100, 2001.
- [15] T. Huynh and K. F. Lee, "Single layer single patch wideband microstrip antenna," *Electronics Letters*, vol. 31, pp. 1310-1311, Aug. 1995.
- [16] F. Bilotti, M. Manzini, A. Alu, and L. Vegni, "Polygonal patch antennas with reactive impedance surfaces," *Journal of Electromagnetic Waves and Applications (JEMWA)*, vol. 20, no. 2, pp. 169-182, 2006.
- [17] C. K. Samuel and R. D. Murch, "Compact integrated diversity antenna for wireless communications," *IEEE Trans. Antennas Propagat.*, vol. 49, no. 6, pp. 954-960, June 2001.
- [18] K. M. Luck, C. L. Mak, Y. L. Chow, and K. F. Lee, "Broadband microstrip patch antenna," *Electronics Letters*, vol. 34, no. 15, July 1998.
- [19] A. A. Eldak, A. Z. Elsherbeni, and C. E. Smith, "Wideband modified bow-tie antenna with single and dual polarization for C and X band applications," *IEEE Trans. Antennas Propagat.*, vol. AP-53, no. 9, pp. 3067-3072, Sept. 2005.
- [20] S. F. Mahmoud and R. K. Deeb, "Characteristics of a circular microstrip patch antenna with a shorting post," *Journal of Electromagnetic Waves and Applications (JEMWA)*, vol. 16, no. 2, pp. 213-226, 2002.
- [21] S. F. Mahmoud and A. F. Almutairi, "A 2-loaded patch as a multiband antenna for wireless communication," *Journal*

of Applied Computational Electromagnetic Society (ACES), pp. 19-25, Nov. 2003.

- [22] A. F. Almutairi, S. F. Mahmoud, and N. Aljuhaishi "Wide-Band circular patch antenna with 2-pin loading for wireless communications," *Journal of Electromagnetic Waves and Applications, JEMWA*, vol. 19, no. 6, pp. 839-851, 2005.



Ali Almutairi Received the B.S. degree in electrical engineering from the University of South Florida, Tampa, Florida, in 1993. In December 1993, he has been awarded a full scholarship from Kuwait University to pursue his graduate studies. He received M.S. and Ph.D. degrees in electrical engineering from the University of Florida, Gainesville, Florida, in 1995 and 2000, respectively. At

the present, he is the Chairman and an associate professor at Electrical Engineering Department, Kuwait University and director of the Wireless Communication Networks Laboratory. His current research interests include CDMA system, multiuser Detection, cellular networks performance issues, coding and modulation.

Dr. Almutairi is a senior member of IEEE and other professional societies and served as a reviewer for many technical publications.



Nasser. Ahmad Al-Juhaishi was born in 1976. He received the B.S.E. degree of Electrical Engineering in the University of Damascus, Syria in 1999 and the M.S.E. degree in electrical engineering from Kuwait University, Kuwait. His research interests involve ultra wideband electro-magnetics, microwaves, and Antennas.



Samir F. Mahmoud: was graduated from the Electronic Engineering Department, Cairo university, Egypt in 1964. He received the M.Sc and Ph.D. degrees in the Electrical Engineering Department, Queen's university, Kingston, Ontario, Canada in 1970 and 1973. During the academic year 1973-1974, he was a visiting research fellow at the Cooperative Institute for Research in Environmental

Sciences (CIRES). Boulder, CO, doing research on Communication in Tunnels. He spent two sabbatical years, 1980-1982, between Queen Mary College, London and the British Aerospace, Stevenage, where he was involved in design of antennas for satellite communication. Currently Dr. Mahmoud is a full professor at the EE Department, Kuwait University. Recently, he has visited several places including Interuniversity Micro-Electronics Centre (IMEC), Leuven, Belgium and spent a sabbatical leave at Queen's University and the Royal Military College, Kingston, Ontario, Canada in 2001-2002. His research activities have been in the areas of antennas, geophysics, tunnel communication, EM wave interaction with composite materials and microwave integrated circuits. Dr. Mahmoud is a Fellow of IET and one of the recipients of the best IEEE/MTT paper for 2003.

Design and Optimization of Single, Dual, and Triple Band Transmission Line Matching Transformers for Frequency-Dependent Loads

M. Khodier

Department of Electrical Engineering, Jordan University of Science & Technology
P.O. Box 3030, Irbid 22110, Jordan; Email: majidkh@just.edu.jo

Abstract – This paper presents a design method for matching a frequency- varying load to a lossless transmission line at N frequency points using N transmission line sections. The formulation is based on the $ABCD$ matrix of a cascaded N -section transmission line, terminated by a complex load. The unknown characteristic impedances and lengths of the sections are found by imposing the matching condition at N frequencies. Analytical solution for the nonlinear equations is known for the $N = 1$ case only; for $N > 1$, analytical solution is difficult to obtain, and therefore, the highly efficient particle swarm optimization method is used to find the design the parameters after casting the design into an optimization problem. Different numerical examples are presented and discussed that illustrate the validity of the proposed design method.

Keywords: Impedance matching, complex load, transmission line transformer, and particle swarm optimization.

I. INTRODUCTION

Multi-band impedance matching is desirable, especially with the emergence of multi-band operation in wireless communication systems [1-3]. Several papers have been published in which different techniques were proposed to design multiband matching transformers [4-14]. Recently, the particle swarm optimization (PSO) method is used to design a multi-band transmission line transformer (TLT) [15], and in [16], the PSO method is used to design a multi-band, two-way, equal split Wilkinson power divider. However, in all of these papers, the load impedance is assumed to be frequency independent, which might be considered as a limitation on the type of loads used. In [17, 18], a dual-band TLT to match complex impedances was presented and applied to wideband high-frequency amplifiers, but the formulation requires the solution of nonlinear equations through some zero-finding numerical routines. Finally, in [19] analysis method for matching complex loads using nonuniform microstrip transmission lines is presented. In this paper, we present an analysis and design method for matching a

frequency- varying load to a lossless transmission line at N frequency points using N uniform TL sections. The analysis is based on the $ABCD$ matrix of a cascaded N -section transmission line, terminated by a complex load. The unknown characteristic impedance and length of each section are found by imposing the matching condition at N frequencies. The resulting nonlinear equations are solved analytically for the $N = 1$ case only; for $N > 1$, analytical solution are difficult to obtain, and therefore, the highly efficient particle swarm optimization method is used after casting the design into an optimization problem.

The PSO algorithm is a multiple-agents optimization algorithm introduced by Kennedy and Eberhart [20-23] while studying the social behavior of groups of animals and insects such as flocks of birds, schools of fish, and swarms of bees. They quickly discovered they have stumbled on an easy and powerful optimization method. Since then, the method has been used in a wide range of optimization problems [24-27].

II. ANALYSIS

Referring to Fig. 1, the transmission ($ABCD$) matrix for the n^{th} transmission line section is given by [28],

$$M_n = \begin{bmatrix} \cos(\beta l_n) & jZ_n \sin(\beta l_n) \\ jY_n \sin(\beta l_n) & \cos(\beta l_n) \end{bmatrix}, \quad n = 1, 2, \dots, N \quad (1)$$

where $\beta = 2\pi/\lambda$, Z_n and l_n are, respectively, the characteristic impedance and length of transmission line section n , and $Y_n = 1/Z_n$. The load impedance is in general complex and frequency dependent, i.e.,

$$Z_L(f) = R_L(f) + jX_L(f) . \quad (2)$$

The $ABCD$ matrix for the load is defined by,

$$M_{N+1} = \begin{bmatrix} 1 & 0 \\ Y_L & 1 \end{bmatrix} \quad (3)$$

where $Y_L = 1/Z_L$. The overall transmission matrix is given by,

$$M = \prod_{n=1}^{N+1} M_n = \begin{bmatrix} m_{11} & m_{12} \\ m_{21} & m_{22} \end{bmatrix}. \quad (4)$$

The input impedance, looking into the input terminals of section 1, is given by,

$$Z_{in} = \frac{m_{11}}{m_{21}}. \quad (5)$$

The complex input reflection coefficient is calculated using,

$$S_{11} = \frac{Z_{in} - Z_0}{Z_{in} + Z_0}. \quad (6)$$

The matching condition requires that,

$$Z_0 = Z_{in}(f_i), i = 1, 2, \dots, N. \quad (7)$$

We should find Z_n and l_n , $n = 1, 2, \dots, N$, such that the above equation is satisfied.

III. PSO ALGORITHM

As mentioned earlier, obtaining an analytical solution from the resulting nonlinear equations for the matching problem becomes extremely difficult, if not impossible, as the number of matching frequencies becomes ≥ 2 , especially when the load is complex. Therefore, instead of going through lengthy analytical derivations, which will end up with the need for the use of optimization process too, we propose the use of the PSO method to design the multi-band multi-section TLT by solving the nonlinear equation (7) after casting it into an optimization problem. For a comprehensive study of the algorithm regarding its implementation, the parameters selection, applications, and other versions of the algorithm, the interested reader is referred to [20-27] and the references mentioned therein. The PSO algorithm, like other evolutionary algorithms, uses the concept of fitness or cost to guide the particles during their search for the optimum solution in the N -dimensional space.

For the current problem, the design is concerned with finding the characteristic impedances and lengths of N -section TLT that matches a lossless transmission line of characteristic impedance Z_0 to a complex load Z_L at N arbitrary frequencies (see Fig. 1). The PSO method is used to find the parameters of the matching transformer

(i.e., the characteristic impedance and length of each section). The following cost function is used,

$$\text{Cost Function} = \sum_{n=1}^N |S_{11}(f_n)|. \quad (8)$$

Although perfect matching at the design frequencies require the cost function to be exactly zero, however, we relaxed this condition and assumed that the matching is practically acceptable whenever the cost function reaches a value of 10^{-4} (-80 dB) or less. This value is used in terminating the PSO algorithm to indicate a solution is found.

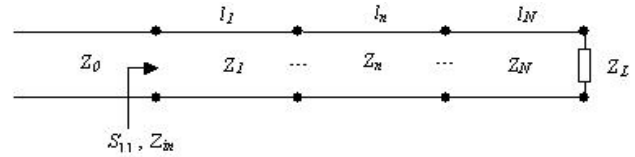


Fig. 1. An N -section, N -band matching transformer connected to a complex load.

IV. RESULTS

A. Single-Section Transformer ($N = 1$)

It is known that this case has analytical solution, and therefore there is no need to use the PSO method. The solution is given by,

$$Z_1 = \sqrt{\frac{Z_0(R_L^2 + X_L^2 - Z_0 R_L)}{R_L - Z_0}} \quad (9a)$$

$$l_1 = \frac{1}{2\pi} \tan^{-1} \left(\frac{Z_1(Z_0 - R_L)}{Z_0 X_L} \right), \quad (9b)$$

provided that either of the following conditions is satisfied,

$$Z_0 < R_L \quad \text{or} \quad Z_0 > R_L + \frac{X_L^2}{R_L}.$$

In particular, there is always a solution if Z_L is real, which reduces to that of the quarter-wave transformer.

B. Dual-Band Transformer ($N = 2$)

For the dual and triple section transformer, it is extremely difficult, if not impossible, to find an analytical solution similar to the case of single section, and that is why the PSO algorithm is used to find the design parameters. Different two-section dual-band transformers are designed with various typical complex loads that could be encountered in practice. Some of the designed

examples are implemented in microstrip lines and the resulting structure is simulated using the electromagnetic simulator software Ansoft Designer [29]. The substrate is FR4 with $\epsilon_r = 4.5$ and thickness = 1.6 mm. The width and length of the microstrip sections are calculated from the characteristic impedance and electrical lengths using PCAAD [30].

1. The first transformer has a series RLC circuit as its load with $R = 100$ ohm, $L = 10$ nH, and $C = 1$ pF. The load impedance versus frequency is shown in Fig. 2. The design frequencies are $f_1 = 1$ GHz and $f_2 = 2$ GHz. The feeding line has $Z_0 = 50$ ohm. The obtained results for the two sections using the PSO were as follows: $Z_1 = 107.78$ ohm and $Z_2 = 82.42$ ohm, while $l_1/\lambda_1 = 0.2332$ and $l_2/\lambda_1 = 0.44$, where λ_1 is the wavelength at f_1 . A typical convergence curve of the PSO algorithm is shown in Fig. 3(a), while the behavior of the reflection coefficient is shown in Fig. 3(b). Clearly, a perfect matching is achieved at the two design frequencies.

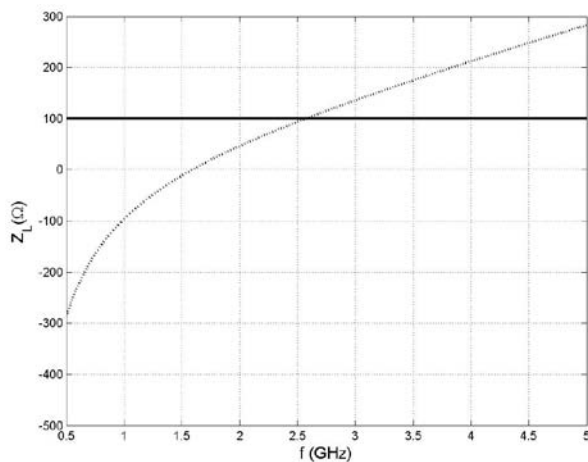


Fig. 2. Impedance of a series RLC load with $R=100$ ohm, $L=10$ nH, and $C=1$ pF.

2. The second example is the same except now the second design frequency is $f_2 = 2.5$ GHz. The obtained results were: $Z_1 = 48.4612$ ohm and $Z_2 = 116.6992$ ohm, while $l_1/\lambda_1 = 0.38242$ and $l_2/\lambda_1 = 0.1421$. Figure 4 displays the variation of $|S_{11}|$ with frequency where it is clear that a perfect matching is achieved at the two frequencies.
3. The third example is the same as the first example, except now $f_2 = 1.1$ GHz. The results for this case were: $Z_1 = 29.6573$ ohm and $Z_2 = 103.1516$ ohm, while $l_1/\lambda_1 = 0.4485$ and $l_2/\lambda_1 = 0.1323$. The reflection coefficient is shown in Fig. 5.
4. The fourth example is the same except now $f_2 = 1.7$ GHz, and $C = \infty$ (i.e., the capacitor in the load is replaced by a short circuit). The results for this case were: $Z_1 = 90.4464$ ohm and $Z_2 = 146.7296$ ohm,

while $l_1/\lambda_1 = 0.3459$ and $l_2/\lambda_1 = 0.4890$. The corresponding reflection coefficient is shown in Fig. 6.

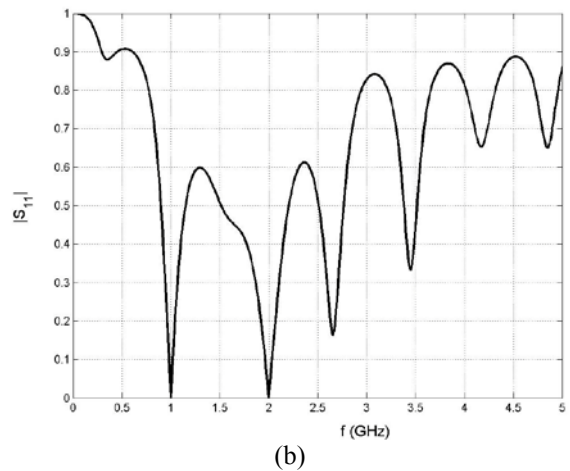
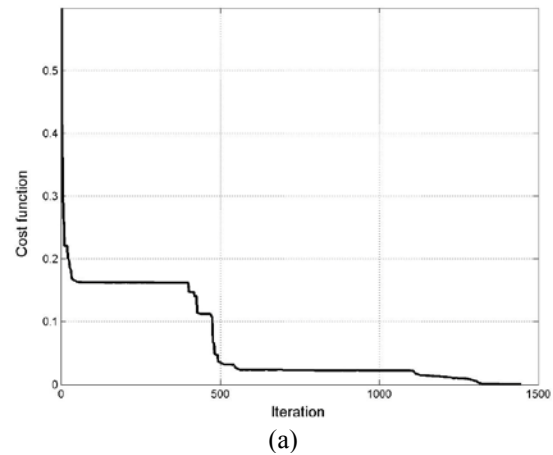


Fig. 3. (a) Convergence of the PSO algorithm. (b) Reflection coefficient versus frequency for example 1.

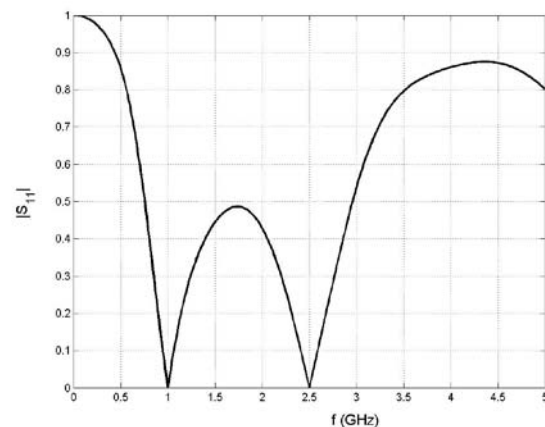


Fig. 4. Reflection coefficient versus frequency for example 2.

5. The fifth example is the same as the fourth except now the inductor is shorted out (i.e., $L = 0$), and the

capacitor is the same as in the first example. The obtained results were: $Z_1 = 153.0174$ ohm and $Z_2 = 116.4692$ ohm, while $l_1/\lambda_1 = 0.2849$ and $l_2/\lambda_1 = 0.3918$. The corresponding reflection coefficient is shown in Fig. 7.

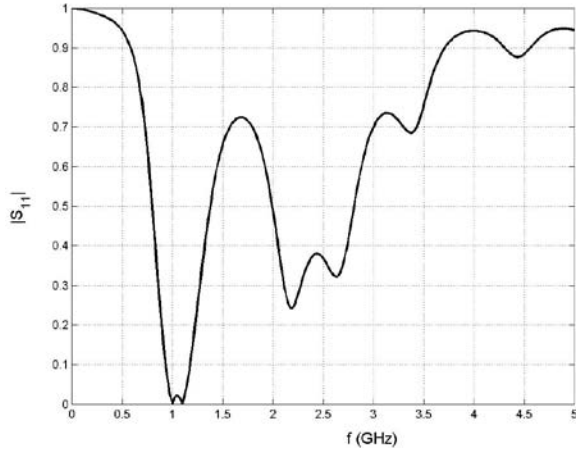


Fig. 5. Reflection coefficient versus frequency for example 3.

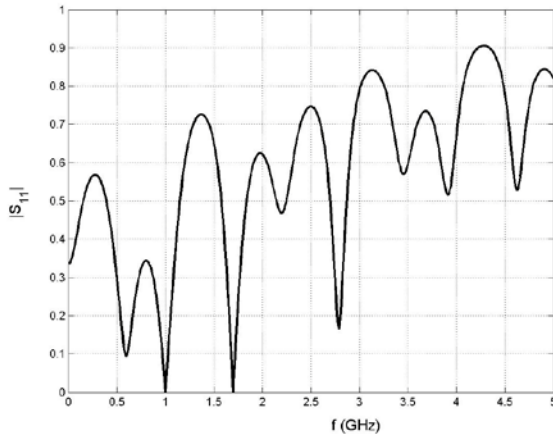


Fig. 6. Reflection coefficient versus frequency for example 4.

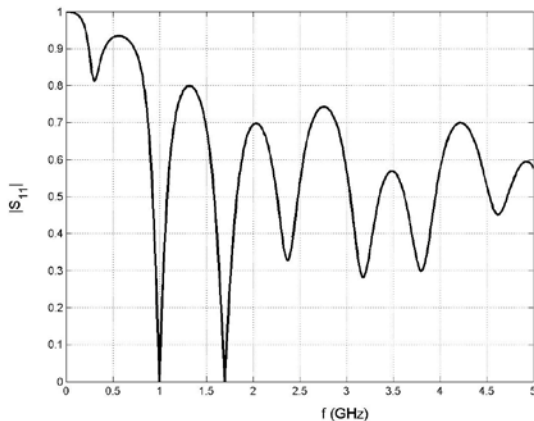


Fig. 7. Reflection coefficient versus frequency for example 5.

6. The sixth example has a parallel RLC as its load, with $R = 100$ ohm, $L = 10$ nH, and $C = 1$ pF whose impedance is shown in Fig. 8. The design frequencies are $f_1 = 1$ GHz and $f_2 = 2$ GHz. The obtained results were: $Z_1 = 91.4413$ ohm and $Z_2 = 69.3849$ ohm, while $l_1/\lambda_1 = 0.2089$ and $l_2/\lambda_1 = 0.1473$. The corresponding reflection coefficient is shown in Fig. 9.

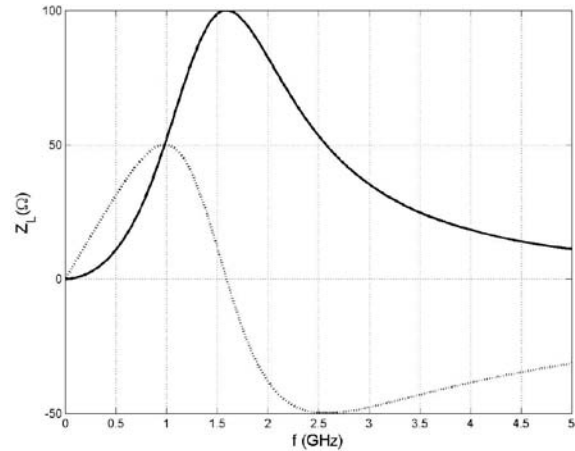


Fig. 8. Impedance of the parallel RLC load with $R = 100$ ohm, $L = 10$ nH, $C = 1$ pF.

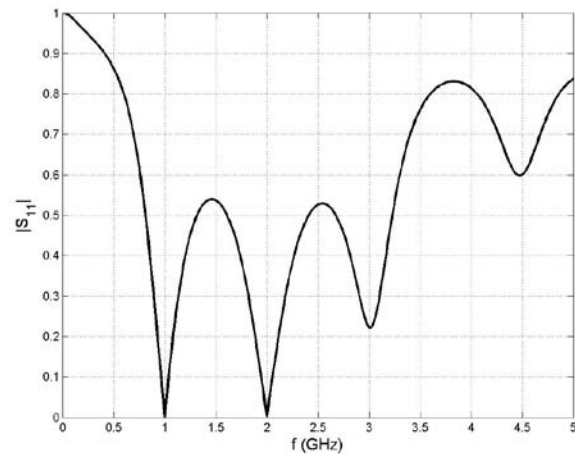


Fig. 9. Reflection coefficient versus frequency for example 6.

7. This example is the same as the sixth, except $f_1 = 0.9$ GHz and $f_2 = 2.4$ GHz. The obtained results were: $Z_1 = 118.2368$ ohm and $Z_2 = 92.0193$ ohm, while $l_1/\lambda_1 = 0.2457$ and $l_2/\lambda_1 = 0.2019$. The reflection coefficient is shown in Fig. 10. The simulation results from Ansoft Designer are also shown, and an acceptable agreement is observed. The difference between the analytical results and simulation results in this example and the following ones are due to the difficulty in designing the microstrip lines that has the correct length and characteristic impedance as the theoretical values.

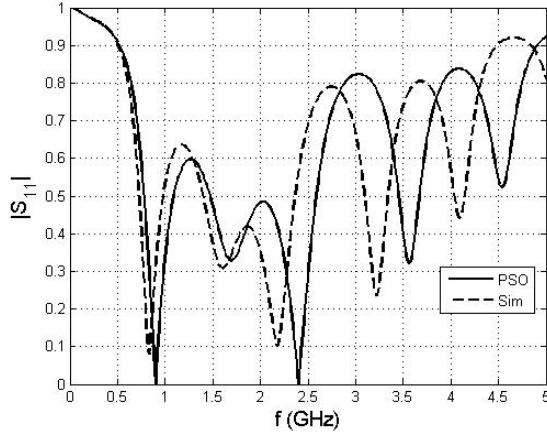


Fig. 10. Reflection coefficient versus frequency for example 7.

8. The load in this example is a dipole antenna, which has many applications in communications and microwave systems. The real and imaginary parts of the input impedance of a wire dipole are given by [31],

$$R_d = \frac{\eta}{2\pi} \left\{ C + \ln(kl) - C_i(kl) + \frac{1}{2} \sin(kl) [S_i(2kl) - 2S_i(kl)] + \frac{1}{2} \cos(kl) [C + \ln(kl/2) + C_i(2kl) - 2C_i(kl)] \right\} \quad (10a)$$

$$X_d = \frac{\eta}{4\pi} \left\{ 2S_i(kl) + \cos(kl) [2S_i(2kl) - S_i(kl)] - \sin(kl) [2C_i(kl) - C_i(2kl) - C_i\left(\frac{2ka^2}{l}\right)] \right\} \quad (10b)$$

where $C = 0.5772$ (Euler's constant), $S_i(x)$ and $C_i(x)$ are the sine and cosine integrals, and a is the wire radius (which is assumed very small compared to the length l of the dipole). The calculated dipole impedance is shown in Fig. 11. The design frequencies were $f_1 = 1$ GHz and $f_2 = 1.8$ GHz, and the obtained design parameters were: $Z_1 = 63.7305$ ohm and $Z_2 = 347.3256$ ohm, while $l_1/\lambda_1 = 0.1758$ and $l_2/\lambda_1 = 0.4729$. The theoretical and simulation reflection coefficients are shown in Fig. 12, and good agreement is obtained. The difference between the results is due to the difficulty in simulating a dipole antenna that has input impedance as the theoretical one given by equation (10). The simulated dipole is a flat one, while the theoretical one is cylindrical.

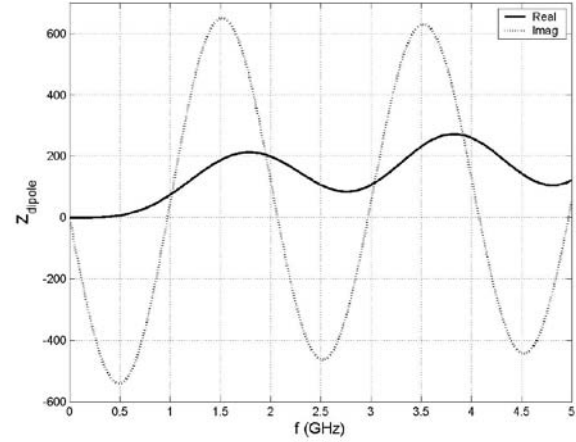


Fig. 11. Impedance of a wire dipole of radius $a = 10^{-5}\lambda_0$, where λ_0 is the wavelength at 1 GHz.

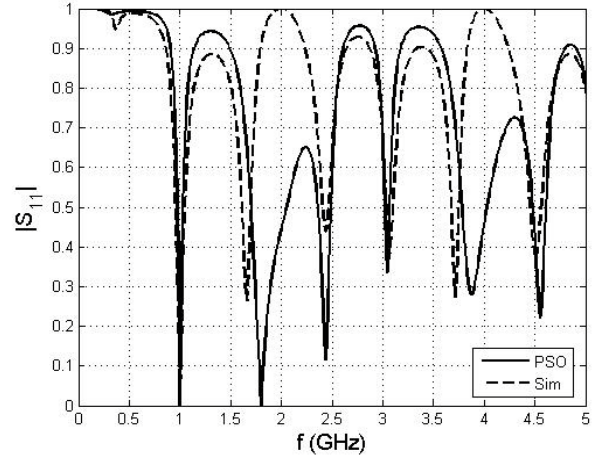


Fig. 12. Reflection coefficient versus frequency for example 8.

C. Triple-Band Transformer ($N = 3$)

Three design examples are given for this case:

9. The load is the series RLC circuit mentioned in example 1, and the design frequencies were: $f_1 = 0.9$ GHz, $f_2 = 1.8$ GHz, and $f_3 = 2.4$ GHz. The obtained design parameters were: $Z_1 = 110.0161$ ohm, $Z_2 = 80.7006$ ohm, and $Z_3 = 102.0823$ ohm, while $l_1/\lambda_1 = 0.2758$, $l_2/\lambda_1 = 0.4187$, and $l_3/\lambda_1 = 0.0708$. The corresponding reflection coefficient is shown in Fig. 13. A very good matching is obtained at the three design frequencies.
10. The load is the parallel RLC circuit mentioned in example 6, and the design frequencies were: $f_1 = 0.9$ GHz, $f_2 = 1.8$ GHz, and $f_3 = 2.4$ GHz. The obtained design parameters were: $Z_1 = 63.3349$ ohm, $Z_2 = 105.6367$ ohm, and $Z_3 = 73.6901$ ohm, while $l_1/\lambda_1 = 0.4767$, $l_2/\lambda_1 = 0.2633$, and $l_3/\lambda_1 = 0.1773$. The corresponding reflection coefficient is shown in Fig. 14. Again, a very good matching is obtained at the three design frequencies.

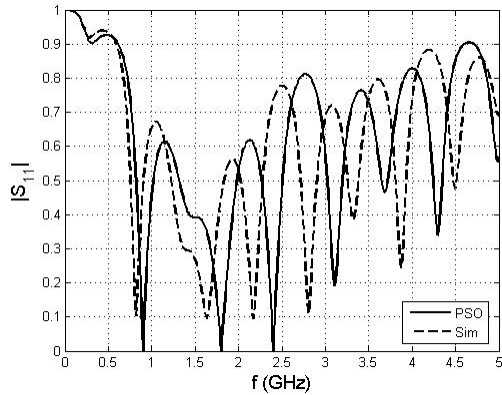


Fig. 13. Reflection coefficient versus frequency for example 9.

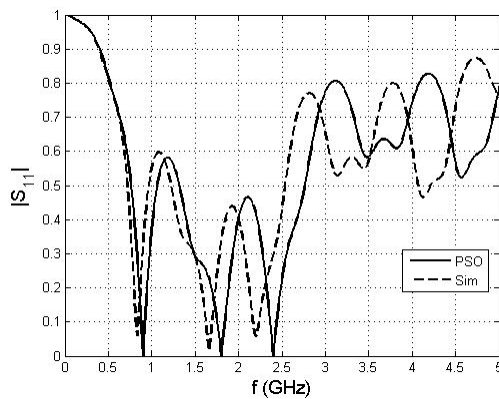


Fig. 14. Reflection coefficient versus frequency for example 10.

11. The load is the dipole antenna of example 8, and the matching frequencies are: $f_1 = 0.9$ GHz, $f_2 = 1.8$ GHz, and $f_3 = 2.4$ GHz. The obtained parameters were: $Z_1 = 164.7378$ ohm, $Z_2 = 26.5777$ ohm, and $Z_3 = 56.5640$ ohm, while $l_1/\lambda_1 = 0.0940$, $l_2/\lambda_1 = 0.4748$, and $l_3/\lambda_1 = 0.1218$. The resulting reflection coefficient from theory and simulation is shown in Fig. 15.

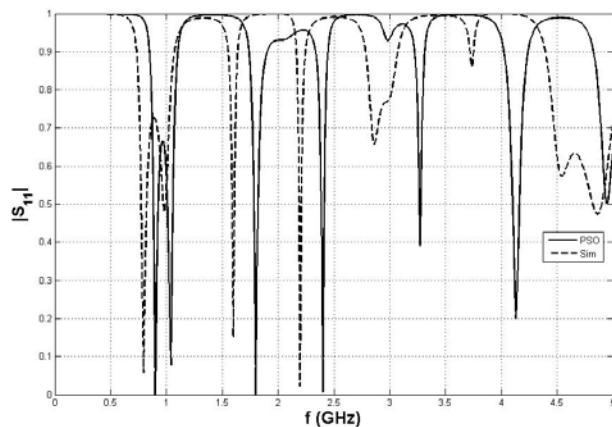


Fig. 15. Reflection coefficient versus frequency for example 11.

V. CONCLUSION

In principle, it is possible to impedance-match a complex load at N frequency points to a lossless line using ordinary N -section TLT. Analytical solution is known for the case $N = 1$ case. For $N > 1$, however, numerical solution is obtained through the use of the PSO algorithm. Different numerical examples were presented which illustrate the idea presented in this paper. It should be mentioned here that not all complex loads can be perfectly matched, and therefore, for some loads the PSO did not reach a solution. For single section, the conditions on the load are clear; for multiple sections, however, these conditions are not clear yet and remain an open area for research.

REFERENCES

- [1] W.-C. Liu, W.-R. Chen, and C.-M. Wu, "Printed double S-shaped monopole antenna for wideband and multiband operation of wireless communications," *IEE Proc.-Microw. Antennas Propag.*, vol. 151, no. 6, pp. 473-476, Dec. 2004.
- [2] W.-C. Liu, "Design of a CPW-fed notched planar monopole antenna for multiband operations using a genetic algorithm," *IEE Proc.-Microw. Antennas Propag.*, vol. 152, no. 4, pp. 273-277, Aug. 2005.
- [3] Y. H. Shum, K. M. Luk, and C. H. Chan, "Multi-band base station antenna with compact microstrip resonant cell filters," *IEE Proc.-Microw. Antennas Propag.*, vol. 151, no. 6, pp. 545-548, Dec. 2004.
- [4] H. Nakajima and M. Muraguchi, "Dual-frequency matching technique and its application to an octave-band (30-60 GHz) MMIC amplifier," *IEICE Trans. Electron.*, vol. E80-C, no. 12, pp. 1614-1621, Dec. 1997.
- [5] C.- M. Tsai, C.- C. Tsai, and S.- Y. Lee, "Nonsynchronous alternating-impedance transformers," *Proc. of Asia Pacific Microwave Conference*, 2001, Taiwan, pp. 310-313.
- [6] K. Wan, Y. Chow, and K. Luk, "Simple design of dual-frequency unequal power-divider," *Electronics Letters*, vol. 37, no. 19, pp. 1171-1173, Sep. 2001.
- [7] Y. Chow and K. Wan, "A transformer of one-third wavelength in two sections – for a frequency and its first harmonic," *IEEE Microwave and Wireless Components Letters*, vol. 12, no. 1, pp. 22-23, Jan. 2002.
- [8] C. Monzon, "Analytical derivation of a two-section impedance transformer for a frequency and its first harmonic," *IEEE Microwave and Wireless Components Letters*, vol. 12, no. 10, pp. 381-382, Oct. 2002.
- [9] C. Monzon, "A small dual-frequency transformer in two sections," *IEEE Trans. on Microwave Theory and Techniques*, vol. 51, no. 4, pp. 1157-1161, April 2003.
- [10] S. Orfanidis, "A two-section dual-band chebyshev impedance transformer," *IEEE Microwave and Wireless*

- Components Letters*, vol. 13, no. 9, pp. 382-384, Sep. 2003.
- [11] G. Castaldi, V. Fiumara, and I. Pinto, "A dual-band chebyshev impedance transformer," *Microwave and Optical Technology Letters*, vol. 39, no. 2, pp. 141-145, Oct. 2003.
- [12] S. Srisathit, S. Virunphun, K. Bandudej, M. Chongcheawchamnan, and A. Worapishet, "A dual-band 3-dB three-port power divider based on a two-section transmission line transformer," *IEEE MTT-S Int. Microwave Symp. Digest*, pp. 35-38, 2003.
- [13] L. Wu, H. Yilmaz, T. Bitzer, A. Pascht, and M. Berroth, "A dual-frequency Wilkinson power divider: for a frequency and its first harmonic," *IEEE Microwave and Wireless Components Letters*, vol. 15, no. 2, pp. 107-109, Feb. 2005.
- [14] M. Chongcheawchamnan, S. Patisang, S. Srisathit, R. Phromloungrsri, and S. Bunnjaweht, "Analysis and design of a three-section transmission-line transformer," *IEEE Trans. on Microwave Theory and Techniques*, vol. 53, no. 7, pp. 2458-2462, July 2005.
- [15] M. Khodier, N. Dib, and J. Ababneh, "Design of multi-band transmission line transformer using particle swarm optimization," *Electrical Engineering*, Springer, vol. 90, no. 4, pp. 293-300, April 2008.
- [16] N. Dib and M. Khodier "Design and optimization of multi-band Wilkinson power divider" *International Journal of RF and Microwave Computer-Aided Engineering*, pp. 14-20, Jan. 2008.
- [17] P. Colantonio, F. Giannini, and L. Scucchia, "A new approach to design matching networks with distributed elements," *Proc. MIKON 2004*, Warsaw, Poland, pp. 811-814, 2004.
- [18] P. Colantonio, F. Giannini, and L. Scucchia, "Matching network design criteria for wideband high-frequency amplifiers," *Int. J. RF and Microwave CAE*, vol. 15, pp. 423-433, 2005.
- [19] M. K. Amirhosseini, "Wideband or multiband complex impedance matching using microstrip volnuniform transmission lines," *Progress In Electromagnetics Research*, PIER 66, pp. 15-25, 2006.
- [20] J. Kennedy and R. C. Eberhart, "Particle swarm optimization," in *Proc. IEEE Int. Conf. Neural Networks*, vol. IV, Perth, Australia, pp. 1942-1948, Dec. 1995.
- [21] Y. Shi and R. C. Eberhart, "Empirical study of particle swarm optimization," in *Proc. Congress Evolutionary Computation*, Washington, DC, pp. 1945-1950, 1999.
- [22] R. C. Eberhart and Y. Shi, "Comparing inertia weights and constriction factors in particle swarm optimization," in *Proc. Congress on Evolutionary Computation*, Piscataway, NJ, pp. 84-88, 2000.
- [23] R. C. Eberhart and Y. Shi, "Particle swarm optimization: developments, applications and resources," in *Proc. Congress on Evolutionary Computation*, Seoul, Korea, pp. 81-86, 2001.
- [24] D. Gies and Y. Rahmat-Samii, "Particle swarm optimization for reconfigurable phase-differentiated array design," *Microwave Opt. Technol. Lett.*, vol. 38, pp. 168-175, Aug. 2003.
- [25] D. W. Boeringer and D. H. Werner, "Particle swarm optimization versus genetic algorithms for phased array synthesis," *IEEE Trans. Antennas Propag.*, vol. 52, no. 3, pp. 771-779, Mar. 2004.
- [26] M. M. Khodier and C. G. Christodoulou, "Linear array geometry synthesis with minimum sidelobe level and null control using particle swarm optimization," *IEEE Trans. Antennas Propagat.*, vol. 53, no. 8, pp. 2674-2679, Aug. 2005.
- [27] J. Ababneh, M. Khodier, and N. Dib, "Synthesis of interdigital capacitors based on particle swarm optimization and artificial neural networks," *International Journal of RF and Microwave Computer-Aided Engineering*, vol. 16, pp. 322-330, July 2006.
- [28] David M. Pozar, *Microwave Engineering*, 4th Ed., Wiley 2005.
- [29] Ansoft Designer v3.5, <http://www.ansoft.com>.
- [30] PCAA 4.0: Personal Computer Aided Antenna Design, Antenna Design Associates, Inc.
- [31] A. Balanis, *Antenna Theory: Analysis and Design*, 2nd Ed., Wiley, 1997.



Majid M. Khodier received the B.Sc. and M.Sc. degrees from Jordan University of Science and Technology, Irbid, Jordan, in 1995 and 1997, and the Ph.D. degree from The University of New Mexico, Albuquerque, in 2001, respectively, all in Electrical Engineering. He worked as a Postdoc in the department of electrical engineering at the University of New Mexico where

he performed research in the areas of RF/photonic antennas for wireless communications, and modeling of MEMS switches for multi-band antenna applications. In September of 2002, he joined the department of electrical engineering at Jordan University of Science and Technology as an Assistant Professor. In February 2008, he became an Associate Professor. His research interests are in the areas of numerical techniques in electromagnetics, modeling of passive and active microwave components and circuits, applications of MEMS in antennas, and RF/Photonic antenna applications in broadband wireless communications, and optimization methods. He published over 30 papers in international journals and refereed conference proceedings. His article entitled "Linear array geometry synthesis with minimum sidelobe level and null control using particle swarm optimization" published in "*IEEE TRANSACTIONS ON ANTENNAS AND PROPAGATION* 53 (8)" in August, 2005 has been recently identified by Thomson Essential Science Indicators to be one of the most cited papers in the research area of "PARTICLE SWARM OPTIMIZATION." Dr Khodier is listed in Marquis who's who in science and engineering, who's who in the world, and is a senior member of the IEEE.

Scan Angle Extension by Array with Pattern Reconfigurable Elements

S. Xiao, Y.-Y. Bai, B.-Z. Wang, and S. Gao

Institute of Applied Physics, University of Electronic Science and Technology of China,
Chengdu, 610054, P. R. China
xiaoshaoqiu@uestc.edu.cn

Abstract – In this paper, a linear phased array with pattern reconfigurable elements is studied to perform a scan angle extension of the array. The developed array can scan its main beam from -70° to 70° in its scanning plane. Compared with the traditional microstrip phased array, the scanning angle is extended remarkably.

Keywords: Microstrip phased array, scan angle extension, and pattern reconfigurable antenna.

I. INTRODUCTION

Phased array can scan its beam and provide a high gain, which results in its extensive applications. Microstrip antenna is utilized frequently in array because they have a compact and stable structure as well as the merit of easy installation [1-3]. There are two main factors to influence the pattern scan of the microstrip array. One is the mutual coupling between elements. Many researchers have studied on this topic and some valuable techniques have been developed to effectively suppress the element mutual coupling, such as using photonic bandgap (PBG) structure and Defected Ground Structure (DGS) [4-7]. The other is the directivity of the element pattern. Generally, the main beam of the microstrip antenna directs to the normal of the element aperture and faint energy is radiated into the space close to the tangent of the ground plane. Thus, when such elements are used to construct a planar phased array, the array cannot also radiate the energy to a large angle away from the normal of the array aperture. However, in some applications, for example, military radar for target scout, it is desired to scan the beam of the phased array in full space. Currently, how to extend the scan angle of the array is becoming a challenge topic in the planar microstrip phased array study.

Reconfigurable antenna has been presented and its operation characteristics, such as patterns and frequencies, are switchable by using PIN diodes or

MEMS switches [8-11]. Due to the ability of reconfiguring pattern, the reconfigurable antenna can improve the beam coverage range of the element pattern. Then the phased array constructed by the pattern reconfigurable antenna has a tremendous potential to extend the scan angle. The array with pattern reconfigurable elements has been studied by J. T. Bernhard et al firstly [12]. In [12], the characteristic of the pattern scan is compared between the proposed array and the traditional microstrip array. However, the reported array has a smaller scan range because of the incompact element configuration and the larger element spacing.

In this paper, an improved reconfigurable antenna element is applied into a linear phased array to extend the scan angle. Compared with the traditional microstrip array, the scanning angle of the developed array is extended remarkably.

II. ANTENNA ELEMENT DESIGN

The element is a pattern reconfigurable microstrip dipole Yagi antenna and its geometry is shown in Fig. 1. The antenna consists of three parallel microstrip dipoles. The width of the microstrip dipole is $W=2\text{mm}$. The center strip length is $L_m=20.6\text{mm}$, and fed by a SMA connector. The feed position is moved $g=8.5\text{mm}$ away from the end of the strip. The two parasitic microstrip dipoles have a same length of $L_r=22.7\text{mm}$. The space between the adjacent dipoles is $S=9.8\text{mm}$. A gaps with a width of $d_m=1.2\text{mm}$ is located close to each end of the parasitic dipole and 2.0mm (d_1) away from the strip end. Four switches, i.e., k_1 , k_2 , k_3 , and k_4 , are installed in four gaps, respectively. The ground plate has an area of $100\times 140\text{mm}^2$. The microstrip substrate have a relative permittivity of $\epsilon_r=4.4$ and a thickness of $H=6.35\text{mm}$.

The antenna can reconfigure its pattern with three states. In *State 1*, k_1 and k_2 are open, k_3 and k_4 are closed. In this case, the right parasitic microstrip dipole is

shorten by opening $k1$ and $k2$ and the left one is elongated by closing $k3$ and $k4$. On the contrary, when $k1$ and $k2$ are closed, $k3$ and $k4$ are open, the configuration of *State 2* is realized.

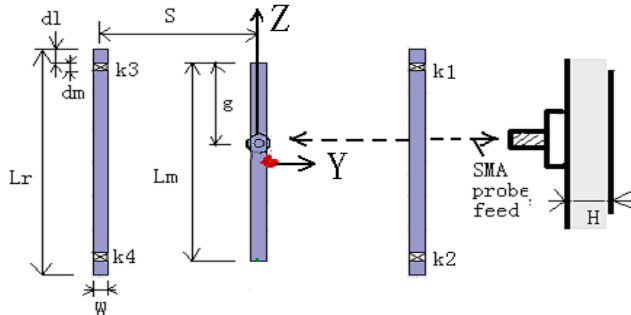


Fig. 1. Geometry of the pattern reconfigurable antenna element.

In this study, an ideal switch models are used to imitate PIN diode or MEMS switches for proof of concept, i.e., the open or closed states of the switches are imitated with the absence or presence of a metal pad with an area of $W \times d_m$. This simplification is acceptable because simulation and measurement show that the mutual coupling between antenna and radiation behavior change little after adding the switches and bias network [13-14]. The electromagnetic simulation software Ansoft HFSS 9.0 is used to study the antenna performances. The antenna that operates in *State 1* is analyzed firstly. The simulated and measured return losses are shown in Fig. 2. A good matching performance is achieved at the frequency of 3.67GHz.

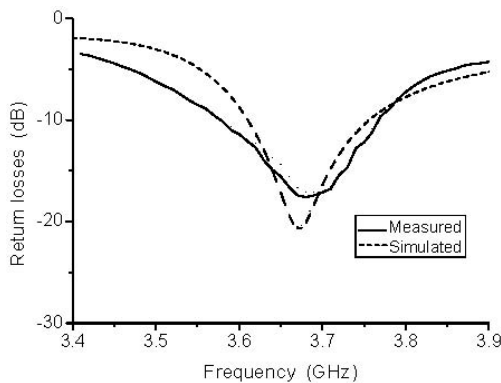


Fig. 2. Simulated and measured return losses for *State 1*.

Because the antenna is fed asymmetrically, the peak direction of radiation pattern is not in xy -plane when the antenna operates at 3.67GHz. A peak gain of 4.1dBi is obtained at the direction of $(\theta=98^\circ, \varphi=2^\circ)$, which is less

than the reported one in [15] because of a compacter antenna structure. The maximum radiation angle in $\theta=90^\circ$ (xy -plane) is $\varphi=44^\circ$. The simulated and measured co-polarization patterns in $\theta=90^\circ$ plane and $\varphi=44^\circ$ plane are shown in Fig. 3. Here, the weak x -polarization components are omitted. The corresponding peak gain in Fig. 3 is 2.1dBi. Because the structure of *State 2* is symmetrical with that of *State 1*, the results for *State 2* are not shown by figures. The corresponding data of two states are listed in Table 1. Form Table 1, it can be shown that the antenna can reconfigure its pattern in xy -plane with an acceptable antenna gain by shifting antenna states between *State 1* and *State 2*.

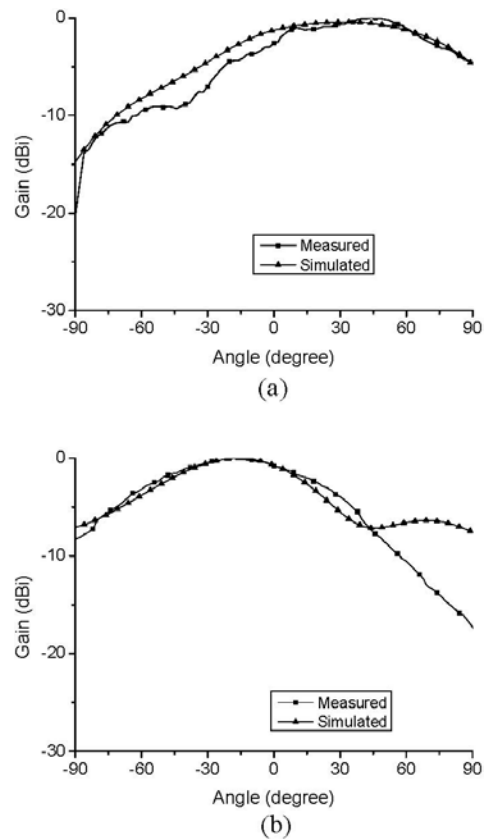


Fig. 3. Simulated and measured radiation patterns at 3.67 GHz in (a) $\theta=90^\circ$ plane (xy -plane) and (b) $\varphi=-44^\circ$ plane for *State 1*.

Table 1. Relative data for pattern reconfigurable antennas.

State	Maximum radiation direction		Beam coverage in xy -plane		Gain	
	full space	xy -plane	3dB	6dB	Full space	xy -plane
1	(52°, 25°)	(90°, 40°)	27° ~ 53°	-50° ~ 79°	4.6	2.2
2	(52°, -25°)	(90°, -40°)	-53° ~ 27°	-79° ~ 50°	4.6	2.2

III. LINEAR PHASED ARRAY FOR SCAN ANGLE EXTENSION

The geometry of the proposed linear phased array is shown in Fig. 4. Eight elements, named *no.1-no. 8*, are arranged along *y*-axis with element space of $d=\lambda/2$, where λ is the wavelength in free space at the operation frequency. The array has a ground plane with an area of $100\text{mm}\times 420\text{mm}$. All of the elements in the phased array operate with the same state and are fed with the same signal amplitude. When the elements in array operate with *State 1*, the simulated return loss at each port and the simulated mutual couplings between two adjacent elements (S_{mn} with $|m-n|=1$) are shown in Fig. 5. In this figure, it can be observed that a return loss of -30dB is achieved for each port and a mutual coupling of less than -20dB is obtained between the adjacent elements at the operation frequency of 3.67GHz . Based on the simulation, the mutual coupling between other elements is decreased further due to larger element spacing. When the elements in array operate in *State 2*, the array performances can be deduced according to the symmetry of the geometry between *State 1* and *State 2*.

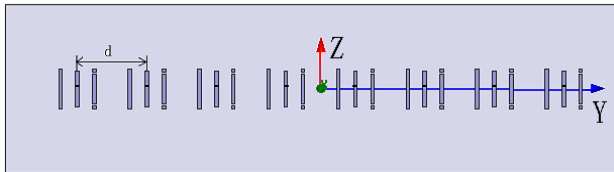


Fig. 4. Geometry of the linear phased array constructed by pattern reconfigurable antenna elements.

The mutual coupling between elements in array can influence severely the array performances. Generally speaking, it can lead to two problems. One is that the active reflection coefficient at each port is increased remarkably when the scan angle away from the array normal is large; and the other is to create the scan blindness in some special angles. Based on the scattering parameter matrix of the array, the active reflection coefficient at each port can be calculated by the following formula,

$$T_m(\theta) = \frac{V_m^{out}}{V_m^{in}} = e^{jkmd \sin \theta} \sum_{n=1}^N S_{mn} e^{-jknd \sin \theta} \quad (1)$$

where m is the element number, θ is the array scan angle and N is the total of the element. The calculated active

reflection coefficients at *Port 1, Port 2, Port 3* and *Port 4* are shown in Fig. 6. It can be observed that a weak active reflection is generated at ports even if the scan angle is large and no total reflection, i.e., no scan blindness, occurs within $\varphi=0^\circ-90^\circ$.

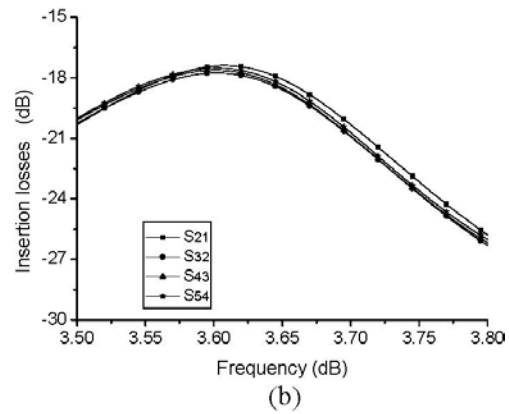
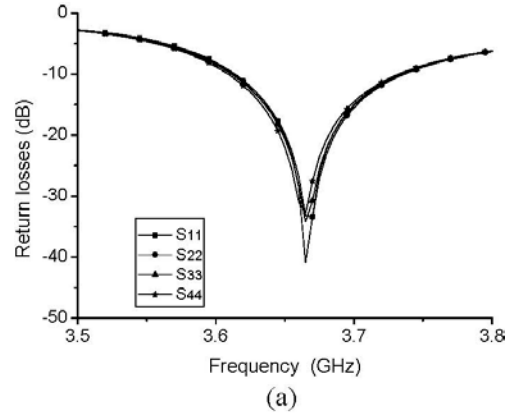


Fig. 5. Simulated (a) return losses at each port and (b) mutual coupling between adjacent elements.

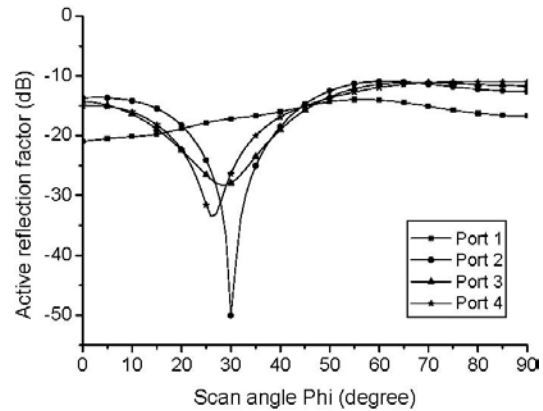


Fig. 6. Simulated active reflection coefficient at feed ports.

The radiation characteristics of the phased array are analyzed by Ansoft HFSS. The progressive phase between two adjacent elements is $\Delta\psi$. Figure 7(a) demonstrates the patterns of the array in xy -plane when the elements operate in *State 1* and with various progressive phases. The results indicate that, as increasing the progressive phase $\Delta\psi$, the scan angle can move from the array normal (x -axis) toward the large angle close to the ground (y -axis) with a good gain performance. The patterns in called plane which is orthogonal to xy -plane and passes through the maximum radiation angle in xy -plane, are plotted in Fig. 7(b).

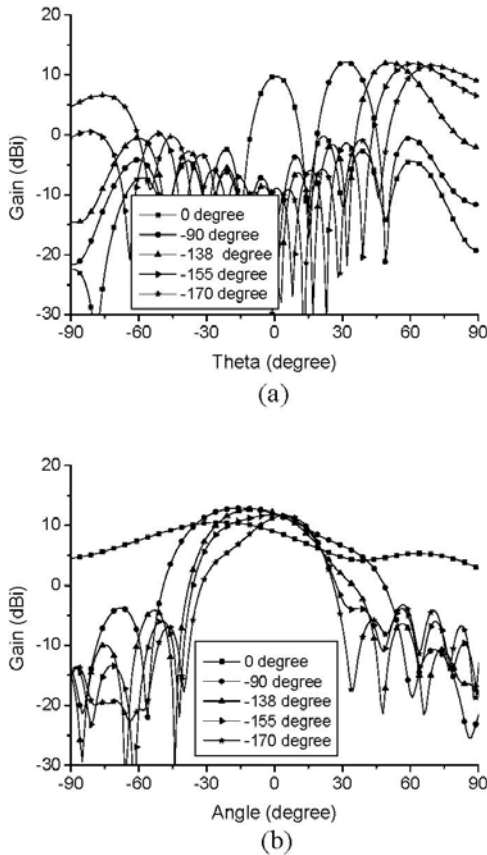


Fig. 7. Radiation pattern of the linear phased array when elements operate in *State 1* and with various progressive phases, (a) xy -plane and (b) E -plane.

The figure shows that the phased array can scan its patterns from $\varphi = -70^\circ$ to 70° in xy -plane. Based on the symmetry, when the elements in the array operate in *State 2* the array performance can be deduced. All of the detailed data of the array scan performance are shown in Table 2. From Table 2, we can observe that the developed linear phased array can scan its patterns from $\varphi = -70^\circ$ to

70° in xy -plane and provide a full angle coverage with 3-dB beam width and good gain performance. Like the single element, the maximum radiation direction of the array is not in xy -plane, however, an acceptable gain performance is achieved when the phased array performs its pattern scan in xy -plane.

Table 2. Pattern scan characteristic of the developed array with various progressive phases.

$\Delta\psi$	Direction(θ_0, φ_0)		Beam coverage in xy -plane		Gain (dBi)	
	Aim	Maximum	3dB	6dB	xy -plane	Full space
<i>State 1</i>						
0°	$(90^\circ, 0^\circ)$	$(46^\circ, 0^\circ)$		$-4^\circ \sim 5^\circ$	7.26	11.3
-20°	$(90^\circ, 7^\circ)$	$(46^\circ, 10^\circ)$		$2^\circ \sim 12^\circ$	7.22	11.2
-40°	$(90^\circ, 14^\circ)$	$(47^\circ, 19^\circ)$		$9^\circ \sim 19^\circ$	7.4	11.2
-60°	$(90^\circ, 21^\circ)$	$(55^\circ, 25^\circ)$	$19^\circ \sim 24^\circ$		8.52	11.1
-70°	$(90^\circ, 25^\circ)$	$(54^\circ, 30^\circ)$	$22^\circ \sim 27^\circ$		8.92	11.52
-90°	$(90^\circ, 32^\circ)$	$(59^\circ, 37^\circ)$	$28^\circ \sim 35^\circ$		9.58	11.70
-110°	$(90^\circ, 39^\circ)$	$(73^\circ, 41^\circ)$	$34^\circ \sim 45^\circ$		9.9	11.93
-138°	$(90^\circ, 51^\circ)$	$(76^\circ, 52^\circ)$	$46^\circ \sim 57^\circ$		9.74	11.82
-155°	$(90^\circ, 61^\circ)$	$(85^\circ, 60^\circ)$	$51^\circ \sim 77^\circ$		9.97	11.04
-170°	$(90^\circ, 70^\circ)$	$(92^\circ, 70^\circ)$	$57^\circ \sim 90^\circ$		10.27	10.57
<i>State 2</i>						
0°	$(90^\circ, 0^\circ)$	$(46^\circ, 0^\circ)$		$-5^\circ \sim 4^\circ$	7.26	11.3
20°	$(90^\circ, -10^\circ)$	$(46^\circ, -10^\circ)$		$-12^\circ \sim 2^\circ$	7.22	11.2
35°	$(90^\circ, -17^\circ)$	$(47^\circ, -19^\circ)$		$-19^\circ \sim 9^\circ$	7.4	11.2
60°	$(90^\circ, -21^\circ)$	$(55^\circ, -25^\circ)$	$-24^\circ \sim 19^\circ$		8.52	11.1
70°	$(90^\circ, -25^\circ)$	$(54^\circ, -30^\circ)$	$-27^\circ \sim 22^\circ$		8.92	11.52
90°	$(90^\circ, -32^\circ)$	$(59^\circ, -37^\circ)$	$-35^\circ \sim 28^\circ$		9.58	11.70
110°	$(90^\circ, -39^\circ)$	$(73^\circ, -41^\circ)$	$-45^\circ \sim 34^\circ$		9.9	11.93
138°	$(90^\circ, -51^\circ)$	$(76^\circ, -52^\circ)$	$-57^\circ \sim 46^\circ$		9.74	11.82
155°	$(90^\circ, -61^\circ)$	$(85^\circ, -60^\circ)$	$-77^\circ \sim 51^\circ$		9.97	11.04
170°	$(90^\circ, -70^\circ)$	$(92^\circ, -70^\circ)$	$-90^\circ \sim 57^\circ$		10.27	10.57

IV. CONCLUSION

A linear phased array with pattern reconfigurable elements is proposed in this paper. The pattern reconfigurable element operates in two switchable states with good performances. The developed linear phased array can perform its pattern scan from $\varphi = -72^\circ$ to 72° in xy -plane and provide a full angle coverage with 3-dB beam width and acceptable gain performance. This study validates the validity of extending the scan angle of the phased array by using the pattern reconfigurable antenna element.

ACKNOWLEDGEMENT

This work was in part supported by aviation Science foundation under grant 20070180003, in part by the new-century talent program of the education department of China under grant NCET070154, in part by national defense research funding under grant 08DZ0229 and in part by the national natural science foundation of China under grant No 60872034.

REFERENCES

- [1] R. Staraj, E. Cambiaggio, and A. Papiernik, "Infinite phased arrays of microstrip antennas with parasitic elements: application to bandwidth enhancement," *IEEE Trans. on Antennas and Propagation*, vol. 42, no. 5, pp. 742-746, 1994.
- [2] A. K. Skrivervic and J. R. Mosig, "Finite phased array of microstrip patch antennas: the infinite array approach," *IEEE Trans. on Antennas and Propagation*, vol. 40, no. 5, pp. 579-582, 1992.
- [3] G. T. Javier, F. W. Parveen, T. C. Michael, and G. C. Christos, "FDTD analysis of finite-sized phased array microstrip antennas," *IEEE Trans. on Antennas and Propagation*, vol. 51, no. 8, pp. 2057-2062, 2003.
- [4] Z. Iluz, R. Shavit, and R. Bauer, "Microstrip antenna phased array with electromagnetic bandgap substrate," *IEEE Trans. on Antennas and Propagation*, vol. 52, no. 6, pp. 1446-1453, 2004.
- [5] Yunqi Fu and Naichang Yuan, "Elimination of scan blindness in phased array of microstrip patches using electromagnetic bandgap materials," *IEEE Antennas and Wireless Propagation Letters*, vol. 3, pp. 63-65, 2004.
- [6] F. Yang and Y. Rahmat-Samii, "Microstrip antennas integrated with electromagnetic band-gap (EBG) structures: a low mutual coupling design for array applications," *IEEE Trans. Antennas Propagat.*, vol. 51, no. 10, pp. 2936-2946, Oct. 2003.
- [7] D.-B. Hou, S. Q. Xiao, B.-Z. Wang, L. Jiang, J. Wang, and W. Hong, "Scan blindness elimination with compact DGSSs in microstrip phased array," Accepted by *IET Microwaves, Antennas & propagation*, 2008.
- [8] S. Q. Xiao, Z. H. Shao, M. Fujise, and B.-Z. Wang, "Pattern reconfigurable leaky-wave antenna design by FDTD method and Floquet's theorem," *IEEE Trans. Antennas Propagate.*, vol. 53, no. 5, pp. 1845-1848, May 2005.
- [9] Yang and Y. Rahmat-Samii, "Patch antennas with switchable slots (PASS) in wireless communications: Concepts, designs, and applications," *IEEE Antennas and Propagation Mag.*, vol. 47, no. 2, pp. 13-29, April 2005.
- [10] D. Peroulis, Kamal Sarabandi, and L. P. B. Katehi, "Design of Reconfigurable Slot Antennas," *IEEE Trans. Antennas Propagate.*, vol. 53, no. 2, pp. 645-654, Feb. 2005.
- [11] J. Zhang and A. Wang, "A survey on reconfigurable antennas," *Microwave and Millimeter Wave Technology International Conference, ICMMT 2008*, vol. 3, pp. 1156-1159, April 2008.
- [12] S. Zhang and J. T. Bernhard, "Performance study of a reconfigurable microstrip parasitic array (RMPA) phased array," *2006 IEEE Antennas and Propagation Society International Symposium*, pp. 2305-2308, 2006.
- [13] F. Yang and Y. Rahmat-Samii, "Patch antenna with switchable slot (PASS): dual frequency operation," *Microwave and Optical Technology Letters*, vol. 31, pp. 165-168, 2001.
- [14] J. Kiriazi and H. Ghali, "Reconfigurable dual-band dipole antenna on silicon using series MEMS switches," *IEEE Antennas and Propagation Society International Symposium 2003*, pp. 403-406, 2003.
- [15] S. Zhang, G. H. Huff, J. Feng, and J. T. Bernhard, "A pattern reconfigurable microstrip parasitic array," *IEEE Trans. on Antennas and Propagation*, vol. 52, no. 10, pp. 2773-2776, 2004.

Quantitative Analysis of Breast Skin for Tumor Detection Using Electromagnetic Waves

¹D. A. Woten and ²M. El-Shenawee

¹Microelectronics-Photonics Program
dwoten@uark.edu

²Electrical Engineering Department, University of Arkansas
Fayetteville, Arkansas 72701

Abstract – This paper supplements the existing knowledge on the breast skin's effect on microwaves for tumor detection in the frequency range 4GHz - 7GHz. A realistic breast model is developed using data of an MRI scan of a physical breast. The breast fibro glandular content along with the tumor's size and location are considered. Numerical results indicate that the skin and tumor signatures could be on the same order of magnitude. This confirms the need to include the skin layer in breast models to minimize the potential of false alarms in tumor detection.

Keywords: Breast model, cancer detection, skin signature, and electromagnetic waves.

I. INTRODUCTION

Breast skin causes inevitable clutter when utilizing electromagnetic waves for cancer detection. In spite of its thickness being only a few millimeters, the skin can obscure the tumor signature. Studies published by radiologists showed that the skin thickness changes as a result of breast abnormalities, complicating the issue further [1]. For microwave imaging, incorporating the skin layer can represent a challenge when implementing computational techniques. These challenges include modeling the complex breast shape along with the varying skin thickness and the corresponding CPU time requirements for simulation.

Existing works addressing the skin simplify the problem in a number of ways. These simplifications include treating the breast as a two-dimensional model [2-7], simplifying the interior and exterior geometries [2-7] and utilizing ideal sources [2-8]. Two-dimensional models treat the breast as continuous flat layers or symmetric shapes which allow the closed form solutions for layered mediums to be utilized, while other simplifications include circular or cylindrical geometries in two or three dimensions [2-6]. In addition plane wave or dipole sources are typically utilized [2-7]. At this time, no single paper has detailed the skin's effect for realistic configurations of the breast shape, interior structure and

practical antenna sources. This purpose of this work is to supplement the existing literature on breast skin effect in the microwave region using a realistic breast shape, interior structure and sources.

El-Shenawee *et al.* showed that the shape reconstruction of breast tumors in three dimensions using gradient methods required up to 26 CPU hours on a 64-bit machine, even though the skin layer was ignored [9]. In another previous study the breast was modeled as a coated sphere to incorporate the skin layer using the Mie Solution [7]. In that work, the error due to ignoring the skin layer was shown to be 3% when receiving in the backscatter direction, versus 30% when receiving in the forward direction. However, that work was preliminary and did not investigate the fibro glandular content, tumor size and location, realistic breast shape or practical sensors.

Human breast skin varies in thickness in each of the four regions of superior, inferior, medial and lateral shown in Fig. 1. The skin tends to be the thickest in the inferior region and thinnest in the lateral region [1]. Utilizing the experimentally acquired data reported in [1] and the fibro glandular interior structure obtained from a patient's MRI scan in [10] allows a realistic breast model to be generated. Broadband planar antennas are used for excitation to calculate the signature of the skin and the breast tumor as will be discussed in the following sections.

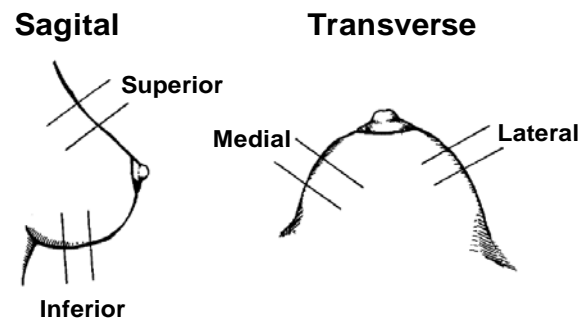


Fig. 1. The four regions of the breast.

II. METHODOLOGY

A. Development of Breast Model

As known, the human breast is a complex biological system containing fatty tissue, ducts, lobules and other fibro glandular tissue. All of these tissues are contained in a nonsymmetrical exterior shape of diverse proportions and a skin layer of varying thickness. To prove the concept of microwave imaging and detection of breast tumors, in the past few years, a variety of simplifications for the breast shape and interior structure were utilized in the literature [2-9, 11].

In this work, the breast model is assumed to contain five homogeneous regions as shown in Fig. 2(a). The interior regions correspond to the fatty breast tissue and the fibro glandular tissue representing the ducts, lobules, fat, etc. Taking 70 cross-sections of each region of the MRI scan allows for the creation of a three-dimensional configuration. Due to the lack of available 3D MRI scan data, we assume circular symmetry for the cross-section of each region shown in Fig. 2(a). For example, the cross-section a-a' is shown in Fig. 2(b) and cross-section b-b' is shown in Fig. 2(c). In this work, the skin layer is chosen to correspond to the values measured by Lee *et al.* [1]. Normal values of skin thickness are used in Figs. 2 to 6, while Fig. 7 shows results of minimum and maximum skin thickness. Normal skin thickness are 1.5mm for the superior region, 1.7mm for the inferior region, 1.5mm for the medial region and 1.3mm for the lateral region. The reported data ranges from 0.75 to 2.3mm for the superior region, from 0.7 to 2.7mm for the inferior region, from 0.6 to 2.4mm for the medial region and from 0.5 to 2.1mm for the lateral region. Outside the breast, a matching medium of oil with $\epsilon_r = 3$ is assumed [12].

Recent measured electrical properties of breast tissues are reported in [13]. The new reported properties of the fibro glandular region are not significantly different from that of the malignant tumor (up to ~10% difference). However, a high contrast was reported to exist between the fatty and tumor tissues (~500%) [13].

The breast model used in this study incorporates the skin with varying thicknesses and with a permittivity of 36 and conductivity of 4 S/m, as reported at 6 GHz in [14]. Frequency dependence is incorporated in the imaginary part of the dielectric constant as reported in [7]. It is important to emphasize that skin thickness, fibro glandular content and tissue properties vary between patients based on physical and hormonal parameters [15].

B. Excitation Source

A three-element array of broadband planar antennas is designed in an effort to focus the beam on the tumor. The array operates between 4GHz and 7GHz when immersed in oil. The array produces a beam focused directly above the central antennas as described in [11],

[16]. The S_{11} of the antenna array shows that the maximum power is radiated at ~5GHz (not presented here but in [16]). The complex input impedance is around $\sim 54 + j4\Omega$ between 4GHz and 7GHz. The antenna array is excited with 100mW input power with the complete design description reported in [11, 16].

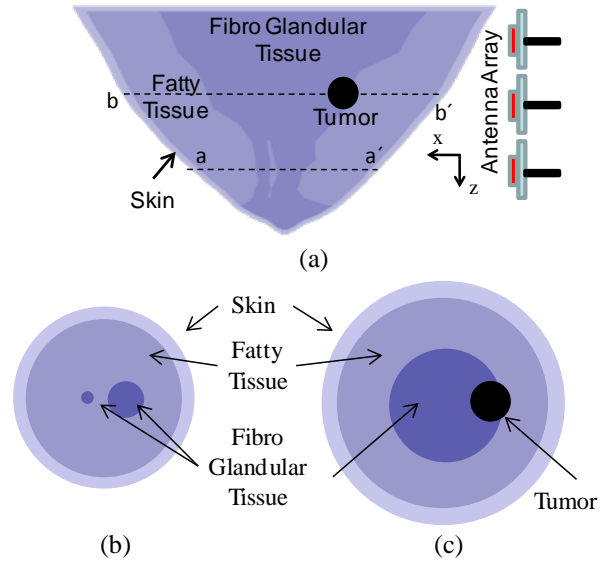


Fig. 2. (a) Breast model developed from MRI scan from [4] with tumor and antenna array, (b) top view of cross-section a-a', and (c) top view of cross-section b-b'.

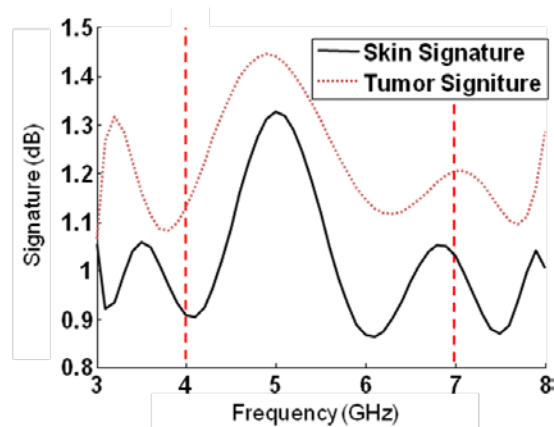


Fig. 3. Skin and tumor signatures for the 100% fibro configuration case. Tumor is located at (6, 0, 0) in Fig. 2(a).

C. Simulations

Integrating the breast model with the broadband array allows for the calculation of realistic skin and tumor signatures. The Ansoft HFSS package is used in this work. The signatures of the skin and tumor are referenced to the S_{11} parameter and are obtained by subtraction for the sake of analysis and comparison. For example, the skin signature was obtained upon subtracting the S_{11} of

the whole breast without a skin layer from the S_{11} with a skin layer ($S_{11}(\text{Breast+Skin}) - S_{11}(\text{Breast})$). Similarly the tumor signature is calculated by subtracting the S_{11} of the whole breast without a tumor from the S_{11} of the breast and tumor ($S_{11}(\text{Breast+Skin+Tumor}) - S_{11}(\text{Breast+Skin})$). The interior breast configuration is varied upon reducing the fibro glandular content while keeping the external breast shape, size, and electrical properties unchanged. The tumor size and location are also varied while keeping its electrical properties unchanged. The complex electrical parameters of breast tissues are obtained using the Cole-Cole curves in [13]. The fibro glandular tissue percentage shown in Fig. 2(a) will be referred to as the 100% fibro case, while a 75% fibro case would represent the same breast shape and size but with the fibro content decreased 25% by radial scaling.

The permittivity and conductivity of the fibro glandular and fatty tissue are reported for a range of frequency from 1-20GHz in [13]. For example, at 5GHz these values are 46 and 4 S/m, respectively, for the fibro glandular tissue and 6 and 1 S/m, respectively, for the fatty tissue [13].

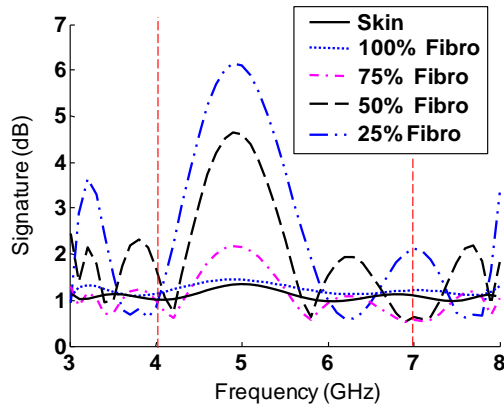


Fig. 4. Skin and tumor signatures for 100%, 75%, 50% and 25% fibro configurations. Tumor is located at (6,0,0) as in Fig. 2(a).

III. NUMERICAL RESULTS AND DISCUSSION

In the first case, the tumor is located at 4cm from the skin as shown in Fig. 2(a). The figure shows that the tumor partially overlaps the fibro glandular and the fatty tissue. The tumor is 10mm in diameter and is located in the direction of the main beam of the antenna array. Figure 3 shows the computed skin and tumor signatures vs. the frequency for 3-8GHz. The signature of the skin and tumor display an oscillatory behavior where the skin signature is smaller than that of the tumor. The difference between the skin and tumor signature is ~ 0.11 dB at 5GHz. These oscillations could be due to the fluctuations in the radiation pattern as a function of the frequency (not shown here but in [16]). In [16], the radiation pattern

showed that the side lobes were significant at some frequencies while disappeared at others.

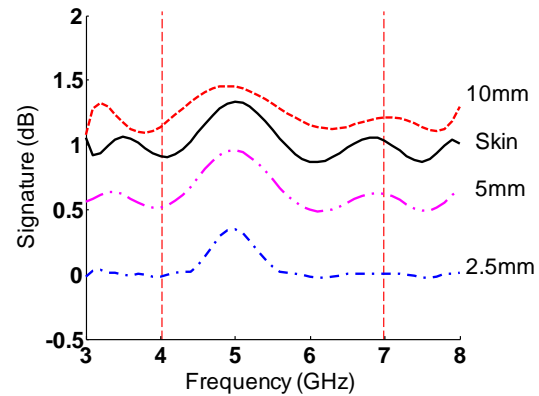


Fig. 5. Skin and tumor signatures for a tumor of diameter 10mm, 5mm and 2.5mm located at (6, 0, 0) in Fig. 2(a).

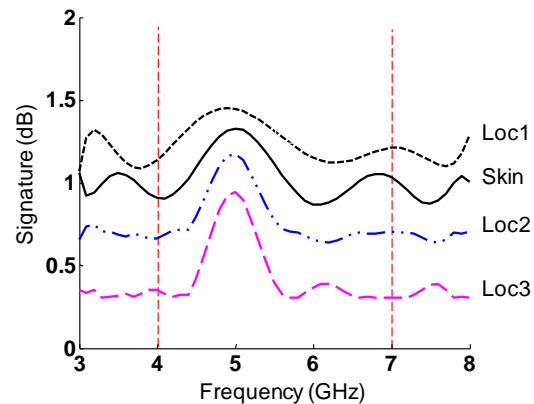


Fig. 6. Skin and tumor signatures for three locations; Loc1: (6,0,0), Loc2: (6,3,0), Loc3: (6,0,3) in Fig. 2(a).

In the second case, the fibro glandular content is reduced to 75%, 50%, and 25% as explained earlier. Accordingly, the tumor gradually changes from being partially overlapping the fibro glandular and fatty tissue (the 100% fibro case) to being totally immersed in the fatty tissue (the 25% fibro case). It is observed that the skin signature, obtained by subtraction, remains almost unvaried regardless of the fibro glandular content.

Figure 4 shows the skin signature vs. that of the tumor for the 100%, 75%, 50%, and 25% fibro content cases. The results show that the skin signature is the smallest in this case. In addition, as the content of fibro glandular tissue decreases, the tumor signature increases up to 6.25 dB for the 25% fibro case. These are anticipated results since with less fibro glandular tissue and more fatty tissue, the contrast between the tumor and surroundings increases leading to larger signature as shown in Fig. 4. This can be explained because the tumor has a higher contrast with the surrounding fatty tissue

(~500%) [13]. The maximum difference between the skin and tumor signatures is observed as ~5.12dB at 5GHz for the 25% fibro case as shown in Fig. 4.

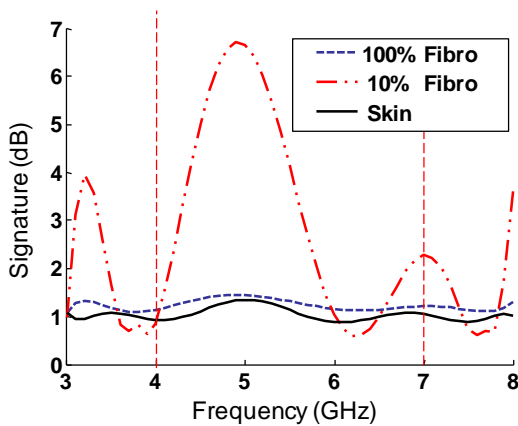


Fig. 7. Skin and tumor signatures for a 10mm tumor.

The third case varies the tumor size while utilizing the original fibro glandular content of 100% in Fig. 1. The diameter of the tumor is varied as 10mm, 5mm and 2.5mm as shown in Fig. 5. It is interesting to note that the skin signature, i.e. the clutter, could dominate the received signal. In other words, the skin signature is larger than that of the tumor of diameters 2.5 mm and 5 mm, in this case. In addition, the signature of a 10 mm tumor differs by only ~0.1dB to that of the skin as shown in Fig. 5.

The fourth case of Fig. 6 investigates the tumor location. As known, the ductal carcinoma in-situ is the most common breast cancer and can form at any location in the vast duct system. Thus, three possible tumor locations are tested in this figure at (6, 0, 0), (6, 3, 0) and (6, 0, 3). The second location, offset in the y-direction, is still in the direction of the main beam of the array while the third location, offset in the z-direction, is outside the direction of the main beam. The results of Fig. 6 show that when the tumor is located at Loc2 (6, 3, 0) and Loc3 (6, 0, 3), the skin signature is larger than that of the tumor. The tumor signature at Loc1 is only 0.1dB larger than that of the skin while it is 0.14dB and 0.49dB smaller than the skin signature for Loc2 and Loc3, respectively.

Figure 7 summarizes the extreme cases which could be encountered in reality. The 100% fibro content in Fig. 2(a) could represent a younger woman with a dense breast. However, the process of menopause increases the relative fat content of the breast, and to represent this, a case with the fibro glandular content of only 10% is considered. Figure 7 depicts the skin signature vs. that of the tumor for these two fibro glandular contents using a 10mm diameter tumor.

The results of Fig 7 show that the 10mm tumor has a

signature larger than that of the skin regardless of the fibro glandular tissue content. The maximum difference between the two signatures is shown in Fig. 8 to be ~5.4dB, i.e. ~6 times larger than the skin signature. However, the signature of a 2.5mm tumor is less than that of the skin, regardless of the fibro glandular content (result not shown). The difference is observed to be ~0.73dB and 1.09dB for the 10% and 100% fibro contents, respectively. The signature of smaller tumors could be theoretically increased when higher frequencies are used, but in reality the penetration depth of the waves will decrease, as expected.

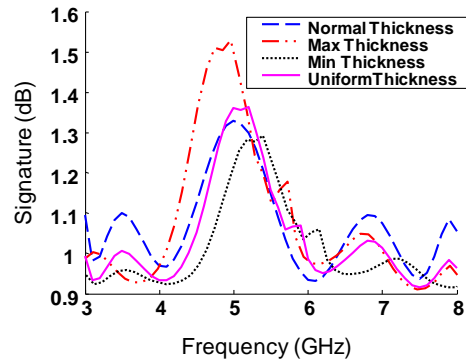


Fig. 8. Skin signatures for several thicknesses with the same breast interior contents. No tumor is included here.

In all above results, it is observed that the skin signature does not significantly change with respect to the interior structure of the breast (mainly the fibro glandular tissue). It is noticed that regardless of the fibro glandular content, tumor location, or size the skin signature is almost unchanged. Therefore, in all above figures, only one skin signature was plotted. This could be explained by the lossy nature of the breast tissue such that the effect of the multiple scattering between the tumor, fibro glandular tissue and the skin layer is diminished.

In all above results, the normal skin thickness reported in [1] was used. On the other hand, the results of Fig. 8 demonstrate the effect of the skin thickness. Figure 8 contains the skin thickness with normal thickness, maximum thickness (>2mm), minimum thickness (<0.7mm), and a uniform thickness of 1.5mm. The minimum and maximum ranges are mentioned in Section II as reported in [1]. The results show that the thickest skin layer has the largest signature, with a maximum of around 1.54dB vs. 1.3dB for the minimum thickness case. The maximum difference in the skin signatures between the thickest and thinnest skin layer is observed to be only ~0.24dB. The results of Fig. 7 indicate that a realistic skin signature could be approximately predicted by calculating the signature of a uniform skin layer of ~1-2mm thickness.

As known, it is almost impossible to predict the breast interior structure of a patient. However, the reconstruction of the exterior shape of the breast can be obtained as reported in [17]. Then a uniform skin layer could be engineered following the reconstructed breast shape in order to calculate its signature as shown in Fig. 8. Upon subtracting the predicted skin signature from the measurements of the signals scattered from the breast, the skin clutter can be removed. This process can help speeding up the computational algorithms for imaging the tumor. This process is expected to introduce some noise into the data, but less than a few dBs.

All above results were obtained using the HFSS package that required 20-24 CPU hours on a quad-core 64bit AMD Opteron workstation.

IV. CONCLUSIONS AND FUTURE WORK

The results of this work show that the signature of the skin could be comparable or even larger than that of the tumor depending on the fibro glandular content of the breast and the size and location of the tumor. This work confirms the importance of accounting for the skin layer in breast cancer detection at the microwave frequency range.

The current breast model can be improved by treating the fibro glandular region of the breast as discrete inclusions instead of a continuous region to incorporate the more heterogeneous nature of breast tissue. However, modeling individual duct systems and lobules along with the vascular system is computationally challenging due to their complex nature and minute feature sizes as reported in [18].

ACKNOWLEDGEMENTS

This work was supported in part by the NSF Graduate Research Fellowship, NSF GK-12 Program, NSF Award Number ECS – 0524042, the Arkansas Biosciences Institute (ABI), and the Women's Giving Circle at the University of Arkansas.

REFERENCES

- [1] T. Lee, M. E. Read, and T. Medsker, "Breast skin thickness: normal range and causes of thickening shown on film –screen mammography," *Journal of Canadian Association of Radiologists*, vol. 35, pp. 365-68, Dec. 1984.
- [2] E. Alanen and I. V. Lindell, "Effect of skin in microwave detection of breast cancer," *IEEE Trans. Microwave Theory and Techniques*, vol. 34, no. 5 pp. 584-588, May 1986.
- [3] T. C. Williams, E. C. Fear, and D. T. Westwick, "Tissue sensing adaptive radar for breast cancer detection-investigations of an improved skin-sensing method," *IEEE Trans. Microwave Theory and Techniques*, vol. 54, no. 4, part 1, pp. 1308-1314, Jun. 2006.
- [4] G. Wang and X. Zeng, "Impact of dispersion in breast tissue on high-resolution microwave imaging for early breast tumor detection," *IEEE Antennas and Propagation Society International Symposium*, vol. 3, pp. 2452-2455, Jun 2004.
- [5] T. Williams, E. C. Fear, and D. W. Westwick, "Tissue sensing adaptive radar for breast cancer detection: investigations of reflections from the skin," *IEEE Antennas and Propagation Society International Symposium*, vol. 3, pp. 2436-2439, June 2004.
- [6] M. Popovic and A. Taflove, "Two-dimensional FDTD inverse-scattering scheme for determination of near-surface material properties at microwave frequencies," *IEEE Trans. Antennas and Propagation*, vol. 52, no. 9, pp. 2366-2373, Sept. 2004.
- [7] S. Pandaraju, "A hybrid algorithm based on Mie theory and evolution strategy for breast cancer imaging," M.S. Thesis, University of Arkansas, Fayetteville, AR, USA, 2006.
- [8] T. C. Williams, J. M. Sill, and E. C. Fear, "Breast surface estimation for radar-based breast imaging systems," *IEEE Trans. Biomedical Engineering*, vol. 55, no. 6, pp. 1678-1686, June 2008.
- [9] M. El-Shenawee and E. Miller, "Spherical harmonics microwave algorithm for shape and location reconstruction of breast cancer tumor," *IEEE Transaction on Medical Imaging*, vol. 25, pp. 1258-1271, Oct. 2006.
- [10] R. Weisskoff, "MRImages," *int.ch.liv.ac.uk*, [Online]. Available: http://int.ch.liv.ac.uk/Lanthanide/Ln_Chemistry_folder/MRI%20folder/MRImages.html. [Accessed Nov. 30, 2007].
- [11] D. Woten, "Artificial neural networks for breast cancer detection using micro antennas," M.S. Thesis, University of Arkansas, Fayetteville, AR, USA, 2007.
- [12] J. M. Sill and E. C. Fear, "Tissue sensing adaptive radar for breast cancer detection: study of immersion liquids," *Electronics Letters*, vol. 41, pp. 113-115, Feb. 2005.
- [13] M. Lazebnik, D. Popovic, L. McCartney, C. B. Watkins, M. J. Lindstrom, J. Harter, S. Sewall, T. Ogilvie, A. Magliocco, T. M. Breslin, W. Temple, D. Mew, J. H. Booske, M. Okoniewski, and S. C. Hagness, "A large-scale study of the ultrawideband microwave dielectric properties of normal, benign, and malignant breast tissues obtained from cancer surgeries," *Physics in Medicine and Biology*, vol. 52, pp. 6093-6115, 2007.

- [14] X. Li and S. C. Hagness, "A confocal microwave imaging algorithm for breast cancer detection," *IEEE Microwave and Wireless Components Letters*, vol. 11, no. 3, Mar. 2001.
- [15] H. Ulger, N. Erdogan, S. Kumanlioglu, and E. Unur, "Effect of age, breast size, menopausal and hormonal status on mammographic skin thickness," *Skin Research and Technology*, pp. 284-289, 2003.
- [16] D. A. Woten and M. El-Shenawee, "Broadband dual linear polarized antenna for statistical detection of breast cancer," *IEEE Antenna and Propagation Letters*, vol. 56, no. 11, Nov. 2008
- [17] M. R. Hajihashemi and M. El-Shenawee, "Breast Shape Reconstruction using Microwave Techniques and The Level Set Method," , *24th Annual Review of Progress in Applied Computational Electromagnetics*, Niagara Falls, Canada, pp. 98-103, Mar. 2008.
- [18] J. Greenlee, S. Shumate, and M. El-Shenawee, "A comprehensive approach to modeling breast cancer," *Proc. Ohio Collaborative Conference on Bioinformatics*, Toledo, Ohio, June 2-4, 2008.



Douglas A. Woten received the B.A. degree with honors in mathematics and the B.A. in physics from Hendrix College, Conway, AR in 2005. He received the M.S. degree in Microelectronics-Photonics from the University of Arkansas in 2007 and is currently pursuing his Ph.D. in the same program. He is a recipient of the National Science Foundation (NSF) Graduate Research Fellowship and two time recipient of the NSF GK-12 Fellowship.



Magda El-Shenawee (M'91) received the B.S. and M.S. degrees in electrical engineering from Assiut University, Assiut, Egypt, and the Ph.D. degree in electrical engineering from the University of Nebraska-Lincoln in 1991. In 1992, she worked as a Research Associate in the Center for Electro-Optics at the University of Nebraska where she focused on the problem of enhanced backscatter phenomena. In 1994 she worked as a Research Associate at the National Research Center, Cairo, Egypt, and in 1997, she worked as Visiting Scholar at the University of Illinois at Urbana-Champaign. In 1999, she joined the MURI team (Multidisciplinary University Research Initiative) at Northeastern University, Boston. Currently, Dr. El-Shenawee is an Associate Professor in the Department of Electrical Engineering at the University of Arkansas, Fayetteville. Her research areas are microwave imaging of breast cancer, computational inverse problems, microwave imaging systems, mathematical biology of breast tumors, MEMS antennas, biophysics of tumors, rough surface scattering, computational electromagnetics, subsurface sensing of buried objects, landmine detection, and numerical methods for microstrip circuits. Dr. El-Shenawee is a member of Eta Kappa Nu electrical engineering honor society.

High Reflector by One-dimensional Quasi-Periodic Thue-Morse Multilayered Band Gap Structure at Ultra High Frequency Band

Y. Trabelsi, N. Ben Ali, Y. Bouazzi, and M. Kanzari

Photovoltaic and Semiconductor Materials Laboratory, El-Manar University-ENIT PO Box 37,
Le Belvedere 1002-Tunis, Tunisia
youssef_trabelsi@yahoo.fr

Abstract — The quasi-periodic Thue-Morse (T-M) multilayered band gap structures are studied at ultra high frequency band (UHF) by using a theoretical model based on matrix method (MM) for any incidence simulator. It is demonstrated that reflection spectrum in this frequency domain cover a great part of UHF band which contains the Global System for Mobile communication (GSM) bands, where the propagation of electromagnetic waves is forbidden in this region for all incident angle and all polarisations. The study of a deformed stack which is constructed according to the quasi-periodic sequences so that the coordinates y of the deformed object was determined through the coordinates x of the Thue-Morse stack in accordance with the following rule $y=x^{k+1}$, where k : the coefficient defining the deformation degree. Consequently, an omni-directional high reflector at UHF band covering the GSM band is established.

Keywords: Photonic crystals, Thue-Morse sequence, and quasi-periodic multilayer system.

I. INTRODUCTION

Photonic crystals (PC) represent an artificially fabricated system and it is characterized by a periodic dielectric medium where the propagation of an electromagnetic wave is prevented in certain frequency bands independently of the direction of the incident wave and of its polarization.

It has potential applications in many such technological areas as waveguides with photonic crystals, substrates for antennas in microwaves, filters or perfect mirrors and in the development of efficient semiconductor light emitters [1]. In addition, it can also control and manipulate the propagation of electromagnetic waves [2-4].

The simplest form of a photonic crystal is the one-dimensional (1D) periodic structure. It consists of a stack of alternating layers having a low and high refractive indices, whose thicknesses satisfy the Bragg condition: $n_L d_L = n_H d_H = \lambda_0/4$ where λ_0 is the reference wavelength. It is known as Bragg Mirror [1, 5, 6].

Quasi-periodic multilayer systems can be considered as suitable models to describe the transition from perfect

periodic structures to random structures [7, 8]. Built according to determinist order quasi-periodic multilayer system, the spectra of this multilayer stacks show very interesting physical properties like the existence of a photonic band gap (PBG) for different frequency regions. The Thue-Morse sequence is one of the well-known examples in 1D aperiodic structure [9].

Additionally, some properties of Thue-Morse quasi-crystals have been studied in different domains [10-12], such as the elastic waves in quasi-regular perpendicular polarisation structures, the localization of light waves, which leads to the appearance of photonic band gaps and the propagation of light in Thue-Morse dielectric multilayer systems [13-15].

Also Negro [16] established large omni-directional photonic band gap of 32 layers from Thue-Morse sequence using Si/SiO₂ material and explained its physical origin. He showed the remarkable scaling properties of the transmission spectra both with wavelet decomposition and Fourier Transform Analysis.

Furthermore, by using the tin sulfide-silica material system, Deopura [17] has developed and determined the formation of a broadband visible reflector with an omnidirectional range greater than 10%. Thus, he calculated and measured the reflectance spectra as a function of wavelength for perpendicular (P) and serial (S) polarisations at different incident angles and he established an omnidirectional reflectivity band from 400 to 780 nm.

The deformation of crystals was introduced by applying a power law so that the coordinates y which represent the transformed object, were determined using the coordinates x of the initial object in accordance with the following rule: $y = x^{1+k}$, with k : the coefficient defining the deformation degree.

The initial phase thickness when we apply the y function is: $\varphi = \frac{2\pi}{\lambda} n d \cos \theta$, which takes the following form:

$$\varphi_j = \frac{2\pi}{\lambda} x_0 (j^{k+1} - (j-1)^{k+1}) \cos \theta_j \quad \text{for } j \geq 1.$$
 With j designating the j^{th} layer and $x_0 = \frac{\lambda_0}{4}$ is the thickness of

each layer of the periodic structure with λ_0 being the reference wavelength.

For the deformed system, the thickness of each layer becomes variable and depends on the j^{th} layer and the deformation degree k . So, the optical thickness of each layer after deformation by the y function takes the following form: $x'_{0j} = x_0(j^{k+1} - (j-1)^{k+1})$ for $j \geq 1$. It is clear that for a given value of k , the quasi-periodic system becomes deformed and the thickness of each layer increases with k increasing. Figure 1 shows, for example, the principle of introducing deformation into the Thue-Morse structure.

Also, the properties of one-dimensional periodic and quasi-periodic photonic crystals with a defect layer have been investigated by Abdel-Rahman et al [18]. In this case, he studied the effect of position, thickness and index of refraction of a defect layer on the transmission spectrum and the defect mode of periodic photonic structure (PPS) as well as Fibonacci quasi-periodic photonic structures.

So in this work we introduce a deformation to the multilayer stack. Deformed stack, which is constructed according to the quasi-periodic generalized Thue-Morse sequence, has been reported in frequency range of the ultra high frequency band. Reflectance spectra reach 100% for the incident angle $[0, \pi/2]$ and all polarisations. So, the transmission is forbidden in this frequency range.

We have shown that the high frequency term in the spectra depends on both order of system and degree of deformation k .

This paper is organized as follows: in the second part, we give the formulation of Matrix Method (MM), including the reflectance spectrum in both S and P polarisations. The models of quasi-periodic generalised Thue-Morse sequence are presented in section III.

The reflectance spectra of this deformed quasi-periodic multilayer structure are discussed in Section IV, it is shown that a high reflector covers the part of frequency in ultra high frequency band including the GSM band width.

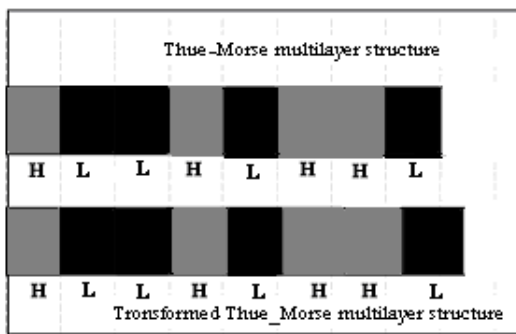


Fig. 1. Transformation of a perfect Thue-Morse multilayer structure into an asymmetric one, for example for $h = 0.1$.

II. MATHEMATICAL THEORY

We employ the MM, including components of the refractive index, to extract transmission, reflection and consider their sensitivity to material and geometrical variation. It can solve the problem of the photonic band structures and the scattering (transmission and reflection) spectra. For stratified layers within m layer, the amplitudes of the electric fields of incident wave E_0^+ , reflected wave E_0^- and transmitted wave E_{m+1}^+ after m layers can be related via the following matrix [19],

$$\begin{pmatrix} E_0^+ \\ E_0^- \end{pmatrix} = \frac{C_1 C_2 C_3 \dots C_{m+1}}{t_1 t_2 t_3 \dots t_{m+1}} \begin{pmatrix} E_{m+1}^+ \\ E_{m+1}^- \end{pmatrix}. \quad (1)$$

The C_j (propagation matrix) for the j^{th} sequence can be written,

$$C_j = \begin{pmatrix} \exp(i\phi_{j-1}) & r_j \exp(-i\phi_{j-1}) \\ r_j \exp(i\phi_{j-1}) & \exp(-i\phi_{j-1}) \end{pmatrix} \quad (2)$$

ϕ_{j-1} indicate the phase shift of the wave between $(j-1)^{\text{th}}$ and j^{th} boundaries and can be obtained by,

$$\phi_0 = 0 \quad (3)$$

$$\phi_{j-1} = \frac{2\pi}{\lambda} \hat{n}_{j-1} d_{j-1} \cos \theta_{j-1} \quad (4)$$

The asymmetry was introduced by applying the power lower, so that the coordinate y which represent the transformed object were determined using the coordinate x of the initial object in accordance with the following rule: $y = x^{k+1}$ here k is the coefficient defining the asymmetry degree in to the Thue-Morse multilayer structure. The initial phase thicknesses when we apply the y function take the following form for $j \geq 1$,

$$\phi_j = \frac{2\pi}{\lambda} \hat{n}_j d_j \cos \theta_j (j^{k+1} - (j-1)^{k+1}) \quad (5)$$

The Fresnel coefficients t_j and r_j can be expressed as follows by using the complex refractive index \hat{n}_j and the complex refractive angle θ_j .

For parallel P- polarization,

$$r_{jp} = \frac{\hat{n}_{j-1} \cos \theta_j - \hat{n}_j \cos \theta_{j-1}}{\hat{n}_{j-1} \cos \theta_j + \hat{n}_j \cos \theta_{j-1}} \quad (6)$$

$$t_{jp} = \frac{2\hat{n}_{j-1} \cos \theta_{j-1}}{\hat{n}_{j-1} \cos \theta_j + \hat{n}_j \cos \theta_{j-1}}. \quad (7)$$

Moreover, for perpendicular S- polarization,

$$r_{js} = \frac{\hat{n}_{j-1} \cos \theta_{j-1} - \hat{n}_j \cos \theta_j}{\hat{n}_{j-1} \cos \theta_{j-1} + \hat{n}_j \cos \theta_j} \quad (8)$$

$$t_{js} = 2 \frac{\hat{n}_{j-1} \cos \theta_{j-1}}{\hat{n}_{j-1} \cos \theta_{j-1} + \hat{n}_j \cos \theta_j}. \quad (9)$$

For both polarisations s and p the transmittance energy T are reduced as,

$$T_s = \text{Re} \left(\frac{\hat{n}_{m+1} \cos \theta_{m+1}}{\hat{n}_0 \cos \theta_0} \right) |t_s|^2 \quad (10)$$

$$T_p = \text{Re} \left(\frac{\hat{n}_{m+1} \cos \theta_{m+1}}{\hat{n}_0 \cos \theta_0} \right) |t_p|^2, \quad (11)$$

Re indicates the real part.

III. GENERALIZED THUE-MORSE MULTILAYER STRUCTURE

One-dimensional quasi-periodic Thue-Morse sequences are multilayer structures consisting of two different materials. They contain two building blocks H and L and can be produced by repeating application of the substitution rules $H \rightarrow HL$ and $L \rightarrow LH$, where H denotes the material with the higher refractive index, and L denotes the material with the lower refractive index. For example, the first few generations S_j of Thue-Morse sequence [20] are as follows: $S_0 = \{H\}$, $S_1 = \{HL\}$, $S_2 = \{HLLH\}$, $S_3 = \{HLLHLHHL\}$ etc.. whereas, the generalized Thue-Morse multilayer is recursively constructed as: $S_{k+1} = (S_k)^n (\overline{S_k})^m$ with $S_1 = H$ and $\overline{S_1} = L$ and arranged according to an inflation rule σ_{T-M} : $H \rightarrow H^m L^n$, $L \rightarrow L^m H^n$ [21]. Based on the characteristics of the construction of Thue-Morse sequences, Fig. 2 shows one dimensional generalised Thue-Morse class quasi-periodic multilayer stacks for 3rd generation. According to Thue-Morse rule, there are 16 layers in this structure. (Note: in the all of this work we have chosen $m=n=1$ i.e., Thue-Morse sequence).

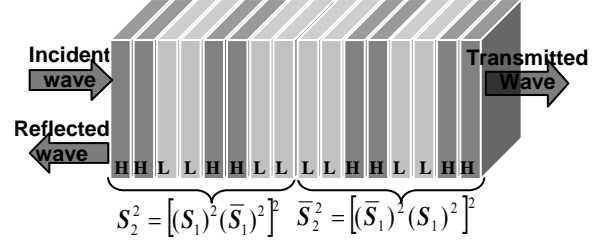


Fig. 2. Schematic representation showing the geometry of the 3rd generation of generalized Thue-Morse quasi-periodic multilayer system for $m=n=2$.

IV. RESULTS AND DISCUSSIONS

In the following numerical investigation, we choose air (L) and Roger (H) as two elementary layers, with refractive indices $n_L=1$ and $n_H=3$, respectively. The thicknesses $d_L=3$ mm and $d_H=1$ mm of the two materials has been chosen to satisfy the Bragg condition: $n_L d_L = n_H d_H = \lambda_0/4$ where $\lambda_0=12$ mm is the reference wavelength.

We use the matrix method to extract the transmission coefficients in the ultra high frequency spectral range which correspond to 0.3GHz-3GHz. We show that the corresponding reflection coefficients exhibit interesting properties. We assume that the front and the back media have refractive index $n_0=1$ (index of air). In Fig. 3, we found that the width of forbidden gap $[\lambda_{Long}-\lambda_{Short}]$ is sensitive to deformation degree k . We notice, for $k=0.05$, a high width of band which covers the spectral domain corresponding to ultra high frequency band (0.3< f <3GHz). Therefore, the PBG covers only the GSM band width included in the studied wavelength range: [285 -350] mm.

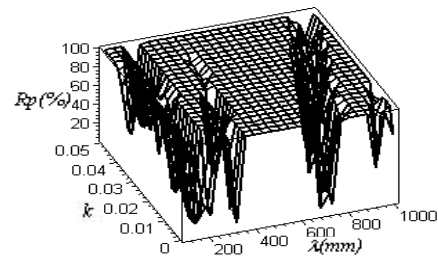


Fig. 3. Reflectance spectra ($R_p(\%)$) in mode P through the 8th level Thue-Morse as function of wavelength and deformation degree k .

The reflectance spectra at 6th order of deformed quasi-periodic Thue-More as functions of wavelength and incident angle θ are shown in Fig. 4. We noticed in this case two basics pseudo photonic band gap. The first forbidden gap is included in GSM band whereas the second band is narrower and covers a greater parts of the wavelength range. So, particularly we interested in the first region which contains a GSM band. We propose a

high reflector in this frequency range where this sample structure, built according the Thue-Morse sequence, inhibits the propagation of waves but there exist peaks of transmission in this frequency range for some value of incident angles. Consequently, a partial photonic band gap is established for the 6th level of Thue-Morse sequence. This result is possible via sample periodic structure, but we can't create a transmission peak inside the basic photonic band gap and generate author pseudo band gap outside the original photonic band gap.

At normal incidence, we note a similarity of reflectance spectra for both polarisations. In fact, for $\theta=0$, the expression of R_s is equal to that of R_p in equation 2. The origin of the fundamental Thue-Morse band gaps can be attributed to local correlations in the form of periodic strings with the corresponding frequency and the layer distributions.

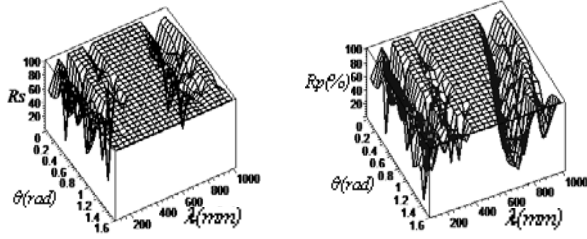


Fig. 4. The reflection spectra through the 6th order of Thue-Morse photonic structures in both modes polarizations (S and P).

It has been shown that multilayer Thue-Morse system with alternating layers do not exhibit a complete photonic band gap where the grey area covers a frequency range for $\theta < 1$ radian (Fig. 5). However, we note another photonic band gap for $\theta > 1$ radian. But their photonic band gap covers a wavelength range between 400 mm and 700 mm where its Fourier spectrum does not exhibit an omni-directional band gap.

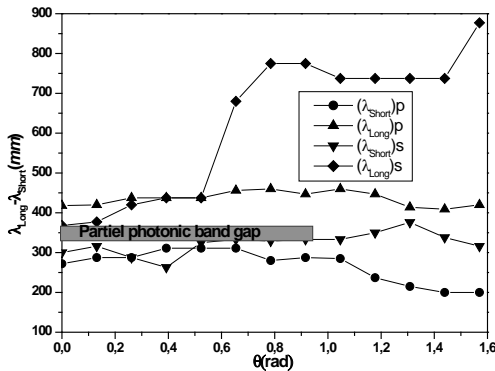


Fig. 5. Variation of limit wavelength of 6th of Thue-Morse sequence in both polarisation S and P as a function of incident angle, with deformation degree ($k=0.05$).

A. Effect of Varying the Order of Thue-Morse with Constant Deformation

The reflection band for the S mode is wider than that for the P mode. Band gaps are shown for this pair material (air/Roger). Increasing the order of T-M sequence, the width of PBG enhances and narrows transmission peaks increase for two spectra R_p and R_s . It is clear that a PBG depends at Thue-Morse orders. So, from the reflectivity spectrum of S_6 in Fig. 4, the photonic band gap is interrupted for $\theta=1$ radian and we can noted in this order of Thue-Morse class do not exhibit any omni-directional high reflection Band.

Moreover, with the increase of the order of Thue-Morse sequence (Fig. 6), a large PBG appears from the 8th order of one-dimensional Thue-Morse multilayered structure and covers the GSM band included in ultra high frequency band. So, a fractal Thue-Morse omni-directional band depends on its sample order and on the choice of value of deformation which fixes the number and thicknesses of the layer.

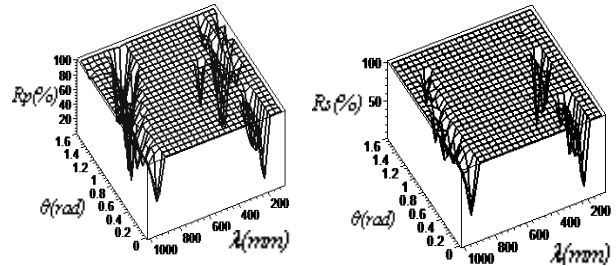


Fig. 6. Reflectance spectra through Thue-Morse multilayer structure as a function of wavelength for TM and TE modes at any incident angles for 8th order of Thue-Morse.

B. Broadening of Omni-directional Photonic Band-Gap

The variation of λ_{long} and λ_{short} for two polarisations S and P marked an omni-directional reflection in a one-dimensional Thue-Morse aperiodic photonic crystal containing the two elements Air and Rogers is determined which broadening versus the order of Thue-Morse sequences where the deformation is fixed to 0.05 (see Fig. 7).

The band gap structure, predicted by the numerical calculations, is clearly identifiable from the 8th Thue-Morse order. Note that this highlight grey area covers all the global systems for mobile communication (GSM) included in ultra high frequency band .which forms a high reflector in this frequency range.

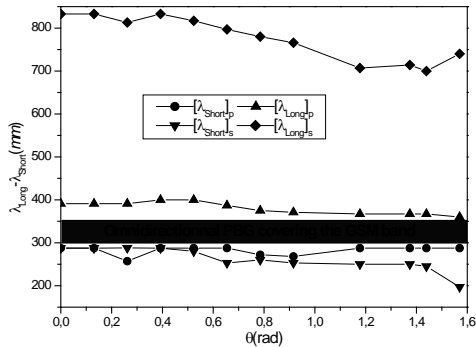


Fig. 7. Variation of limit wavelength of 8th of Thue-Morse sequence in both polarisation S and P as a function of incident angle, with deformation degree ($k=0.05$).

V. CONCLUSION

Omni-directional reflection through one-dimensional Thue-Morse class quasi-crystal were investigated. We analysed the reflectance spectrum using Matrix method. A forbidden gap has shown in ultra high frequency band which covers the all GSM band width frequency for all incident angles and both polarizations. We also found that a high reflector band gap in ultra high frequency range is generated by all elements of system built according to Thue-Morse sequence.

REFERENCES

- [1] K. Agi, E. R. Brown, O. B. McMahon, C. Dill, and K. J. Malloy, "Design of ultra wideband photonic crystals for broadband antenna applications," *Electron. Lett.*, vol. 30, no. 25, pp. 2166–2167, 8 December 1994.
- [2] E. Yablonovitch, "Inhibited spontaneous emission in solid-state physics and electronics," *Phys. Rev. Lett.*, vol. 58, no. 20, pp. 2059–2062, 1987.
- [3] S. Hong-Yi, L. Zhi-Yuan, G. Ben-Yuan, "Defect modes in multiple-constituent one-dimensional photonic crystals examined by an analytic Bloch-mode approach," *Chin. Phys. Lett.*, vol. 22, no. 2, pp. 365, 2005.
- [4] D. Cassagne, A. Barra, and C. Jouanin, "Defects and diffraction in photonic crystals," *Superlattices and Microstructures*, vol. 25, no. 1/2, pp. 343–346, JAN-FEB 1999.
- [5] P. Yeh, "Optical Waves in Layered Media," *John Wiley & Sons*, New York, ISBN: 0-471-82866-1, 1988.
- [6] Luigi Moretti, Ilaria Rea, Lucia Rotiroli, Ivo Rendina, Giancarlo Abbate, Antigone Marino, and Luca De Stefano, "Photonic band gaps analysis of Thue-Morse multilayers made of porous silicon," *Optics Express*, vol. 14, no. 13, pp. 6264, 26 June 2006.
- [7] M. E. Zoorob, D. B. Charlton, M. G. J. Parker, J. J. Baumberg, and M. C. Netti, "Complete photonic bandgaps in 12-fold symmetric quasicrystals," *Nature*, vol. 404, pp. 740–743, 13 Apr 2000.
- [8] D. Zhang, Z. Li, W. Hu, and B. Cheng, "Broadband optical reflector—an application of light localization in one dimension," *Appl. Phys. Lett.*, vol. 67, no. 17, pp. 2431–2432, 1995.
- [9] L. Dal Negro, M. Stolfi, Y. Yi, and J. Michel, "Photon band gap properties and omnidirectional reflectance in Si/SiO₂ Thue–Morse quasicrystals," *App. Phys. Lett.*, vol. 84, no. 25, pp. 5186–5188, 21 June 2004.
- [10] V. Agarwal and Miguel E Mora-Ramos, "Optical characterization of polytype Fibonacci and Thue–Morse quasiregular dielectric

- structures made of porous silicon multilayers," *J. Phys. D: Appl. Phys.*, vol. 40, pp. 3203–3211, 4 May 2007.
- [11] V. R. Velasco and J. E. Zarate, "Elastic waves in quasi-periodic structures," *Elsevier science, Prog. Surf. Sci.*, vol. 67, pp. 383–402, 2001.
- [12] M. S. Vasconcelos and E. L. Albuquerque, "Transmission fingerprints in quasiperiodic dielectric multilayers," *Phys. Rev. B*, vol. 59, no. 17, pp. 11128–11131, 1999.
- [13] L. Dal Negro, M. Stolfi, Y. Yi, J. Michel, X. Duan, L. C. Kimerling, J. LeBlanc, and J. Haavisto, "Photon band gap properties and omnidirectional reflectance in Si/SiO₂ Thue–Morse quasicrystals," *Appl. Phys. Lett.*, vol. 84, no. 25, pp. 5186, 2004.
- [14] F. Qui, R. W. Peng, X. Q. Huang, X. F. Hu, Mu Wang, A. Hu, S. S. Jiang, and D. Feng, "Omnidirectional reflection of electromagnetic waves on Thue–Morse dielectric multilayers," *Europhys. Lett.* vol. 68, no. 5, pp. 658–663, 2004.
- [15] Luigi Moretti, Ilaria Rea, Lucia Rotiroli, Ivo Rendina, Giancarlo Abbate, Antigone Marino, and Luca De Stefano, "Photonic band gaps analysis of Thue-Morse multilayers made of porous silicon," *Optics Express*, vol. 14, no. 13, pp. 6264–6272, 2006.
- [16] L. Dal Negro, M. Stolfi, Y. Yi, J. Michel, X. Duan, L. C. Kimerling, J. LeBlanc, and J. Haavisto, "Omnidirectional reflectance and optical gap properties of Si/SiO₂, Thue–Morse quasicrystals," *Mat. Res. Soc. Symp. Proc.*, vol. 817, 2004.
- [17] M. Deopura, C. K. Ullal, B. Temelkuran, and Y. Fink, "Dielectric omnidirectional visible reflector," *Optics Letters*, vol. 26, no. 15, pp. 1197–1199, 1 Mars 2001.
- [18] E. Abdel-Rahman and A. Shaarawi, "Defect mode in periodic and quasiperiodic one-dimensional photonic structures," *Journal of Materials Science: Materials in Electronics*, DOI number: 10.1007/s10854-007-9496-x, 2007.
- [19] F. Abeles, "Recherches sur la propagation des ondes electromagnetiques sinusoidales dans les milieux stratifies Application aux couches minces," PhD thesis, Faculte des sciences de l'Universite de Paris, France, 1950.
- [20] N. Liu, "Propagation of light waves in Thue-Morse dielectric multilayers," *Phys. Rev. B*, vol. 55, pp. 3543–3547, 1997.
- [21] N. Stefanou, V. Karathanos, and A. Modinos, "Scattering of electromagnetic waves by periodic structures," *J. Phys.: Condens. Matter*, vol. 4, pp. 7389–7400, September 1992.

Youssef Trabelsi received the M.Sc. degree in electronic devices from El-Manar University- faculty of Sciences of Tunis, Tunisia in 2006. He is currently working toward a Ph.D. degree in physics at the faculty of Sciences of Tunis. His current research interests include quasi-periodic photonic band gap structure in microwave domain, antenna with photonic band gap substrate.

Naim Ben Ali received the degree in industrial engineering in 2007 and the M.Sc. degree in genius of industrial systems from El-Manar University- National School of engineers of Tunis, Tunisia in 2008. He is currently working toward a Ph.D. degree in industrial engineering at the same school. His current research interests include 1D photonic band gap structure.

Yassine Bouazzi received the degree in industrial engineering in 2006 and the M.Sc. degree in genius of industrial systems from El-Manar University- National School of engineers of Tunis, Tunisia in 2007. He is currently working toward a Ph.D. degree in industrial engineering at the same school. His current research interests include 1D quasi-periodic photonic band gap structure in optical domain.

Mounir Kanzari professor of physics from El-Manar University- National School of engineers of Tunis, Tunisia. He received the Ph.D. degree in 1992 from the National School of engineers of Tunis, Tunisia. His current research interests include Physics and engineering of advanced materials and photonics.

Simulation of Lightning Return Stroke Currents and Its Effect to Nearby Overhead Conductor

¹M. O. Goni, ²E. Kaneko, and ³A. Ametani

¹Faculty of Electrical & Electronic Engineering,

Khulna University of Engineering & Technology, Bangladesh

²Faculty of Engineering, University of the Ryukyus, Okinawa, Japan

³Department of Electrical Engineering, Doshisha University, Kyoto, Japan

¹osman@ieee.org, ²kaneko@eee.u-ryukyu.ac.jp, ³aametani@mail.doshisha.ac.jp

Abstract – A nearby lightning strike can induce significant currents in long horizontal and vertical conductors. Although the magnitude of the current in this case is much smaller than that encountered during a direct strike, the probability of occurrence and the frequency content are higher. In view of this, appropriate knowledge of the characteristics of such induced currents is relevant for the interpretation of recorded currents. Considering these, the present paper discusses a modeling procedure that permits simulation of lightning-induced voltages or currents on overhead lines due to nearby lightning strikes. The hypothesis of perfect conducting ground, generally adopted in studies on the subject, is discussed in order to better assess the validity of the simulation results. In this paper, a homogeneous non-perfect ground is also investigated for its influence on lightning-induced voltages. The procedure for analyses of the voltages induced on an overhead line by a nearby lightning return stroke with a striking point at unequal distances from the line terminations is presented. The analysis shows that lightning-induced voltages depend on the soil conductivity.

Keywords: Finite difference time domain (FDTD) method, ground conductivity, horizontal conductor, induced voltage, and nearby lightning strike.

I. INTRODUCTION

Sensitive and sophisticated electronic components are increasingly used in data-transmission networks, in power system equipment (circuit breakers, disconnectors, control and protection circuits), and in household appliances. These components, compared to electromechanical ones used in the past, may suffer logic upset or damage at significantly lower levels of induced electromagnetic interference particularly from transients. Transients caused by lightning (direct and/or indirect) can be one of the major causes of malfunction or even destruction of those components. In particular, lightning-induced voltages, which can cause micro-interruptions of the power supply or disruption in telecommunication or data-transmission networks

during thunderstorms, have been seriously revisited due to the increasing demand by customers for good quality in the power supply and reliability in the transmission of information. The opening of the telecommunication market, followed now by that of the electrical power market is only accelerating this trend.

As a result, the evaluation of lightning induced disturbances on both overhead and buried conductors has recently been attracted considerable attention [1–4]. Typical examples are power transmission and distribution cables, submarine fiberoptic cables, and telecommunication cables. There is no clear explanation in the power system literature about the relation between the number of outages during thunderstorms and lightning flash density in the proximity of the failure place. However, a case reported in Sweden, in which one high-voltage and several distribution transformers exploded during a heavy thunderstorm, leaving 11000 people without electricity for 24 hours, is symptomatic of the impending danger of lightning, in particular as it occurred in a highly developed country. This case also shows that the interruption of information and electric supply in a modern society can have severe consequences. A lightning stroke in the proximity of a big hotel in Lausanne, Switzerland, induced a voltage in the satellite antenna and destroyed the TV sets in the building. Direct lightning strokes on trees during heavy thunderstorms caused accidents and death to human and animals in rural areas of Bangladesh. A two-year survey of lightning-induced voltages on telecommunication lines has been performed in the 1990s in France [4]. A total number of 16000 short events (lightning pulses on the telecommunication line, lightning and/or switching pulses on the mains) have been recorded at nine sites during the measurement period. From these events, 27 peak values exceeded 1.5 kV, with a maximum value of 3.5 kV, which represents a dangerous value for any kind of telecommunication equipment.

The interaction between lightning and installations can be any one of the following:

1) Direct, if a lightning stroke directly hits a line connected to the installation or the equipment.

2) Indirect, if the strike is at a distance and the currents are induced by the electromagnetic field generated by the lightning discharge.

To analyze the effects of indirect lightning strikes on transmission lines or various equipment, it is necessary to go through the following steps:

1) The development of lightning return-stroke models, which means the modeling of the spatial-temporal distribution of the current in the lightning channel.

2) Radiated electromagnetic fields by such a current distribution including propagation effects over a soil with finite conductivity.

3) The evaluation of the voltages induced on nearby overhead lines resulting from the coupling between the electromagnetic field and the line conductors.

The aim of this paper is to present the simulation results of currents and voltages showing the lightning induced disturbances on horizontal conductors either terminated or grounded at the ends. Even though extensive experimental investigations have been performed on the effect of nearby lightning on vertical conductors and/or tower (e.g., [4,5]), to the best of our knowledge, simulation characterization for horizontal overhead conductors with different conductivities is limited in the scientific literature.

An indirect lightning strike can induce appreciable currents in both horizontal and vertical conductors. The magnitudes of such induced currents are definitely much lower than those experienced during a direct hit. However, their frequency of occurrence is comparatively higher. Accurate knowledge of the characteristics of induced currents would help in the characterization and classification of currents recorded on instrumented conductors. Such knowledge would also be useful for the study of the electromagnetic noise/interference caused by the induced currents on electrical and electronic systems in the vicinity, and for systems mounted on the conductors (towers). For a rough estimate of the number of strikes in the surrounding area, the information on the annual frequency of induction due to a strike in the vicinity can be used in conjunction with the number of direct hits. In view of these facts, investigations on the characteristics of the induced effects seem to be essential.

II. METHOD OF ANALYSIS

Numerical electromagnetic analysis is becoming a powerful approach to analyze a transient which is hard to solve by a conventional circuit-theory based approach such as the Electromagnetic Transient Program (EMTP) [6]. It follows from a solution of Maxwell's equations for boundary conditions of the EM field at the surface of the conductor and the earth. However, it is still based on some idealistic hypotheses, such as homogeneous earth and ideal contact between the conductor and the

soil. Additionally, only a few papers consider nonlinear phenomena [7].

Unfortunately, there is no systematically developed and reliable set of experimental data available that would serve as a standard, so we consider here the EM model as the basis for comparison.

Numerical electromagnetic analyses based on the Finite difference time domain (FDTD) method are effective to analyze the transient response of a large solid conductor or electrode. The accuracy of this method, applied to such an analysis, has been fully investigated in comparison with an experiment and shown to be satisfactory [8]. As this method requires long computation time and large memory capacity, the analysis is restricted to rather small spaces.

The FDTD method employs a simple way to discretize a differential form of Maxwell's equations. In the Cartesian coordinate system, it generally requires the entire space of interest to be divided into small rectangular cells and calculates the electric and magnetic fields of the cells using the discretized Maxwell's equations. As the material constant of each cell can be specified arbitrarily, a complex inhomogeneous medium can be easily analyzed. To analyze fields in an open space, an absorbing boundary has to be set on each plane which limits the space to be analyzed, so as to avoid reflection there. In the present analysis, the second-order Mur's method [9] is employed to represent absorbing planes.

So far in most of FDTD analyses of transient and steady-state voltages, large solid electrodes [8,10], which can be decomposed into small cubic cells, have been chosen and thin-wire electrodes have been dealt with. This is because an equivalent radius of a thin wire in a lossy medium has already been developed [11,12]. In the present paper, an equivalent radius for a thin wire in lossy medium is utilized with the help of the concept proposed for an aerial thin wire [11]. The validity is already tested by comparing grounding-resistance values obtained through FDTD simulations on simple buried structures with theoretical values [12,13]. The FDTD method also yields reasonably accurate lightning-induced voltages on a horizontal wire above ground by lightning strikes to a tall grounded object [14].

A. Models for Analysis

As an electromagnetic field produced by lightning is basically responsible for the current induction, a model to be employed for study must be based on the electromagnetic model. Thus, the present paper employs the electromagnetic model, which ensures reliable description of the associated field problem and has been successfully employed in the literature for the estimation of currents and fields in the vicinity [15-17].

In measuring a transient response of a horizontal electrode, a horizontal current lead wire and a horizontal

voltage reference wire have been used [8,18], although it is desirable to place the horizontal conductors perpendicular to one another in order to reduce undesired inductions. Recently, Tsumura *et al.* [13] recommended that the perpendicular arrangement of the voltage reference wire is an appropriate one. However, the difference in the evaluated voltage peaks due to wire arrangements is only 6%.

A 1/50 reduced-scale model is considered here in order to simulate a lightning stroke initiated at ground level. The upward leader induces voltages on the nearby horizontal overhead line by the electromagnetic field.

Figure 1 shows a representative arrangement of the horizontal conductor system in which AB is considered to be a horizontal copper conductor of 4 m in length. Both ends of the conductor are terminated to the ground. The length of the vertical current lead wire is taken to be 5 m and is placed at a distance of 50 cm from the horizontal overhead line. Pulse current was injected from the bottom of the model channel with an internal impedance of 50 Ω. The vertical lightning channel is considered to be a perfectly conducting cylinder excited by a delta-gap step voltage source. The arbitrary voltage source produces a steep-front wave having a risetime of 4.1 ns to 119 V. The voltage waveform is sustained another 40 ns with a slow rise of the voltage to 180 V. Then it goes to zero [11]. The current pulse generator was modeled as a z-directional voltage source, of which the waveform was given by a piecewise linear approximation of its open voltage as in Fig. 2. The source waveform is assigned in such a way as to allow the propagation time through the entire horizontal and other associated conductor system.

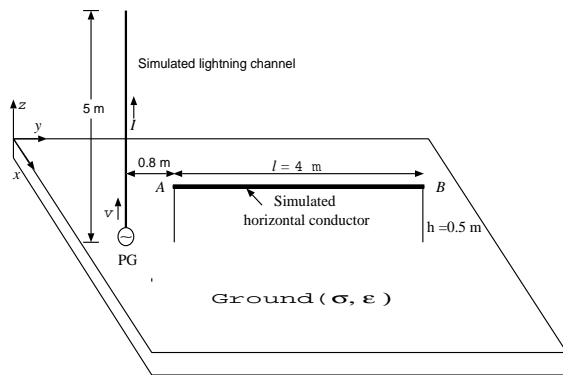
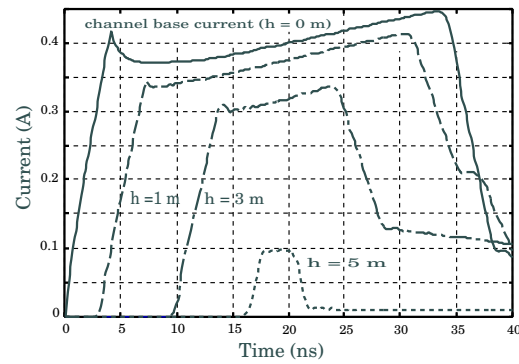
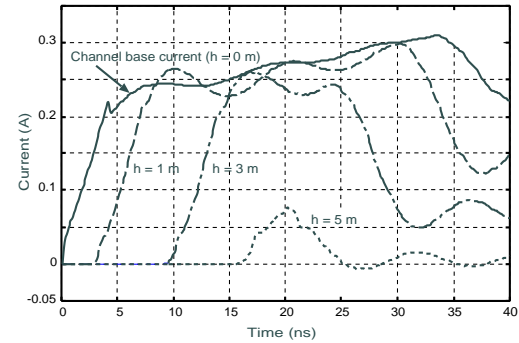


Fig. 1. Arrangement of the simulated lightning return-stroke channel for the calculation of currents and voltages induced on a nearby overhead line of unequal distance from the terminated ends.

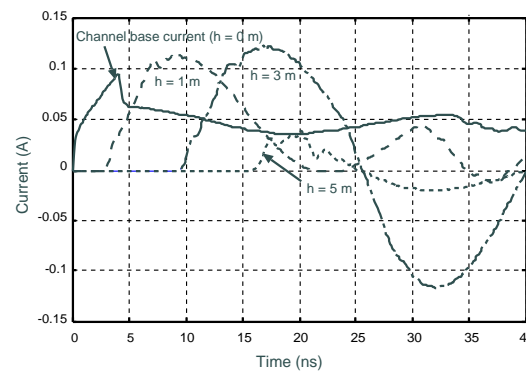
For the present FDTD simulation, the conductor system shown in Fig. 1 is surrounded by a large rectangular analysis space of 2 m, 6 m, and 2 m in the *x*, *y* and *z* directions respectively, with space length $\Delta s = 5$ cm. An earth is placed at the bottom of the



(a) $\sigma = 5.8 \times 10^7$ S/m.



(b) $\sigma = 10$ mS/m.



(c) $\sigma = 1$ mS/m.

Fig. 2. Current waveforms for different heights of the vertical lightning channel with different ground conductivities.

analysis space with a thickness of 10 cm and a resistivity $\rho = 1.69 \times 10^{-8} \Omega \cdot \text{m}$. The gap length is maintained as the space length Δs of the conductor system at which a voltage probe or current probe is placed to record the voltage and current. The time step for the simulation was determined by equation (14) of [11] with $\alpha = 0.001$, and all the six boundaries of the cell were treated as second-order Liao's absorbing boundaries. The radius of the horizontal thin wire was taken into account by the method discussed in the previous paper and $0.23\Delta s = 1.15$ cm of radius was chosen accordingly [11,12].

The FDTD method is normally a time-consuming

method. However, progress of computers in terms of speed and memory has been considerable, and even a personal computer can be used for the FDTD calculation here. In fact, the simulations presented in this paper were performed by a personal computer with Intel Pentium 4, 2.80 GHz CPU and 512 MB RAM. Responses are calculated up to 40 ns for the reduced-scale model (2 m × 6 m × 2 m) with a time increment of 0.096 ns. Therefore, the computation time for the present scaled models are about 4 min respectively, regardless of ground parameters.

The current distribution, $I(z, t)$, along the lightning channel for the case of strike initiated at ground, is given by Baba and Rakov [19],

$$I(z, t) = \frac{1 + \rho_{gr}}{2} I_{sc}(0, t - \frac{z}{v}) \quad (1)$$

where v is the return-stroke speed and $I_{sc}(0, t)$ is the lightning short-circuit current injected at $z = 0$ instead of $z = h$, which is also known as the channel-base current, and ρ_{gr} is the current reflection coefficient at the channel base. Typical values of v are one-third to two-thirds of c . Figure 2 shows the computed waveforms of the current distribution using the FDTD method which can also be represented by equation (1). The current distribution for the case of strikes to a tall object and for the case of strikes to flat ground correspond to the same lightning discharge, as required for examining the influence of strike object. In the FDTD calculations, the lightning channel and strike object can also be represented by a vertical array of current sources [20]. The arbitrary waveform of lightning short-circuit current $I_{sc}(h, t)$ or $I_{sc}(0, t)$ is specified by the current waveform proposed by Noda *et al.* [11]. In the case of a lightning strike to flat ground, the current reflection coefficient at the channel base (ground) is set to $\rho_{gr} = 1$ ($Z_{ch} \gg Z_{gr}$), where Z_{ch} and Z_{gr} are the equivalent impedance of the lightning channel and grounding impedance of the strike object, respectively. The assumption $\rho_{gr} = 1$ is supported by the results from triggered-lightning experiments that show that lightning is capable of lowering its grounding impedance to a value that is always much lower than the equivalent impedance of the lightning channel [21,22]. It can be seen that in the TL model, the longitudinal current $I(z', t)$ in a straight and vertical lightning channel at an arbitrary height z' and time t is expressed as follows,

$$I(z', t) = I(0, t - \frac{z'}{v}).$$

B. Analyzed Results

Figure 2 shows the channel currents at different heights due to injected lightning return stroke current at ground with different soil conductivities. Channel current waveforms with a copper ground (as shown in Fig. 2(a)) are determined mainly by the characteristics of the injected current waveforms. These currents are treated

as the total current waveform I_{tot} , at different heights calculated using the FDTD method for a vertical perfectly conducting cylinder excited at its bottom by a lumped source [23]. The current waveform at $z = 0$ m (bottom) of Fig. 2(a) is also considered as an incident current due to this lumped source. If we consider the vertical phased current source array along the channel, then the peaks of all the current waveforms at different heights would be the same (e.g., Fig. 3 of [23]). In this case, those current waveforms are to be treated as incident current waveforms at different heights. Thus the scattered current can be obtained as $I_{scat} = I_{tot} - I_{inc}$.

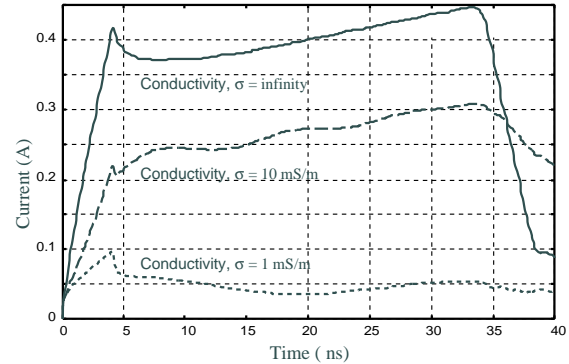


Fig. 3. Channel base currents for different soil conditions.

As seen in Fig. 2(a), the current pulse attenuation is accompanied by the lengthening of its tail while the rise-time of the current pulse is almost constant. These characteristics of the current waveforms are different for different ground conductivities. The magnitude of the channel currents are decreasing with decreasing of ground conductivity. Because of the finite ground conductivities, the curves of the channel currents in Figs. 2(b) and 2(c) exhibit nonlinear characteristics after their first peaks. Figure 3 illustrates the channel base currents computed by the FDTD method with different soil conductivities. It is evident from this result that the channel base current decreases with decreasing ground conductivity.

Figure 4 shows the normalized currents computed at different heights of the lightning channel characterized by a finite ground ($\sigma = 10$ mS/m). Here the normalization is termed by the ratio of the channel current at specific height to the channel base current (e.g., $I_n(z, t) = I(z, t)/I(0, t)$). Figure 5 illustrates the scattered current waveforms, I_{scat} , at different heights with a copper ground.

Figures 6 and 7 show the waveforms of the vertical electric field and azimuthal magnetic field respectively at the near end of the terminated overhead horizontal conductor due to a nearby lightning strike to flat ground. Similarly, Figs. 8 and 9 correspond to the waveform of the electric and magnetic fields at the distant end. Those

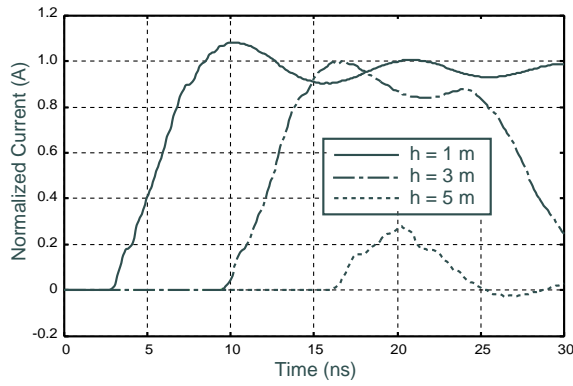


Fig. 4. Normalized currents observed at different heights of the return-stroke elevated channel for a finite ground conductivity ($\sigma = 10 \text{ mS/m}$).

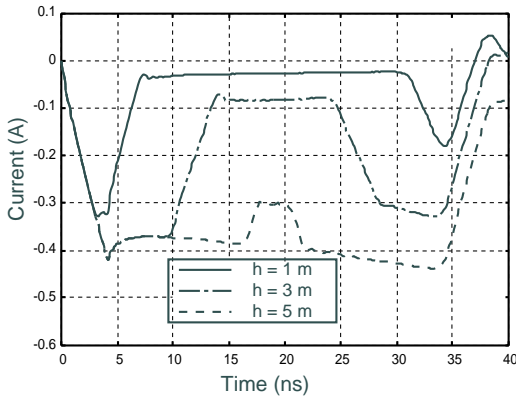


Fig. 5. Scattered current waveforms, I_{scat} , at different heights obtained as the difference between the total current and the incident current for the lumped source with a copper ground.

results are obtained for different ground conditions. The fields nearer to the striking location are larger in magnitude than at the far end. This result agrees satisfactory with other simulation (Numerical Electromagnetic Code (NEC-2)) and experimental results (Figs.3(a) and 4(a) of Pokharel *et al.* [24]). The validity of the results of vertical electric field E_z and azimuthal magnetic field H_ϕ at the ground surface due to a vertical lightning strike to flat highly conducting ground using the FDTD method has already been examined with corresponding fields calculated using exact analytical expressions derived by Thottappillil *et al.* [25]. The later expressions are valid for the TL model, vertical channel terminating on flat, perfectly conducting ground, and return-stroke velocity equal to the velocity of light ($v = c$). In the FDTD procedure, we used the distribution of current along the lightning channel given by equation (1) with ($v = c$) and $\rho_{gr} = 1$, which was represented by a vertical array

of current sources. The lightning short-circuit current $I_{sc}(0, t)$ was the same as that proposed by Nucci *et al.* [26].

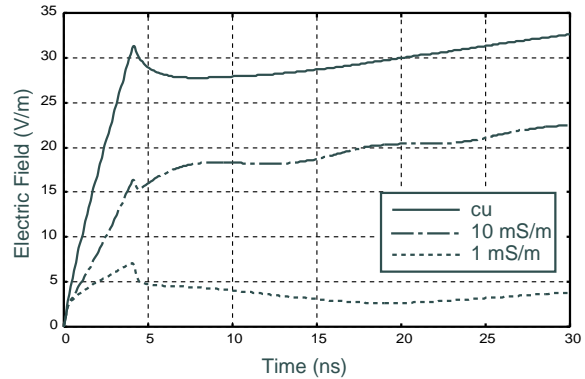


Fig. 6. Waveforms for the vertical electric field at the near end of the terminated overhead conductor due to a lightning strike to a flat ground with different soil conditions.

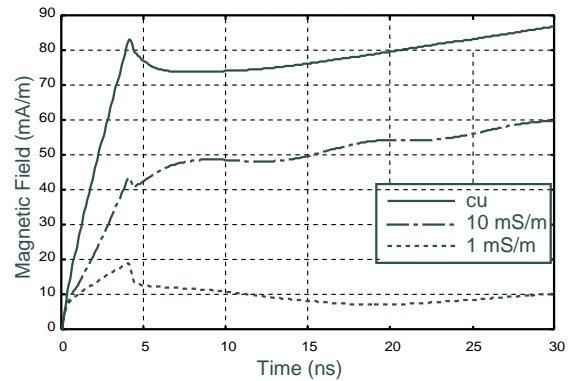


Fig. 7. Waveforms for the azimuthal magnetic field at the near end of the terminated overhead conductor due to a lightning strike to a flat ground with different soil conditions.

Thottappillil *et al.*'s analytical expressions for E_z and H_ϕ on the ground surface at a distance d from the lightning channel are reproduced as follows,

$$E_z(d, t) = \frac{I(0, t - d/c)}{2\pi\epsilon_0 cd}, \quad (2)$$

$$H_\phi(d, t) = \frac{I(0, t - d/c)}{2\pi d}. \quad (3)$$

Note that equation (2) gives the exact total electric field, which is the sum of the electrostatic, induction, and radiation components, and equation (3) gives the exact total magnetic field which is the sum of the induction and radiation components [25]. Hence, Figs. 6 to 9 show the field computation based on the analytical formula [25] using the FDTD results for the currents.

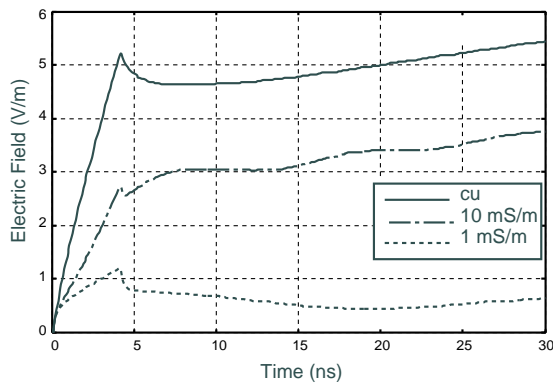


Fig. 8. Waveforms for the vertical electric field at the far end of the terminated overhead conductor due to a lightning strike to a flat ground with different soil conditions.

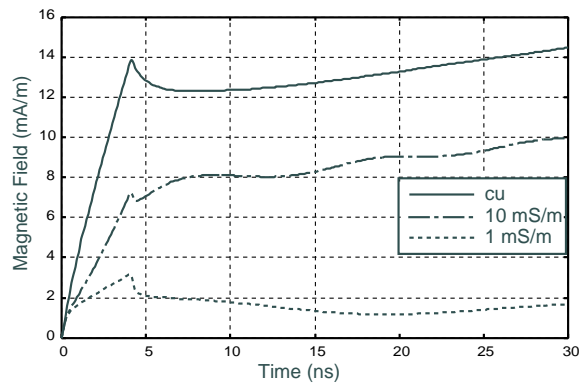


Fig. 9. Waveforms for the azimuthal magnetic field at the far end of the terminated overhead conductor due to a lightning strike to a flat ground with different soil conditions.

Now the induced currents at the terminated ends of the overhead horizontal line computed for grounds having various soil conditions are shown in Figs. 10(a) and 10(b). These induced currents are due to the coupling between the electromagnetic field and the line conductor. The first peak of this induced current in proximity to the lightning source is large in the case with infinite conductivity. The polarity of the induced current with infinite ground conductivity is observed to be different from current waves with finite ground as distance increases from the striking location.

C. Terminations at Equidistance from the Source

Figure 11 illustrates the case with a simulated lightning channel in which the same return stroke current is considered at the bottom of the channel. Now the stroke location is equidistant from the line terminations and at 50 cm from the line center of a 1/50 reduced-scale model. By using the aforementioned approach, it is possible to

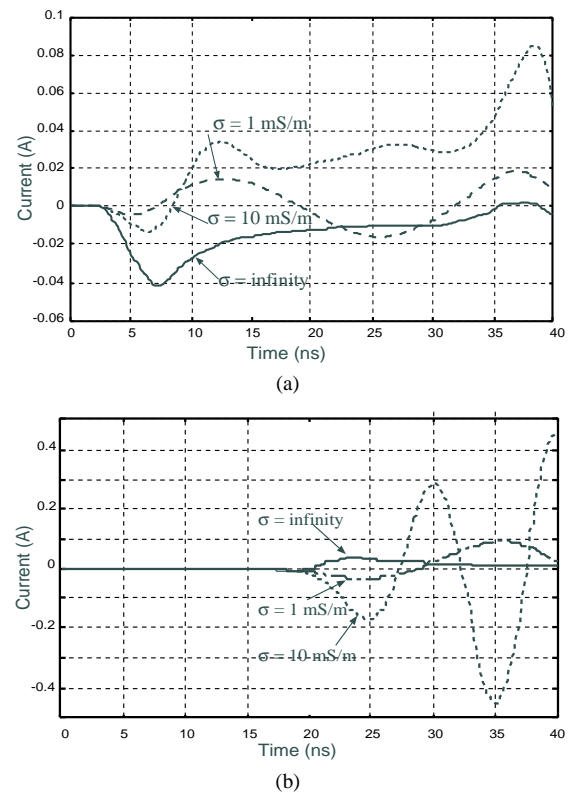


Fig. 10. Induced currents at the terminated ends of the overhead horizontal conductor for varying soil conductivities; a) near end, and b) far end.

simulate and analyze the effect of protection elements installed at the entrance of a substation, control building of a communication tower, or even household appliances. The dimension of the analysis space and cell size are taken to be the same as assumed in the earlier section. Figure 12 represents the induced currents at the terminated ends equidistant from the stroke location for varying soil conditions. Similar characteristics for the induced currents has also been observed in Fig. 10(a). Induced voltages due to a nearby lightning strike at the center of the overhead horizontal conductor are represented in Fig. 13. These voltages are computed across the overhead line and a auxiliary potential wire. Results show that decreasing ground conductivity also decreases the induced voltages on the overhead horizontal line. These properties are good agreement with the results obtained by Pokharel *et al.* [Fig. 11 of [24]] using a Sommerfeld integral and a Norton's approximation. Although there are some differences in the wavetails because of the computational method considered in this work. Figure 14 shows the magnetic field distribution at $t = 40$ ns on the $y-z$ plane, when a part of the incoming wave reflects at the earth surface (a snapshot of its animation visualized by MATLAB). Those fields penetrate the nearby conductor and induce currents on it.

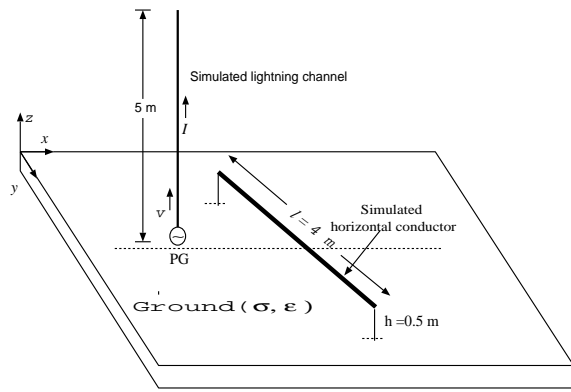


Fig. 11. Arrangement of the simulated lightning channel equidistant from the terminated both ends of the overhead horizontal conductor.

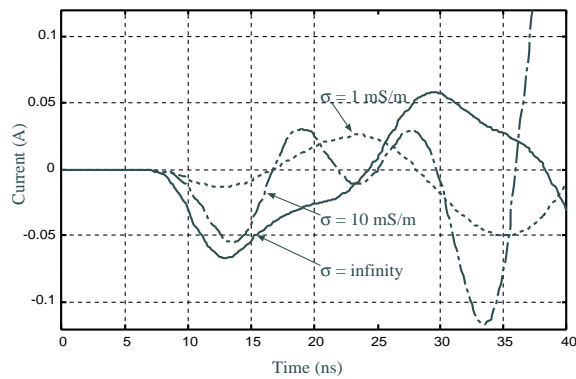


Fig. 12. Induced currents at the terminated ends of the overhead horizontal conductor equidistant from the simulated lightning source for various soil conductivities.

III. CONCLUSIONS

A time-domain method for numerical electromagnetic analysis, i.e., FDTD, is applied to analyze the proximity effect due to a nearby lightning stroke to flat ground. Induced currents and voltages are investigated at the near and far ends of the terminated horizontal conductor which is at a short distance from the stroke location. The effects of ground conductivity depending on soil conditions are also evaluated and presented in this paper. The validity of the results are examined with the analytical data and also with simulation results using NEC-2. Although it is difficult to analyze the large computational domain including finitely conducting ground, the FDTD method offers more accurate results and advantages over NEC-2.

The electric and magnetic fields are calculated using the well known analytical expression considering the currents calculated here by the FDTD method. A nearby lightning stroke at the center position of the horizontal overhead conductor has been analyzed and induced voltages are measured at the line in order to investigate the

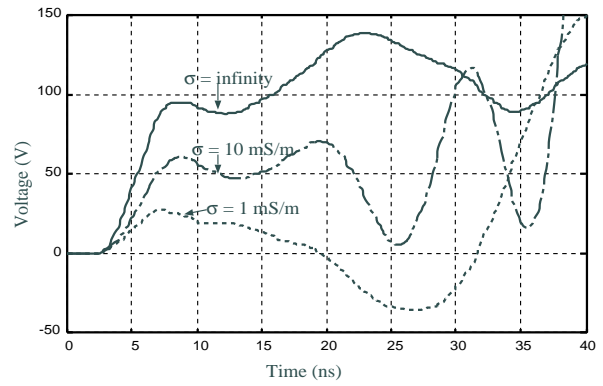


Fig. 13. Induced voltages at the nearest location of the horizontal conductor computed across the conductor and auxiliary potential wire with different soil conductivities.

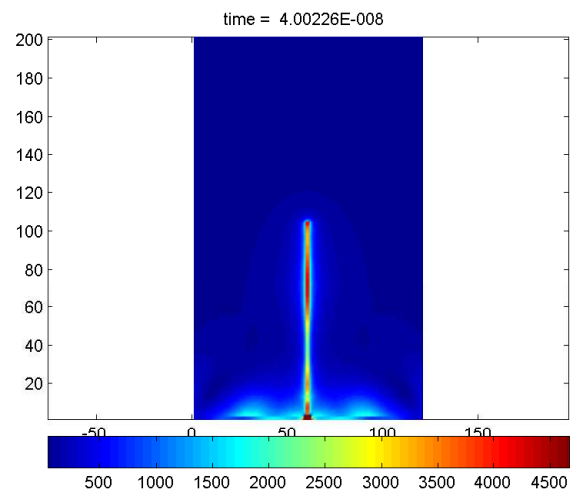


Fig. 14. Magnetic field strength (A/m) at $t = 40$ ns corresponding to gray scale at the bottom; unit of vertical and horizontal axes is in cells ($\Delta s = 5$ cm).

performance of surge arrester connected to the line with different ground conductivities. Furthermore, this work examines the behavior of vertical lightning channel current with different ground conditions and gives insightful results for a scaled model which facilitates the analysis with larger scale model including surge protectors.

The above findings regarding the lightning-induced voltages in the absence of a tall strike object have important implications for optimizing lightning protection means for telecommunication and power distribution lines.

REFERENCES

[1] F. M. Tesche, A. W. Kalin, B. Brandly, B. Reusser, M. Isnoz, D. Tabara, and P. Zwiackner, "Estimates of lightning-induced voltage stresses within buried

- shielded conduits," *IEEE Trans. Electromagn. Compat.*, vol. 40, pp. 492–504, 1998.
- [2] B. Djebbari, L. Guerin, and M. Gleonec, "Conducted EM disturbances on the telecommunication terminal equipment ports," *Int. Symp. EMC*, Rome, Italy, Sep. 13–16, 1994.
- [3] M. G. Sorwar, H. Ahmed, and M. M. Ali "Analysis of transients in overhead telecommunication subscriber line due to nearby lightning return stroke," *IEEE Int. Symp. Electromagn. Compat.*, vol. 2, pp. 1083–1088, Aug. 1998.
- [4] M. Ishii, K. Michishita, and Y. Hongo, "Experimental study of lightning-induced voltage on an overhead wire over lossy ground," *IEEE Trans. Electromagn. Compat.*, vol. 41, no. 1, pp. 39–45, Feb. 1999.
- [5] U. Kumar, V. Hegde, and V. Shivanand, "Preliminary studies on the characteristics of the induced currents in simple down conductors due to a nearby lightning strike," *IEEE Trans. Electromagn. Compat.*, vol. 48, no. 4, pp. 805–816, Nov. 2006.
- [6] Working Group of IEEJ, "Numerical electromagnetic analysis and its application to power system transients," *IEEJ WG Report*, 2003–2007.
- [7] T. Mozumi, Y. Baba, M. Ishii, N. Nagaoka, and A. Amatani "Numerical electromagnetic field analysis of archn voltages during a back-flashover on a 500 kV twin circuit line," *IEEE Power Delivery*, vol. 18, no. 1, pp. 207–213, 2003.
- [8] K. Tanabe, "Novel method for analyzing dynamic behavior of grounding systems based on the FD-TD method," *IEEE Power Eng. Rev.*, vol. 21, no. 9, pp. 55–57, Sep. 2001.
- [9] G. Mur, "Absorbing boundary conditions for the finite-difference approximation of the time-domain electromagnetic-field equation," *IEEE Trans. Electromagn. Compat.*, vol. EMC-23, no. 4, pp. 377–382, 1981.
- [10] K. S. Yee, "Numerical solution of initial boundary value problems involving Maxwell's equation in isotropic media," *IEEE Trans. Antennas and Propagation*, vol. AP-14, no. 4, pp. 302–307, 1966.
- [11] T. Noda and S. Yokoyama, "Thin wire representation in finite difference time domain surge simulation," *IEEE Trans. Power Delivery*, vol. 17, no. 3, pp. 840–847, 2002.
- [12] Y. Baba, N. Nagaoka, and A. Ametani, "Numerical analysis of grounding resistance of buried thin wires by the FDTD Method," *Int. Conf. on Power Syst. Trans(IPST)*, New Orleans, USA, 2003.
- [13] M. Tsumura, Y. Baba, N. Nagaoka, and A. Ametani, "FDTD simulation of a horizontal grounding electrode and modeling of its equivalent circuit," *IEEE Trans. Electromagn. Compat.*, vol. 48, no. 4, pp. 817–825, Nov. 2006.
- [14] Y. Baba and V.A. Rakov, "Voltage induced on an overhead wire by lightning strikes to a nearby tall grounded object," *IEEE Trans. Electromagn. Compat.*, vol. 48, no. 1, pp. 212–224, Feb. 2006.
- [15] Y. Baba and M. Ishii, "Numerical electromagnetic field analysis of lightning current in tall structures," *IEEE Trans. PWRD*, vol. 16, no. 2, pp. 324–328, Apr. 2001.
- [16] Y. Baba and M. Ishii, "Characteristics of electromagnetic return-stroke models," *IEEE Trans. Electromagn. Compat.*, vol. 45, no. 1, pp. 129–134, Feb. 2003.
- [17] B. Kordi, R. Moini, W. Janischewskyj, A. M. Hussein, V. O. Shostac, and V. A. Rakov, "Application of the antenna theory model to a tall tower struck by lightning," *J. Geophys. Res.*, vol. 108, pp. ACL 7/1–ACL7/9, no. D17 4542, 2003.
- [18] K. Tanabe, A. Asakawa, T. Noda, M. Sakae, M. Wada and H. Sugimoto, "Verifying the novel method for analyzing transient grounding resistance based on the FD-TD method through comparison with experimental results," *CRIEPI Report*, no.99043, 2000. (in Japanese)
- [19] Y. Baba and V. A. Rakov, "On the use of lumped sources in the lightning return stroke models," *J. Geophys. Res.*, vol. 110, D03101, doi:10.1029/2004JD005202, Feb. 2005.
- [20] Y. Baba and V. A. Rakov, "On the transmission line model for lightning return stroke representation," *Geophys. Res. Lett.*, vol. 30, no. 24, p. 2294, doi:10.1029/2003GL018407, Dec. 2003.
- [21] V. A. Rakov, M. A. Uman, K. J. Rambo, M. I. Fernandez, R. J. Fisher, G. H. Schetzer, R. Thottappillil, A. Eybert-Berard, J. P. Berlandis, P. Lalande, A. Bonamy, P. Laroche, and A. Bondiou-Clergerie, "New insights into lightning processes gained from triggered-lightning experiments in Florida and Alabama," *J. Geophys. Res. Lett.*, vol. 103, no. D12, pp. 14117–14139, 1998.
- [22] V. A. Rakov, "Transient response of a tall object to lightning," *IEEE Trans. Electromagn. Compat.*, vol. 43, no. 4, pp. 654–661, Nov. 2001.
- [23] Y. Baba and V. A. Rakov, "On the mechanism of attenuation of current waves propagating along a vertical perfectly conducting wire above ground: Application to lightning," *IEEE Trans. Electromagn. Compat.*, vol. 47, no. 3, pp. 521–532, Aug. 2005.
- [24] R. K. Pokharel, M. Ishii, and Y. Baba, "Numerical electromagnetic analysis of lightning-induced voltage over ground of finite conductivity," *IEEE Trans. Electromagn. Compat.*, vol. 45, no. 4, pp. 651–656, Nov. 2003.
- [25] T. Thottappillil, J. Schoene, and M. A. Uman, "Return stroke transmission line model for stroke speed

near or equal to that of light,” *Geophys. Res. Lett.*, vol. 28, no. 18, pp. 3593–3596, 2001.

- [26] C. A. Nucci, G. Diendorfer, M. A. Uman, F. Rachidi, M. Ianoz, and C. Mazzetti, “Lightning return stroke current models with specified channel-base current: A review and comparison,” *J. Geophys. Res.*, vol. 95, no. D12, pp. 20395–20408, 1990.



Md. Osman Goni was born in Bangladesh on February, 1971. He received his B.S. degree in electrical and electronic engineering from Bangladesh Institute of Technology, Khulna in 1993. He joined the Institute in 1994. He received M.S. degree and D. Eng. degree from the University of the Ryukyus, Japan in 2001 and 2004 respectively. He is currently an assistant professor and has been engaged in teaching and research in

digital signal and image processing, electric power and energy system, electromagnetic energy engineering, electromagnetic theory, electromagnetic fields computation, transient phenomena, lightning and EMP effects on power and telecommunication networks, FDTD method, MoM, NEC-2, lightning surge analysis, vertical conductor problems, EMTP etc. He is the author or co-author of about 20 scientific papers presented at international conferences and published in reviewed journals.



Eiji Kaneko was born in Japan, on September 16, 1952. He received M.S. degree from Nagoya University in 1977. He joined in Toshiba Corporation in April 1977 and engaged in research and development of vacuum interrupter and discharge. He received D. Eng. degree from Nagoya University in 1989. He is now professor of University of the Ryukyus. He has been engaged in teaching and research on electric power and

energy system engineering, electromagnetic energy engineering etc. Dr. Kaneko is a member of IEEE and IEE of Japan.



Akihiro Ametani received the B.S. and M.S. degrees from Doshisha University, Kyoto, Japan, in 1966 and 1968, respectively, and the Ph.D. degree from the University of Manchester Institute of Technology (UMIST), Manchester, U.K., in 1973. He was with Doshisha University from 1968 to 1971, UMIST from 1971 to 1974, and the Bonneville Power Administration, Portland, OR, for the summers of 1976 to

1981. He has been a Professor at Doshisha University since 1985. He was the Director of the Institute of Science and Engineering of Doshisha University from 1997 to 1998 and the Dean of the Library and Computer/Information Center from 1998 to 2001. Dr. Ametani is a Chartered Engineer in the U.K., a Distinguished Member of CIGRE, and a Fellow of the IEE. He has been a Vice President of the IEE of Japan since 2004.

Dispersion Analysis of a Negative Group Velocity Medium with MATLAB

G. Monti and L. Tarricone

Department of Innovation Engineering, University of Lecce, Italy
giuseppina.monti@unile.it, luciano.tarricone@unile.it

Abstract – The dispersive behavior of a waveguide loaded with a metamaterial slab is investigated by means of common mathematical tools demonstrating the existence of a superluminal propagation region. More specifically, MATLAB has been used to investigate the influence of the propagating pulse shape on the possibility to achieve a propagation characterized by a negative group delay. Results achieved in this way have also been validated by means of a Finite Difference Time Domain code.

Keywords: Anomalous dispersion, left-handed media, negative group velocity, gaussian pulse, and MATLAB.

I. INTRODUCTION

Metamaterials (MM) are an appealing new frontier of electromagnetic research, attractive for a wide range of applications. More specifically, media with negative values of the constitutive parameters ($\epsilon < 0$, $\mu < 0$), firstly investigated by Veselago [1], have recently attracted a great interest in the scientific community. Among these, the following classes of materials can be identified:

- *Epsilon-Negative* (ENG): media with a negative electrical permittivity and a positive magnetic permeability;
- *Mu-Negative* (MNG): media with a positive electrical permittivity and a negative magnetic permeability;
- *Double Negative* (DNG): media with both the electrical permittivity and the magnetic permeability less than zero (conversely, conventional media with positive values of these parameters are defined Double Positive -DPS).

In the last years, theoretical and experimental studies have demonstrated that the unusual dispersion characteristics of these media induce interesting phenomena, such as: reversed refraction, reversed Doppler effect, backward or superluminal propagation [1-8].

In this paper we focus on the possibility to observe the superluminal propagation phenomenon in these artificial structures; specifically we investigate the dispersive behavior of a MM slab-loaded waveguide (WG) [6-8] demonstrating the existence of a negative group velocity region.

Furthermore, two useful strategies of analysis are presented: a numerical method and an approximated analytical approach.

It is proved that a useful preliminary analysis can be easily performed by means of common mathematical tools such as MATLAB [8]. It is also demonstrated that by using the effective medium theory a more detailed analysis can be approached in an efficient way by means of a Finite Difference Time Domain (FDTD) [9] code based on the Auxiliaries Differential Equations (ADE) method to deal with dispersive media.

Both approaches have been used to investigate the influence of the propagating pulse shape on the Negative Group Velocity (NGV) phenomenon.

The paper is structured as follows: first, the superluminal propagation phenomenon is briefly introduced in section II, and then the dispersion characteristic of a WG loaded by a MM-slab is given in section III.

Later on sections IV and V describe the analytical approach and the FDTD code here proposed, whilst in section VI we report the results obtained for the propagation of modulated signals in a MM-slab-loaded WG. Finally some conclusions are drawn in section VII.

II. SUPERLUMINAL PROPAGATION

For a small-bandwidth signal propagating in a medium characterized by an effective propagation constant γ_{eff} ($\gamma_{eff} = \alpha_{eff} + j\beta_{eff}$), many different kinds of velocity can be defined. To introduce them it can be useful to expand the phase propagation constant in a Taylor series,

$$\begin{aligned} \beta(\omega) &\approx \beta(\omega_0) + \left. \frac{d\beta(\omega)}{d\omega} \right|_{\omega_0} \Delta\omega + \\ &\quad + \frac{1}{2} \left. \frac{d^2\beta(\omega)}{d\omega^2} \right|_{\omega_0} \Delta\omega^2 + \dots = \\ &= \beta_0 + \beta'_0 \Delta\omega + \frac{1}{2} \beta''_0 \Delta\omega^2 + \dots, \\ &\quad \Delta\omega = (\omega - \omega_0). \end{aligned} \tag{1}$$

where the angular frequency ω_0 is the carrier frequency of the propagating signal, whose time characteristic can be written as,

$$\begin{aligned}\tilde{\mathbf{E}}(t, \omega_0) &= E_u(t, \omega_0) \hat{\mathbf{u}} = A(t) \cos(\omega_0 t) \hat{\mathbf{u}} = \\ &= \Re\{A(t) \exp(j\omega_0 t)\} \hat{\mathbf{u}}.\end{aligned}\quad (2)$$

Related to the zero- and first-order term of equation (1), we can introduce:

- *The phase velocity*, which is the propagation velocity of the sinusoidal signal appearing in equation (2),

$$v_{p,eff}(\omega_0) = \left(\frac{\omega}{\beta_{eff}} \right)_{\omega_0} = \frac{\omega_0}{\beta_0}.\quad (3)$$

- *The group velocity* (v_g), which is the velocity by which the $A(t)$ peak travels,

$$v_{g,eff} = \left[\frac{d\beta_{eff}}{d\omega} \right]^{-1} = (\beta')^{-1}.\quad (4)$$

The medium dispersion properties are related to the second-order term of equation (1), commonly known as ‘second-order dispersion’: it is equal to zero for non-dispersive media, whilst it is greater or less than zero respectively for a normal or an anomalous dispersion medium.

The term ‘superluminal’ refers to propagation with values of v_g/v_p negative, or greater than the speed of light in vacuum (c).

It is well known that in some media (a possible example being a hollow waveguide) v_p can be superluminal; the phenomenon can be easily explained by considering that v_p has not a physical meaning, indeed it represents the velocity of propagation of a perfectly monochromatic wave of light which is not a real entity.

More surprising it appears the phenomenon of superluminal values of v_g , due to the existence of media with anomalous dispersion regions.

As observed by Sommerfeld and Brillouin [10], the misunderstanding lies in identifying the signal peak velocity with the carried information velocity, so that superluminal values of v_g seem to be inconsistent with Einstein’s relativity theory. In [10], by considering a Lorentz medium, they showed that a relativistically causal propagation is exclusively connected to the velocity by which the signal switching-on instant travels (the so called front velocity) which must be limited exactly by c .

These topics are still much debated. Sommerfeld’s reasoning has been confirmed by a large number of theoretical and experimental results demonstrating that the superluminal v_g phenomenon can be observed in

several artificial structures [3-5,11-13], such as the DNG medium made of alternating layers of wire arrays and Split Ring Resonators (SRRs) arrays (SRR-wire medium) [14]. In the following, it will be showed that similar observations can be developed for a waveguide loaded by a MM-slab and, in order to investigate how the propagating signal time shape acts on the superluminal propagation phenomenon, the results obtained for the propagation of amplitude modulated signals will be reported and discussed.

III. DISPERSION ANALYSIS OF A WAVEGUIDE LOADED BY A MM SLAB

A. The SRR Particle

A typical Split Ring Resonator (SRR) is shown in Fig. 1; it consists of two concentric rings interrupted by a gap, and was firstly proposed by Pendry [15] as elementary building block of a medium with negative values of the magnetic permeability (MNG medium). The SRR is a strongly resonant structure, whose resonant behavior is excited by an external time-varying magnetic field perpendicular to the ring surface, inducing currents that produce a magnetic field that may either oppose or enhance the incident field, thus resulting in positive or negative effective permeability.

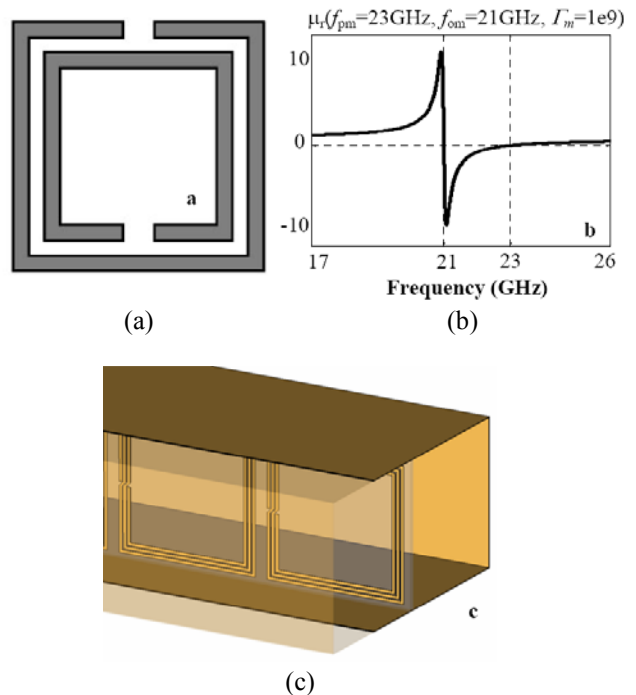


Fig. 1. (a) The Split Ring Resonator particle. (b) The Split Ring Resonator magnetic effective relative permeability. (c) The analyzed structure: a waveguide loaded with a Mu-Negative-slab consisting of an array of spiral resonators on a dielectric substrate.

Nowadays this particle has been studied and experimentally characterized extensively in the literature, demonstrating that an array of SRRs on a dielectric substrate exhibits MNG behavior around the SRR's resonant frequency. The corresponding effective magnetic permeability is given by [4, 16],

$$\mu_{r,eff}(\omega) = \left(1 - \frac{\omega_{pm}^2 - \omega_{om}^2}{\omega^2 + j\omega\Gamma_m - \omega_{om}^2} \right) \quad (5)$$

where Γ_m is the magnetic damping constant, whilst ω_{pm} and ω_{om} are respectively the SRR magnetic plasma and resonance frequencies. They determine the frequency range in which the SRR array behaves as an effective homogeneous (MNG) medium (see Fig. 1(b)).

Furthermore, in order to simplify the design at high frequency or to enhance the SRR magnetic response, in the last years, several modified resonator structures have been proposed, such as: the single ring, the spiral resonator, etc. [17,18].

B. SRR-Slab Loaded WG

One of the more attractive applications for MNG media has been suggested in [6-7], where an array of SRRs on a dielectric substrate has been used as loading slab of a hollow metallic waveguide (WG) to achieve useful stop-band or pass-band behaviors [6-7] (see Fig. 1(c)).

The dispersion equation of the dominant TE_{10} WG mode becomes,

$$\beta_{TE,10} = \beta_0 \sqrt{\mu_{r,eff} \left(1 - \frac{\omega_c^2}{\omega^2} \right)} \doteq \beta_0 n_{eff} \quad (6)$$

where β_0 is the free-space phase propagation constant, ω_c is the WG cutoff frequency; consequently, depending on the values assumed by the SRR parameters, a pass-band/stop-band behavior can be generated below/above ω_c .

By using the effective refractive index of the MM-loaded WG, introduced in equation (9), we have,

$$\begin{aligned} v_p &= \frac{\omega}{\beta_{eff}} = \frac{c}{\Re\{n_{eff}\}}, \\ v_g &= \Re\left\{ \frac{d\beta_{eff}}{d\omega} \right\}^{-1} = \Re\left\{ n_{eff} + \omega \frac{dn_{eff}}{d\omega} \right\}^{-1}, \\ \frac{\tau_g}{d} &= \Re\left\{ n_{eff} + \omega \frac{dn_{eff}}{d\omega} \right\}. \end{aligned} \quad (7)$$

being τ_g/d the normalized group delay.

Figure 2 compares the normalized phase propagation constant and group delay of the MM-loaded WG with those corresponding to the SRR-wire medium analyzed in [4] with $\omega_{pe} = \omega_c$ and $\Gamma_e = 0$ (the realistic values reported in [4] have been used for the SRR medium, whilst ω_c has been fixed to 40 GHz which is the value assumed for ω_{pe} in [4]): an anomalous dispersion region, characterized by simultaneously negative values of v_g (Negative Group Velocity-NGV) and v_p , can be noticed around the SRR resonant frequency. Furthermore, according to [6], a pass-band with backward propagation characteristic can be also observed below the WG cutoff frequency.

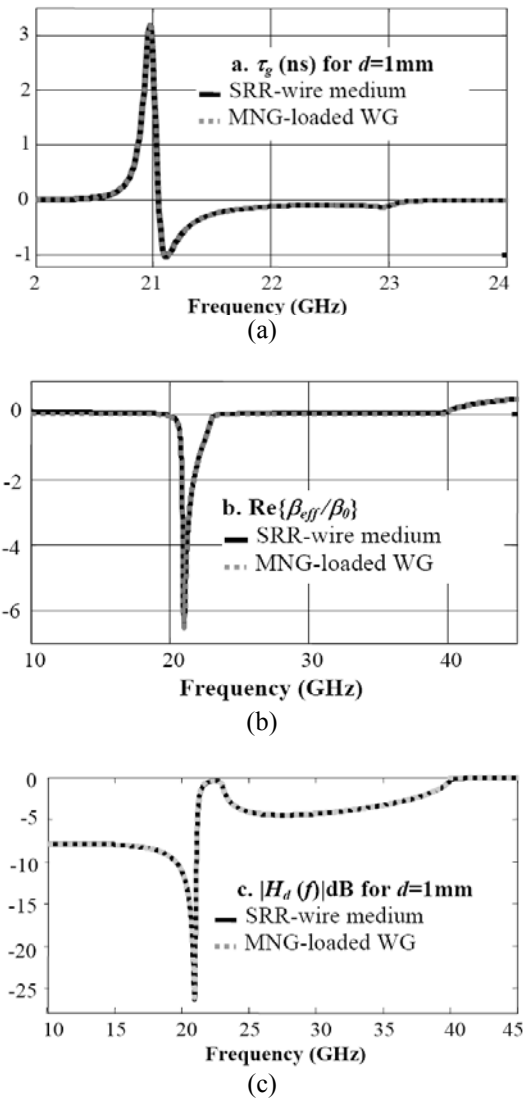


Fig. 2. Comparison between the Split Ring Resonator-wire medium analyzed in [4] and the waveguide loaded by a Mu-Negative (MNG) slab ($f_{pm}=23\text{GHz}$, $f_{om}=21\text{GHz}$, $f_c=40\text{GHz}$). (a) Group delay calculated for $d=1\text{mm}$, (b) propagation constant, and (c) attenuation calculated for $d=1\text{mm}$.

IV. ANALYTICAL APPROACH

The proposed approach refers to a MM-slab, characterized by an effective refractive index and phase propagation constant,

$$n_{\text{eff}} = \sqrt{\varepsilon_{r,\text{eff}}} \sqrt{\mu_{r,\text{eff}}} = n'_{\text{eff}} - jn''_{\text{eff}}, \quad (8)$$

$$\beta_{\text{eff}} = \frac{\omega}{c} n_{\text{eff}} = \beta'_{\text{eff}} - j\beta''_{\text{eff}}.$$

For a plane wave, with angular frequency ω , impinging on the slab front-face with an angle θ_i , the slab transfer function is given by [4],

$$H_d(\omega) = \frac{T_{12}T_{21} \exp\{-j\beta_{\text{eff}} \cos(\theta_i) d\}}{1 - R_{12}^2 \exp\{-j2\beta_{\text{eff}} \cos(\theta_i) d\}} =$$

$$= |H_d(\omega)| \exp\{+\phi(\omega)\} \approx \exp\{-j\beta_{\text{eff}} d\} \quad (9)$$

$$\left\{ \sin(\theta_t) = \sin(\theta_i) \frac{n_1}{n_{\text{eff}}} \right\}.$$

Being T_{ij} and R_{ij} , respectively the Fresnel's transmission and reflection coefficients at the slab interface with respect to the surrounding medium (with a refractive index n_l).

In the case of a normal incidence (i.e., $\theta_i = 0$), we have,

$$H_d(\omega) = |H_d(\omega)| \exp\{-j\beta_{\text{eff}} d\}. \quad (10)$$

We assume a linear polarization and an amplitude modulation for the incident field, so that in the time domain it can be expressed as in equation (2), where the time envelope, $A(t)$, is assumed to be a slowly varying function. Employing $H_d(\omega)$, and assuming that $\phi(\omega)$ can be expanded around ω_0 as a Taylor series arrested to the second-order term,

$$\phi(\omega) \approx \phi(\omega_0) + \left. \frac{d\phi(\omega_0)}{d\omega} \right|_{\omega_0} \Delta\omega +$$

$$+ \frac{1}{2} \left. \frac{d^2\phi(\omega_0)}{d\omega^2} \right|_{\omega_0} \Delta\omega^2 \triangleq \tilde{\phi}(\omega). \quad (11)$$

The signal transmitted by the slab can be determined by using the approach proposed in [19]; indeed, by using the Direct/Inverse Fourier transformation (DFT/IFT) we have,

$$E_u(t, d) = \frac{1}{\sqrt{2\pi}} \int_{-\infty}^{+\infty} E_u(\omega, \omega_0) |H_d(\omega)| e^{+\{\phi(\omega) + j\omega t\}} d\omega \approx$$

$$= \frac{1}{\sqrt{2\pi}} \int_{-\infty}^{+\infty} E_u(\omega, \omega_0) |H_d(\omega)| e^{+\{\tilde{\phi}(\omega) + j\omega t\}} d\omega. \quad (12)$$

Being $E_u(\omega, \omega_0)$ the Electric Field Fourier Transform (FT). The main difference, with respect to the analysis performed in [19], is that, due to the resonant behavior of the MM effective magnetic permeability given in equation (5), in the case under analysis the hypothesis of transfer function with nearly constant amplitude is not applicable.

Considering that the transfer function of a real slab must have a Hermitian symmetry,

$$H_d(-\omega) = H_d(\omega)^* \Rightarrow \text{IFT}\{H_d(\omega)\} \in \Re e \quad (13)$$

equation (12) becomes,

$$E_u(t, d) = \text{IFT}\{\text{FT}\{E_u(t, d=0)\} H_d\} =$$

$$= \frac{2\Re e}{\sqrt{2\pi}} \left\{ \int_0^{+\infty} \text{FT}\{E_u(t, d=0)\} H_d e^{+\{\tilde{\phi}(\omega) + j\omega t\}} d\omega \right\} = \quad (14)$$

$$\triangleq 2\Re e\{\text{IFT}^+\{\text{FT}\{E_{u,0}(t)\} \tilde{H}_d(d)\}\}.$$

By discretizing the input signal and substituting the FT/IFT with the Discrete Fourier Transform (DFT)/Inverse Discrete Fourier Transform (IDFT), we have,

$$E_z(t, f_0, d=0)$$

discretization, N points

$$\downarrow$$

$$\sum_{K=1}^N E_z(kT_c, f_0, d=0) \quad , \quad H_d(f)$$

DFT, N points DFT, N/2 points

$$\downarrow \qquad \qquad \qquad \downarrow$$

$$\sum_{K=1}^N E_z\left(\frac{k}{N} f_c, f_0, d=0\right) \quad , \quad \sum_{K=1}^{N/2} H_d\left(\frac{k}{N} f_c, d\right)$$

$$\downarrow$$

$$\left\{ \sum_{K=1}^{N/2} E_z\left(\frac{k}{N} f_c, f_0, d=0\right) \times H_d\left(\frac{k}{N} f_c, d\right) \right\} \quad (15)$$

IDFT, N points

$$\downarrow$$

$$\sum_{K=1}^N E_z(kT_c, f_0, d)$$

where f_c is the sampling frequency and T_c the sampling time ($f_c = 1/T_c$) which must be fixed according to Shannon's theorem. The response to any input signal can be now calculated by using a common and efficient mathematical tool, such as, for instance, MATLAB [19].

In this way, the effect of the dispersive behavior of a MM on finite bandwidth signals can be easily evaluated. Figure 2(c) shows the amplitude of the transfer function corresponding to the SRR-loaded WG (the SRR and WG parameters are the same assumed in the previous section). We can see that the NGV region corresponds to an absolute minimum of H_d .

This is in agreement with the analysis developed in [20], demonstrating that any causal medium with a linear refractive index must exhibit superluminal propagation regions centered at the frequency corresponding to an absolute maximum of the medium absorption.

In the following, equation (15) will be employed to study the propagation of amplitude-modulated signals in this anomalous dispersion region.

V. THE FDTD CODE

In order to validate the results obtained by using the analytical approach presented in the previous section we use a proprietary FDTD tool in a Total Field /Scattered Field (TF/SF) formulation using Mur's II order boundary conditions [9]. The TF/SF formulation allows the evaluation of the slab response to a modulated signal in a 1-D environment, reducing considerably the computational time.

Furthermore, by modeling the MM-loaded WG as an effective homogeneous medium with a relative effective magnetic permeability given by equation (5) and a relative effective electric permittivity given by,

$$\varepsilon_{r,eff} = \left(1 - \frac{\omega_c^2}{\omega^2}\right). \quad (16)$$

The analysis with the FDTD code has been approached in an efficient way by using the Auxiliary Differential Equation method to deal with time dispersion [9]. More specifically the following phasor polarization currents have been employed to simulate the propagation of a plane-wave electric field, with linear polarization, normally impinging on the MM-loaded waveguide,

$$\begin{aligned} J_p(\omega) &= \frac{j\omega\varepsilon_0\omega_{pe}^2}{(-\omega^2)} E(\omega), \quad M_p(\omega) = \\ &= j\omega\mu_0 \left(\frac{\omega_{pm}^2 - \omega_{om}^2}{\omega_{om}^2 + j\omega\Gamma_m - \omega^2} \right) H(\omega). \end{aligned} \quad (17)$$

The electric polarization current (J_p) given in equation (17) is related to the dispersion equation of the dominant TE_{10} WG mode (i.e., to $\varepsilon_{r,eff}$), whilst the magnetic polarization current (M_p) allows to account the SRR-slab (i.e., it is related to $\mu_{r,eff}$).

VI. RESULTS

Referring to Fig 1(c), in this section we assume that a signal such that given in equation (2) is applied at the input port of a MM-slab loaded WG. By fixing the WG length equal to d , equation (15) and the FDTD code have

been used to calculate the time-domain characteristic of the propagating signal at the output port. In the following we report some results obtained by assuming that the time envelope of the input signal is a real function. More specifically, the shapes of the propagating signal have been fixed in order to investigate the assertions made in [14], where the NGV phenomenon has been attributed to asymmetrical energy absorption from the propagating signal: Crisp pointed out that the attenuation experienced by a propagating pulse depends on the time derivative of its time envelope. Consequently, in the following, the case of signals with a trailing and leading portion characterized by an exponential, a sinusoidal and a constant time derivative have been considered (see Fig. 3). Furthermore, as evident from Figs. 3 and 4, the simulated signals exhibit different types of discontinuities, allowing evaluating how the 'well-behaved' property of the propagating pulse influences the NGV phenomenon.

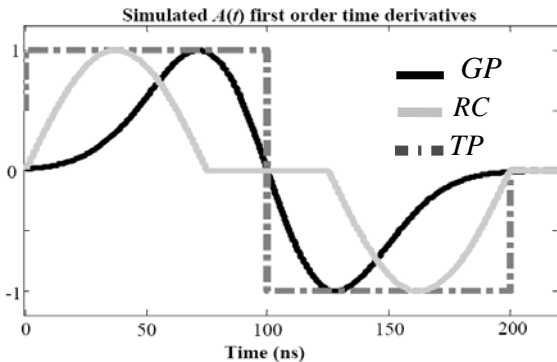


Fig. 3. Normalized first order time derivatives of the time envelope of the simulated signals.

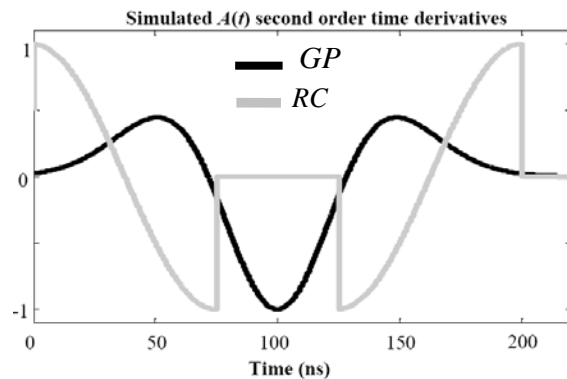


Fig. 4. Normalized second order time derivatives of the Gaussian and Raised Cosine function.

A. Gaussian Pulse

The propagation of a small bandwidth Gaussian Pulse (GP) in an NGV medium is a well known topic [11-14, 21]. It has firstly theoretically investigated by Garrett and McCumber [21], which demonstrated that under

some easily verified hypotheses the GP propagates at superluminal group velocity preserving its shape; starting from Faxvog's [11] results, the phenomenon has been confirmed by several experimental observations.

Consequently, in order to validate both the analytical approach and the FDTD code presented in the previous sections, we start our analysis assuming that the input signal time envelope is a (GP) function,

$$A(t) = GP(t, \sigma) = S \exp\left\{-\frac{(t - \tau)^2}{\sigma^2}\right\}. \quad (18)$$

The results obtained by solving equation (15) with MATLAB are coincident with those obtained by using the FDTD code; they are reported in Fig. 5.

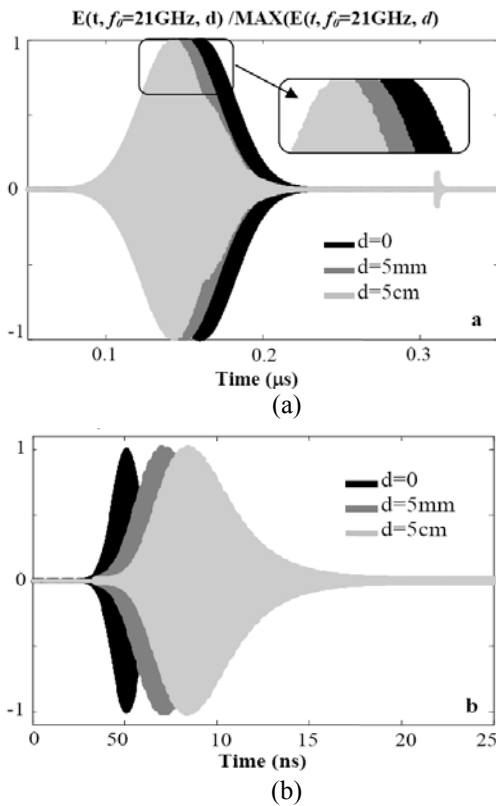


Fig. 5. Results obtained by using equation (14) for the propagation of a Gaussian Pulse (GP) in a waveguide loaded with a Split Ring Resonator slab ($f_{\text{pm}}=23\text{GHz}$, $f_{\text{om}}=21\text{GHz}$, $f_c=40\text{GHz}$): (a) GP characterized by $\sigma=30\text{ns}$, $\tau=0.16\mu\text{s}$, (b) GP characterized by $\sigma=1\text{ns}$ and $\tau=15\text{ns}$.

Figure 5(a) refers to a small-bandwidth GP ($\sigma=30\text{ns}$ and $\tau=0.16\mu\text{s}$) modulating a carrier signal at $f_0=21\text{GHz}$. The solution time required on a Pentium 4-2.8 GHz with the MATLAB approach was equal to 27 seconds (s).

As expected the pulse peak experiences a negative group delay during the propagation (i.e., the peak of the output pulse precedes that of the input pulse).

With reference to an absorbing medium with a Lorentzian inhomogeneous line shape, a similar phenomenon has been attributed by Crisp to an energy absorption which, with respect to those corresponding to a constant amplitude light beam, is greater in the case of a rising amplitude (positive time derivative), and smaller in the case of a decreasing amplitude (negative time derivative).

In Fig. 5(b) the results are given for the same analysis obtained for a broadband GP ($\sigma=1\text{ns}$ and $\tau=15\text{ns}$, solution time on a Pentium 4-2.8 GHz equal to 25s). In this case our calculation predicts that the pulse peak travels at a positive group velocity.

B. Raised Cosine

The group velocity concept is related to the peak of the propagating pulse; consequently, in order to deeply investigate the NGV phenomenon, the case of a propagating signal with a not-defined amplitude peak has been also considered in our analysis.

More specifically, we studied the propagation of a Raised Cosine (RC) signal,

$$A(t) = RC(t) = \begin{cases} S & , \quad |t'| \leq (1 - \rho)2T \\ Sf(t) & , \quad (1 - \rho)2T \leq |t'| \leq (1 + \rho)2T, \\ 0 & , \quad \text{elsewhere} \end{cases} \quad (19)$$

$$f(t) = \left\{ 1 - \sin\left[\frac{\pi}{\rho}\left(\frac{|t'|}{4T} - \frac{1}{2}\right)\right] \right\}.$$

From equation (19) it is evident that $A(t)$ has a leading and trailing portion with a sinusoidal time derivative (see Fig. 3), and that a constant amplitude portion is also present in its time characteristic.

As in the GP case, two RC signals have been simulated (referred in the following as RC1/2): RC1 is a small bandwidth signal, so that its frequency characteristic is within the anomalous dispersion region of the MM-loaded WG, whilst RC2 is a broadband signal: its spectrum has a significant amplitude in both regions of anomalous and normal dispersion corresponding to NGV and backward propagation.

As noted from Figs. 6 and 7, where the results obtained with MATLAB are reported, in both cases the propagating signal experiences a strong distortion: the signal energy concentrates at the switch-on/off instants and at the instants corresponding to the transition from the sinusoidal to the flat portion of the RC pulse. From Fig. 4 it is evident that these instants correspond to jump discontinuities for the second-order time derivative of the RC function.

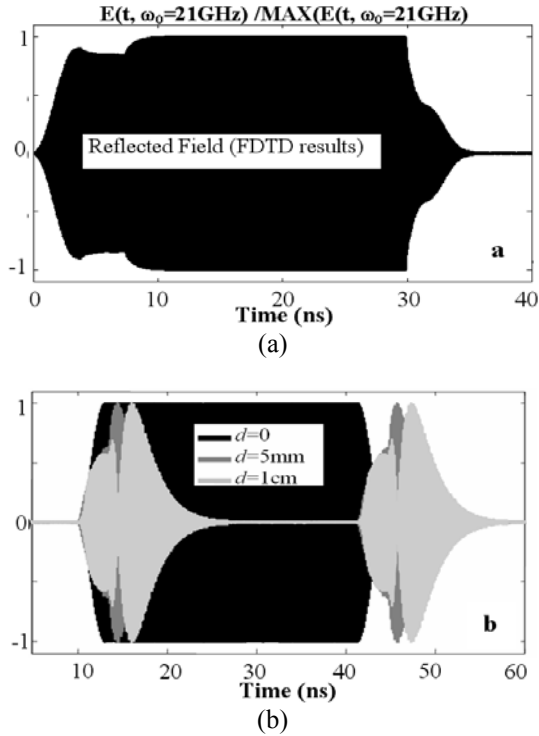


Fig. 6. Results obtained for the propagation of a Raised Cosine function ($\rho=0.1$, $T=7.8\text{ns}$, $f_0=21\text{GHz}$) in the Split Ring Resonator-loaded waveguide ($f_{\text{pm}}=23\text{GHz}$, $f_{\text{om}}=21\text{GHz}$, $f_c=40\text{GHz}$). (a) Reflected field calculated by using the ADE-FDTD-TF/SF code. (b) Time characteristic obtained with MATLAB for different values of d .

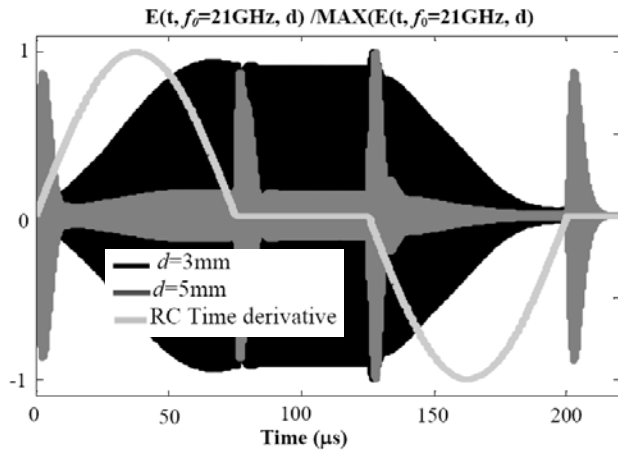


Fig. 7. Results obtained by using equation (14) for the propagation of a Raised Cosine (RC) function in the Split Ring Resonator loaded waveguide ($f_{\text{pm}}=23\text{GHz}$, $f_{\text{om}}=21\text{GHz}$, $f_c=40\text{GHz}$). The RC parameters are: $\rho=0.6$, $T=31.25\text{ns}$, $f_0=21\text{GHz}$.

C. Triangular Pulse

To conclude, we analyze the case of a triangular function as modulating signal,

$$A(t) = TP(t) = \begin{cases} \left(\frac{t}{T}\right), & t \in [0, T] \\ \left(\frac{2T-t}{T}\right), & t \in [T, 2T] \end{cases} \quad (20)$$

From equation (20) we can see that in this case the leading and trailing portion exhibit a constant derivative respectively equal to $-1/T$ and to $1/T$ (see Fig. 3). The results obtained for this broadband TP are given in Fig. 8, they are similar to the one obtained for the GP pulse: due to the asymmetric attenuation experienced by the TP spectrum amplitude (see Fig 8(a)), the output signal is distorted.

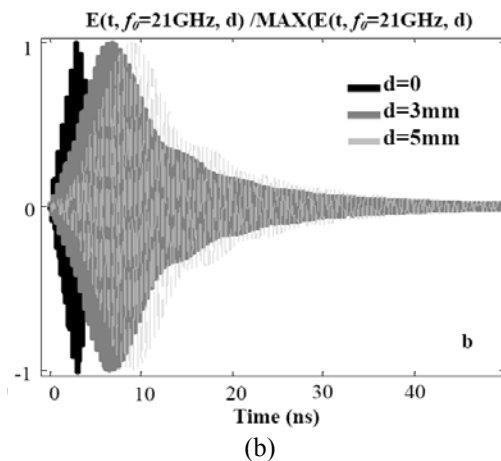
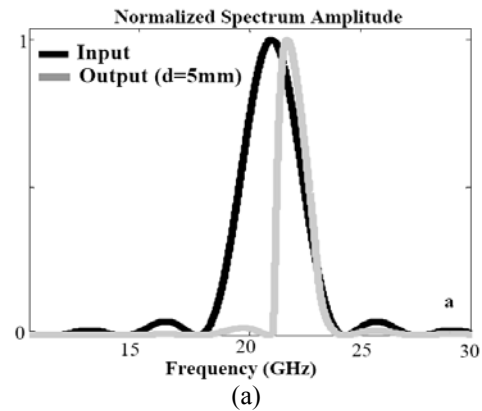


Fig. 8. Results obtained for a Triangular Pulse characterized by $T=0.3\text{ns}$ and $f_0=21\text{GHz}$: (a) comparison between the spectrum amplitude of the input signal and those of the output signal; (b) time domain characteristics obtained with MATLAB for different values of d .

In Fig. 9 the results are given for a *TP* with $T=100\text{ns}$. We can see that, as in the small-bandwidth *RC* case, the signal experiences a strong distortion: the *TP* energy concentrates at the instants corresponding to a jump discontinuity for the first-order time derivative of the *TP* function. Furthermore, from Fig. 9(a), we can see that the attenuation experienced by the *TP* spectrum amplitude is strongly asymmetric.

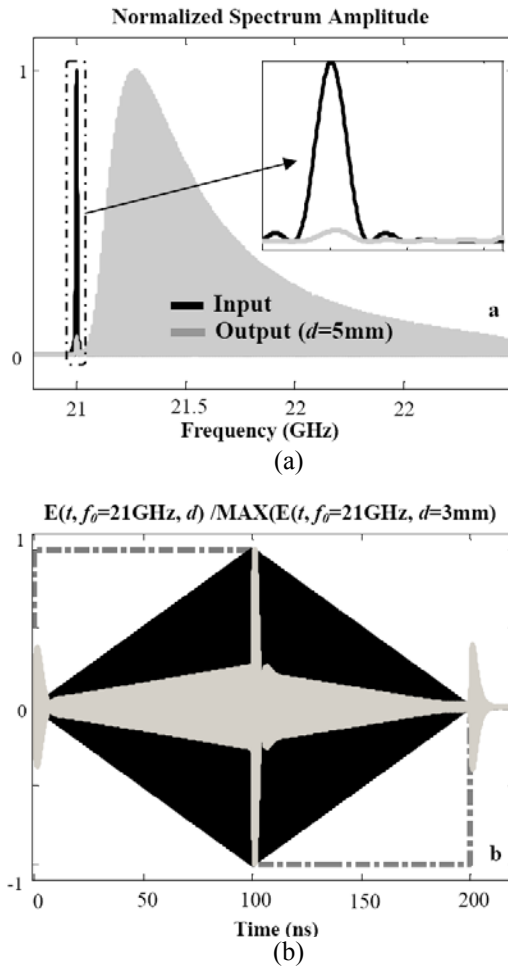


Fig. 9. Results obtained for a Triangular Pulse characterized by $T=100\text{ns}$ and $f_0=21\text{GHz}$: (a) comparison between the spectrum amplitude of the input signal and those of the output signal, (b) time domain characteristics obtained with MATLAB for $d=3\text{mm}$ (the broken line is the time derivative of the input signal time envelope).

VII. CONCLUSIONS

In this paper, two strategies for the analysis of a waveguide loaded with a Mu-Negative material have been proposed:

– An approximated analytical approach implemented with MATLAB: reported results demonstrate that it allows to immediately evaluate the effects of the dispersive

behaviour of an effective homogeneous medium on a finite bandwidth propagating signal representing a useful strategy for the so called dispersion engineering;

– An FDTD code: based on the effective medium theory and on the Auxiliary Differential Equations method, a very efficient formulation of the problem under analysis has been suggested.

Both approaches have been used to investigate situations of superluminal propagation. More specifically, we firstly theoretically demonstrate the existence of an anomalous dispersion region in the waveguide dispersion characteristic, then, we analyze the effects of this negative velocity behavior on amplitude modulated signals.

Three different time envelopes have been considered:

- The well behaved Gaussian (GP) function;
- The Raised Cosine (RC) function which presents jump discontinuities in the second order time derivative;
- The Triangular (TP) function which presents jump discontinuities in the first order time derivative;

In all cases a broadband and a small-bandwidth signal have been considered. As expected the small-bandwidth GP experiences a negative group delay preserving its shape, whilst the RC and TP signal are strongly distorted after the propagation: the propagating signal energy concentrates at the instants corresponding to the jump discontinuities respectively in the second and first order time derivative. The phenomenon is due to the strongly asymmetric attenuation experienced by the spectrum amplitude of the propagating signals. The relevant consequence is that only the well behaved Gaussian Pulses, characterized by single-lobe spectrum amplitude, experience a negative group delay, preserving its shape during the propagation.

REFERENCES

- [1] V. G. Veselago, "The electrodynamics of substances with simultaneously negative values of permittivity and permeability," *Soviet Physics USPEKI*, vol. 10, no. 4, pp. 509-514, Jan-Feb. 1968.
- [2] M. Mojahedi and G. V. Eleftheriades, *Negative Refraction Metamaterials: Fundamental Properties and Applications*, IEEE Press-Wiley Interscience, John Wiley & Sons Inc., pp. 381-411, 2005.
- [3] M. Mojahedi, K. J. Malloy, G. V. Eleftheriades, J. Woodley, and R. Y. Chiao, "Abnormal wave propagation in passive media," *IEEE Journ. of Selected Topics in Quantum Electronics*, vol. 9, pp. 3039, 2003.
- [4] J. Woodley and M. Mojahedi, "Negative group velocity in left-handed materials," *Antennas and Propagat. Society Symp.*, vol. 4, pp. 643-646, 2005.
- [5] O. F. Siddiqui, M. Mojahedi, and G. V. Eleftheriades, "Periodically loaded transmission line

- with effective negative refractive index and negative group velocity," *IEEE Trans. Antenn. Propagat.*, vol. AP-51, no. 10, pp. 2619-2625, 2003.
- [6] R. Marqués, J. Mariel, F. Mesa, and F. Medina, "Left-Handed simulation and transmission of EM waves in subwavelength split-ring resonator-loaded metallic waveguide," *Physical Review Letters*, vol. 89, no. 18, 2002.
- [7] G. Lubkowski, C. Damm, B. Bandlow, R. Schuhmann, M. Schüßler, and T. Weiland, "Waveguide miniaturization using spiral resonator and dipole arrays," *Proc. of the 36th Europ. Microw. Conf.*, pp. 1312-1315, 2006.
- [8] G. Monti, L. Tarricone, "Dispersion Engineering with MATLAB," *Proc. of the 23th ACES conf.*, March 2007.
- [9] A. Taflove, *Computational Electrodynamics, The Finite Difference Time-Domain Method*, Artech House, Norwood, MA, 1995.
- [10] L. Brillouin, *Wave Propagation and Group Velocity*, Academic, New York, 1960.
- [11] F. R. Faxvog, C. Y. Chow, T. Bieber, and J. A. Carruthers, "Measured pulse velocity greater than c in a neon absorption cell," *Appl. Physics Lett.*, vol. 17, no. 5, 1970.
- [12] S. Chu and S. Wong, "Linear pulse propagation in an absorbing medium," *Phys. Rev. Lett.*, vol. 48, pp. 738-741, 1982.
- [13] E. L. Bolda, J. C. Garrison, and R. Y. Chiao, "Optical pulse propagation at negative group velocities due to a nearby gain line," *Phys. Review A*, vol. 49, pp. 2938-2947, 1994.
- [14] M. D. Crisp, "Concept of group velocity in resonant pulse propagation," *Physical Review A* 4, iss. 5, pp. 2104 - 2108, 1971.
- [15] J. B. Pendry, A. J. Holden, D. J. Robbins, and W. J. Stewart, "Magnetism from conductors, and enhanced non-linear phenomena," *IEEE Trans. on Microw. Theory and Techn.*, vol. 47, no. 11, pp. 2075-2084, 1999.
- [16] D. R. Smith, W. J. Padilla, D. C. Vier, S. C. Nemat Nasser, and S. Schultz, "Composite medium with simultaneously negative permeability and permittivity," *Phys. Rev. Lett.*, vol. 84, pp. 4184-4187, 2000.
- [17] J. D. Baena, R. Marqués, and F. Medina, "Artificial magnetic metamaterial design by using spiral resonators," *Phys. Rev. B*, vol. 69, pp. 014402, 2004.
- [18] J. García-García, F. Martín, J. D. Baena, R. Marqués, and L. Jelinek, "On the resonances and polarizabilities of split ring resonators," *Journ. of the Applied Physics*, vol. 98, 033103 (1-9), 2005.
- [19] G. Monti, L. Tarricone, "Gaussian pulse expansion of modulated signals in a double-negative slab," *IEEE Trans. on Microw. Theory and Techn.*, vol. 54, no. 6, pp. 2755-2761, 2006.

- [20] Eric L. Bolda, Raymond Y. Chiao, and John C. Garrison, "Two theorems for the group velocity in dispersive media," *Phys. Rev. A* 48, 3890, 1993.
- [21] C. G. B. Garrett and D. E. McCumber, "Propagation of a gaussian light pulse through an anomalous dispersion medium," *Phys. Rev. A*, vol. 1, p. 305-313, 1970.



G. Monti received the Laurea degree in Telecommunication Engineering (with honours) from the University of Bologna (Italy), in 2003, and the Ph.D. in Information Engineering from the University of Salento (Italy), in 2007. She is currently with the University of Salento, where she is a temporary researcher. She has co-authored more than 30 papers appeared in international conferences and journals. Her current research interest includes the analysis and applications of artificial media, the design of microwave components and MEMS-based reconfigurable antennas and devices.



L. Tarricone received the Laurea degree (cum-laude) in electronic engineering and the Ph.D. degree from Rome University "La Sapienza," Rome, Italy, in 1989 and 1994, respectively. Since 1994, he has been a Researcher at the University of Perugia, Italy, and since 1998, he has been a Professore Incaricato of electromagnetic (EM) fields and EM compatibility. Since November 2001, he is with the University of Salento (Italy) where he is Associate Professor of Electromagnetic Fields. He has authored approximately 200 scientific papers. His main contributions are in the modeling of microscopic interactions of EM fields and biosystems, and in numerical methods for efficient CAD of microwave circuits and antennas. He is currently involved in the FDTD analysis of human-antenna interaction, novel CAD tools and procedures for microwave circuits, and EM parallel computing.

RCS Estimation of 3D Metallic Targets Using the Moment Method and Rao-Wilton-Glisson Basis Functions

G. K. Carvajal, D. J. Duque, and A. J. Zozaya

Electronics and Communications Department, Applied Electromagnetics Lab.
Carabobo University, Valencia, Venezuela
azozaya@uc.edu.ve

Abstract – This work deals on the estimation of the radar cross section (RCS) of five three-dimensional conductive objects: the metallic sphere, NASA almond, single ogive, double ogive and conesphere, using the Moment Method. The Rao-Wilton-Glisson (RWG) basis functions were used to expand the surface current of targets inside the Electric Field Integral Equation (EFIE). Triangular domains of RWG basis functions were constructed using MATLAB tessellation capabilities and a MATLAB code was developed and run to solve the electromagnetic scattering problem. As a result five RCS graphs, one for each target, were obtained. The accuracy of the program was validated by comparing the obtained results with those reported in the Literature.

Keywords: Radar Cross Section (RCS), Method of Moments (MoM), Electric Field Integral Equation (EFIE), Rao-Wilton-Glisson (RWG) basis functions, and Computational Electromagnetics (CEM).

I. INTRODUCTION

It is well known that the problem of *Electromagnetic Scattering* for targets of arbitrary shape is either difficult or impossible to treat analytically. This is due among others to the complicated effect of targets curvatures, corners, and dielectrics which could overlap the target. This is the reason why in order to get an inside into the scattering mechanism, available numerical methods must be used.

This work deals on the estimation of the radar cross section (RCS) of five three-dimensional conductive objects: the metallic sphere, NASA almond, single ogive, double ogive and conesphere, using the moment method [1]. Most of this objects are radar benchmark targets widely used for the validation of computational electromagnetic codes. Their geometries are well described in [2].

The electric current and charge densities at the target surface are expanded using the Rao-Wilton-Glisson (RWG) basis functions [3]. Discretization of target surface is achieved using MATLAB tessellation capabilities taking into account the work of Makarov [4]. Although the MATLAB built-in functions are used for writing the

code and for rendering the results, this paper emphasizes the main equations but not on transcribing the code.

This article is organized in the following way: Section 2 presents the theoretical concepts used for the problem. Section 3 presents the numerical approach used to obtain a solution for the scattering problem of electrical conductive objects using the MoM and the RWG basis function. In Section 4 the numerical results obtained from simulation are presented and, finally, in Section 5 conclusions are given.

II. THEORETICAL CONCEPTS

A. The Radar Cross Section

The radar cross section (RCS) is a figure of merit that quantifies the amount of electromagnetic energy scattered in a given direction. The RCS, denoted by the greek letter σ is defined as follow [5,6],

$$\sigma(\boldsymbol{\kappa}^i, \boldsymbol{\kappa}^s) = \lim_{r \rightarrow \infty} \left(4\pi r^2 \frac{|\mathbf{E}^s|^2}{|\mathbf{E}^i|^2} \right) \quad (1)$$

where \mathbf{E}^i is the incident field in a direction $\boldsymbol{\kappa}^i$, \mathbf{E}^s is the scattered field in a direction $\boldsymbol{\kappa}^s$. Whether the directions $\boldsymbol{\kappa}^i$ and $\boldsymbol{\kappa}^s$ coincide or not, we talk about monostatic RCS or bistatic RCS, respectively. In the present work we will focus on the monostatic RCS, even though the bistatic RCS can also be computed easily.

B. The Electric Field Integral Equation

In *free space*, where a scatterer could be in the presence of a forced incident electric field \mathbf{E}^i , there will be a resultant electric field \mathbf{E} , given by $\mathbf{E} = \mathbf{E}^i + \mathbf{E}^s$. In this assumption, the field \mathbf{E}^s would be the scattered field. Over a Perfect Electric Conductor (PEC) scatterer surface, the tangential component of the electric field must vanish, hence,

$$\mathbf{n} \times (\mathbf{E}^i + \mathbf{E}^s) = 0 \quad (2)$$

where \mathbf{n} is the scatterer's surface normal vector. The *Equivalence Principle* [5] establishes as a sources for \mathbf{E}^s , a current density \mathbf{J}_s and a superficial density of charges ρ_s , both related through the *continuity* of current

$\rho_s = -\frac{\nabla \cdot \mathbf{J}_s}{j\omega}$. Hence, the \mathbf{E}_s could be computed by the following expression,

$$\mathbf{E}_s = -j\omega \mathbf{A} - \nabla V \quad (3)$$

with

$$\begin{aligned} \mathbf{A}(\mathbf{r}) &= \frac{\mu}{4\pi} \int_{S'} \mathbf{J}_s(\mathbf{r}') G(r, r') dS', \\ V(r) &= \frac{1}{4\pi\epsilon} \int_{S'} \rho_s(r') G(r, r') dS', \end{aligned}$$

where $G(r, r') = \frac{e^{-j\kappa|r-r'|}}{|r-r'|}$, \mathbf{r} and \mathbf{r}' are the position vectors for observation and source points respectively, $\kappa = \omega\sqrt{\mu\epsilon}$ is the wavenumber, and finally S' is the scatterer's surface seen as a source domain. By means of simple substitutions, and taking into account that $-j\omega\rho = \nabla' \cdot \mathbf{J}$, equation (2) is rewritten as follows,

$$\begin{aligned} \mathbf{n} \times j \frac{\omega\mu}{4\pi} \int_{S'} [\mathbf{J}_s(\mathbf{r}') G(r, r') + \\ \frac{1}{\kappa^2} \nabla \nabla' \cdot \mathbf{J}_s(\mathbf{r}') G(r, r')] ds' = \mathbf{n} \times \mathbf{E}_i. \quad (4) \end{aligned}$$

The equation (4) is a integral equation of first kind [7] in the form $\mathcal{L}(\mathbf{u}) = \mathbf{v}$ known as the electric field integral equation (EFIE), where one recognizes,

$$\begin{aligned} \mathcal{L}() &\equiv \\ \mathbf{n} \times j \frac{\omega\mu}{4\pi} \int_{S'} [() G(r, r') + \frac{1}{\kappa^2} \nabla \nabla' \cdot () G(r, r')] ds' \\ \mathbf{u} &\equiv \mathbf{J}_s \\ \mathbf{v} &\equiv \mathbf{n} \times \mathbf{E}_i. \end{aligned}$$

For most of practical targets, equation (4) can not be solved analytically, but must be solved numerically. Equation (4), in principle, will be used to compute the induced current on the PEC scatterer surface.

III. THE NUMERICAL SOLUTION

The numerical solution to equation (4) will be obtained using the moment method as described in [1]. The RWG basis function \mathbf{f}_n will be used for the expansion of the induced current \mathbf{J}_s [3].

A. Filling the impedance matrix

To fill the impedance matrix Z , two integrals: the integral of the inner product definition $Z_{mn} = \langle \mathbf{w}_m, \mathcal{L}(\mathbf{f}_n) \rangle = \int_{S_m} \mathbf{w}_m \cdot \mathcal{L}(\mathbf{f}_n)$ and the convolution integral given by $\mathcal{L}(\mathbf{f}_n)$ must be solved $N \times N$ times [1]. The complexity of the former will be determined by the election of the *weighting* function \mathbf{w}_m . The weighting functions \mathbf{w}_m must be in the rank of \mathcal{L} preferably, to accelerate the convergence [1]. Nevertheless, this premise is not restrictive [8]. Although there exist several possibilities for the choosing of \mathbf{w}_m , in this work it is preferred to use Galerkin approach as Rao et al. [3] suggested.

1) *Numerical Integration*: The integral $Z_{mn} = \int_{S_m} \mathbf{f}_m \cdot \mathcal{L}(\mathbf{f}_n) dS_m$ will be approximated by the product of its argument evaluated at the barycenter (center of mass) of each triangle and their areas respectively. Hence,

$$\begin{aligned} Z_{mn} &= \int_{T_m^+} \mathbf{f}_m \cdot \mathcal{L}(\mathbf{f}_n) dS + \int_{T_m^-} \mathbf{f}_m \cdot \mathcal{L}(\mathbf{f}_n) dS \quad (5) \\ &\approx \frac{l_m}{2} \left[\boldsymbol{\rho}_m^{c+} \cdot \mathcal{L}(\mathbf{f}_n)|_{\boldsymbol{\rho}_m^{c+}} + \boldsymbol{\rho}_m^{c-} \cdot \mathcal{L}(\mathbf{f}_n)|_{\boldsymbol{\rho}_m^{c+}} \right] \end{aligned}$$

where $\boldsymbol{\rho}_m^{c\pm}$ is the position vector for the barycenters of triangles T_m^\pm and l_m is the length of the common edge. Taking into account the definition for \mathcal{L} , equation (5) is written as,

$$\begin{aligned} Z_{mn} &= j\omega l_m \left(\mathbf{A}_{m^+,n} \cdot \frac{\boldsymbol{\rho}_m^{c+}}{2} + \mathbf{A}_{m^-,n} \cdot \frac{\boldsymbol{\rho}_m^{c-}}{2} \right) + \\ & \quad l_m (V_{m^-,n} - V_{m^+,n}) \quad (6) \end{aligned}$$

where

$$\begin{aligned} \mathbf{A}_{m^\pm,n} &= \frac{\mu}{4\pi} \int_{S'} \mathbf{f}_n \frac{e^{-j\kappa R_m^\pm}}{R_m^\pm} dS', \\ V_{m^\pm,n} &= -\frac{1}{4\pi j\omega\epsilon} \int_{S'} \nabla' \cdot \mathbf{f}_n \frac{e^{-j\kappa R_m^\pm}}{R_m^\pm} dS', \end{aligned}$$

and $R_m^\pm = |\mathbf{r}_m^{c\pm} - \mathbf{r}'|$.

Finally, developing equation (6) is obtained for Z_{mn} ,

$$\begin{aligned} Z_{mn} &= \\ \frac{l_m}{8} \left(\frac{j\eta\kappa}{\pi} \right) \boldsymbol{\rho}_m^{c\pm} \cdot \int_{T_n^+ + T_n^-} \mathbf{f}_n G(\mathbf{r}_m^{c\pm}, \mathbf{r}') dS' \pm \\ \frac{l_m l_n}{4} \left(\frac{j\eta}{\pi\kappa} \right) \left[\frac{1}{A_n^+} \int_{T_n^+} G(\mathbf{r}_m^{c\pm}, \mathbf{r}') \right. \\ \left. - \frac{1}{A_n^-} \int_{T_n^-} G(\mathbf{r}_m^{c\pm}, \mathbf{r}') \right] \quad (7) \end{aligned}$$

where $\boldsymbol{\rho}_m^{c\pm}$ and $\mathbf{r}_m^{c\pm}$ are position vectors for the barycenters of triangles T_m^\pm measured locally and globally, respectively.

To solve the remaining integrals in equation (7), several approaches can be followed [9,10]. Particular, for this work, it has been adopted to use the so call *barycentric subdivision* [4,11]. According to this, any triangle T is subdivided in 9 subtriangles applying the 1/3 rule. Hence, the integrand is considered *constant* in any of the subtriangles. Due to this procedure the singularity of equation (4) is avoided because of subtriangle's midpoints for each source triangles T_n^\pm never coincide with centers of observation triangles T_m^\pm . The barycentric subdivision is resumed as,

$$\int_S g(\mathbf{r}) dS = \frac{A}{9} \sum_{k=1}^9 g(\mathbf{r}_k^c). \quad (8)$$

Applying equation (8) to equation (7), one obtains,

$$Z_{mn} = j \frac{l_m l_n}{144\pi} \omega \mu \rho_m^{c\pm} \cdot \sum_{k=1}^9 \rho_k^{c\pm} G(\mathbf{r}_m^{\pm}, \mathbf{r}_k^{c\pm}) + \rho_k^{c-} G(\mathbf{r}_m^{\pm}, \mathbf{r}_k^{c-}) \pm j \frac{l_m l_n}{36\pi} \frac{1}{\omega \epsilon} \sum_{k=1}^9 G(\mathbf{r}_m^{\pm}, \mathbf{r}_k^{c+}) - G(\mathbf{r}_m^{\pm}, \mathbf{r}_k^{c-}). \quad (9)$$

Equation (9) shows that $Z_{mn} \equiv Z_{mn+} + Z_{mn-}$. Both terms defined in the following way,

$$Z_{mn+} = j \frac{l_m l_n}{144\pi} \omega \mu \sum_{k=1}^9 \rho_m^{c\pm} \cdot \rho_k^{c+} g_m^{\pm}(\mathbf{r}_k^{c+}) \pm j \frac{l_m l_n}{36\pi} \frac{1}{\omega \epsilon} \sum_{k=1}^9 g_m^{\pm}(\mathbf{r}_k^{c+}) \quad (10a)$$

$$Z_{mn-} = j \frac{l_m l_n}{144\pi} \omega \mu \sum_{k=1}^9 \rho_m^{c\pm} \cdot \rho_k^{c-} g_m^{\pm}(\mathbf{r}_k^{c-}) \pm j \frac{l_m l_n}{36\pi} \frac{1}{\omega \epsilon} \sum_{k=1}^9 g_m^{\pm}(\mathbf{r}_k^{c-}), \quad (10b)$$

where $g_m^{\pm}(\mathbf{r}_k^{c\pm}) = G(\mathbf{r}_m^{\pm}, \mathbf{r}_k^{c\pm})$.

Even when the definitions in equation (10) could be trivial, they give the opportunity to fill $[Z]$ using a *triangle-triangle* approach instead of a *edge-edge* approach, making the filling of $[Z]$ faster.

B. Computing the Scattered Field

Once the \mathbf{J}_s has been computed through the MoM equation $[Z][I] = [V]$, the scattered field \mathbf{E}_s must be determined to estimate the RCS $\sigma(\kappa^i, \kappa^s)$. The approach used in this work to compute \mathbf{E}_s is based on the *dipole approximation* (see Fig. 1) [4].

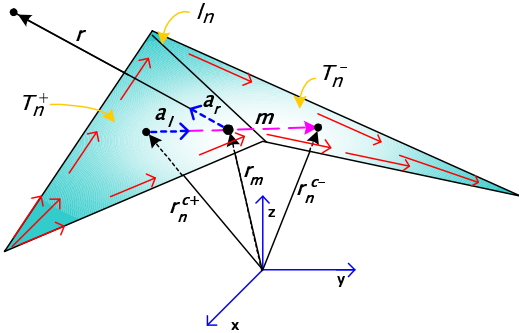


Fig. 1. Equivalent dipole associated with a generic RWG basis function.

This approach states for the particular case that: *The electric field radiated by one single RWG basis function f_n can be approximated at far distances by that one of*

a dipole placed from \mathbf{r}_n^{c+} to \mathbf{r}_n^{c-} with current moment $\mathbf{I}\Delta\mathbf{l} = I_n l_n (\mathbf{r}_n^{c-} - \mathbf{r}_n^{c+})$. Hence, the generalized expression for the \mathbf{E}_s would be the following,

$$\mathbf{E}_s = \sum_{n=1}^N j \kappa \eta \frac{e^{-j\kappa|\mathbf{r}-\mathbf{r}_m|}}{4\pi|\mathbf{r}-\mathbf{r}_m|} (\mathbf{M} - \mathbf{m}) \quad (11)$$

$$\mathbf{H}_s = \sum_{n=1}^N j \kappa \frac{e^{-j\kappa|\mathbf{r}-\mathbf{r}_m|}}{4\pi|\mathbf{r}-\mathbf{r}_m|} (\mathbf{m} \times \mathbf{a}_r), \quad (12)$$

with $\mathbf{M} = (\mathbf{r} \cdot \mathbf{m})/\mathbf{r}^2$, $\mathbf{m} = m \mathbf{a}_l$ according to Fig. 1 and N is the number of edges in the target discretization.

IV. SIMULATION AND RESULTS

In order to evaluate the method explained in the preceding sections, a total of five targets were chosen. These targets have been extensively used by the electromagnetics community as benchmark targets to validate computational electromagnetic methods. To illuminate them, a plane wave is used as the electromagnetic incident field. The parametric equations that model their surfaces can be found in [2]. The chosen targets are presented in Fig. 2.

Figure 3 represents the RCS computed for the metallic sphere as a function of the frequency. It has been performed a frequency sweep in the range of $0.1 \leq \frac{2\pi a}{\lambda} \leq 6$ with $a = 1\text{m.}$, the radius of the sphere. In Fig. 3 the computed RCS is plotted in continuous red line, while the benchmark values already reported in [12] are plotted using blue rhombus.

Figure 4 represents the monostatic RCS computed for the metallic almond at 1.19 GHz. It is decomposed in terms of vertical σ_{VV} and horizontal σ_{HH} polarized radar cross section as a function of incident angle ϕ , starting from 0° and stopping at 180° using 0.125° as a step size. The elevation angle is zero. Zero degrees azimuth corresponds to an incident on the tip. At 1.19 GHz the metallic almond is one wavelength long. The incident angle is the azimuth in a standard spherical coordinate system. The σ_{VV} and σ_{HH} are defined when $|\mathbf{E}_i| = 1$ as,

$$\sigma_{VV} = \lim_{r \rightarrow \infty} 4\pi r^2 |\mathbf{E}_s^V|^2 \quad (13)$$

$$\sigma_{HH} = \lim_{r \rightarrow \infty} 4\pi r^2 |\mathbf{E}_s^H|^2. \quad (14)$$

The computed estimations of vertical and horizontal RCS are plotted in blue and red continuous line, while the benchmark reported in [2] is plotted as rhombus and squares, respectively.

Figure 5 represents the monostatic RCS computed for the metallic single ogive at 1.18 GHz. The RCS for both, the vertical and the horizontal are plotted in dBsm, as a function of the azimuth angle. The elevation angle is zero again. Zero degrees azimuth correspond to an incident normal to a tip of the metallic single ogive. As

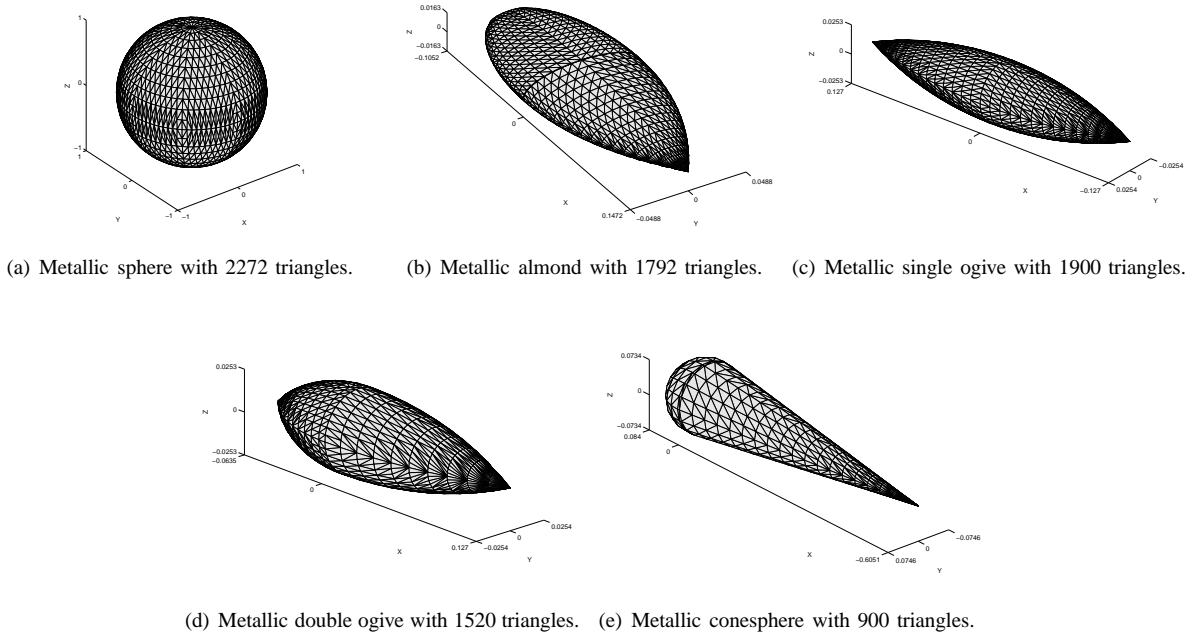


Fig. 2. Chosen Target to validate the method.

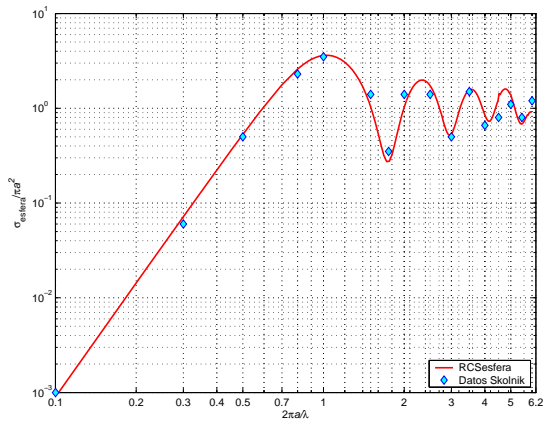


Fig. 3. Estimated RCS for the Metallic Sphere as a function of frequency.

expected, the vertically and horizontally polarized RCS are equal at 0° and 180° of azimuth in Fig. 5. At 1.18 GHz, the metallic single ogive is one wavelength long. The computed estimations for vertical and horizontal RCS are plotted in blue and red continuous line, respectively, while the benchmark is plotted as rhombus and squares.

Figure 6 represents the monostatic RCS computed for the metallic double ogive at 1.57 GHz. It is decomposed in terms of vertical σ_{VV} and horizontal σ_{HH} polarized radar cross section as a function of incident angle ϕ . The RCS for both the vertical and the horizontal polarized RCS are plotted in dBSM. The elevation angle is zero. At 1.57 GHz the metallic double ogive is one wavelength long.

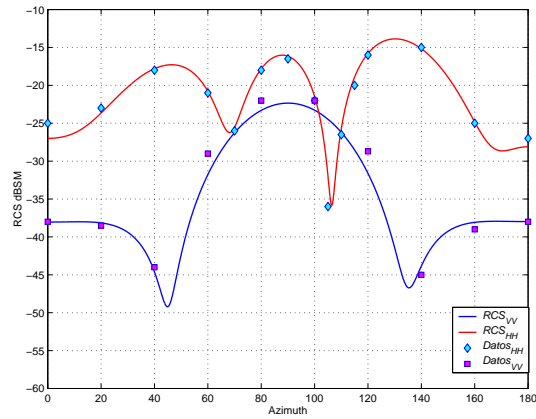


Fig. 4. Estimated σ_{VV} and σ_{HH} for the metallic almond as a function of the incident angle ϕ .

Figure 7 represents the monostatic RCS computed for the metallic cone-sphere at 869 MHz. Both horizontal and vertical polarizations are plotted against azimuthal angle. Zero degrees azimuth is toward the pointed end. At 869 MHz, this target is two wavelength long. Good agreement between the computed RCS and those used as a reference is observed from the previous figure.

V. CONCLUSIONS

In this work, the Method of Moments (MoM) with Rao-Wilton-Glisson basis functions has been used to develop and test a method for the estimation of the radar cross section for metallic conductive object of arbitrary

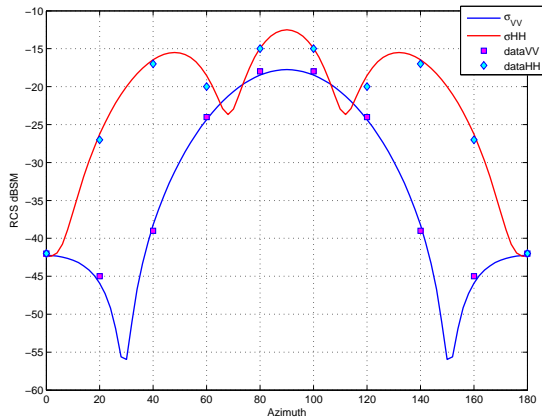


Fig. 5. Estimated σ_{VV} and σ_{HH} for the metallic single ogive as a function of the incident angle ϕ .

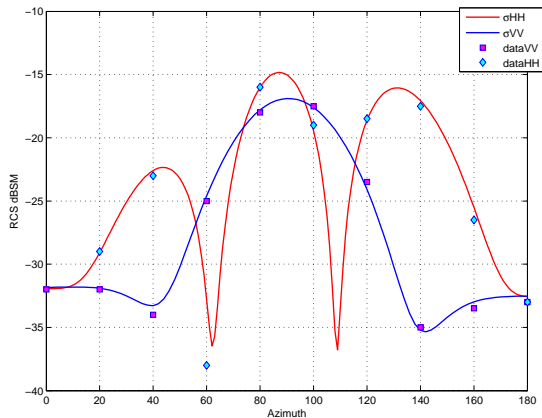


Fig. 6. Estimated σ_{VV} and σ_{HH} for the metallic double ogive as a function of the incident angle ϕ .

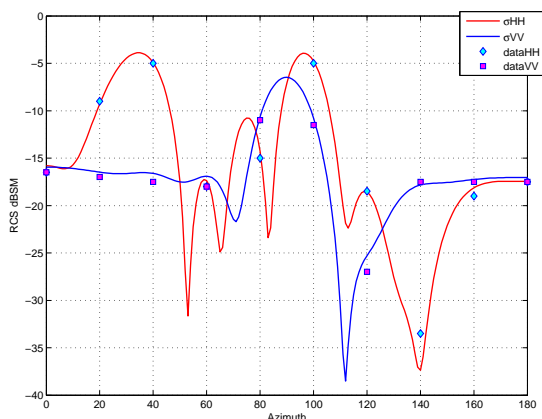


Fig. 7. Estimated σ_{VV} and σ_{HH} for the metallic cone-sphere as a function of the incident angle ϕ .

shape. It has used five extensively used targets to test and validate the method employed. Excellent agreement is seen between the computed results and those already reported in previous investigation. The numerical procedure already described can be easily extended to scatterers of any geometrical shape.

REFERENCES

- [1] R. F. Harrington, *Field Computation by Moment Methods*, MacMillan, U.S.A., New York, 1968.
- [2] J. L. Volakis, "Benchmark radar targets for the validation of computational electromagnetics programs," *IEEE Antennas and Propagation Magazine*, vol. 35, pp. 84–89, 1993.
- [3] S. M. Rao, D. R. Wilton, and A. W. Glisson, "Electromagnetic scattering by surfaces of arbitrary shape," *IEEE Transactions on Antennas and Propagation*, vol. 30, no. 3, pp. 409–418, May 1982.
- [4] S. N. Makarov, *Antenna Modeling EM with MATLAB®*, Wiley-Interscience, 2002.
- [5] R. F. Harrington, *Time-Harmonic Electromagnetics Fields*, McGraw-Hill, U.S.A., 1961.
- [6] K. F. Warnick, "Computational electromagnetics course notes," <http://www.ee.byu.edu/faculty/warnick/>, January 2004.
- [7] F. G. Tricomi, *Integral Equations*, Interscience Publishers, Inc., 1957.
- [8] T. K. Sarkar, "A note on the choice weighting functions in the method of moments," *IEEE Transactions on Antennas and Propagation*, vol. 33, no. 4, pp. 436–441, April 1985.
- [9] J. S. Savage and A. F. Peterson, "Quadrature rules for numerical integration and tetrahedra," *IEEE Antennas and Propagation Magazine*, vol. 38, no. 3, pp. 100–102, June 1996.
- [10] R. D. Graglia, "On the numerical integration of the linear shape functions times the 3-d green's function or its gradient on a plane triangle," *IEEE Transactions on Antennas and Propagation*, vol. 41, no. 10, pp. 1448–1455, October 1993.
- [11] Y. Kamen and L. Shirman, "Triangle rendering using adaptive subdivision," *IEEE Computer Graphics and Applications*, pp. 95–103, March/April 1998.
- [12] M. I. Skolnik, *Introduction to Radar Systems*, McGraw Hill, 1980.



D. J. Duque received his degree in electrical engineering from the University of Carabobo in Venezuela in 2005. In 2007 he completed his M.Sc from both the Universitat Politècnica de Catalunya in Spain and the Politecnico di Torino in Italy. He is currently working toward his PhD in Applied Electromagnetic at the Technische Universiteit Eindhoven in the Netherlands. His research interests include Antenna Design, Electromagnetics Theory and its computational aspects.



G. Carvajal received her degree of Electrical Engineer in 2005 at University of Carabobo (Venezuela). In 2007 she finished her master's studies from the European double degree master program MERIT, at Universitat Politècnica de Catalunya (Spain) and Politécnico di Torino (Italy). Currently she is pursuing the doctoral degree at the Department of Radio and Space Science of Chalmers University of Technology (Sweden). Her principal fields of interests for research include remote sensing and applied electromagnetism.



A. J. Zozaya received the electronic engineering degree from the Polytechnic University of the National Armed Forces (IUP-FAN), Maracay, Venezuela, in 1991 and the Doctor degree from the Polytechnic University of Catalonia (UPC), Barcelona, Spain, in 2002. He joined the Electronic and Communication Department of the University of Carabobo, Valencia, Venezuela, in 1994 where he is currently an Associated Professor and the Head of the Applied Electromagnetic Laboratory. His research interests include RF power amplifier linearization techniques and computational electromagnetic.

A Fast Spectral Domain Solver for the Characterization of Larger Microwave Structures in Multilayered Environments

T. Vaupel

Research Institute for High Frequency Physics and Radar Techniques, FGAN E.V.
Neuenahrer Str. 20, 53343 Wachtberg, Germany
vaupel@fgan.de

Abstract – A new kind of fast spectral domain method is presented for the solution of integral equations related to planar structures embedded in multilayered media. It is based on the well-known spectral domain Green's function for multilayered media to construct a diagonalized translation operator on the Cartesian wavenumber plane to efficiently evaluate the matrix-vector multiplications during the iterative solution process. This allows fast integral equation solutions for arbitrary layer arrangements similar as with fast multipole methods (FMM) for structures in free space. The convergence properties of the involved spectral domain integrals related to the group interactions are drastically improved by different integration path deformation strategies combined with enhanced Legendre-Filon and Laguerre quadrature techniques. Together with the use of diakoptic preconditioners, only a small number of iterations are required with the pertinent Krylov subspace solvers, typically leading to a significantly higher computational performance than comparable commercial integral equation solvers.

Keywords: Planar-3D-structures, multilayered media, fast integral equation solver, adaptive integration path deformation, extended quadrature techniques, and diakoptic preconditioner.

I. INTRODUCTION

A large class of structures like microstrip or combined slot/microstrip configurations can be modeled as so-called Planar-3D structures embedded within multilayered medias. Using the method of moments (MoM) in combination with the Green's function of the multilayered environment reduces the discretization effort to the strip and/or slot areas of the structure. However, due to the growing complexity of microwave circuits and antennas, the number of unknowns can easily become prohibitive, if standard MoM implementations are applied. To overcome the large computational effort of the standard MoM, different fast integral equation solvers for microstrip structures have been proposed. First implementations were based on a combination of the conjugate gradient method with the fast Fourier transform (CG-FFT) for structures in free space [1,2] and its extension to microstrip structures

[3]. A further extension using the discrete complex-image technique for the characterization of the layered medium was presented in [4]. Other approaches make use of the adaptive integral method (AIM) for accelerating the matrix-vector products combined as well with the complex-image technique [5]. Methods based on the fast multipole method (FMM) and complex-image techniques are given in [6,7]. However, the numerical efficiency of the complex-image technique may strongly depend on the number of required complex images. Another approach employing a fast multipole method (FMM) can be found in [8] but is restricted to a thin grounded dielectric slab. These drawbacks are partly overcome by the fast inhomogeneous plane wave algorithm, presented in [9], which is well suited for scatterers located above an arbitrary multilayered medium or for buried objects.

In contrast to these methods, an approach completely based on the spectral domain Green's function of the multilayered medium is presented in this paper. The corresponding Green's function can be easily computed for arbitrary layer/metallization arrangements with the same numerical performance and accuracy, even for problematic configurations like e.g. thin glue layers embedded in much thicker sub/superstrate environments. The method is based on the construction of a diagonalized translation operator on the cartesian wavenumber plane to compute the far interactions between non-overlapping groups of basis functions. The interactions of near-neighbour groups are computed using the matrix entries of the conventional MoM analogously to other fast integral equation formulations. The far interactions are formulated as spectral domain integrals but have bad convergence properties if only real cartesian wavenumbers are used. Thus, an extension on complex integration paths is used on one hand to circumvent singularities of the integrand [11] and on the other hand to get an exponential decay of the integrands. To achieve this decay, the proposals given in [12] are modified in such a way that the employed integration paths do not cross any singularities of the integrands. However, for large group separations the numerical efficiency is still affected by an oscillatory behavior of the integrands. These oscillations are compensated with some modifications of a Legendre-Filon quadrature given in [11] as well. Furthermore, the exponential decay

rate on the modified integration paths depends on the lateral distance of the participated groups which makes it difficult to account for the fast decay rate concerning group interactions with large lateral distances. Therefore an extended Laguerre quadrature technique is introduced which provides practically the same decay rate for all group far interactions. The overall performance of this approach is decisively improved by employing Krylov subspace solvers with extended diakoptic preconditioners [13] for the treatment of the linear systems of equations leading to a very fast convergence of the iterative solution process for a large class of structures. Since our method is still a two-level approach, the numerical complexity for the matrix-vector product evaluation reaches $\approx O(N^{1.5})$ with an optimized group size [14] whereas we get roughly $\approx O(N)$ for the storage complexity.

II. FORMULATION

A. General Outline of The Fast Algorithm

In a first step, the structure to be analyzed is decomposed into groups, which comprise typical components like couplers, patches, spiral inductors etc. (see Fig. 1). In this context, also a subsequent partitioning into small squares as in [8] may be applied, but with the risk of dissecting resonant components of the structure such as antenna patches what can severely deteriorate the convergence properties of the method. In this paper the studies are focused on microstrip/stripline structures, which can be characterized with the surface impedance boundary condition on the metallizations,

$$\vec{E}_s(x, y)|_{tan} = Z_F(x, y) \vec{J}_e(x, y) + \vec{E}_i(x, y)|_{tan}. \quad (1)$$

However, the method can also be extended on mixed structures consisting of both microstrip/stripline and coplanar/slotline components as presented in [15]. Based on equation (1), an integral equation for the surface currents can be formulated in the spectral domain,

$$\begin{aligned} & \frac{1}{4\pi^2} \int_{k_y} \int_{k_x} \overleftrightarrow{G}_J^E(k_x, k_y) \cdot \vec{J}_e(k_x, k_y) e^{jk_x x + jk_y y} dk_x dk_y |_{tan} \\ & = Z_F(x, y) \vec{J}_e(x, y) + \vec{E}_i(x, y)|_{tan} \end{aligned} \quad (2)$$

where $\overleftrightarrow{G}_J^E(k_x, k_y)$ and $\vec{J}_e(k_x, k_y)$ are the Fourier transforms of the multilayered medium Green's function and the surface currents, respectively, whereas Z_F is a surface impedance and \vec{E}_i comprises the excitation. The surface currents are discretized with subdomain basis functions \vec{f}_m by,

$$\vec{J}_e(x, y) = \sum_{m=1}^N I_m \vec{f}_m(x, y). \quad (3)$$

At the moment asymmetric rooftop functions arranged on arbitrary nonuniform orthogonal meshes are used, which typically show also a sufficient modeling

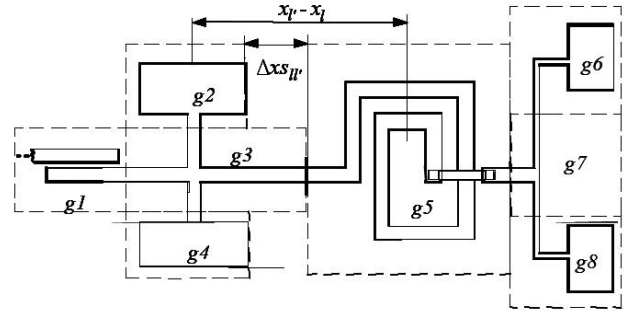


Fig. 1. Section of a typical microstrip structure with group decomposition and numbering.

flexibility for geometries with oblique or curved margins, if suitable edge-meshing techniques are employed [16]. For the solution of the integral equation with the Galerkin testing procedure, equation (2) is multiplied by the basis functions itself. The subsequent integration over these testing functions \vec{f}_n leads to,

$$\begin{aligned} & \int_x \int_y \vec{f}_n(x, y) \cdot \vec{E}_s(x, y) dx dy = \\ & \int_{k_y} \int_{k_x} [\overleftrightarrow{T}_{l'l'}(k_x, k_y) \cdot \vec{F}_m(k_x, k_y)] \cdot \vec{F}_n^*(k_x, k_y) dk_x dk_y \\ & , n \in g_l, m \in g_{l'}, \end{aligned} \quad (4)$$

introducing a spectral domain translation operator between the groups g_l and $g_{l'}$

$$\overleftrightarrow{T}_{l'l'}(k_x, k_y) = \overleftrightarrow{G}_J^E(k_x, k_y) e^{jk_x(x_l - x_{l'})} e^{jk_y(y_l - y_{l'})}. \quad (5)$$

Furthermore,

$$\vec{F}_{l'm}(k_x, k_y) = \int_x \int_y \vec{f}_m(x, y) e^{jk_x(x_{l'} - x)} e^{jk_y(y_{l'} - y)} dx dy \quad (6)$$

is the Fourier transform of the expansion function \vec{f}_m related to the center $\vec{\rho}_{l'} = (x_{l'}, y_{l'})$ of group $g_{l'}$ near this expansion function. Analogously $\vec{F}_{ln}^*(k_x, k_y)$ is the Fourier transform of the test function \vec{f}_n related to the center $\vec{\rho}_l = (x_l, y_l)$ of group g_l near this test function.

To get a fast algorithm for the matrix-vector product evaluation,

$$Z_{far} \cdot \vec{I} = \vec{b}, \quad (7)$$

where Z_{far} is the matrix with the far interactions (not explicitly generated) and a similar efficiency as with standard fast multipole methods (FMM) in free space, the contribution to the elements of the right hand side of equation (7) $\vec{b} = (b_1, \dots, b_n, \dots, b_N)^T$ with regard to the groups g_l and g_l' is carried out by the integral,

$$b_{n,l'l'} = \int_{k_x} \int_{k_y} \vec{F}_{ln}^*(k_x, k_y) \cdot \overleftrightarrow{T}_{l'l'}(k_x, k_y) \cdot \vec{J}_{l'}(k_x, k_y) dk_x dk_y \quad (8)$$

which is evaluated numerically by,

$$b_{n,ll'} \approx \sum_{k_{xi}, k_{yi}} w_{k_{xi}} w_{k_{yi}} \vec{F}_{ln}^*(k_{xi}, k_{yi}) \cdot \overleftrightarrow{T}_{ll'}(k_{xi}, k_{yi}) \cdot \vec{J}_{l'}(k_{xi}, k_{yi}), \quad (9)$$

where k_{xi}, k_{yi} are suited sampling points of the cartesian wavenumber plane and $w_{k_{xi}}, w_{k_{yi}}$ are appropriate integration weights.

In this representation, the spectral current density of all groups $g_{l'}$ with centers $\vec{\rho}_{l'}$ (source groups) is formed in the spectral domain by,

$$\vec{J}_{l'}(k_{xi}, k_{yi}) = \sum_{m \in g_{l'}} I_m \vec{F}_{l'm}(k_{xi}, k_{yi}), \quad l' = 1, \dots, N_g \quad (10)$$

with N_g the number of groups. Equation (10) forms the aggregation process whereas equations (8) and (9) corresponds to the translation and disaggregation step, finally the elements of the complete right hand side of equation (7) are generated by,

$$b_n = \sum_{\substack{l' \neq l + NN \\ l'=1}}^{N_g} b_{n,ll'}, \quad l = 1, \dots, N_g \quad (11)$$

where NN indicates near-neighbour groups.

However, if the spectral domain integrations equation (8) are carried out using standard quadrature techniques with real wavenumbers k_x and k_y , significant convergence problems occur due to integrand singularities, a slow decay and an oscillatory behavior of the integrands. To overcome these drawbacks, at first a special decomposition of the cartesian wavenumber plane is employed.

B. Decomposition of The Cartesian Wavenumber Plane

The decomposition of the cartesian wavenumber plane is shown in Fig. 2 together with the schematical arrangement of the sampling points k_{xi}, k_{yi} . The first quadrant is decomposed into an inner area A_{in} and three outer areas A_{out1} to A_{out3} . The other quadrants are decomposed analogously.

The Green's function contains singularities in terms of branchpoints and poles related to guided waves like surface or parallel plate waves. The localizations of guided wave poles and branchpoints are restricted by $|k_{xp}|, |k_{yp}| < k_0 \sqrt{\epsilon_{r,max}}$, where k_{xp} and k_{yp} are the real locations of the singularities forming concentric rings within the inner areas and $\epsilon_{r,max}$ is the maximum permittivity of all layers. Furthermore, k_{Bx} and k_{By} denote the real locations of the branchpoints.

For the wavenumber k_x , the chosen integration path deformations in the inner areas are sketched in Fig. 3 a). The integration path extends from $-k_i$ on the real axis with a vertical and horizontal path section to $-jk_{xym}$, then through the origin along the branch cuts to $+jk_{xym}$

and finally to $+k_i$ back to the real axis. The choice for k_i is done with a numerical localization algorithm searching for the location $|k_{xpm}|$ of the pole with the largest propagation constant of the corresponding guided wave. Then the value k_i is chosen by $k_i \approx 1.1 \cdot |k_{xpm}|$ leading to a minimization of the inner area extension.

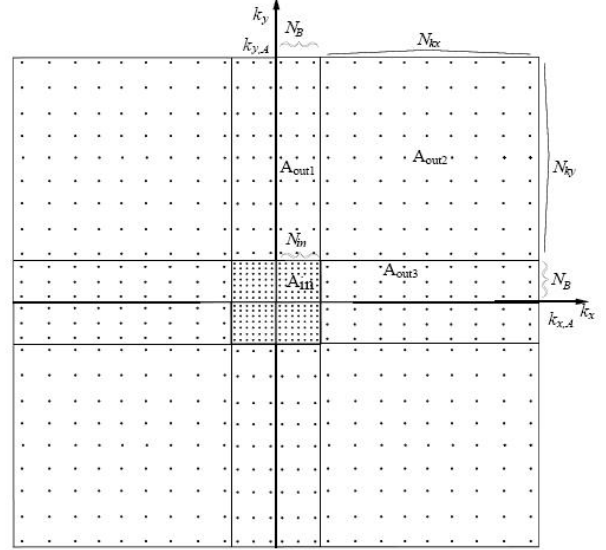


Fig. 2. Decomposition of the cartesian wavenumber plane with schematical distribution of sampling points.

This path is simultaneously used for the k_y -wavenumber.

C. Cancellation of Oscillatory Integrand Behavior

The integration paths in the inner area parallel to the real axis have the parametrization,

$$k_u(t_u) = t_u \pm jk_{xym}, \quad t_u \in [-k_i, k_i], \text{ real}, \quad u = x \text{ or } y. \quad (12)$$

The behavior of the integrands of equation (8) with regard to the variables t_x and t_y and the above integration paths can be well approximated by,

$$\text{INT}_{n,ll'}(t_x, t_y) \approx C_{in} \vec{F}_n^*(t_x, t_y) \cdot \overleftrightarrow{G}_J(t_x, t_y) \cdot \vec{J}_{0l'}(t_x, t_y) e^{jt_x(x_l - x_{l'})} e^{jt_y(y_l - y_{l'})} \quad (13)$$

where \vec{F}_n and $\vec{J}_{0l'}$ are now the Fourier transforms of the basis function f_n and the current distribution $\vec{J}_{l'}$ of group $g_{l'}$ with regard to the origin of the coordinate system (not to the group centers) and a factor C_{in} not depending on t_x and t_y . The terms \vec{F}_n and $\vec{J}_{0l'}$ are actually evaluated in the implementation i.e., the translation operator $T_{ll'}$ is only implicitly involved to emphasize the analogies with fast multipole methods and to represent the integrand behavior.

Thus, the integrand mainly shows an oscillatory behavior due to the both exponentials containing the group center distances $(x_l - x_{l'})$ and $(y_l - y_{l'})$. To largely cancel out these oscillations, the product $\overleftrightarrow{T}_{ll'}$

$(k_x, k_y) \cdot \vec{J}_l(k_x, k_y)$ is multiplied by the compensating exponentials $e^{-jt_x(x_l-x_{l'})}$ and $e^{-jt_y(y_l-y_{l'})}$. To account for these compensative multiplications, specific integration weights w_{txi}^{Leg} , w_{tyi}^{Leg} for the disaggregation process are determined.

If we emphasize on the integration with regard to t_x over an interval $t_x \in [t_{xa}, t_{xb}]$ and $F(t_x)$ is denoted as the smooth part of e.g., the integrand equation (13), we can write,

$$\int_{t_{xa}}^{t_{xb}} F(t_x) e^{jt_x(x_l-x_{l'})} dt_x \approx C_{sc} \sum_{i=0}^{N_{Leg}-1} F(t_{xi}) w_{txi}^{Leg} \quad (14)$$

where the weights w_{txi}^{Leg} of this special quadrature are the solutions of the linear system of equations,

$$\sum_{i=0}^{N_{Leg}-1} p_n(t_i) w_{txi}^{Leg} = \int_{-1}^1 p_n(t) e^{j d t} dt, \quad n = 0, \dots, N_{Leg}-1 \quad (15)$$

with $p_n(t)$ denoting the Legendre polynomials of order n and t_i are the roots of the Legendre polynomial of order N_{Leg} (i.e the number of used sampling points), and $d = (t_{xb} - t_{xa})(x_l - x_{l'})/2$. Furthermore, we have introduced a scaling factor $C_{sc} = \frac{1}{2}(t_{xb} - t_{xa})e^{j\frac{1}{2}(t_{xb}+t_{xa})(x_l-x_{l'})}$. Further details of the derivation and solution of equations (14) and (15) leading to this combined Legendre-Filon quadrature are given in [11]. The integration with regard to k_y is performed analogously.

On the vertical path sections on or parallel to the imaginary axis no oscillations occur, but we have an exponential increasing and decreasing behavior which becomes distinctive for large group distances. Therefore, this behavior is compensated as well by using a slightly modified integration technique as explained above. With these measures the number of sampling points N_{in} in the inner areas can be restricted to about 10-15 for both wavenumbers k_x, k_y using maximum group sizes of a few wavelengths.

D. Integration Path Deformations in The Outer Wavenumber Plane

These integrand oscillations are also present in the outer integration areas, if real wavenumbers k_x, k_y are employed. In this case the integrands of equation (8) behave like,

$$\begin{aligned} \text{INT}_{n,l,l'}(k_x, k_y) &\approx \\ C_{out} \vec{F}_n^*(k_x, k_y) \cdot \overset{\leftarrow E}{G}_J(k_x, k_y) \cdot \vec{J}_{0l'}(k_x, k_y) \\ e^{jk_x(x_l-x_{l'})} e^{jk_y(y_l-y_{l'})}. \end{aligned} \quad (16)$$

Additionally, the Green's functions show a linear growing behavior with $k_x, k_y \rightarrow \infty$, if source and observation points are in the same plane $z = \text{const}$. Thus, convergence of the integrals is only achieved by the decay of

the Fourier transforms of the group current distributions and the test basis functions.

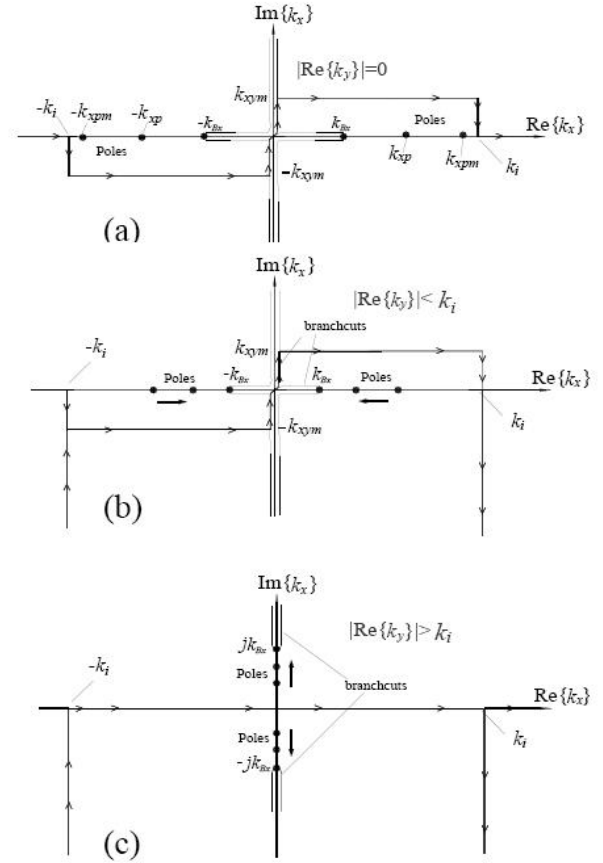


Fig. 3. Employed integration path deformations with singularity locations and migrations.

The overall convergence is therefore typically very poor and additionally depends on the group geometries. To achieve an extensive convergence acceleration, an adapted complex integration path deformation is employed in the outer areas. This integration path deformation depends on the values of the lateral group distances $|(x_l - x_{l'})|$ and $|(y_l - y_{l'})|$.

If $|(x_l - x_{l'})| > |(y_l - y_{l'})|$ is valid as given for the group arrangement in Fig. 4(a), the lateral group distance in x -direction causes the largest oscillations of the integrand equation (16). Choosing a complex integration path for the wavenumber k_x beginning from $k_x = \pm k_i$ according to,

$$k_x(t) = \pm k_i - jt, \quad t \geq 0, \text{ real}, \quad (17)$$

then the corresponding oscillating exponential is transformed into a decaying exponential from this point,

$$e^{jk_x(t)(x_l-x_{l'})} = e^{\pm jk_i(x_l-x_{l'})} e^{-t(x_{l'}-x_l)} \quad (18)$$

provided that $(x_{l'} - x_l) > 0$.

However, it can be shown that an overall decay of the whole integrand equation (16) on the path equation (17) is only given if the group domains do not overlap with regard to this direction i.e., if we have a finite separation with a distance $\Delta x_{s_{ll'}} > 0$ (see Fig. 1 and Fig. 4(a)). As will be shown later, the decay behavior of the integrand equation (16) for larger values t in equation (17) is dominated by the exponential $e^{-t\Delta x_{s_{ll'}}$. Therefore, the following case differentiation is made:

If $|\Delta x_{s_{ll'}}| > |\Delta y_{s_{ll'}}|$ (see Fig. 4(a)), then a complex integration path for k_x is used according to equation (17) whereas k_y remains real in the outer areas.

If $|\Delta y_{s_{ll'}}| > |\Delta x_{s_{ll'}}|$ (see Fig. 4(b)), then the complex integration path for k_y ,

$$k_y(t) = \pm k_i - jt, \quad t \geq 0, \quad \text{real}, \quad (19)$$

is used, whereas k_x remains real, correspondingly the integrand decay is dominated by $e^{-t|\Delta y_{s_{ll'}}|}$ in this case.

If the first case is valid, $\Delta x_{s_{ll'}}$ must not be negative i.e., the observation group must be located left from the source group. Analogously, $\Delta y_{s_{ll'}}$ must not be negative in the second case i.e., the observation group must be located below the source group. If these geometrical configurations are not fulfilled, the roles of source and observation groups are simply exchanged. This means, that in these cases the aggregation step equation (10) extends over the conjugate complex Fourier transforms $\tilde{F}_{ln}^*(k_{xi}, k_{yi})$ whereas the disaggregation step equation (9) is performed with the simple Fourier transforms $\tilde{F}_{lm}(k_{xi}, k_{yi})$.

An overview of the pole and branchpoint migration together with the introduced integration path deformations for the wavenumber k_x is given in Fig. 3(b) and (c). Figure 3(b) shows the circumstances for the case $0 < \text{Re}(k_y) < k_i$. In this case, the poles due to guided waves and the branchpoints $\pm k_{Bx}$ are located near the real axis. Thus, they are circumvented by the rectangularly shaped integration path of the inner areas. Beginning from $k_x = \pm k_i$, the integration paths proceed parallel to the imaginary axis. If $\text{Re}(k_y)$ becomes larger, the poles and branchpoints migrate towards the origin. In the case $\text{Re}(k_y) > k_i$ (Fig. 3(c)) they proceed together with the branchcuts on the imaginary axis. Therefore the rectangularly shaped integration path can be replaced by a path on the real axis in this case. The significant advantage of this choice of path deformation is given by the fact, that no poles and branchcuts are crossed, thus no residue contributions must be considered.

However, despite of the exponential decay behavior achieved by the introduced complex integration paths, an oscillating exponential always remains e.g., in the case $|\Delta x_{s_{ll'}}| > |\Delta y_{s_{ll'}}|$, the term $e^{jk_y(y_l - y_{l'})}$ must be considered. Furthermore, we have a larger number of oscillation cycles in the outer areas compared to the inner areas, since the integration intervals are larger than in the inner areas (see Fig. 1). Applying the Legendre-

Filon quadrature outlined above during the disaggregation process, the exponential $e^{-jk_y(y_n - y_{l'})}$ is used for the compensation of the oscillations with regard to k_y instead of $e^{-jk_y(y_l - y_{l'})}$. Here, $\vec{\rho}_n = (x_n, y_n)$ denotes the lateral location of the individual test basis function $\vec{f}_n(x, y)$ with regard to the origin of the main coordinate system. With this individual treatment of each test function during the disaggregation process, the best oscillation suppression is reached what is especially important for larger groups.

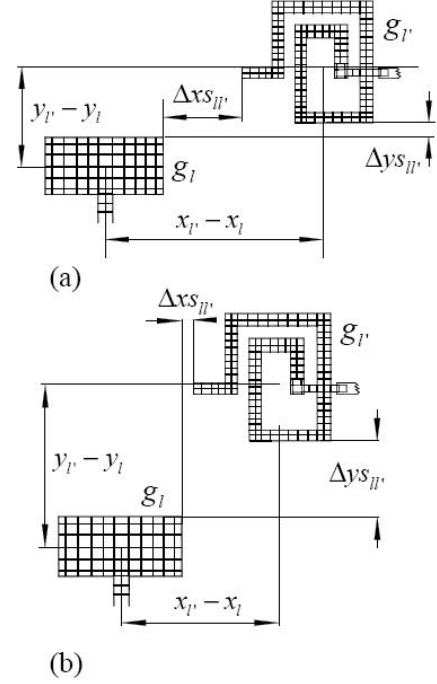


Fig. 4. Group constellations in context with integration path deformations in the outer areas.

The additional effort for computing the quadrature weights for the individual test functions is practically negligible. Although we have no exponential decay for the integrand with regard to the remaining real wavenumber, the upper integration boundary $k_{x,A}, k_{y,A}$ can be restricted to about $15 k_0$ with a number of sampling points N_{k_x}, N_{k_y} of about 5-8.

E. Extended Laguerre Quadrature Applied to The Outer Integrands

Now the integrals over the outer areas already show excellent convergence properties due to the outlined integration path deformations and quadrature techniques. However, the exponential decay rate on the paths equations (17) and (19) strongly depends on the non-overlapping group distances $\Delta x_{s_{ll'}}$ or $\Delta y_{s_{ll'}}$, which is a severe drawback for an integration technique using a rigid sampling point distribution.

The essential decay behavior of the group interaction integrands is demonstrated in Fig. 5 (a), depicting a linear

patch array with 6 patches where each patch is considered as one group. If we consider the interactions of group 1 with the other groups, then the first non-neighbour group is the third one in this case, leading to the minimum non-overlapping group distance $\Delta x_{s_{min}} = \Delta x_{s_{13}}$, providing the slowest decay rate. To analyze the essential decay behavior of the group interaction integrands, the patch currents are described by one symmetric rooftop function for each patch. The exponential behavior of the Fourier transform with regard to k_x of such a rooftop function is simply given by,

$$F_{l'}(k_x) = \left(w - \frac{w}{2} (e^{j\frac{w}{2}k_x} + e^{-j\frac{w}{2}k_x}) \right) e^{jx_{l'}k_x} \quad (20)$$

i.e., the further dependence $\sim \frac{1}{k_x^2}$ is not considered here. The exponential behavior of the interaction integrand of observation group 1 with the other non-neighbour source groups is then defined by $\text{INT}_{1l'}(k_x) = F_1^*(k_x) F_{l'}(k_x)$, $l' = 3, \dots, 6$, i.e., the influence of the Green's function is neglected for this representation. Figure 5(b) shows the behavior of the interaction integrands $\text{INT}_{1l'}(k_x)$ and of the exponential $e^{-k_x \Delta x_{s_{1l'}}$ on the path $k_x = k_i - jt$ with $w = 12$ mm, $\Delta x_{12} = 5$ mm, $f = 10$ GHz and $k_i = \sqrt{2.2}k_0$. All curves are normalized to 0 dB for $t = 0$. As expected it can be recognized that the decay rate of the integrands for small values of t is even larger than the decay rate of the corresponding exponential $e^{-k_x \Delta x_{s_{1l'}}$, but for larger t both expressions quickly show the same decay rate.

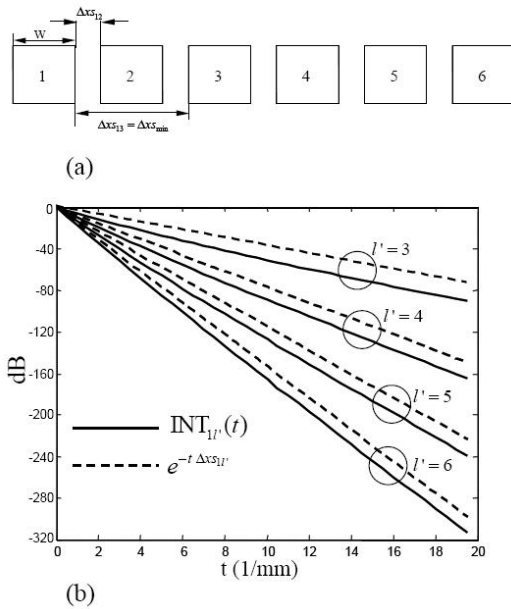


Fig. 5. Linear test array (a) and the decay behavior of the corresponding interaction integrands (b).

If the sampling points for the integration are adjusted to the slowest decay rate with regard to a chosen group decomposition, the integrands with significantly faster decay rates cannot be evaluated with sufficient accuracy

applying these sampling points. To get rid of these different decay rates, the products $\vec{T}_{ll'}(k_x, k_y) \cdot \vec{J}_{l'}(k_x, k_y)$ are multiplied by corresponding increasing exponentials $e^{+t\alpha}$, where for small separations $\alpha = \Delta x_{s_{min}}$ is chosen and $\alpha = \Delta x_{s_{ll'}}$ for all separations larger than $\approx 2\Delta x_{s_{min}}$.

To account for these multiplications, again special integration weights are determined. If we emphasize on the integration with regard to k_x on the path equation (17) and using the substitution $t' = \Delta x_{s_{min}} t$ it can be written,

$$I = \int_0^\infty F(k_x(t)) e^{-\Delta x_{s_{ll'}} t} dt = \frac{1}{\Delta x_{s_{min}}} \int_0^\infty F\left(k_x\left(\frac{t'}{\Delta x_{s_{min}}}\right)\right) e^{-\left(\frac{\Delta x_{s_{add}}}{\Delta x_{s_{min}}} + 1\right) t'} dt' \approx \frac{1}{\Delta x_{s_{min}}} \sum_{s=0}^{N_{Lag}-1} F\left(k_x\left(\frac{t_s}{\Delta x_{s_{min}}}\right)\right) w_s^{Lag} \quad (21)$$

$F(k_x)$ denotes the smooth decaying part of the integrand and $\Delta x_{s_{ll'}} = \Delta x_{s_{min}} + \Delta x_{s_{add}}$ was used. In the case of a group interaction with the minimum separation $\Delta x_{s_{min}}$ (i.e., $\Delta x_{s_{add}} = 0$), the exponential of the second integral in equation (21) becomes $e^{-t'}$. Such weighting function is related with the standard Laguerre quadrature, thus the weights w_s^{Lag} can be directly derived with this quadrature rule in this case. The sampling points t_s are the roots of the Laguerre polynomial of order N_{Lag} . However, this quadrature becomes less accurate for separations $\Delta x_{ll'}$ larger than about $2\Delta x_{s_{min}}$. For these cases, extended Laguerre quadrature weights are computed, using a similar variational approach as for the outlined Legendre-Filon quadrature. This leads to the linear system of equations,

$$\sum_{s=0}^{N_{Lag}-1} l_n(t_s) w_s^{Lag} = \int_0^\infty l_n(t) e^{-\left(\frac{\Delta x_{s_{add}}}{\Delta x_{s_{min}}} + 1\right) t} dt, \quad n = 0, \dots, N_{Lag} - 1 \quad (22)$$

where $l_n(t)$ are the Laguerre polynomials of order n using the same sampling points t_s as the standard Laguerre quadrature. The right hand side is efficiently computed by means of the integral $\int_0^\infty t^n e^{-\alpha t} dt = n!/\alpha^{n+1}$. By this quadrature technique, all contributions with exponential decay can be evaluated with the same sampling points and accuracy. The number of necessary sampling points N_{k_x} and N_{k_y} on the paths equations (17) and (19) amounts to approx. 5–7 and can be further reduced for interactions with large separations.

F. Near-Zone Matrix and Preconditioning Strategies

While the interactions between the well separated groups can be computed by the methods described above, the interactions between near-neighbour groups must be evaluated directly by computing the matrix entries of the standard MoM. This is done with the methods outlined in [11] based on an asymptotic extraction technique for convergence acceleration. However, it can be noted that the outlined integration techniques given above can also be applied for the computation of the standard MoM matrix entries with high accuracy and efficiency, if the participated basis functions do not overlap.

The entries of this near-zone matrix Z_{near} are stored in the compressed sparse row (CSR) format (see e.g., [17]). This near-zone matrix is also used to build a preconditioner for the pertinent Krylov subspace solvers. At first, a Transpose Free Quasi Minimum Residual (TFQMR) method was employed [18], showing already very good convergence properties, but the currently implemented Generalized Minimum Residual (GMRES)-solver shows so far the best convergence for a large class of structures.

If we have a pure microstrip or aperture structure, the system matrix is symmetric, thus a sparse Cholesky factorization of the near-zone matrix is applied,

$$Z_{near} = C \cdot C^T. \quad (23)$$

For this factorization a special kind of sparse LDL^T -factorization based on a pure row-wise access on the matrix entries is used at first. This LDL^T -factorization is subsequently transformed into the desired Cholesky factorization, which is stored in the modified sparse row (MSR) format. Furthermore, matrix fill-ins are permitted during the factorization process, whereas the number of these matrix fill-ins is reduced by a proper group numbering in advance. The localizations of the fill-ins are determined during a symbolic factorization to guarantee a correct storage allocation.

This Cholesky factorization is subsequently used as a split preconditioner according to,

$$C^{-1} Z C^{-T} C^T \cdot \vec{I} = C^{-1} \cdot U, \quad Z = Z_{far} + Z_{near}. \quad (24)$$

The required forward/backward substitutions to carry out equation (24) are as well implemented using a pure row-wise access on the entries of the Cholesky factorization. Since the groups can also be interpreted as so-called macro basis functions of the structure within diakoptic strategies [13,19], we refer to the explained techniques also as a diakoptic preconditioning.

III. APPLICATIONS

For a first validation, the bistatic radar cross section (RCS) of a 4×4 patch array on a grounded dielectric slab is analyzed (Fig. 6(a)).

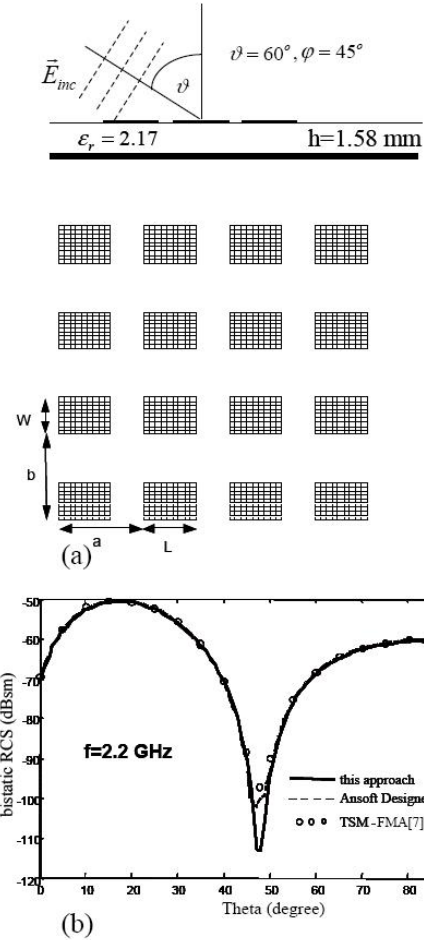


Fig. 6. Reflectarray (a) and bistatic RCS computations with different methods (b); $a=b=60.0$ mm, $W=26.0$ mm, $L=36.6$ mm.

Similar as in [8], where the structure was examined at first, a homogeneous discretization was chosen with 2300 unknowns altogether. Each patch was considered as one group. Additionally, the structure was analyzed with the Planar-EM solver of Ansoft Designer with about the same number of RWG (Rao Wilton Glisson) basis functions.

The comparison of the bistatic RCS ($\vartheta - \vartheta$) in Fig. 6(b) shows a very good agreement, only the behavior around the minimum of the RCS at about 48 degrees is predicted slightly different by the three methods. However, the overall computation time of this approach amounts to only 2.5 sec. (3 GHz AMD-PC, used for all examples), whereas more than 30 sec. are needed with the solver of Ansoft Designer on the same computer.

As a second example a microstrip antenna array with feeding network consisting of up to four subarrays with 32 elements is considered. Figure 7 (a) shows the structure geometry and the discretization using an edge-meshing for the patches. Further details of the geometry parameters are given in [11,5]. Each subarray was decomposed into 9 groups as indicated by the dashed rectangles by hands

of the first subarray. Figure 7 (b) shows the current distribution at 9.42 GHz.

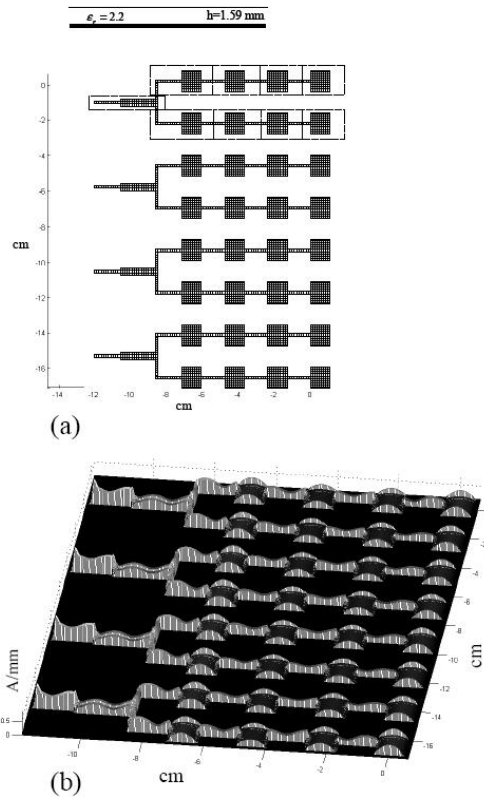


Fig. 7. Microstrip antenna array (a) with computed current distribution (b).

For results and performance comparisons, the structure was analyzed with Ansoft Designer as well using about the same number of unknowns. Using our diakoptic preconditioner and GMRES implementation, only 2-3 iterations are needed for a residual error of less than 1 percent. Table 1 shows the comparison of the overall solution time in seconds depending on the number of subarrays and unknowns N .

Table 1. Comparison of the numerical performance for a microstrip antenna array.

subarrays (N)	This approach	Ansoft Designer
1 (1625)	5	19
2 (3250)	12	55
3 (4875)	24	115
4 (6500)	38	131(fast solver)

It can be recognized that this approach is up to more than four times faster than the simulations of Ansoft Designer. In the case of four subarrays, Ansoft Designer makes use of a fast matrix compression algorithm using multilevel strategies, based on a singular value decomposition (SVD) [20] indicated with fast solver in the table. However,

the application of this method is only advantageous for problems with more than 5000 unknowns, whereas the approach proposed in this paper shows an increased efficiency already for small problems.

Figure 8 shows the results for the far-field antenna patterns. Whereas the E-plane patterns show slight differences between both methods, the H-plane patterns are nearly congruent except for minor deviations at ± 40 degrees. However, the pattern results are also influenced by the meshing modalities to some extend.

As a final example, the monostatic RCS of larger reflectarrays is examined, first characterized in [21] with an entire domain approach. Figure 9 shows the largest array with 11x11 patches together with the used discretization of 17182 unknowns and a typical group decomposition indicated by the dashed rectangles. For an accurate current description, again an edge-meshing was applied.

A comparison of the numerical performance of this approach and Ansoft Designer in terms of overall solution time in seconds is given in Table 2.

Table 2. Comparison of the numerical performance for two reflectarrays.

array type (N)	This approach	Ansoft Designer
7x7 (6958)	12-25	138 (fast solver)
11x11 (17182)	60-139	650 (fast solver)

However, for the fast spectral domain solver the necessary number of iterations and therefore the solution time depends on frequency, whereas nearly the same time is needed by Ansoft Designer for all frequency points. For the fast spectral domain approach, the worst convergence appears at the resonance frequencies with 4-6 necessary iterations, whereas for the remaining frequencies only 2-3 iterations are required for a residual error of less than 1 percent. Although the fast spectral domain approach is currently based only on a two-level strategy, it is up to one magnitude faster than the multilevel algorithms of Ansoft Designer.

The results for the monostatic RCS ($\vartheta - \vartheta$) are given in Fig. 10(a) for the three methods. The curves of this approach and Ansoft Designer are nearly congruent, whereas slight differences are observed for the entire domain method especially at the first patch resonance around 2.71 GHz and the minimum at about 3.25 GHz. Due to the incident angle of $\varphi = 45^\circ$ of the exciting plane wave, both patch resonances are excited as illustrated by hands of the current distribution (this approach) in Fig. 10(b) (first resonance) and Fig. 10(c) (second resonance).

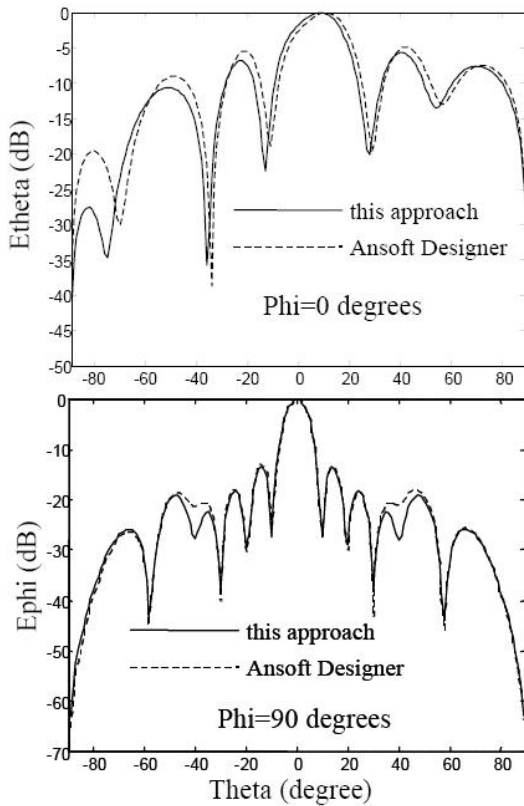


Fig. 8. Far-field pattern comparison for the antenna array of Fig. 7.

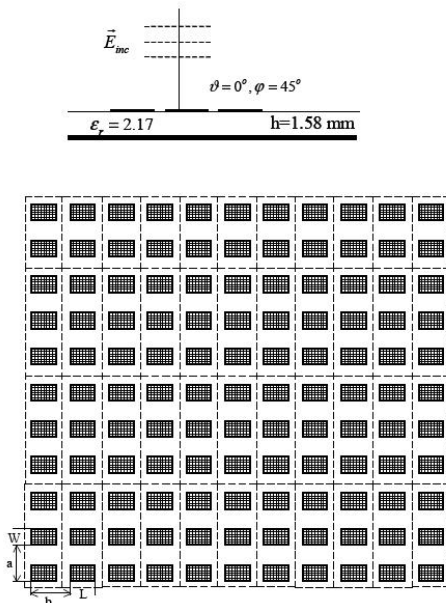


Fig. 9. Reflectarray with 11x11 patches with discretization and group decomposition; $a=b=55.517$ mm, $W=26.0$ mm, $L=36.6$ mm.

The detailed numerical behavior of the fast spectral domain solver is given in Fig. 11 based on computations

of reflectarrays of 3x3 elements up to 11x11 elements with three iterations. Additionally the behavior of Ansoft Designer is outlined. As indicated in the diagrams, Ansoft Designer uses a standard MoM up to 5000 unknowns (6x6-array) and switches over to its fast matrix compression algorithm (fast SVD solver) beginning with the 7x7-reflectarray. According to [20], the numerical complexity of this fast SVD solver should reach $O(N \log N)$ concerning the matrix-vector product evaluation (Fig. 11(a)).

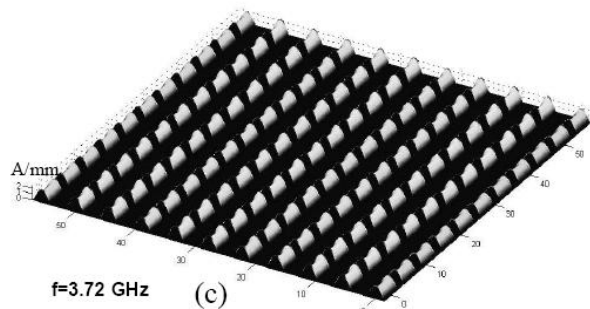
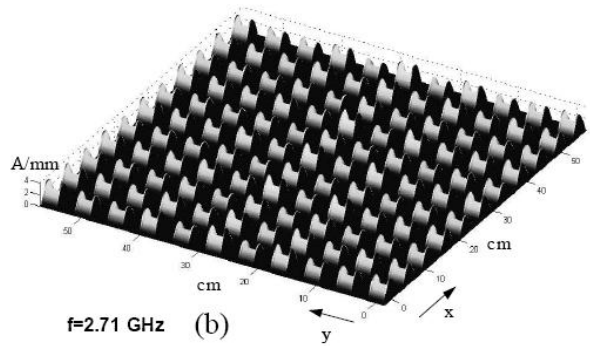
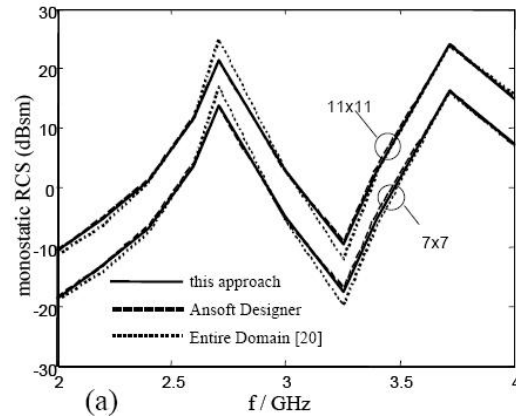


Fig. 10. Comparison of the monostatic RCS of the 11x11 reflectarray (Fig. 9) and a 7x7 reflectarray computed with different methods (a). Computed current distribution at the first (b) and second patch resonance (c).

Since the necessary number of iterations increases noticeably with increasing number of unknowns, the overall numerical complexity of Ansoft Designer (solid line) is obviously larger than $O(N \log N)$. In contrast to this, the number of necessary iterations remains roughly constant

using the fast spectral domain solver, thus the complexity is only slightly higher than $O(N^{1.5})$. This slightly higher complexity is caused by the additional computation of the sparse Cholesky factorization and the forward-backward substitutions in conjunction with the employment of the diakoptic preconditioning. Figure 11(b) shows the memory requirements of both approaches. Whereas the storage complexity of this approach is slightly higher than $O(N)$, the memory requirement of Ansoft Designer shows a quite complicated behavior, but is typically significantly higher than observed with this approach.

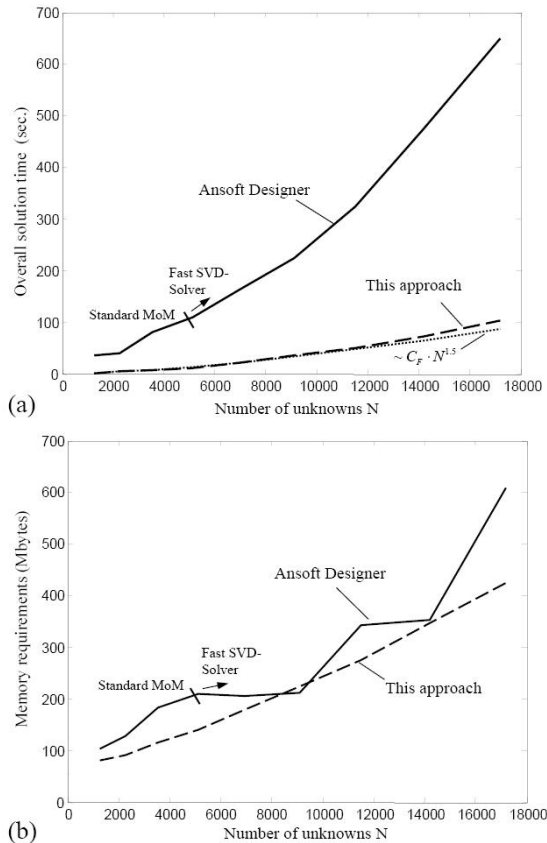


Fig. 11. Comparison of the overall computation time versus number of unknowns (a); Behavior of the storage requirements (b).

The same structures were also analyzed in [7] with a fast multipole approach based on a modified complex discrete image method using a Pentium IV 2.4 GHz PC. In [7], a 3×3 and a 7×7 array with 1737 and 8428 unknowns was computed with 0.6 seconds and 7.49 seconds per iteration, respectively. If we consider the lower clock rate of the computer used in [7], this would result in roughly the same computational effort with 0.54 seconds and 7.47 seconds per iteration using this approach and the same number of unknowns.

IV. CONCLUSIONS

This paper has introduced a new kind of fast spectral domain solver for the characterization of larger microwave structures embedded in arbitrary multilayered media with a similar numerical complexity than fast multipole methods for structures in free space. The group interactions within the fast matrix-vector product computations are evaluated in the cartesian wavenumber plane, where adaptive integration path deformations and enhanced integration techniques such as higher-order Legendre-Filon and extended Laguerre quadrature rules lead to a high accuracy with a low integration effort. Together with diakoptic preconditioning techniques, a fast convergence of the pertinent Krylov subspace solvers is achieved, leading to a very good overall numerical performance of the whole framework. This is demonstrated by means of several applications and comparisons with other solvers, showing a significantly higher computational performance than a comparable commercial software package whereas a similar performance is observed in comparison with a fast multipole method modified for the treatment of multilayered media. The next investigations aim for a substantial reduction of quadrature points by an optimization of the integration path deformations and a further improved treatment of the evanescent wave contributions.

REFERENCES

- [1] T. K. Sarkar, E. Arvas, and S. S. Rao, "Application of FFT and conjugate gradient method for the solution of electromagnetic radiation from electrically large and small conducting bodies," *IEEE Trans. Microwave Theory Tech.*, vol. 34, pp. 635–640, May 1986.
- [2] M. F. Catedra, J. G. Cuevas, and L. Nuno, "A Scheme to Analyze Conducting Plates of Resonant Size Using the Conjugate-Gradient Method and the Fast Fourier Transform," *IEEE Trans. Antennas Propagat.*, vol. 36, no. 12, pp. 1744–1752, Dec. 1988.
- [3] J. Basterrechea and M. F. Catedra, "Electromagnetic Analysis of Complex Microstrip Structures Using a CG-FFT scheme," *IEEE MTT-S Symp. Dig.*, vol. 35, no. 8, pp. 991–996, Aug. 1987.
- [4] Y. Zhuang, K.-L. Wu, C. Wu, and J. Litva, "A combined full-wave CG-FFT method for rigorous analysis of large microstrip antenna arrays," *IEEE Trans. Antennas Propagat.*, vol. 44, no. 1, pp. 102–109, Jan. 1996.
- [5] F. Ling, C.-F. Wang, and J.-M. Jin, "An efficient algorithm for analyzing large-scale microstrip structures using adaptive integral method combined with discrete complex-image method," *IEEE Trans. Microwave Theory Tech.*, vol. 48, pp. 832–838, May 2000.

- [6] P. A. Macdonald and T. Itoh, "Fast simulation of microstrip structures using the fast multipole method," *Int. J. Numer. Modell. Electron. Networks Devices Fields*, no. 9, pp. 345–357, 1996.
- [7] J. X. Wan, T. M. Xiang, and C. H. Liang, "The fast multipole algorithm for analysis of large-scale microstrip antenna arrays," *Progress in Electromagnetic Research*, Pier 49, pp. 239–255, 2004.
- [8] J.-S. Zhao, W. C. Chew, C.-C. Lu, E. Michielssen, and J. Song, "Thin-stratified medium fast-multipole algorithm for solving microstrip structures," *IEEE Trans. Microwave Theory Tech.*, vol. 46, no. 4, pp. 395–403, April 1998.
- [9] B. Hu and W. C. Chew, "Fast inhomogeneous plane wave algorithm for electromagnetic solutions in layered medium structures: Two dimensional case," *Radio Science*, vol. 35, no. 1, pp. 31–43, Jan.-Feb. 2000.
- [10] D. V. Ginste, E. Michielssen, F. Olyslager, and D. De Zutter, "An efficient perfectly matched layer based multilevel fast multipole algorithm for large planar microwave structures," *IEEE Trans. Antennas Propagat.*, vol. 54, no. 5, pp. 1538–1548, May 2006.
- [11] T. Vaupel, T. F. Eibert, and V. Hansen, "Spectral domain analysis of large (M)MIC-structures using novel quadrature methods," *Int. Journal of Num. Modelling: Electronic Networks, Devices and Fields*, Jan.-Febr., pp. 23–38, 2005.
- [12] M. S. Garino, G. Vecchi, and M. Orefice, "Efficient spectral evaluation of mutual coupling between planar antennas," *Radio Science*, vol. 35, no. 2, pp. 511–523, March-April 2000.
- [13] T. Vaupel, T. F. Eibert, and V. Hansen, "Diakoptic basis function grouping techniques applied to the method of moment solution of (M)MIC-structures," *IEEE AP Symposium Digest 2003*, Columbus, Ohio, vol. 2, pp. 1059–1062.
- [14] W. C. Chew, J.-M. Jin, E. Michielssen, and J. Song, *Fast and Efficient Algorithms in Computational Electromagnetics*, Boston, MA: Artech House, 2001.
- [15] T. Vaupel and V. Hansen, "Electrodynamic analysis of combined microstrip and coplanar/slotline structures with 3-D components based on a surface/volume integral-equation approach," *IEEE Trans. Microwave Theory Tech.*, vol. 47, no. 9, pp. 1788–1800, Sep. 1999.
- [16] T. Vaupel and T. F. Eibert, "Recent developments and applications of a spectral domain planar-3D solver," *4th European Workshop on Conformal Antennas*, Stockholm, Sweden, pp. 71–74, May 23-24 2005.
- [17] Y. Saad, *Iterative methods for sparse linear systems*. SIAM books, 2nd edition, 2000.
- [18] R. W. Freund, "Conjugate gradient-type methods for linear systems with complex symmetric coefficient matrices," *SIAM J. Sci. Stat. Comput.*, vol. 13, no. 2, pp. 425–448, especially p. 429, Jan. 1992.
- [19] S. Ooms and D. De Zutter, "A new iterative diakoptics-based multilevel moments method for planar circuits," *IEEE Trans. Microwave Theory Tech.*, vol. 46, no. 3, pp. 280–291, March 1998.
- [20] S. Kapur and D. Long, "IES³: A fast integral equation solver for efficient 3-Dimensional extraction," *IEEE/ACM International Conference on Computer-Aided Design*, pp. 448–455, Nov. 1997.
- [21] A. S. King and W. J. Bow, "Scattering from a finite array of microstrip patches," *IEEE Trans. Antennas Propagat.*, vol. 40, no. 7, pp. 770–774, July 1992.

An Adaptive Approximate Inverse-Based Preconditioner Combined with the Fast Multipole Method for Solving Dense Linear Systems in Electromagnetic Scattering

B. Carpentieri

Institute for Mathematics and Scientific Computing, Karl-Franzens University,
A-8010 Graz, Austria
bruno.carpentieri@uni-graz.at

Abstract – We discuss preconditioning strategies for solving large Electric Field Integral Equation systems. We consider several algebraic preconditioners for solving the dense linear system arising from the Galerkin discretization of the pertinent integral equation. We show that approximate inverse methods based on Frobenius-norm minimization techniques can be very effective to reduce the number of iterations of Krylov subspace solvers for this problem class. We describe the implementation of the preconditioner within the Fast Multipole Algorithm and we illustrate how to reduce the construction cost by using static pattern selection strategies. Finally, we present deflating techniques based on low-rank matrix updates to enhance the robustness of the approximate inverse on tough problems. Experiments are reported on the numerical behavior of the proposed method on a set of realistic industrial problems.

Keywords: spectral corrections, electromagnetic scattering applications, and Frobenius-norm minimization method.

I. INTRODUCTION

In this study we consider the scattering problem from a perfectly conducting object Ω with boundary Γ and assume that the domain Ω is illuminated by an incident plane wave $(\vec{E}_{inc}, \vec{H}_{inc})$ of angular frequency $\omega = ck = 2\pi c/\lambda$, where the constant c is the speed of light, k is the wavenumber and $\lambda = c/f$ is the wavelength (f is the frequency). We concentrate our attention on the Electric Field Integral Equation (EFIE) formulation that reads as: find the surface current \vec{j} such that for all tangential test functions \vec{j}^t , we have,

$$\begin{aligned} \int_{\Gamma} \int_{\Gamma} G(|y-x|) \left(\vec{j}(x) \cdot \vec{j}^t(y) \right. \\ \left. - \frac{1}{k^2} \text{div}_{\Gamma} \vec{j}(x) \cdot \text{div}_{\Gamma} \vec{j}^t(y) \right) dx dy \\ = \frac{i}{kZ_0} \int_{\Gamma} \vec{E}_{inc}(x) \cdot \vec{j}^t(x) dx. \quad (1) \end{aligned}$$

In equation (1) we denote by $G(|y-x|) = \frac{e^{ik|y-x|}}{4\pi|y-x|}$

the Green's function and by $Z_0 = \sqrt{\mu_0/\epsilon_0}$ the characteristic impedance of vacuum (ϵ is the electric permittivity and μ the magnetic permeability). This formulation is the only one that can be used to model arbitrary geometries, including those with cavities, disconnected parts, breaks on the surface and is the most difficult to solve by iterative methods. However, the solution techniques described in this paper are applicable to other integral formulations as well, such as the Combined Field Integral Equation (CFIE) and the Magnetic Field Integral Equation (MFIE) [1]. The Galerkin discretization of equation (1) leads to dense and complex linear systems of equations,

$$Ax = b \quad (2)$$

whose coefficient matrix A is symmetric for EFIE, non-symmetric for CFIE and MFIE. Each entry of the coefficient matrix is associated with the interaction of a pair of triangles in the mesh; the entries of the unknown vector x are associated with the vectorial flux across an edge in the mesh, and the right-hand side b depends on the frequency and the direction of the illuminating wave. Although efficient out-of-core direct solvers have been developed for this problem class [2, 3], the huge storage requirement remains the main bottleneck to the viability of integral equation methods for solving high-frequency scattering problems in electromagnetism. The use of iterative methods can solve the memory limits of direct solvers but their success depends much on the underlying integral formulation. The CFIE formulation gives rise to well conditioned systems, and the number of iterations of nonsymmetric Krylov solvers scale as $\mathcal{O}(n^{0.25})$. On EFIE, Krylov methods scale as $\mathcal{O}(n^{0.5})$, thus preconditioning is mandatory to use.

II. SOLUTION TECHNIQUES

The design of robust preconditioners for boundary integral equations can be challenging; many important research papers (see e.g. [4–7]) have addressed this issue in recent years. Simple preconditioners like the diagonal of A , diagonal blocks, or a band can be effective only when the coefficient matrix has some degree of diagonal

dominance depending on the integral formulation. Block diagonal preconditioners are generally more robust than their point-wise counterparts, but may require matrix permutations or renumbering of the grid points to cluster the large entries close to the diagonal.

In Table 1 we report on experiments with various algebraic preconditioners on a sphere of 1 meter length illuminated at 190 MHz, modeled using *EFIE*. The mesh is depicted in Fig. 1. Although the size is small, the problem is representative of realistic electromagnetic scattering calculations and is difficult to solve for many iterative solvers and preconditioners. Incomplete factorizations can be effective for solving nonsymmetric dense systems [5] and hybrid integral formulations [8], but on the EFIE the triangular factors can be very ill-conditioned due to the indefiniteness of A [9]. Although pivoting may help to circumvent numerical instabilities and improve the performance [10], the parallelization may require significant efforts. Approximate inverse methods are generally less prone to instabilities on indefinite systems and they are inherently parallel. Owing to the rapid decay of the discrete Green’s function, the location of the large entries in the inverse matrix exhibit some structure, and only a very small number of its entries have large magnitude compared to the others that are much smaller. Several preconditioners of this type have been proposed in electromagnetism (see for instance [4, 7, 11–13]). The approximate inverse can be computed in factorized or unfactorized form, depending on the fact that the preconditioner is expressed as a single matrix or as the product of two (or more) matrices. For a small sphere, we display in Fig. 2 the sparsity pattern of A^{-1} (on the left) and L^{-1} , the inverse of its Cholesky factor (on the right), respectively, where all the entries smaller than 5.0×10^{-2} have been dropped after a symmetric scaling such that $\max_i |a_{ji}| = \max_i |\ell_{ji}| = 1$. The inverse factors L^{-1} can be totally unstructured (see Fig. 2(b)), while entries of A^{-1} decay very rapidly far from the diagonal (see Fig. 2(a)).

Table 1. Number of iterations required by Krylov solvers using various preconditioners to reduce the initial residual by six orders of magnitude on a model problem (see Fig. 1).

Precon	GMRES(50)	Bi-CGSTAB	UQMR	TFQMR
M_j	473	257	354	228
<i>SSOR</i>	245	185	281	266
<i>ILU</i> (0)	+500	385	394	439
<i>AINV</i>	+500	+500	+500	+500
<i>SPAI</i>	61	48	93	40

In this work, we describe an algebraic approximate inverse preconditioner based on Frobenius-norm minimization with a static pattern selection strategy for this problem class. The approximate inverse is computed as the matrix M that minimizes the Frobenius-norm of the

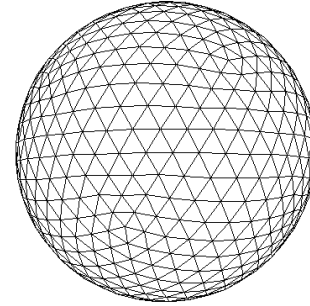


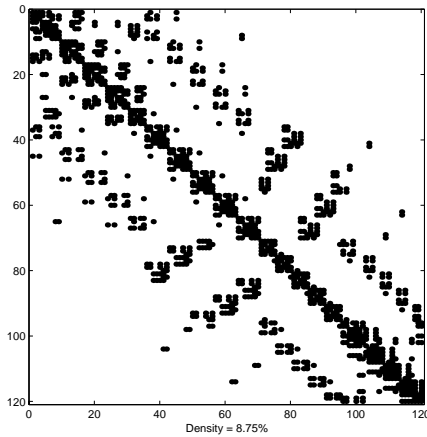
Fig. 1. Model problem, a sphere of 1 meter length, illuminated at 190 MHz. The mesh is discretized with 2430 edges.

error matrix $\|I - AM\|_F$, subject to certain sparsity constraints. The Frobenius norm allows the decoupling of the constrained minimization problems into n independent linear least-squares problems, one for each column (resp. row) of M when preconditioning from the right (resp. left). The independence of these least-squares problems follows immediately from the identity,

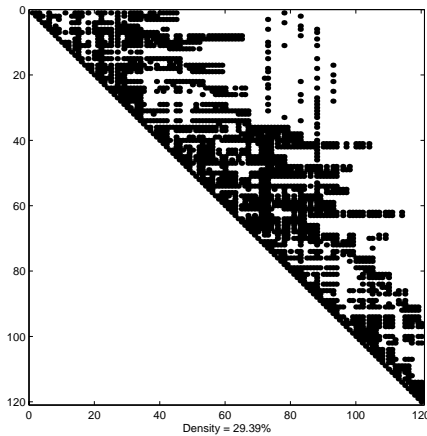
$$\|I - AM\|_F^2 = \sum_{j=1}^n \|e_j - Am_{\bullet j}\|_2^2 \tag{3}$$

where e_j is the j th canonical unit vector and $m_{\bullet j}$ is the column vector representing the j th column of M . Both the construction and the application of M are inherently parallel. The preconditioner is combined with the Multilevel Fast Multipole Algorithm (MLFMA) [14, 15] exploiting the box-wise partitioning of the object available in the MLFMA. MLFMA partitions the mesh of the object by recursive subdivision into disjoint aggregates of small size compared to the wavelength, each roughly formed by an equal number of separate triangles. The number of levels for the box-wise partitioning is determined so that the size of the smallest box is of the order of $\lambda/2$. We skip the description of the MLFMA as it is out of the scope of this paper; details of the parallel implementation we use are found in [16, 17]. The nonzero pattern of the approximate inverse is computed in advance using the sparsity structure of the near-field matrix. More precisely, the structure of the column of the preconditioner associated with a given edge in the mesh is defined by retaining all the edges within the box itself and one level of neighboring boxes [18]. Thus the preconditioner is constructed from a sparse approximation of the dense coefficient matrix and it has a sparse block structure; each block is a dense matrix associated with one box. Indeed the least-squares problems corresponding to edges within the same box are identical because they are defined using the same nonzero structure and the same set of entries of A . It

means that we only have to compute one QR factorization per box. Blocking the columns enables us to reduce the algorithmic complexity of computing M to $\mathcal{O}(n)$. Parallelism can be exploited by assigning disjoint subsets of boxes to different processors and performing the least-squares solutions independently on each processor. We remark that the preconditioner computed by Frobenius-norm minimization is not guaranteed to be symmetric; we may enforce symmetry in M by reflecting at each step the computed entries with respect to the diagonal, and then solving a reduced least-squares problem to compute the remaining entries below the diagonal.



(a) Sparsity pattern of $\text{sparsified}(A^{-1})$.



(b) Sparsity pattern of $\text{sparsified}(L^{-1})$.

Fig. 2. Sparsity patterns of the inverse of A (on the left) and of the inverse of its lower triangular factor (on the right), where all the entries whose relative magnitude is smaller than 5.0×10^{-2} are dropped. The test problem, representative of the general trend, is a small sphere.

In our numerical experiments, reported in the next section, we observe a lack of robustness of the approximate inverse on tough configurations due to the presence of small eigenvalues that cluster near zero in their natural trajectory towards point one of the spec-

trum of the preconditioned matrix under the action of the preconditioner. This consideration motivates us to introduce a stabilization step after computing M , which deflates a small group of eigenvalues close to zero in the spectrum of MA . Deflating techniques have proved to be useful to accelerate the convergence of iterative methods for general linear systems (e.g. [19–21]). We consider equation (2) and we denote by M_1 the left preconditioner, meaning that we solve,

$$M_1 A x = M_1 b. \quad (4)$$

We assume that the preconditioned matrix $M_1 A$ is diagonalisable, that is,

$$M_1 A = V \Lambda V^{-1} \quad (5)$$

with $\Lambda = \text{diag}(\lambda_i)$, where $|\lambda_1| \leq \dots \leq |\lambda_n|$ are the eigenvalues and $V = (v_i)$ the associated right eigenvectors. We denote by $U = (u_i)$ the associated left eigenvectors; we then have $U^H V = \text{diag}(u_i^H v_i)$, with $u_i^H v_i \neq 0, \forall i$. Let V_ε be the set of right eigenvectors associated with the set of eigenvalues λ_i with $|\lambda_i| \leq \varepsilon$. Similarly, we define by U_ε the corresponding subset of left eigenvectors.

Theorem 1: Let

$$A_c = U_\varepsilon^H M_1 A V_\varepsilon,$$

$$M_c = V_\varepsilon A_c^{-1} U_\varepsilon^H M_1$$

and

$$M = M_1 + M_c.$$

Then MA is diagonalisable and we have $MA = V \text{diag}(\eta_i) V^{-1}$ with

$$\begin{cases} \eta_i = \lambda_i & \text{if } |\lambda_i| > \varepsilon, \\ \eta_i = 1 + \lambda_i & \text{if } |\lambda_i| \leq \varepsilon. \end{cases}$$

A_c represents the projection of the matrix $M_1 A$ on the coarse space defined by the approximate eigenvectors associated with its smallest eigenvalues. **Proof**

We first remark that $A_c = \text{diag}(\lambda_i u_i^H v_i)$ with $|\lambda_i| \leq \varepsilon$ and so A_c is nonsingular. A_c represents the projection of the matrix $M_1 A$ on the space spanned by the approximate eigenvectors associated with its smallest eigenvalues.

Let $V = (V_\varepsilon, V_{\bar{\varepsilon}})$, where $V_{\bar{\varepsilon}}$ is the set of $(n - k)$ right eigenvectors associated with eigenvalues $|\lambda_i| > \varepsilon$.

Let $D_\varepsilon = \text{diag}(\lambda_i)$ with $|\lambda_i| \leq \varepsilon$ and $D_{\bar{\varepsilon}} = \text{diag}(\lambda_j)$ with $|\lambda_j| > \varepsilon$.

The following relations hold: $MAV_\varepsilon = V_\varepsilon(D_\varepsilon + I_k)$ where I_k denotes the $(k \times k)$ identity matrix, and $MAV_{\bar{\varepsilon}} = V_{\bar{\varepsilon}}D_{\bar{\varepsilon}}$ since $U_\varepsilon^H V_{\bar{\varepsilon}} = 0$; then we have

$$MAV = V \begin{pmatrix} D_\varepsilon + I_k & 0 \\ 0 & D_{\bar{\varepsilon}} \end{pmatrix}.$$

Theorem 2: Let W be such that

$$\tilde{A}_c = W^H A V_\varepsilon \text{ has full rank,}$$

$$\tilde{M}_c = V_\varepsilon \tilde{A}_c^{-1} W^H$$

and

$$\tilde{M} = M_1 + \tilde{M}_c.$$

Then $\tilde{M}A$ is similar to a matrix whose eigenvalues are

$$\begin{cases} \eta_i = \lambda_i & \text{if } |\lambda_i| > \varepsilon, \\ \eta_i = 1 + \lambda_i & \text{if } |\lambda_i| \leq \varepsilon. \end{cases}$$

Proof

With the same notation as for Proposition 1 we have: $\tilde{M}A V_\varepsilon = V_\varepsilon(D_\varepsilon + I_k)$ and, $\tilde{M}A V_{\tilde{\varepsilon}} = V_{\tilde{\varepsilon}}D_{\tilde{\varepsilon}} + V_\varepsilon C$ with $C = A_c^{-1}W^H A V_{\tilde{\varepsilon}}$; then we have

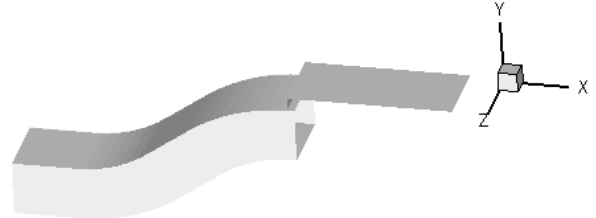
$$\tilde{M}A V = V \begin{pmatrix} D_\varepsilon + I_k & C \\ 0 & D_{\tilde{\varepsilon}} \end{pmatrix}.$$

For right preconditioning, that is $AM_1 y = b$, similar results hold. We should point out that in the nonsymmetric case a natural choice exists for the operator W , i.e. to select $W = V_\varepsilon$, that saves the computation of left eigenvectors. These formulations enable us to move to one any set of eigenvalues lying in any particular region of the spectrum; if for some particular applications some eigenvalues different from the smallest ones perturb the convergence they can be removed by the same technique. The application of the correction update at each iteration step costs $2nk + k^2$, where k is the size of the coarse space. The novelty of this study with respect to that conducted in [19] is to use MLFMA for computing approximations to the smallest eigenvalues and their corresponding approximate eigenvectors. We use the Implicitly Restarted Arnoldi Method implemented in the ARPACK package [22] that only requires matrix-vector products for the spectral computation. Thus the resulting preconditioner is nearly matrix-free.

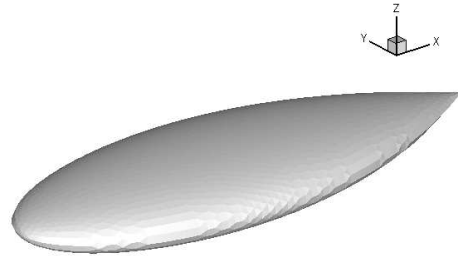
III. PERFORMANCE ANALYSIS

In Table 2 we report on the results of the approximate inverse (referred to as *SPAI*) of an experiment on the Cobra problem (Fig. 3(a), $n = 60695$) and on the Almond problem (Fig. 3(b), $n = 104793$), two standard test cases in the electromagnetic community. For both geometries, the scattering problem is modeled using the EFIE and the integral equation is discretized by the Galerkin method. We use the Fast Multipole Method for computing approximate matrix-vector products; we refer to [17] for the numerical implementation of the multipole

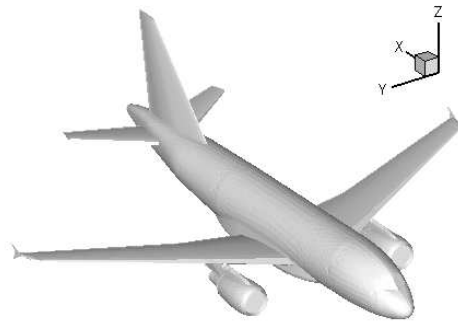
code. The experiment are run in single precision on eight processors of a Compaq Alpha server. The Compaq Alpha server is a cluster of symmetric multiprocessors. Each node consists of four DEC Alpha processors (EV 6, 1.3 GFlops peak) that share 512 MB of memory. We observe the favorable numerical scalability of the preconditioner for reasonably large value of the restart parameter and the $\mathcal{O}(n)$ complexity of computing M thanks to the blocking strategy.



(a) The Cobra problem. It represents an air intake and has size 67.9 cm \times 23.3 cm \times 11 cm.



(b) The Almond problem. The size is 2.5 m.



(c) The aircraft problem: an industrial civil aircraft from a European company. It represents a real-life model problem in an industrial context.

Fig. 3. Geometries considered for the numerical experiments. Courtesy of EADS-CCR Toulouse.

In Table 3, we show the parallel scalability of the implementation of the preconditioner in the FMM code on an industrial civil aircraft from a European company, a real-life model problem in an industrial context (the mesh is depicted in Fig. 3(c)). We solve systems of increasing size on a larger number of processors, keeping the number of unknowns per processor constant. It can be observed the very good parallel scalability of the construction and of the application of the preconditioner

typical of approximate inverse methods; for the matrix-vector product operation, the $n \log n$ factor appears in the results.

Table 2. Number of iterations and elapsed time required to reduce the initial residual by 10^{-3} on 8 processors of the Compaq machine, except those marked with (k) , that were run on k processors.

Almond						
Size	Density SPAI	Time SPAI	GMRES(∞)		GMRES(120)	
			Iter	Time	Iter	Time
104793	0.19	6m	234	20m	253	17m
419172	0.05	21m	413	2h 44m	571	2h 26m
943137	0.02	49m	454	3h 35m ⁽³²⁾	589	5h 55m

Cobra						
Size	Density SPAI	Time SPAI	GMRES(∞)		GMRES(120)	
			Iter	Time	Iter	Time
60695	0.24	2m	369	26m	516	23m
179460	0.09	7m	353	1h 11h	406	1h 2m

Table 3. Parallel scalability of the aircraft problem (see Figure 3(c)).

Problem size	Nb procs	Construction time (sec)	Elapsed time precondition (sec)	Elapsed time mat-vec (sec)
112908	8	513	0.39	1.77
221952	16	497	0.43	2.15
451632	32	509	0.48	2.80
900912	64	514	0.60	3.80

Finally, in Tables 4 to 6 we analyze the effect of using low-rank deflation techniques on the robustness of the iterative method. We study initially the numerical behavior of the preconditioner on a set of small test problems that are representative of realistic scattering calculations in electromagnetism. The model problems are:

Example 1: a cylinder with a hollow inside (110 MHz, $n = 1080$);

Example 2: a cylinder with a break on the surface (60 MHz, $n = 1299$);

Example 3: a satellite (220 MHz, $n = 1701$);

Example 4: a parallelepiped (420 MHz, $n = 2016$); and

Example 5: a sphere (190 MHz, $n = 2430$).

For physical consistency, we have set the frequency of the incident wave so that there are about ten discretization points per wavelength. In each case, we take as initial guess $x_0 = 0$, and the right-hand side is such that the exact solution of the system is known. We consider the formulation described in Theorem 2 and we apply the spectral updates on top of the preconditioned system $AM_1y = b$. In Table 4 we show the number of iterations required by GMRES to obtain convergence for increasing size of the coarse space up to 20. The

Table 4. Number of iterations required by GMRES and SQMR preconditioned by a Frobenius-norm minimization method updated with spectral corrections to reduce the normwise backward error by 10^{-8} for increasing size of the coarse space.

Size of the coarse space	GMRES(m), Toler. 1e-8					SQMR
	m=10	m=30	m=50	m=80	m=110	
Example 1						
Unprec.	+1500	+1500	+1500	651	423	271
0	358	213	144	79	79	103
4	313	169	109	68	68	78
8	294	138	76	58	58	60
12	190	96	52	51	51	52
16	184	80	47	47	47	40
20	174	61	44	44	44	44
Example 2						
Unprec.	+1500	+1500	+1500	+1500	+1500	439
0	+1500	+1500	496	311	198	161
4	279	192	152	125	93	117
8	188	147	129	90	84	97
12	196	148	131	91	83	82
16	183	137	114	74	74	73
20	168	130	100	69	69	68
Example 3						
Unprec.	+1500	+1500	+1500	1404	1193	519
0	268	174	130	79	79	92
4	259	150	99	66	66	77
8	225	109	77	58	58	66
12	117	81	56	52	52	56
16	105	74	49	49	49	48
20	96	58	44	44	44	46
Example 4						
Unprec.	1100	566	434	309	262	185
0	145	113	90	71	71	61
4	125	97	74	61	61	54
8	101	78	58	56	56	49
12	86	70	52	51	51	42
16	81	64	49	49	49	41
20	77	62	47	47	47	39
Example 5						
Unprec.	1241	374	277	216	208	140
0	297	87	75	66	66	51
4	345	66	64	58	58	40
8	55	43	40	40	40	33
12	52	43	38	38	38	34
16	52	44	39	39	39	34
20	53	45	40	40	40	34

numerical experiments are performed in double precision complex arithmetic on a SGI Origin 2000 and the number of iterations are for right preconditioning. We observe that the linear systems are difficult to solve as GMRES does not converge or converges slowly with no preconditioner. We can see that the introduction of the low-rank updates can remarkably accelerate the iterative solution. By selecting up to 10 eigenpairs the number of iterations decreases by at least a factor of two on most of the reported experiments and convergence becomes nearly independent from the restart parameter. On Example 2,

the preconditioning updates enable fast convergence of GMRES with a low restart whereas no convergence was obtained in 1500 iterations without updates.

Table 5. Number of amortization vectors required by the IRAM algorithm to compute approximate eigenvalues nearest zero and the corresponding right eigenvectors. The computation of the amortization vectors is relative to GMRES(10) and a tolerance of 10^{-8} .

Size of the coarse space	Number of Amortization Vectors				
	Ex. 1	Ex. 2	Ex. 3	Ex. 4	Ex. 5
4	7	1	28	9	-
8	4	1	4	6	1
12	2	1	2	4	1
16	2	1	2	7	1
20	4	1	2	6	1

Table 6. Experiments using a sparse approximate inverse preconditioner and spectral deflation combined with MLFMA.

Cobra problem, $n = 60695$ - frequency = 10.0 GHz					
	Dimension of the coarse space				
	0	5	10	15	
GMRES(10)	2719 (1^h 10^m)	1458 (42^m)	594 (12^m)	517 (11^m)	
GMRES(∞)	378 (18^m)	262 (9^m)	216 (7^m)	188 (6^m)	

Almond problem, $n = 104793$ - frequency = 2.6 GHz					
	Dimension of the coarse space				
	0	10	30	50	
GMRES(50)	1524 (1^h 17^m)	883 (45^m)	368 (20^m)	284 (5^m)	
GMRES(∞)	242 (14^m)	134 (9^m)	92 (6^m)	77 (6^m)	

In Table 5 we show the number of *amortization* vectors relative to GMRES(10), that is the number of right-hand sides that have to be considered to amortize the extra cost for the eigencomputation. In bistatic radar cross section calculations, linear systems with the same coefficient matrix and up-to hundreds of different right-hand sides are solved, ranging over the complete set of directions between the transmitter and the receiver. In Table 6 the low-rank deflation technique is combined with the FMM. We report on an experiment on the Cobra problem (Fig. 3(a), $n = 60695$) and on the Almond problem (Fig. 3(b), $n = 104793$). We see on the Cobra problem that with a preconditioning update of only 10 eigenvectors and setting very low restart in GMRES, we are able to reduce the number of iterations by nearly a factor of six; a significant reduction of both number of iterations and solution time is also observed on the Almond problem as well owing to the fact that we use low-accurate MLFMA for computing the spectral information. On that computer, the temporary disk space that can be used by the out-of-core solver is around 189

GB. On that hardware the CPU time is also reduced by a factor of six.

IV. CONCLUDING REMARKS

We have presented experiments with an adaptive preconditioning method constructed on top of an approximate inverse preconditioner for solving dense linear systems of equations arising in electromagnetic scattering applications. The results show that the proposed method can be very effective to accelerate the convergence of iterative Krylov solvers. Sparse approximate inverses based on Frobenius-norm minimization are very good candidates for preconditioning this problem class for their inherent parallelism and their proved numerical stability on indefinite systems. We have shown that the construction cost can be controlled using static pattern selection strategies and the performance can be enhanced significantly using deflating techniques.

ACKNOWLEDGEMENTS

The author would like to thank the EMC-CERFACS Team (Toulouse, France) for providing with the MoM code and the EADS-CRC company (Toulouse, France) for providing with the MLFMA code and the large test examples for the numerical experiments. The author is grateful to the anonymous referees for their valuable comments and suggestions that greatly improved the presentation of this paper.

REFERENCES

- [1] A.F. Peterson, S.L. Ray, and R. Mittra. *Computational Methods for Electromagnetics*. IEEE Press, 1997.
- [2] G. Alléon, S. Amram, N. Durante, P. Homsy, D. Pogarielloff, and C. Farhat, "Massively parallel processing boosts the solution of industrial electromagnetic problems: High performance out-of-core solution of complex dense systems," In M. Heath, V. Torczon, G. Astfalk, P. E. Bjørstad, A. H. Karp, C. H. Koebel, V. Kumar, R. F. Lucas, L. T. Watson, and Editors D. E. Womble, editors, *Proceedings of the Eighth SIAM Conference on Parallel*. SIAM Book, Philadelphia, Minneapolis, Minnesota, USA, 1997.
- [3] W. C. Chew and Y. M. Wang. A recursive T-matrix approach for the solution of electromagnetic scattering by many spheres. *IEEE Transactions on Antennas and Propagation*, vol. 41, no. 12, pp. 1633–1639, 1993.
- [4] K. Chen. An analysis of sparse approximate inverse preconditioners for boundary integral equations. *SIAM J. Matrix Analysis and Applications*, vol. 22, no. 3, pp. 1058–1078, 2001.

- [5] K. Sertel and J. L. Volakis. Incomplete LU preconditioner for FMM implementation. *Micro. Opt. Tech. Lett.*, vol. 26, no. 7, pp. 265–267, 2000.
- [6] A. Grama, V. Kumar, and A. Sameh. On n-body simulations using message-passing parallel computers. In Sidney Karin, editor, *Proceedings of the 1995 SIAM Conference on Parallel Processing, San Francisco, CA, USA*, 1995.
- [7] S. A. Vavasis. Preconditioning for boundary integral equations. *SIAM J. Matrix Analysis and Applications*, vol. 13, pp. 905–925, 1992.
- [8] J. Lee, C.-C. Lu, and J. Zhang. Incomplete LU preconditioning for large scale dense complex linear systems from electromagnetic wave scattering problems. *J. Comp. Phys.*, vol. 185, pp. 158–175, 2003.
- [9] B. Carpentieri, I. S. Duff, L. Giraud, and M. Magolomonga Made. Sparse symmetric preconditioners for dense linear systems in electromagnetism. Technical Report TR/PA/01/35, CERFACS, Toulouse, France, 2001. Also Technical Report RAL-TR-2002-016. Preliminary version of the article accepted for publication in *Numerical Linear Algebra with Applications*.
- [10] T. Malas and L. Gürel. Incomplete LU preconditioning with multilevel fast multipole algorithm for electromagnetic scattering. *SIAM J. Scientific Computing*, 2007. Accepted for publication.
- [11] G. Alléon, M. Benzi, and L. Giraud. Sparse approximate inverse preconditioning for dense linear systems arising in computational electromagnetics. *Numerical Algorithms*, vol. 16, pp. 1–15, 1997.
- [12] A. R. Samant, E. Michielssen, and P. Saylor. Approximate inverse based preconditioners for 2D dense matrix problems. Technical Report CCEM-11-96, University of Illinois, 1996.
- [13] J. Lee, C.-C. Lu, and J. Zhang. Sparse inverse preconditioning of multilevel fast multipole algorithm for hybrid integral equations in electromagnetics. Technical Report 363-02, Department of Computer Science, University of Kentucky, KY, 2002.
- [14] L. Greengard and V. Rokhlin. A fast algorithm for particle simulations. *Journal of Computational Physics*, vol. 73, pp. 325–348, 1987.
- [15] J. Song, C.-C. Lu, and W. C. Chew. Multilevel fast multipole algorithm for electromagnetic scattering by large complex objects. *IEEE Transactions on Antennas and Propagation*, vol. 45, no. 10, pp. 1488–1493, 1997.
- [16] E. Darve. The fast multipole method: Numerical implementation. *J. Comp. Phys.*, vol. 160, no. 1, pp. 195–240, 2000.
- [17] G. Sylvand. *La Méthode Multipôle Rapide en Electromagnétisme : Performances, Parallélisation, Applications*. PhD thesis, Ecole Nationale des Ponts et Chaussées, 2002.
- [18] B. Carpentieri, I. S. Duff, and L. Giraud. Sparse pattern selection strategies for robust Frobenius-norm minimization preconditioners in electromagnetism. *Numerical Linear Algebra with Applications*, vol. 7, no. 7-8, pp. 667–685, 2000.
- [19] B. Carpentieri, I. S. Duff, and L. Giraud. A class of spectral two-level preconditioners. *SIAM J. Scientific Computing*, vol. 25, no. 2, pp. 749–765, 2003.
- [20] J. Erhel, K. Burrage, and B. Pohl. Restarted GMRES preconditioned by deflation. *J. Comput. Appl. Math.*, vol. 69, pp. 303–318, 1996.
- [21] Y. Saad. Projection and deflation methods for partial pole assignment in linear state feedback. *IEEE Trans. Automat. Contr.*, vol. 33, no. 3, pp. 290–297, 1988.
- [22] R. Lehoucq, D. Sorensen, and P. Vu. *ARPACK User's Guide: Solution of LargeScale Eigenvalue Problems with Implicitly Restarted Arnoldi Methods*. Society for Industrial and Applied Mathematics, Philadelphia, 1998.



Bruno Carpentieri received a Ph.D. degree in Computer Science from Institut National Polytechnique of Toulouse, France, in 2002. He is a Postdoctoral Fellow at the Institut of Mathematics and Scientific Computing of Karl-Franzens University in Graz, Austria. His research interests include numerical linear algebra, high performance computing, Computational Fluid Dynamics, Computational Electromagnetics.

Fast and Accurate Cascaded Particle Swarm Gradient Optimization Method for Solving 2-D Inverse Scattering Problems

M. Farmahini-Farahani, R. Faraji-Dana, and M. Shahabadi

Center of Excellence on Applied Electromagnetic Systems, School of Electrical & Computer Engineering, University of Tehran, P.O. Box 14395-515, Tehran, Iran
(m.farmahini@ece.ut.ac.ir, reza@ut.ac.ir, shahabad@ut.ac.ir)

Abstract – In this paper, a fast and accurate technique for solving the inverse scattering problem of two-dimensional objects made of perfect conductor is proposed. In this technique which is called cascaded particle swarm gradient, the solving procedure is properly divided into two steps. In the first step, the position and the equivalent radius of the unknown objects is estimated while in the second step, the accurate shape function of the objects is determined. The former step is performed by a global optimizer namely particle swarm optimization (PSO) technique and the latter is carried out by the well-known gradient method. In this work, the forward scattering problem is solved by the equivalent source method. Several numerical examples are presented to examine the proposed algorithm especially in handling the challenging multi-object problems with concave shape functions in the presence of measurement errors. The results show that the proposed algorithm is about 75 times faster than a conventional PSO while yielding a higher accuracy.

Keywords: Cascaded particle swarm gradient, inverse scattering, and equivalent source method.

I. INTRODUCTION

Inverse scattering problem generally deals with the extraction of some features of inaccessible objects from the field scattered by them. The information of interest usually includes the shape and material characteristics of the unknown objects. Inverse scattering has many important applications in remote sensing, medical and seismic imaging, non-destructive testing, etc.

The electromagnetic inverse scattering problem is inherently ill-posed and non-linear [1, 2]. A large number of inversion techniques have been developed to solve a variety of electromagnetic inverse scattering problems. While One-dimensional (1-D) problems are more of theoretical importance, two-dimensional (2-D) problems are more realistic and can widely be utilized in practice. It can also be extended to the general case of three-dimensional problems. Here, a 2-D inverse problem for

perfectly conducting objects will be investigated.

Reconstruction algorithms are categorized into two main classes of analytical and numerical. The numerical reconstruction algorithms can be formulated as an optimization problem. Therefore, they can be solved using either global or local optimizers. The majority of proposed numerical inversion algorithms utilize local optimization methods. Some of the well-known methods of this class are the Newton-Kantorovitch method [3], Born iterative method [4], the distorted Born iterative method [5], the local shape function [6] and the conjugate gradient method [7]. However, all of the above mentioned inversion algorithms utilize deterministic optimization methods (DOMs) which are based on the gradient concept. The DOMs generally need an appropriate starting point and a well-behaved cost function to find the global extremum although this is not always guaranteed in practice. Due to these limitations, new global inversion algorithms based on global optimizers are proposed. Global optimization methods, including neural networks, simulated annealing, genetic algorithm (GA), and particle swarm optimization are generally based on evolutionary strategies. These optimization methods have numerous advantages such as implementation simplicity and robustness with respect to initial conditions. However, they generally demand a large number of cost function evaluations, which is always time consuming. It is believed that combined approaches which appropriately benefit from both kinds of optimizers and/or adapt themselves to the nature of the problem would perform more efficiently. For instance, in [8], the cost function evaluation part of the PSO is replaced by a gradient optimizer to achieve a faster convergence. Moreover, [9] has presented a combination of various evolutionary strategies and quasi-deterministic optimizers for efficient optimizing of frequency selective surfaces.

In [10], the inverse problem of a 2-D conductor is solved using *a priori* knowledge of the conductor shape as an initial guess for the gradient optimizer while in [11], GA as a global optimizer is utilized to solve the same problem. Considering the nature of this problem, namely

the fact that it can be divided into two steps of finding a preliminary approximation and extracting exact features, it seems likely that a hybrid method which appropriately combines local and global optimizers can adapt itself to the problem more efficiently.

In this paper, because of some similarity between the scattered fields of the unknown object and those of a circular cylinder of an equivalent radius, we first estimate the position and the approximate radius of the unknown object. Obviously, this searching process must be implemented by a global optimizer. In the next step, a local optimizer uses the initial position and radius obtained by the global optimizer and generates the exact shape profile. Here, PSO is used as a global optimizer. Afterwards, a well-known quasi-Newton method called BFGS (Broyden-Fletcher-Goldfarb-Shanno) [12, 13] is used as a local optimizer.

The paper is organized as follows: In Section II, the formulations of forward and inverse problems are briefly presented and then the inverse problem is formulated as a minimization problem. In Section III, the proposed cascaded PSO-Gradient algorithm is demonstrated. Section IV presents numerical results for single and multiple-object inverse problems with concave profiles and noisy scattered information.

II. FORMULATION OF THE PROBLEM

The geometry of a typical 2-D inverse problem is depicted in Fig. 1. A perfect cylindrical conductor is placed in free space along the z -axis and a set of receivers are placed on a surrounding circle. The parametric shape function for the object can be described in a local polar form as,

$$\rho_b' = \rho_b'(\varphi), \quad 0 \leq \varphi \leq 2\pi, \quad O' = \rho_0 \angle \varphi_0, \quad \rho_b = \rho_b' + \rho_0, \quad (1)$$

where the subscript b stands for boundary and O' is the origin of a local coordinate system in which the shape function is described. An electromagnetic plane wave with E_z component is incident upon the cylinder at the incident angle φ_{inc} . Assuming the time harmonic function of $e^{j\omega t}$, we express the incident wave by,

$$\mathbf{E}^{inc}(x, y) = E_z^{inc}(x, y) \hat{\mathbf{z}} = e^{jk_0(x \cos \varphi_{inc} + y \sin \varphi_{inc})} \hat{\mathbf{z}} \quad (2)$$

where k_0 is the wave number in free space. Since the incident wave can only produce a z -directed surface electric current, J_z^s , one can obtain the integral equation relating the incident field to the induced current on the conductor by applying the PEC boundary condition at the surface of the cylinder, i.e., $E_z^t = E_z^s + E_z^{inc} = 0$. Although

the Method of Moments (MoM) is the prominent numerical technique for solving this type of problems, [14] gives an easier and faster method to find the scattered field based on the equivalent source concept. In this method, the perfectly conducting cylinder is replaced by a set of longitudinal fictitious electric current filaments parallel to the z -axis which are properly positioned inside the contour C .

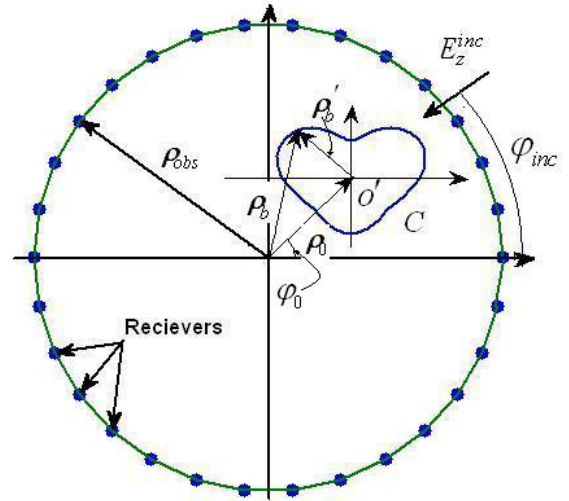


Fig. 1. Geometry of the problem.

According to the equivalence theorem if the electric field produced by these currents satisfies boundary conditions of the perfect conductor object, then the scattered field from the conductor object is equal to the electric field produced by the currents. The total electric field radiated by the currents is given by,

$$E_z(\rho) = -\sum_{m=1}^{N_I} \frac{k_0 \eta}{4} I_m H_0^{(2)}(k_0 |\rho - \rho_m^s|) \quad (3)$$

where the superscript s in ρ_m^s stands for source, η is the free space intrinsic impedance, N_I is the number of current filaments, $H_0^{(2)}$ is the Hankel function of second kind and zero order and I_m and ρ_m^s represent the magnitude and position vector of the current m -th filament, respectively. To solve the forward problem, it is enough to fulfill PEC boundary condition on the cylinder boundary by equating the total radiated electric field from current filaments of equation (3) and the incident electric field of equation (2) to zero on the surface of the perfect conductor. By selecting N_I points on the boundary (ρ_m^b) and satisfying the boundary condition for these points, which is equivalent to the point-matching technique in MoM, a set of N_I linear equations is obtained for the

unknown current filaments. Having access to the forward scattering problem solution, one can also solve the inverse problem. In this problem, the object shape function and its associated current filaments must be found such that the radiated electric field becomes the same as the electric field measured at the observation points. The deviation from this ideal case can be measured by using a mean square error criterion defined as,

$$e = \sum_{m=1}^{N_{obs}} \left| E_{meas}^{obs}(\rho_m^{obs}) - E_I^{obs}(\rho_m^{obs}) \right|^2 \quad (4)$$

where the superscript "obs" stands for the observation, N_{obs} is the number of the observation points, ρ_m^{obs} is the position vector of the m -th observation point, E_{meas}^{obs} is the measured electric field and E_I^{obs} is the electric field radiated by equivalent current filaments at the observation points. Cumulative error e must be minimized to yield a satisfactory object reconstruction.

To complete the formulation, one should represent the shape function of the object in a parametric form. Reference [11] suggests a parametric polar form in a local coordinate system, i.e.,

$$\rho(\varphi) = \sum_{n=0}^{N_c/2} a_n \cos(n\varphi) + \sum_{n=1}^{N_c/2} b_n \sin(n\varphi), \quad O' = \rho_0 \angle \varphi_0 \quad (5)$$

where N_c is the number of trigonometric terms in the approximate series. In this way, the cost function e is represented as a function of a vector of parameters. This vector, X can be presented for shape function (5) as,

$$X = [a_0, a_1, \dots, a_{N_c/2}, b_1, b_2, \dots, b_{N_c/2}, \rho_0, \varphi_0]. \quad (6)$$

Therefore, the total number of parameters in equation (6) becomes $N = N_c + 3$. The procedure described above can easily be extended to a multi-illumination case where there exists more than one incident electric field. It can also be modified for scattering of multiple objects [10, 11].

III. CASCADED PARTICLE SWARM-GRADIENT OPTIMIZATION

It is clear that e is a function of the profile of the cylinder, so the inverse scattering problem is reduced to the strategy of finding a proper shape profile (X vector) that minimizes e . In this paper, a novel cascaded strategy provides the proper X in two steps. In the first step, a

rough approximation of the shape function is acquired using PSO and in the second step the gradient optimizer provides the exact shape using the rough approximation.

It is expected that the scattered field of the unknown cylindrical object and a circular cylinder have the maximum similarity when the circular cylinder is placed in the position of the unknown object and have a proper equivalent radius. This can be explained with the help of an example. Fig. 2 depicts an arbitrary shape function given by $\rho(\varphi) = 0.3 + 0.05 \cos(2\varphi) + 0.08 \sin(3\varphi)$ placed in $0.5 \angle 0^\circ$ and its equivalent circular cylinder with the same center and equivalent radius. The incident electric field is located at $\varphi_{inc} = 0$. The magnitude of the scattered field of the original object and that of its equivalent circular cylinder sampled on a circle with a radius of 2 wavelengths are plotted in Fig. 3. The similarity between the two scattered fields is obvious. However, it does not necessarily mean that there is no other circular cylinder leading to a smaller error. In general, increasing the number of incident fields will significantly improve the convergence.

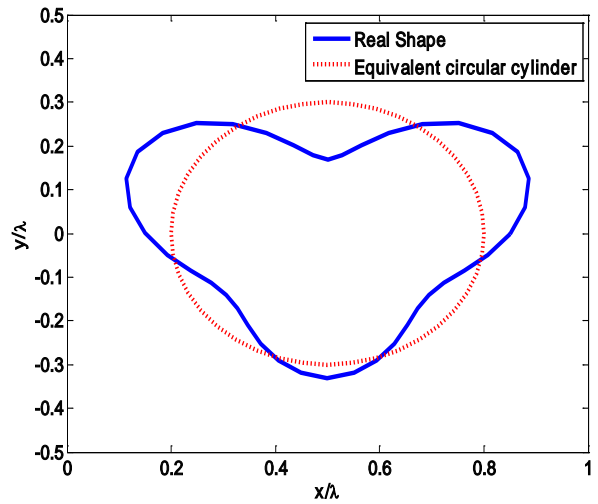


Fig. 2. Arbitrary shape function and its equivalent circular cylinder.

Hence, an initial approximation of the position and the shape of the unknown scatterer can be found by moving the center of a circular cylinder having a variable radius in the search space and comparing the calculated scattered field with the measured scattered field of the unknown object. This searching step is implemented using PSO which is considered as a global optimizer. PSO is a multi-agent stochastic algorithm that emulates food searching process of natural swarms. PSO has a conceptually simple and sensible algorithm based on

Newtonian concept of position and velocity. A detailed description of this technique can be found in [15, 16].

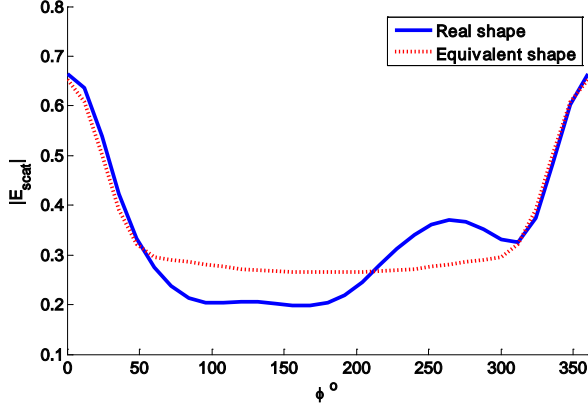


Fig. 3. Absolute value of scattered fields for Fig. 2 objects.

In the first step of the proposed cascaded algorithm, the optimization parameter vector is defined as follows,

$$X = [r_0^{(1)}, r_0^{(2)}, \dots, r_0^{(N_o)}, \rho_0^{(1)}, \rho_0^{(2)}, \dots, \rho_0^{(N_o)}, \varphi_0^{(1)}, \varphi_0^{(2)}, \dots, \varphi_0^{(N_o)}] \quad (7)$$

where $r_0^{(n)}$, $\rho_0^{(n)}$ and $\varphi_0^{(n)}$ are the equivalent radius and the polar coordinate components of the n -th unknown object, respectively. Then the values of $a_0^{(n)}$, $\rho_0^{(n)}$, and $\varphi_0^{(n)}$ in equation (6) are replaced by $r_0^{(n)}$, $\rho_0^{(n)}$, and $\varphi_0^{(n)}$ respectively, while other parameters are set to zero. In the next step, the initial position and radius of the object serves as an appropriate initial guess for a gradient based optimizer [10]. The well-known quasi-Newton method, BFGS, is adopted for this stage to yield accurate shape functions.

After evaluating the performance of individual parts of algorithm, they are unified to establish a cascaded operation which we have named as cascaded *particle swarm gradient method*.

IV. NUMERICAL RESULTS AND DISCUSSION

To examine the proposed method and to show its accuracy and convergence, several numerical experiments have been performed. The following mean square error function has been defined to quantitatively measure the accuracy of the shape functions,

$$SE = \left[\frac{1}{N_I N_o} \sum_{n=1}^{N_o} \sum_{m=1}^{N_I} \frac{(\rho_{n,m}^{opt} - \rho_{n,m}^{true})^2}{(\rho_{n,m}^{true})^2} \right]^{1/2} \quad (8)$$

In all these experiments, the dimensions are normalized to the wavelength and the observation points are placed on a circle with a radius equal to 2 wavelengths. In addition, N_{obs}, N_I, N_c are set to 30, 20 and 6, respectively. The search ranges for r_0, ρ_0, φ_0 are whit in $0.1 \leq r_0 \leq 1, 0 \leq \rho_0 \leq 1.5$ and $0 \leq \varphi_0 \leq 360^\circ$. SNR and PSO iterations are also selected to be 20dB and 200, respectively. As a first example, the shape function used in [11] is selected. The shape profile is given by $\rho(\varphi) = 0.3 + 0.05 \sin(2\varphi)$ in local polar coordinate whose center is placed at $0.5 \angle 90^\circ$. Moreover, two incident electric fields are assumed with incidence angles equal to 0 and π . Additive white Gaussian noise (AWGN) is added to the measured data with SNR=20dB. In [11], a real coded genetic algorithm is proposed for the profile reconstruction of the 2-D conducting objects. It optimizes the whole X vector, namely 9 parameters in this case, simultaneously. In our method, however there are only 3 parameters for position and equivalent radius to be optimized using a global optimizer in the first step and 7 parameters for coefficients of the shape function in equation (6) in the second step. PSO converged after 200 iterations to the values $\rho_0 = 0.4987, \varphi_0 = 89.96^\circ$ $r_0 = 0.3040$, and BFGS started with these initial values as initial and converged after 13 iterations.

Besides, a simple PSO code is utilized to solve the same problem. It should be mentioned that the range of variables in (6) is defined in such a way that both methods search over the same area. Figure 4 shows the true profile, the equivalent circular cylinder found by PSO, the final PSO-BFGS reconstructed profile and the simple PSO reconstructed one. Figure 5 shows the convergence of cascaded PSO-gradient for the shape of Fig. 5 compared with the ordinary PSO.

While the cascaded PSO-BFGS solves the problem in just 12 seconds with $SE=1.6\%$ it takes 15 minutes for the ordinary PSO to converge with $SE=3\%$. This indeed shows the superiority of the proposed method over an ordinary PSO. PSO-BFGS is about 75 times faster than the ordinary PSO and provides a slightly better accuracy in this particular example. To examine robustness of the algorithm against noise, the above example is solved for various amounts of added noise. Figure 6 shows the SE versus SNR. Achieving a SE of 10.12% at SNR=2.5dB demonstrates the excellent noise immunity of the proposed technique.

As the second example, two objects of shape functions $\rho(\varphi) = 0.3 + 0.05 \sin(3\varphi)$ and $\rho(\varphi) = 0.3 + 0.05 \sin(2\varphi)$ are selected and placed at $0.5 \angle 90^\circ$ and $0.5 \angle 270^\circ$ locations, respectively. The existence of two objects with concave shapes makes this example more challenging compared to the previous one.

Again two angles of incidence namely zero and π are selected. The SNR of the measured data was set to 20dB. After 750 iterations, the first step of the algorithm converged to values of $r_0^{(1)} = 0.307, \rho_0^{(1)} = 0.513, \varphi_0^{(1)} = 89.7^\circ$ for the upper object and $r_0^{(2)} = 0.306, \rho_0^{(2)} = 0.497, \varphi_0^{(2)} = 269.7^\circ$ lower one.

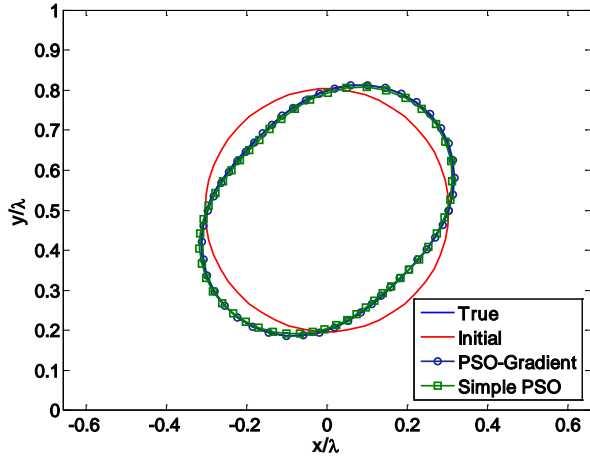


Fig. 4. True, initial guess, and reconstructed profile with PSO-BFGS and ordinary PSO.

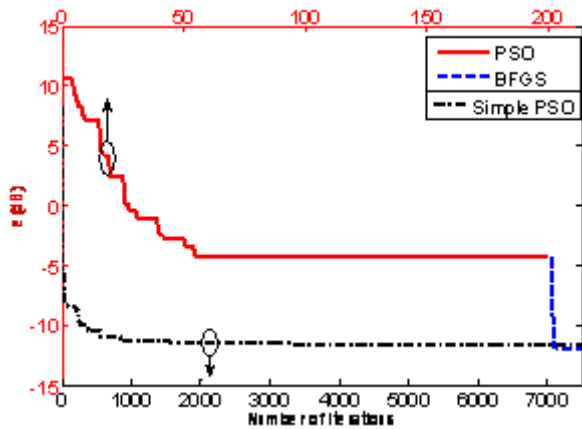


Fig. 5. Convergence of the cascaded PSO-BFGS compared with an ordinary PSO for the reconstruction of the shape function of Fig. 4.

These values were used as the initial guess for the gradient algorithm which converged after 19 iterations. Figure 7 shows the true profiles, the equivalent circular cylinders found by PSO, and the final reconstructed profiles. Figure 8 presents the cost function variations during cascaded PSO-BFGS iterations. Clearly, the proposed method can effectively solve the inverse problem in the case of multi-scatterers. The total computation time for achieving SE=6.05% is less than two minutes on a P4-3.2 GHz PC. It should be noted that the deviation observed at the bottom of the upper object is due to the multi-scattering effect.

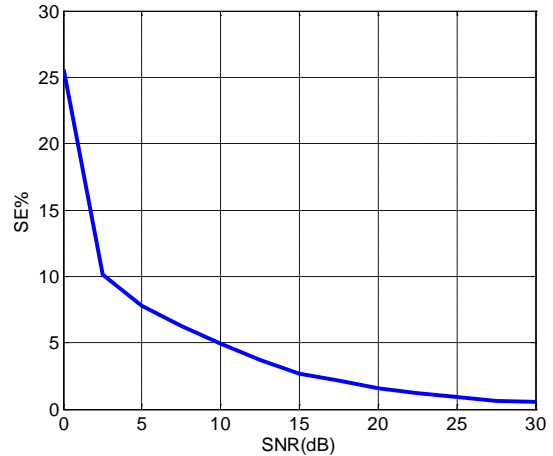


Fig. 6. Variations of SE versus SNR.

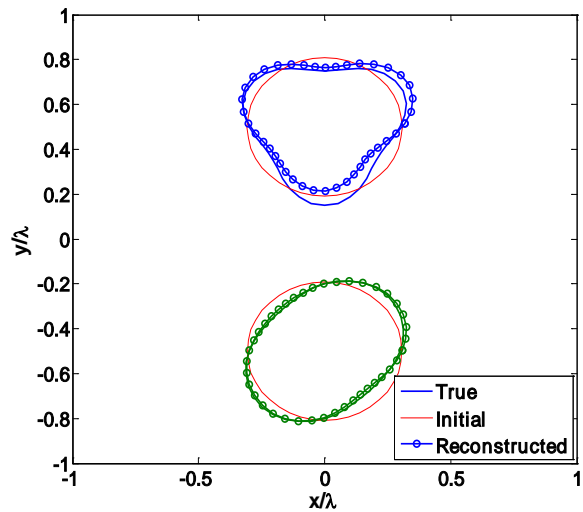


Fig. 7. True, initial, and reconstructed profiles of two scatterers using cascaded PSO BFGS.

To investigate the performance of the two parts of the algorithm against concavity, a statistical experiment is carried out. The ratio of a_n/a_0 or b_n/a_0 can be changed to obtain a variety of profiles with different concavities. Different values of a_2/a_0 and b_3/a_0 can produce three types of profiles, namely elliptical, tri-lobe and their combination. The PSO part is operated 1000 times for different profiles of each type. For each type, the most concaved shape profile for which the performance of the PSO part is still acceptable and the obtained equivalent circle is depicted in Table. 1. The percentage of PSO failed hits, denoted by the FP parameter, demonstrates the performance of PSO in finding the equivalent circle for each profile. The FP values presented in the table.1 demonstrates the satisfactory performance of the PSO part in finding a proper initial guess even for very concave shape functions.

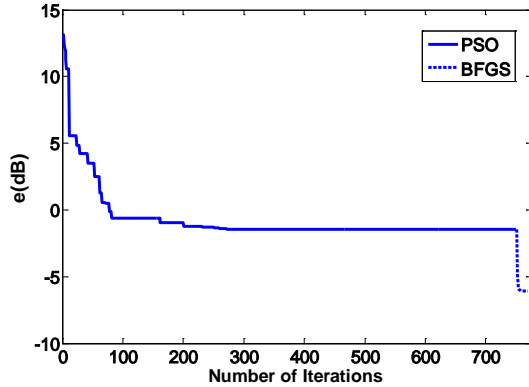

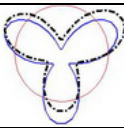



Fig. 8. Convergence of the proposed method in reconstruction of the profiles of Fig. 7.

It is important to address the performance of the Gradient part against concavity of the shape profile. To do this, the initial circles from Table. 1 are used in the BFGS algorithm as the starting point and the final shape functions are obtained. The obtained shape functions from gradient part are also depicted in Table. 1 (thick dashed lines) and the corresponding shape errors (SE) are also presented. Unsurprisingly, the gradient part fails to give an accurate shape function for the tri-lobe profile; however, the result is still similar to the original shape. A quasi-gradient approach to address this problem is now under investigation.

Furthermore, the angle of incidence is an important issue in multi-objects cases. For instance, the algorithm will fail if we set the incident angles around $\pi/2$ or $3\pi/2$ in the second example. The numerical results indicate that the suitable combination of the global and local optimization techniques as achieved in the proposed method has improved the accuracy and reduced the computation time significantly while avoiding the well-known disadvantages of both techniques.

Table 1. Obtained shape functions from gradient part.

	$\frac{a_2}{a_0}$	$\frac{b_3}{a_0}$	Profile	FP(%)	SE(%)
3	0.2	0		11.9	6
8	0	0.75		12.8	32.3
10	0.25	0.25		8.5	23.3
True shape function (thick solid line) corresponding equivalent circle (thin solid line) Estimated shape function (thick dashed line)					

V. CONCLUSION

In this paper, a cascaded PSO gradient optimization method suitable for solving the inverse scattering problem of 2-D perfect conductors is presented. The versatility of the proposed method is shown by applying it to challenging case of multi-objects with concave shapes and noisy data. The numerical results show satisfactory performance of the proposed method considering the important criteria of computation time and the achieved accuracy.

REFERENCES

- [1] A. J. Devancy, "Nonuniqueness in the inverse scattering problem," *J.Math. Phys.*, vol. 19, no. 7, pp. 1526–1531, 1978.
- [2] M. Bertero and C. De Mol, "Stability problems in inverse diffractions," *IEEE Trans. Antennas Propagat.*, vol. AP-29, no. 2, pp. 368–372, 1981.
- [3] A. Roger, "Newton–Kantorovitch algorithm applied to electromagnetic inverse problem," *IEEE Trans. Antennas Propagat.*, vol. AP-29, pp. 232–238, 1981.
- [4] M. Moghaddam and W. C. Chew, "Nonlinear two-dimensional velocity profile inversion using Time-domain data," *IEEE Trans. Geosci. Remote* vol. 30, pp. 147–156, Jan. 1992.
- [5] W. C. Chew and Y. M. Wang, "Reconstruction of two-dimensional permittivity using the distorted Born iterative method," *IEEE Trans. Med. Imag.*, vol. 9, pp. 218–225, 1990.
- [6] W. C. Chew and G. P. Otto, "Microwave imaging of multiple conducting cylinders using local shape functions," *IEEE Microwave Guided Wave Lett.*, vol. 2, pp. 284–286, July 1992.
- [7] R. V. McGahan and R. E. Kleinman, "Image reconstruction using real data," *IEEE Trans. on Antennas and Propagation*, vol. 38, pp. 39–59, Mar. 1996.
- [8] M. Ghaffari-Miab, M. Ghaffari-Miab, A. Farmahini-Farahani, R. Faraji-Dana, and C. Lucas, "An efficient hybrid swarm intelligence-gradient optimization method for complex time Green's functions of multilayer media," *Progress In Electromagnetics Research*, PIER 77, 181–192, 2007.
- [9] A. Fallahi, M. Mishrikey, C. Hafner, and R. Vahldieck, "Efficient procedures for the optimization of frequency selective surfaces," *IEEE Trans. on Antennas and Propagation*, vol. 56, no. 5, pp. 1340–1349, May 2008.
- [10] C. Y. Lin and Y. W. Kiang, "Inverse scattering for conductors by the equivalent source method," *IEEE Trans. on Antennas and Propagation*, vol. AP-44 pp. 310–315.

- [11] A. Qing, C. K. Lee, and L. Jen, "Electromagnetic inverse scattering of two-dimensional perfectly conducting objects by real coded genetic algorithm," *IEEE Trans. Geosci. Remote Sensing*, vol. 39, pp. 665-676, Mar. 2001.
- [12] D. Goldfarb, "A family of variable metric updates derived by variational means," *Mathematics of Computing*, vol. 24, pp. 23-26, 1970.
- [13] Fletcher, R., "A new approach to variable metric algorithms," *Computer Journal*, vol. 13, pp. 317-322, 1970.
- [14] A. Kirsch, R. Kress, P. Monk, and A. Zinn, "Two methods for solving the inverse acoustic scattering problem," *Inverse Problems*, vol. 4, pp. 749-770, 1988.
- [15] J. Robinson and Y. Rahma-Samii, "Particle swarm optimization in electromagnetics," *IEEE Trans. on Antennas and Propagation*, vol. 52, no. 2, pp. 397-408, Feb. 2004.
- [16] N. Jin and Y. Rahmat-Samii, "Advances in particle swarm optimization for antenna design: real number, binary, single-objective and multi-objective implementations," *IEEE Trans. on Antennas and Propagation*, vol. 55, no. 3, pp. 556-567, Mar. 2007.



research interests are inverse scattering, spatial power combining and optimization methods in Electromagnetics.

Mohsen Farmahini Farahani received the B.Sc. from Iran University of Science and Technology (with honors) in electrical engineering in 2006 and M.Sc. degree from the University of Tehran in 2009, both in electrical engineering. He is currently a research associate with the School of Electrical and Computer Engineering, University of Tehran. His



1994, he joined the School of Electrical and Computer Engineering, University of Tehran, where he is currently a Professor. He has been engaged in several academic and executive responsibilities, among which was his deanship of the Faculty of Engineering for more than four years, up until summer 2002, when he was elected as the University President

Reza Faraji-Dana received the B.Sc. degree (with honors) from the University of Tehran, Tehran, Iran, in 1986 and the M.A.Sc. and Ph.D. degrees from the University of Waterloo, Waterloo, ON, Canada, in 1989 and 1993, respectively, all in electrical engineering.

He was a Postdoctoral Fellow with the University of Waterloo for one year. In

by the university council. He was the President of the University of Tehran until December 2005. He is the author of several technical papers published in reputable international journals and refereed conference proceedings.

Prof. Faraji-Dana has been the Chairman of the IEEE-Iran Section since March 2007. He received the Institution of Electrical Engineers Marconi Premium Award in 1995.



Mahmoud Shahabadi received the B.Sc. and M.Sc. degrees from the University of Tehran, Iran, and the Ph.D degree from Technische Universitaet Hamburg-Harburg, Germany, all in electrical engineering in 1988, 1991, and 1998, respectively. In 1998, he joined the School of Electrical and Computer Engineering, University of Tehran, where he is currently an Associate

Professor. From 2001 to 2004, he was with the Department of Electrical and Computer Engineering, University of Waterloo, Canada, as a Visiting Professor. Additionally he is a co-founder and CTO of MASSolutions Inc., a Waterloo-based company with a focus on advanced low-profile antenna array systems. His research interests and activities encompass various areas of microwave and millimeter-wave engineering as well as photonics. Computational electromagnetics for microwave engineering and photonics find his special interest. He is currently conducting research and industrial projects in the field of antenna engineering, photonic crystals, left-handed materials, and holography. Dr. Shahabadi was awarded the 1998/1999 Prize of the German Metal and Electrical Industries, Nordmetall, for his contribution to the field of millimeterwave holography.

Layer-Based Integration Arithmetic of Conformal PML

Y. J. Zhang and Q. Sun

School of Aeronautics
Northwestern Polytechnical University, Xi'an, 710072, P.R. China
zyj19191@nwpu.edu.cn

Abstract – As an efficient artificial truncating boundary condition, conformal perfectly matched layer (CPML) is a multilayer anisotropic absorbing media domain. The conventional finite element analysis of CPML generates a large scale coefficient matrix that leads to prohibitive cost to solve. This paper proposes layer-based integration arithmetic, in which, the CPML multilayer integration is substituted by layer-wise summing of monolayer integration on the normal direction, with considering relative dielectric constant and permeability as constants in each very thin monolayer. The arithmetic needs to divide CPML into through-thickness elements of multiple layers, while the coefficient matrix of each element is evaluated by the layer-based integration. Numerical experiments show that the layer-based integration arithmetic is reliable and CPML under this arithmetic becomes a high-efficiency absorbing boundary condition.

Keywords: conformal PML, layer-based integration arithmetic, and absorbing boundary condition.

NOMENCLATURE

μ_r	relative permeability
ε_r	relative dielectric constant
k_0	wave number
λ	wave length
\mathbf{E}	electric field
$\overline{\Lambda}$	constitutive parameter of PML in tensor
$ \mathbf{A} $	determinant of matrix \mathbf{A}
\mathbf{A}^{-1}	inverse matrix of matrix \mathbf{A}
time	time of iterations, unit is second

I. INTRODUCTION

The perfectly matched layer (PML) concept introduced by Berenger [1], is an efficient method for truncating the unbounded spatial domain in electromagnetic radiation and scattering problems. Although the PML approach was originally introduced in the context of the finite-difference time-domain (FDTD) method [1], it has been found useful [2] in mesh truncation in the finite element method (FEM) as well. It

has recently been verified that artificial anisotropic media, with properly designed permittivity and permeability tensors, can absorb electromagnetic waves irrespective of their frequency and angle of incidence [3]. Kuzuoglu and Mittra [4] designed first conformal PML, which provides an efficient FEM mesh truncation, especially for problems involving electrically large antennas and complicated scatterers. Some versions of the conformal PML (CPML) suited to the FEM implementation were generalized in [5, 6].

For problems as demanding of computational resources as electromagnetic scattering, the conformal PML boundary is always desirable. Generally 6~10 layers of conformal PML meet absorbing condition, but more layers are needed for large complicated scatterers. Unfortunately, the layer is so thin that CPML is divided into large quantity of elements in adequate fine size, and finite element analysis of CPML generates a large scale coefficient matrix that leads to prohibitive cost to solve. For reducing quantity of elements, some research works [7-10] are implemented, but not settle this problem completely. To overcome this difficulty, we develop layer-based integration arithmetic, in which, multilayer integration of CPML elements is substituted by layer-wise summing of monolayer integration on the normal direction.

The contents of this paper include the layer-based integration arithmetic of conformal PML, arithmetic implementation and numerical experiments, which demonstrate both the applicability and effectiveness of the arithmetic.

II. CONFORMAL PML FORMULATION

In this section, we start by reviewing the definition of the conformal PML [5]; only the equations relevant to our implementation are presented.

For a general anisotropic PML, the constitutive parameters must be of the form $\overline{\mu} = \mu_r \overline{\Lambda}$ and $\overline{\varepsilon} = \varepsilon_r \overline{\Lambda}$. In the case of a conformal PML, the tensor is expressed as,

$$\overline{\Lambda} = \mathbf{u}\mathbf{u}\left(\frac{s_2 s_3}{s_1}\right) + \mathbf{v}\mathbf{v}\left(\frac{s_1 s_3}{s_2}\right) + \mathbf{w}\mathbf{w}\left(\frac{s_1 s_2}{s_3}\right). \quad (1)$$

Here, the conformal PML domain is a smooth convex shell, which encloses the scatterer a small distance away. Let S be the inner surface of this shell; at any given point P on S , the unit vectors \mathbf{u} and \mathbf{v} coincide with the principal directions, and \mathbf{w} is the unit surface normal. Assume that there are local coordinates u , v and w running in the \mathbf{u} , \mathbf{v} , and \mathbf{w} directions, and w takes the value zero on surface S ; then the points of constant w correspond to a parallel surface S' at a distance w from S . If the principal radii at point P are given by $r_{01}(u, v)$ and $r_{02}(u, v)$, then for point $P'(u, v, w)$ on S' , they will be given by $r_1(u, v, w) = r_{01}(u, v) + w$ and $r_2(u, v, w) = r_{02}(u, v) + w$.

The tensor values in the parentheses give geometrical and physical information on the conformal PML as,

$$\begin{cases} s_1 = (r_{01} + \int_0^w s(\zeta) d\zeta) / r_1 \\ s_2 = (r_{02} + \int_0^w s(\zeta) d\zeta) / r_2 \\ s_3 = s \end{cases} \quad (2)$$

where s is the complex stretching variable [5] in the w -direction.

Assume that u , v , w are coordinate component in local coordinate system \mathbf{u} , \mathbf{v} , and \mathbf{w} , so matrix of $\overline{\overline{\Lambda}}$ in local coordinate system is given by,

$$\overline{\overline{\Lambda}}_{u,v,w} = \begin{bmatrix} s_2 s_3 & 0 & 0 \\ s_1 & & \\ 0 & s_1 s_3 & 0 \\ & s_2 & \\ 0 & 0 & s_1 s_2 \\ & & s_3 \end{bmatrix}. \quad (3)$$

III. LAYER-BASED INTEGRATION ARITHMETIC

For 3-D electromagnetic scattering solution under PML absorbing boundary, scattering field can be described as following vector wave equations,

$$\nabla \times \left(\frac{1}{\overline{\overline{\mu_r}}} \cdot \nabla \times \mathbf{E}^s \right) - k_0^2 \overline{\overline{\varepsilon_r}} \cdot \mathbf{E}^s = \mathbf{0} \quad (4)$$

where \mathbf{E}^s is scattering electric field.

Applying variational principle to equation (4), the resulting functional is written as,

$$F(\mathbf{E}^s) = \frac{1}{2} \iiint_V \left[\frac{1}{\overline{\overline{\mu_r}}} (\nabla \times \mathbf{E}^s) \cdot \overline{\overline{\Lambda}}^{-1} \cdot (\nabla \times \mathbf{E}^s) - k_0^2 \overline{\overline{\varepsilon_r}} \mathbf{E}^s \cdot \overline{\overline{\Lambda}} \cdot \mathbf{E}^s \right] dV \quad (5)$$

The functional (5) is discretized by finite elements; formulation of element matrix is expressed as,

$$K_{ij} = \iiint_V \left[\frac{1}{\overline{\overline{\mu_r}}} (\nabla \times N_i) \cdot \overline{\overline{\Lambda}}^{-1} \cdot (\nabla \times N_j) - \iiint_V k_0^2 \overline{\overline{\varepsilon_r}} N_i \cdot \overline{\overline{\Lambda}} \cdot N_j \right] dV \quad (6)$$

where N_i and N_j are vector basis functions.

The conformal PML is multilayer anisotropic absorbing media that is shown as Fig. 1, so formulation of the k^{th} layer element matrix is written as,

$$K_{ij_k} = \iiint_V \left[(\nabla \times N_i) \cdot (\overline{\overline{\mu_{rk}}})^{-1} \cdot (\nabla \times N_j) - \iiint_V k_0^2 N_i \cdot \overline{\overline{\varepsilon_{rk}}} \cdot N_j \right] dV \quad (7)$$

where k is number of medium layer, n is total layer number, h_k is thickness of the k^{th} layer, $\overline{\overline{\mu_{rk}}} = \overline{\overline{\mu_r}} \overline{\overline{\Lambda_k}}$ and $\overline{\overline{\varepsilon_{rk}}} = \overline{\overline{\varepsilon_r}} \overline{\overline{\Lambda_k}}$ are relative dielectric constant and permeability of the k^{th} layer conformal PML, $\overline{\overline{\Lambda_k}}$ is determined by geometric parameters of the k^{th} layer.

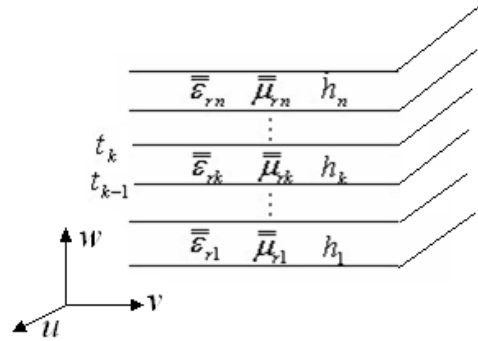


Fig. 1. n layers of conformal PML.

Because monolayer of conformal PML is very thin, layer-face size of solid element should be enough fine to match the thin thickness of monolayer. Especially, when CPML possesses many layers, CPML domain is divided into large quantities of solid elements. The conventional finite element analysis of CPML generates a large scale coefficient matrix that leads to prohibitive cost to solve.

Fortunately, relative dielectric constant and permeability may be considered as constants in each thin layer, so CPML multilayer integration is substituted by layer-wise summing of monolayer integration on the normal direction. The arithmetic needs to divide CPML into through-thickness elements of multiple layers, while the coefficient matrix of each element is evaluated by the layer-based integration. Detail is described as following.

Right hand of equation (6) is rewritten as two integrals,

$$A_{ij} = \iiint_V \frac{1}{\mu_r} (\nabla \times \mathbf{N}_i) \cdot (\bar{\bar{\Lambda}})^{-1} \cdot (\nabla \times \mathbf{N}_j) dV \quad (8)$$

$$B_{ij} = \iiint_V k_0^2 \varepsilon_r \mathbf{N}_i \cdot \bar{\bar{\Lambda}} \cdot \mathbf{N}_j dV \quad (9)$$

In equation (8) layer-based integration along the normal direction is written as,

$$\begin{aligned} A_{ij} &= \iiint_V \frac{1}{\mu_r} (\nabla \times \mathbf{N}_i) \cdot (\bar{\bar{\Lambda}})^{-1} \cdot (\nabla \times \mathbf{N}_j) dV \\ &= \int_{-1}^1 \int_{-1}^1 \int_{-1}^1 \frac{1}{\mu_r} (\nabla \times \mathbf{N}_i) \cdot (\bar{\bar{\Lambda}})^{-1} \\ &\quad \cdot (\nabla \times \mathbf{N}_j) \cdot |J| dudvdw \\ &= \int_{-1}^1 \int_{-1}^1 \left[\sum_{k=1}^n \int_{t_{k-1}}^{t_k} (\nabla \times \mathbf{N}_i) \cdot (\bar{\bar{\mu}}_{rk})^{-1} \right. \\ &\quad \cdot (\nabla \times \mathbf{N}_j) \cdot |J| dw \left. \right] dudv \\ &= \int_{-1}^1 \int_{-1}^1 \left[\sum_{k=1}^n \int_{-1}^1 (\nabla \times \mathbf{N}_i) \cdot (\bar{\bar{\mu}}_{rk})^{-1} \right. \\ &\quad \cdot (\nabla \times \mathbf{N}_j) \cdot |J| \frac{h_k}{t} dw_k \left. \right] dudv \end{aligned} \quad (10)$$

where J is 3-D isoparametric Jacobi matrix [11], t is total thickness of conformal PML.

$$J = \begin{bmatrix} \frac{\partial x}{\partial u} & \frac{\partial y}{\partial u} & \frac{\partial z}{\partial u} \\ \frac{\partial x}{\partial v} & \frac{\partial y}{\partial v} & \frac{\partial z}{\partial v} \\ \frac{\partial x}{\partial w} & \frac{\partial y}{\partial w} & \frac{\partial z}{\partial w} \end{bmatrix} \quad (11)$$

$$t = \sum_{m=1}^n h_m, \quad (12)$$

$$t_k = t_{k-1} + \frac{2h_k}{t}, \quad k = 1, 2, \dots, n, \quad t_0 = -1, \quad (13)$$

$$\begin{aligned} w &= \frac{1-w_k}{2} t_{k-1} + \frac{1+w_k}{2} t_k \\ &= \frac{1-w_k}{2} \left(t_k - \frac{2h_k}{t} \right) + \frac{1+w_k}{2} t_k \\ &= \frac{h_k}{t} (w_k - 1) + t_k \end{aligned} \quad (14)$$

where h_k is small enough, so we simplify integration function in equation (10) as,

$$A_{ij} = \int_{-1}^1 \int_{-1}^1 \left[\sum_{k=1}^n (\nabla \times \mathbf{N}_i) \cdot (\bar{\bar{\mu}}_{rk})^{-1} \cdot (\nabla \times \mathbf{N}_j) A_k h_k \right] dudv \quad (15)$$

where A_k is integrating factor of $|J|$ on the surface $w_k = 0$,

$$\begin{cases} A_k = \sqrt{A_{kx}^2 + A_{ky}^2 + A_{kz}^2} |k \\ A_{kx} = \frac{\partial y}{\partial u} \frac{\partial z}{\partial v} - \frac{\partial z}{\partial u} \frac{\partial y}{\partial v} \\ A_{ky} = \frac{\partial z}{\partial u} \frac{\partial x}{\partial v} - \frac{\partial x}{\partial u} \frac{\partial z}{\partial v} \\ A_{kz} = \frac{\partial x}{\partial u} \frac{\partial y}{\partial v} - \frac{\partial y}{\partial u} \frac{\partial x}{\partial v} \end{cases} \quad (16)$$

Similarly, layer-based integration formula of equation (9) can be obtained,

$$B_{ij} = \int_{-1}^1 \int_{-1}^1 \left[\sum_{k=1}^n k_0^2 \mathbf{N}_i \cdot \bar{\bar{\varepsilon}}_{rk} \cdot \mathbf{N}_j A_k h_k \right] dudv \quad (17)$$

Considering that electromagnetic field distribution is nonlinear in multilayer of conformal PML, second-order or higher order vector basis functions are essential to evaluation precision in the layer-based integration arithmetic. In this paper, we employ second-order vector basis functions [12].

IV. NUMERICAL EXPERIMENTS

In this section, in order to verify the accuracy and efficiency of layer-based integration arithmetic, we implement the arithmetic in three classical experiments.

1- Metal sphere, its diameter is 0.666λ , incidence wave spreads along Z , frequency is 300 MHz, as following Fig. 2(a).

- 2- Metal ellipsoid shell, its major axis is 1.0λ , its minor axis is 0.5λ , incidence wave spreads along Z , frequency is 3 GHz, as following Fig. 2(b).
- 3- Metal wing, its span length is 5.0λ , its chord length is 2.46λ , its maximum height is 0.28λ , incidence wave spreads along X , frequency is 300 MHz, as following Fig. 2(c).

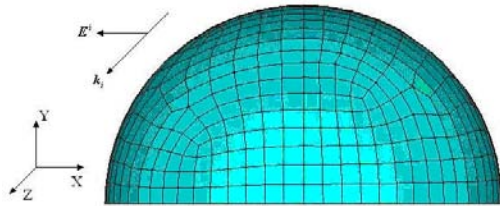


Fig. 2(a). Metal sphere.

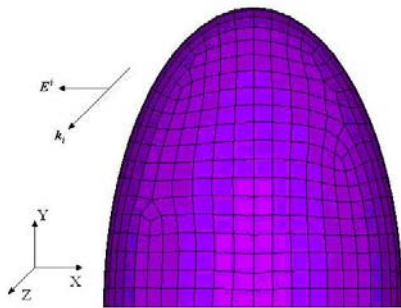


Fig. 2(b). Metal ellipsoid shell.

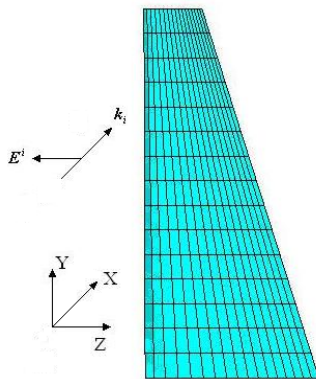


Fig. 2(c). Metal wing.

In the experiments, we employ curve hexahedra vector element in [12] and ICCG method to solve system equations in [13]. Results are obtained with 512M-memory computer. All programs are developed in FORTRAN90 compiled language.

In Fig. 3, we compare evaluation precision of the layer-based integration arithmetic with 6 layers of CPML for solving bistatic RCS of experiments under different element sizes. θ and φ are spherical coordinates. The results show that CPML under the layer-based integration

arithmetic is more accurate and reasonable under $\lambda/50$ element size. The main cause is that the normal direction and principal radius of curvature of CPML are calculated more accurately under $\lambda/50$ element size than under $\lambda/20$ element size, especially on small curvature radius domain.

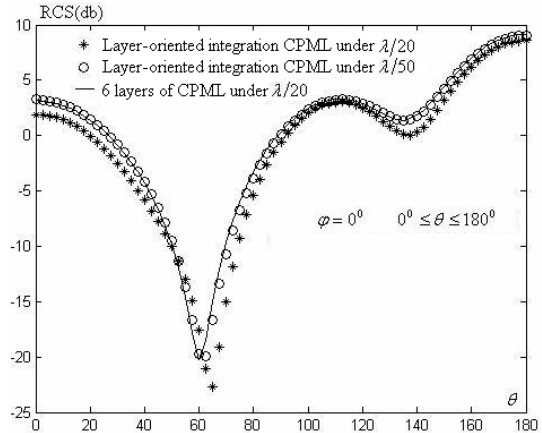


Fig. 3(a). Bistatic RCS of metal sphere.

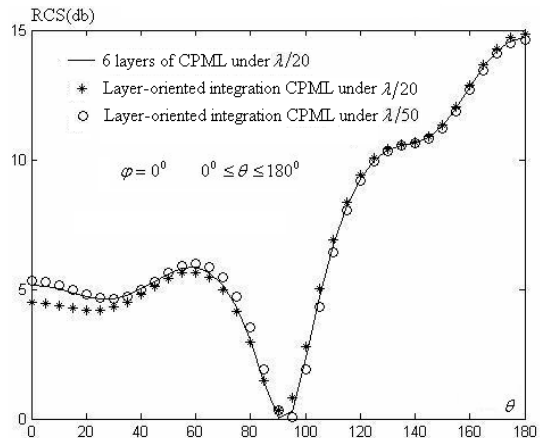


Fig. 3(b). Bistatic RCS of metal ellipsoid shell.

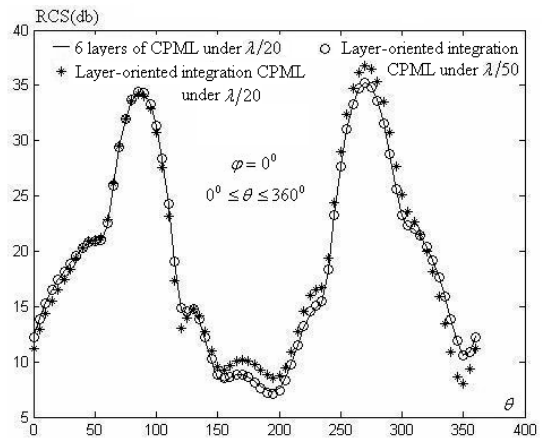


Fig. 3(c). Forward bistatic RCS of metal wing.

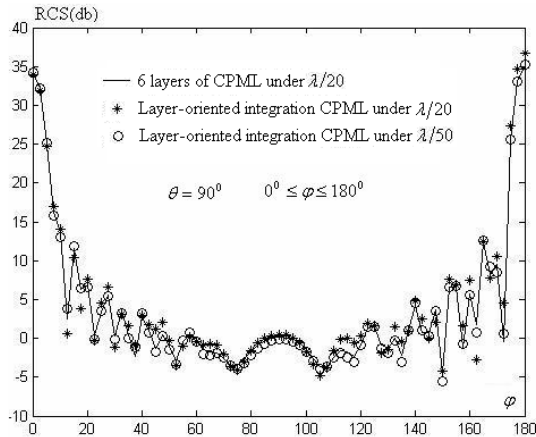


Fig. 3(d). Side bistatic RCS of metal wing.

In Table 1, we compare scale and speed of the layer-based integration arithmetic with 6 layers of CPML under different element sizes. The results show that CPML under the layer-based integration arithmetic costs much less scale and time than 6 layers of CPML.

Table 1. Scale and time of solution

Ex	CPML	Element size	Element quantity	Time(s)
1	6 layers	$\lambda/20$	14880	16.97
	layer-based integration	$\lambda/50$	8542	9.124
2	6 layers	$\lambda/20$	83455	112.5
	layer-based integration	$\lambda/50$	51668	70.36
3	6 layers	$\lambda/20$	180112	264.3
	layer-based integration	$\lambda/50$	117466	149.2

V. CONCLUSION

For reducing quantity of elements in multilayer CPML domain, we develop the layer-based integration arithmetic to evaluate integrations of multilayer elements. In view of its high efficiency on complicated objects, CPML under this arithmetic shows great promise as an ideal absorber for electromagnetic scattering analysis.

ACKNOWLEDGEMENT

The support of Science and technology Innovation Foundation of Northwestern Polytechnical University (W016143) is gratefully acknowledged.

The support of National Natural Science Foundation of China (No. 10477018) is gratefully acknowledged.

REFERENCES

- [1] J. P. Berenger, "A perfectly matched layer for the absorption of electromagnetic waves," *L Comp. Phys.*, vol. 114, no. 2, pp. 185-200, 1994.
- [2] U. Peke1 and R. Mittra, "A finite element method frequency-domain application of the perfectly matched layer (PML) concept," *Microwave Opt. Technol. Lett.*, vol. 9, no. 8, pp. 117-122, 1995.
- [3] Z. S. Sacks, D. M. Kingsland, R. Lee, and J.-F. Lee, "A perfectly matched anisotropic absorber for use as an absorbing boundary condition," *IEEE Trans. Antennas Propagat.*, vol. 43, no. 12, pp. 1460-1463, 1995.
- [4] M. Kuzuoglu and R. Mittra, "Mesh truncation by perfectly matched anisotropic absorbers in the finite element method," *Microwave Opt. Technol. Lett.*, vol. 12, no. 3, pp. 136-140, 1996.
- [5] F. L. Teixeira and W. C. Chew, "Analytical derivation of a conformal perfectly matched absorber for electromagnetic waves," *Microwave Opt. Technol. Lett.*, vol. 17, no. 4, pp. 231-236, 1998.
- [6] P. Liu, J. D. Xu, and W. Wan, "A finite-element realization of a 3-d conformal pml," *Microwave Opt. Technol. Lett.*, vol. 30, no. 3, pp. 170-173, 2001.
- [7] C. Guérin and G. Tanneau, "A shell element for computing 3D eddy currents -application to transformers," *IEEE Trans. Magn.*, vol. 31, no. 3, pp. 1360-1363, 1995.
- [8] J. M. Jin, *The Finite Element Method in Electromagnetics*, 2nd ed., New York: Wiley, 2002.
- [9] A. L. Radovinskii, "General theorems of the electromechanics of thin elastic shells," *Journal of Applied Mathematics and Mechanics*, vol. 53, no. 4, pp. 514-519, 1989.
- [10] Rajeev Thottappillil, Martin A. Uman, and Nelson Theethayi, "Electric and magnetic fields from a semi-infinite antenna above a conducting plane," *Journal of Electrostatics*, vol. 61, no. 3, pp. 209-221, 2004.
- [11] Weng Cho Chew, *Fast and Efficient Algorithms in Computational Electromagnetics*, Boston: Artech House, 2001.
- [12] Li jianghai and Sun qin, "Constructing a class of orthogonal-reinforced hierarchical hexahedra vector FE," *Chinese Journal for Computational Physics*, vol. 23, no. 1, pp. 32-36, 2006.
- [13] Y. J. Zhang and Q. Sun, "Improved ICCG method for large scale sparse linear equations," *Chinese Journal of Computational Physics*, vol. 24, no. 5, pp. 581-584, 2007.

2009 INSTITUTIONAL MEMBERS

AUSTRALIAN DEFENCE LIBRARY
Northcott Drive
Canberra, A.C.T. 2600 Australia

BAE SYSTEMS
W423A Warton Aerodome
Preston, Lancashire
United Kingdom PR4 1AX

DARTMOUTH COLLEGE
6193 Murdough Center
Hanover, NH 03755-3560

DSTO-DSTORL EDINBURGH
Jets AU/33851-99, PO Box 562
Milsons Point, NSW
Australia 1565

DTIC-OCP/LIBRARY
8725 John J. Kingman Rd. Ste 0944
Ft. Belvoir, VA 22060-6218

ELLEDIEMME
Libri Dal Mondo
PO Box 69/Poste S. Silvestro
Rome, Italy 00187

ELSEVIER
Bibliographic Databases
PO Box 2227
Amsterdam, Netherlands 1000 CE

ENGINEERING INFORMATION, INC
PO Box 543
Amsterdam, Netherlands 1000 Am

ETSE TELECOMUNICACION
Biblioteca, Campus Lagoas
Vigo, 36200 Spain

FGAN-FHR
Neuenahrerstrasse 20
Wachtberg, Germany 53343

FLORIDA INTERNATIONAL UNIV
10555 W. Flagler Street
Miami, FL 33174

GEORGIA TECH LIBRARY
225 North Avenue, NW
Atlanta, GA 30332-0001

HANYANG UNIVERSITY
Paiknam Academic Info. Ctr Library
17 Haengdang-Dong
Seongdong-Ku
Seoul, South Korea 133-791

HRL LABS, RESEARCH LIBRARY
3011 Malibu Canyon
Malibu, CA 90265

IEE INSPEC/Acquisitions Section
Michael Faraday House
6 Hills Way
Stevenage, Herts UK SG1 2AY

IND CANTABRIA
PO Box 830470
Birmingham, AL 35283

INSTITUTE FOR SCIENTIFIC INFO.
Publication Processing Dept.
3501 Market St.
Philadelphia, PA 19104-3302

L-3 IS
1133 Wood Valley Drive
Woodway, TX 76712

LIBRARY – DRDC OTTAWA
3701 Carling Avenue
Ottawa, Ontario, Canada K1A OZ4

LIBRARY of CONGRESS
Reg. Of Copyrights
Attn: 40T Deposits
Washington DC, 20559

LINDA HALL LIBRARY
5109 Cherry Street
Kansas City, MO 64110-2498

LULEA UNIV. OF TECHNOLOGY
Porson
Lulea, Sweden 97187

MISSISSIPPI STATE UNIV LIBRARY
PO Box 9570
Mississippi State, MS 39762

MISSOURI S&T
400 W 14th Street
Rolla, MO 56409

MIT LINCOLN LABORATORY
Periodicals Library
244 Wood Street
Lexington, MA 02420

NATIONAL DEFENSE ACADEMY
1-10-20 Hashirimizu
Yokosuka, Kanagawa
239-8686 Japan

NAVAL POSTGRADUATE SCHOOL
Attn: J. Rozdal/411 Dyer Rd./ Rm 111
Monterey, CA 93943-5101

NDL KAGAKU
C/O KWE-ACCESS
PO Box 300613 (JFK A/P)
Jamaica, NY 11430-0613

OHIO STATE UNIVERSITY
1320 Kinnear Road
Columbus, OH 43212

OVIEDO LIBRARY
PO BOX 830679
Birmingham, AL 35283

PENN STATE UNIVERSITY
126 Paterno Library
University Park, PA 16802-1808

DAVID J. PINION
1122 E PIKE STREET #1217
SEATTLE, WA 98122

SOUTHWEST RESEARCH
INSTITUTE
6220 Culebra Road
San Antonio, TX 78238

SWETS INFORMATION SERVICES
160 Ninth Avenue, Suite A
Runnemede, NJ 08078

TELSTRA
13/242 Exhibition Street
Melbourne, Victoria
3000 Australia

TIB & UNIV. BIB. HANNOVER
DE/5100/G1/0001
Welfengarten 1B
Hannover, Germany 30167

TU DARMSTADT
Schlossgartenstrasse 8
Darmstadt, Hessen
Germany D-64289

UNIV OF CENTRAL FLORIDA LIB.
4000 Central Florida Boulevard
Orlando, FL 32816-8005

UNIVERSITY OF KANSAS –
WATSON
1425 Jayhawk Blvd 210S
Lawrence, KS 66045-7594

UNIVERSITY OF MISSISSIPPI
JD Williams Library
University, MS 38677-1848

UNIVERSITY OF PALERMO
PO Box 69- Poste S. Silvestr
Rome, 00187, Italy

VIRTUAL EM INC.
2019 Georgetown Blvd.
Ann Arbor, MI 48105

ACES COPYRIGHT FORM

This form is intended for original, previously unpublished manuscripts submitted to ACES periodicals and conference publications. The signed form, appropriately completed, MUST ACCOMPANY any paper in order to be published by ACES. PLEASE READ REVERSE SIDE OF THIS FORM FOR FURTHER DETAILS.

TITLE OF PAPER:

RETURN FORM TO:

Dr. Atef Z. Elsherbeni
University of Mississippi
Dept. of Electrical Engineering
Anderson Hall Box 13
University, MS 38677 USA

AUTHORS(S)

PUBLICATION TITLE/DATE:

PART A - COPYRIGHT TRANSFER FORM

(NOTE: Company or other forms may not be substituted for this form. U.S. Government employees whose work is not subject to copyright may so certify by signing Part B below. Authors whose work is subject to Crown Copyright may sign Part C overleaf).

The undersigned, desiring to publish the above paper in a publication of ACES, hereby transfer their copyrights in the above paper to The Applied Computational Electromagnetics Society (ACES). The undersigned hereby represents and warrants that the paper is original and that he/she is the author of the paper or otherwise has the power and authority to make and execute this assignment.

Returned Rights: In return for these rights, ACES hereby grants to the above authors, and the employers for whom the work was performed, royalty-free permission to:

1. Retain all proprietary rights other than copyright, such as patent rights.
2. Reuse all or portions of the above paper in other works.

3. Reproduce, or have reproduced, the above paper for the author's personal use or for internal company use provided that (a) the source and ACES copyright are indicated, (b) the copies are not used in a way that implies ACES endorsement of a product or service of an employer, and (c) the copies per se are not offered for sale.

4. Make limited distribution of all or portions of the above paper prior to publication.

5. In the case of work performed under U.S. Government contract, ACES grants the U.S. Government royalty-free permission to reproduce all or portions of the above paper, and to authorize others to do so, for U.S. Government purposes only.

ACES Obligations: In exercising its rights under copyright, ACES will make all reasonable efforts to act in the interests of the authors and employers as well as in its own interest. In particular, ACES REQUIRES that:

1. The consent of the first-named author be sought as a condition in granting re-publication permission to others.
2. The consent of the undersigned employer be obtained as a condition in granting permission to others to reuse all or portions of the paper for promotion or marketing purposes.

In the event the above paper is not accepted and published by ACES or is withdrawn by the author(s) before acceptance by ACES, this agreement becomes null and void.

AUTHORIZED SIGNATURE

TITLE (IF NOT AUTHOR)

EMPLOYER FOR WHOM WORK WAS PERFORMED

DATE FORM SIGNED

Part B - U.S. GOVERNMENT EMPLOYEE CERTIFICATION

(NOTE: if your work was performed under Government contract but you are not a Government employee, sign transfer form above and see item 5 under Returned Rights).

This certifies that all authors of the above paper are employees of the U.S. Government and performed this work as part of their employment and that the paper is therefor not subject to U.S. copyright protection.

AUTHORIZED SIGNATURE

TITLE (IF NOT AUTHOR)

NAME OF GOVERNMENT ORGANIZATION

DATE FORM SIGNED

PART C - CROWN COPYRIGHT

(NOTE: ACES recognizes and will honor Crown Copyright as it does U.S. Copyright. It is understood that, in asserting Crown Copyright, ACES in no way diminishes its rights as publisher. Sign only if *ALL* authors are subject to Crown Copyright).

This certifies that all authors of the above Paper are subject to Crown Copyright. (Appropriate documentation and instructions regarding form of Crown Copyright notice may be attached).

AUTHORIZED SIGNATURE

TITLE OF SIGNEE

NAME OF GOVERNMENT BRANCH

DATE FORM SIGNED

Information to Authors

ACES POLICY

ACES distributes its technical publications throughout the world, and it may be necessary to translate and abstract its publications, and articles contained therein, for inclusion in various compendiums and similar publications, etc. When an article is submitted for publication by ACES, acceptance of the article implies that ACES has the rights to do all of the things it normally does with such an article.

In connection with its publishing activities, it is the policy of ACES to own the copyrights in its technical publications, and to the contributions contained therein, in order to protect the interests of ACES, its authors and their employers, and at the same time to facilitate the appropriate re-use of this material by others.

The new United States copyright law requires that the transfer of copyrights in each contribution from the author to ACES be confirmed in writing. It is therefore necessary that you execute either Part A-Copyright Transfer Form or Part B-U.S. Government Employee Certification or Part C-Crown Copyright on this sheet and return it to the Managing Editor (or person who supplied this sheet) as promptly as possible.

CLEARANCE OF PAPERS

ACES must of necessity assume that materials presented at its meetings or submitted to its publications is properly available for general dissemination to the audiences these activities are organized to serve. It is the responsibility of the authors, not ACES, to determine whether disclosure of their material requires the prior consent of other parties and if so, to obtain it. Furthermore, ACES must assume that, if an author uses within his/her article previously published and/or copyrighted material that permission has been obtained for such use and that any required credit lines, copyright notices, etc. are duly noted.

AUTHOR/COMPANY RIGHTS

If you are employed and you prepared your paper as a part of your job, the rights to your paper initially rest with your employer. In that case, when you sign the copyright form, we assume you are authorized to do so by your employer and that your employer has consented to all of the terms and conditions of this form. If not, it should be signed by someone so authorized.

NOTE RE RETURNED RIGHTS: Just as ACES now requires a signed copyright transfer form in order to do "business as usual", it is the intent of this form to return rights to the author and employer so that they too may do "business as usual". If further clarification is required, please contact: The Managing Editor, R. W. Adler, Naval Postgraduate School, Code EC/AB, Monterey, CA, 93943, USA (408)656-2352.

Please note that, although authors are permitted to re-use all or portions of their ACES copyrighted material in other works, this does not include granting third party requests for reprinting, republishing, or other types of re-use.

JOINT AUTHORSHIP

For jointly authored papers, only one signature is required, but we assume all authors have been advised and have consented to the terms of this form.

U.S. GOVERNMENT EMPLOYEES

Authors who are U.S. Government employees are not required to sign the Copyright Transfer Form (Part A), but any co-authors outside the Government are.

Part B of the form is to be used instead of Part A only if all authors are U.S. Government employees and prepared the paper as part of their job.

NOTE RE GOVERNMENT CONTRACT WORK: Authors whose work was performed under a U.S. Government contract but who are not Government employees are required so sign Part A-Copyright Transfer Form. However, item 5 of the form returns reproduction rights to the U. S. Government when required, even though ACES copyright policy is in effect with respect to the reuse of material by the general public.

January 2002

INFORMATION FOR AUTHORS

PUBLICATION CRITERIA

Each paper is required to manifest some relation to applied computational electromagnetics. **Papers may address general issues in applied computational electromagnetics, or they may focus on specific applications, techniques, codes, or computational issues.** While the following list is not exhaustive, each paper will generally relate to at least one of these areas:

- 1. Code validation.** This is done using internal checks or experimental, analytical or other computational data. Measured data of potential utility to code validation efforts will also be considered for publication.
- 2. Code performance analysis.** This usually involves identification of numerical accuracy or other limitations, solution convergence, numerical and physical modeling error, and parameter tradeoffs. However, it is also permissible to address issues such as ease-of-use, set-up time, run time, special outputs, or other special features.
- 3. Computational studies of basic physics.** This involves using a code, algorithm, or computational technique to simulate reality in such a way that better, or new physical insight or understanding, is achieved.
- 4. New computational techniques** or new applications for existing computational techniques or codes.
- 5. “Tricks of the trade”** in selecting and applying codes and techniques.
- 6. New codes, algorithms, code enhancement, and code fixes.** This category is self-explanatory, but includes significant changes to existing codes, such as applicability extensions, algorithm optimization, problem correction, limitation removal, or other performance improvement. **Note: Code (or algorithm) capability descriptions are not acceptable, unless they contain sufficient technical material to justify consideration.**
- 7. Code input/output issues.** This normally involves innovations in input (such as input geometry standardization, automatic mesh generation, or computer-aided design) or in output (whether it be tabular, graphical, statistical, Fourier-transformed, or otherwise signal-processed). Material dealing with input/output database management, output interpretation, or other input/output issues will also be considered for publication.
- 8. Computer hardware issues.** This is the category for analysis of hardware capabilities and limitations of various types of electromagnetics computational requirements. Vector and parallel computational techniques and implementation are of particular interest.

Applications of interest include, but are not limited to, antennas (and their electromagnetic environments), networks, static fields, radar cross section, inverse scattering, shielding, radiation hazards, biological effects, biomedical applications, electromagnetic pulse (EMP), electromagnetic interference (EMI), electromagnetic compatibility (EMC), power transmission, charge transport, dielectric, magnetic and nonlinear materials, microwave components, MEMS, RFID, and MMIC technologies, remote sensing and geometrical and physical optics, radar and communications systems, sensors, fiber optics, plasmas, particle accelerators, generators and motors, electromagnetic wave propagation, non-destructive evaluation, eddy currents, and inverse scattering.

Techniques of interest include but not limited to frequency-domain and time-domain techniques, integral equation and differential equation techniques, diffraction theories, physical and geometrical optics, method of moments, finite differences and finite element techniques, transmission line method, modal expansions, perturbation methods, and hybrid methods.

Where possible and appropriate, authors are required to provide statements of quantitative accuracy for measured and/or computed data. This issue is discussed in “Accuracy & Publication: Requiring, quantitative accuracy statements to accompany data,” by E. K. Miller, *ACES Newsletter*, Vol. 9, No. 3, pp. 23-29, 1994, ISBN 1056-9170.

SUBMITTAL PROCEDURE

All submissions should be uploaded to ACES server through ACES web site (<http://aces.ee.olemiss.edu>) by using the upload button, journal section. Only pdf files are accepted for submission. The file size should not be larger than 5MB, otherwise permission from the Editor-in-Chief should be obtained first. Automated acknowledgment of the electronic submission, after the upload process is successfully completed, will be sent to the corresponding author only. It is the responsibility of the corresponding author to keep the remaining authors, if applicable, informed. Email submission is not accepted and will not be processed.

PAPER FORMAT (INITIAL SUBMISSION)

The preferred format for initial submission manuscripts is 12 point Times Roman font, single line spacing and single column format, with 1 inch for top, bottom, left, and right margins. Manuscripts should be prepared for standard 8.5x11 inch paper.

EDITORIAL REVIEW

In order to ensure an appropriate level of quality control, papers are peer reviewed. They are reviewed both for

technical correctness and for adherence to the listed guidelines regarding information content and format.

PAPER FORMAT (FINAL SUBMISSION)

Only camera-ready electronic files are accepted for publication. The term “**camera-ready**” means that the material is neat, legible, reproducible, and in accordance with the final version format listed below.

The following requirements are in effect for the final version of an ACES Journal paper:

1. The paper title should not be placed on a separate page. The title, author(s), abstract, and (space permitting) beginning of the paper itself should all be on the first page. The title, author(s), and author affiliations should be centered (center-justified) on the first page. The title should be of font size 16 and bolded, the author names should be of font size 12 and bolded, and the author affiliation should be of font size 12 (regular font, neither italic nor bolded).
2. An abstract is required. The abstract should be a brief summary of the work described in the paper. It should state the computer codes, computational techniques, and applications discussed in the paper (as applicable) and should otherwise be usable by technical abstracting and indexing services. The word “Abstract” has to be placed at the left margin of the paper, and should be bolded and italic. It also should be followed by a hyphen (–) with the main text of the abstract starting on the same line.
3. All section titles have to be centered and all the title letters should be written in caps. The section titles need to be numbered using roman numbering (I. II.)
4. Either British English or American English spellings may be used, provided that each word is spelled consistently throughout the paper.
5. Internal consistency of references format should be maintained. As a guideline for authors, we recommend that references be given using numerical numbering in the body of the paper (with numerical listing of all references at the end of the paper). The first letter of the authors’ first name should be listed followed by a period, which in turn, followed by the authors’ complete last name. Use a coma (,) to separate between the authors’ names. Titles of papers or articles should be in quotation marks (“ ”), followed by the title of journal, which should be in italic font. The journal volume (vol.), issue number (no.), page numbering (pp.), month and year of publication should come after the journal title in the sequence listed here.
6. Internal consistency shall also be maintained for other elements of style, such as equation numbering. As a guideline for authors who have no other preference, we suggest that equation numbers be placed in parentheses at the right column margin.

7. The intent and meaning of all text must be clear. For authors who are not masters of the English language, the ACES Editorial Staff will provide assistance with grammar (subject to clarity of intent and meaning). However, this may delay the scheduled publication date.
8. Unused space should be minimized. Sections and subsections should not normally begin on a new page.

ACES reserves the right to edit any uploaded material, however, this is not generally done. It is the author(s) responsibility to provide acceptable camera-ready pdf files. Incompatible or incomplete pdf files will not be processed for publication, and authors will be requested to re-upload a revised acceptable version.

COPYRIGHTS AND RELEASES

Each primary author must sign a copyright form and obtain a release from his/her organization vesting the copyright with ACES. Copyright forms are available at ACES, web site (<http://aces.ee.olemiss.edu>). To shorten the review process time, the executed copyright form should be forwarded to the Editor-in-Chief immediately after the completion of the upload (electronic submission) process. Both the author and his/her organization are allowed to use the copyrighted material freely for their own private purposes.

Permission is granted to quote short passages and reproduce figures and tables from an ACES Journal issue provided the source is cited. Copies of ACES Journal articles may be made in accordance with usage permitted by Sections 107 or 108 of the U.S. Copyright Law. This consent does not extend to other kinds of copying, such as for general distribution, for advertising or promotional purposes, for creating new collective works, or for resale. The reproduction of multiple copies and the use of articles or extracts for commercial purposes require the consent of the author and specific permission from ACES. Institutional members are allowed to copy any ACES Journal issue for their internal distribution only.

PUBLICATION CHARGES

All authors are allowed for 8 printed pages per paper without charge. Mandatory page charges of \$75 a page apply to all pages in excess of 8 printed pages. Authors are entitled to one, free of charge, copy of the journal issue in which their paper was published. Additional reprints are available for a nominal fee by submitting a request to the managing editor or ACES Secretary.

Authors are subject to fill out a one page over-page charge form and submit it online along with the copyright form before publication of their manuscript.

ACES Journal is abstracted in INSPEC, in Engineering Index, DTIC, Science Citation Index Expanded, the Research Alert, and to Current Contents/Engineering, Computing & Technology.